Thermal Investigations on a High-Speed Direct Injection Diesel Engine

A thesis submitted in partial fulfilment of the requirements for the degree of Doctor of Philosophy

Nick Papaioannou

Exeter College

DPhil, Michaelmas 2018

Abstract

Modern compression ignition engines offer higher thermal efficiency compared to gasoline engines, thus offering superior fuel consumption performance and lower CO_2 emissions, a major greenhouse gas. With future legislation pushing the automotive manufacturers for even lower fleet average CO_2 emissions the compression ignition engine can assist in achieving these goals, however further research is required to extend their efficiency.

Understanding where the chemical energy of the fuel is transferred during the combustion process and from that identifying strategies that can assist in converting part of these energy flow terms into useful piston work can help enhance the engine's efficiency. This work looked into the study of these energy flows by using a first law analysis approach and by developing the necessary instrumentation and methods that allow for the more accurate measurement of the various energy flows, subsequently increasing the accuracy of the first law analysis.

Two thermal studies were carried out on a single cylinder diesel engine. The first study investigated the effect of different high-pressure EGR strategies on engine efficiency and emissions, in an attempt to reduce the negative effects of EGR application on soot emissions under two load/speed conditions. The second study compared the effects of different piston material on engine efficiency under two speed/load conditions. A baseline aluminium design, was compared against an alloy steel piston which, due to its lower thermal conductivity, was shown to provide lower heat transfer losses during combustion thus increasing efficiency.

The results of the thermal studies showed that ~40% of fuel energy was transferred to the exhaust. Therefore, being able to accurately measure the exhaust temperature can offer significant insights to engine designers. The exhaust event is highly unsteady and the exhaust temperature is typically measured using a 3 mm sheathed thermocouple which, due to its thermal mass, cannot capture this transient event. Instead, a time-average measurement is only possible. This can result in an under prediction of the exhaust enthalpy since the measured temperature is lower than that of the flow field of interest due to measurement errors.

A lumped capacitance model was developed in order to better understand the behaviour of thermocouple sensors under an unsteady flow environment. The sensors are subject to both dynamic errors, due to their thermal inertia, and conduction and radiation errors due to temperature gradients between the sensor and the surrounding environment. Understanding how different size thermocouples react under unsteady flow conditions has the potential to improve the measurement process and increase the accuracy of the measured exhaust temperature.

A temperature reconstruction method was developed which can correct both the dynamic and conduction errors that are prevalent during the engine cycle, thus approaching the true exhaust gas temperature. This technique requires the use of thermocouples with different thermal masses, thus resulting in a different response under the same flow conditions. This reconstructed temperature then allowed the estimation of exhaust enthalpy on a mass-average basis improving the accuracy of the first law analysis.

Table of Contents

Abstract ii
Contribution to the body of knowledge vi
List of publications vii
Nomenclature viii
Acknowledgements x
1 Thesis Background 1
1.1 Introduction 1
1.2 Diesel combustion, emission formation and legislation 2
1.2.1 Emissions formation 5
1.2.2 Legislation and emissions compliance 10
1.2.3 Emission control and exhaust after-treatment 12
1.3 Improving the thermal efficiency of the diesel engine 17
1.4 Transfer of heat and energy in IC engines 24
1.5 Measurement of temperature using thermocouples 37
1.5.1 Dynamic error using temperature sensors 39
1.6 Conclusions 41
2 Experimental equipment and methodology 43
2.1 Single-cylinder diesel engine 43
2.2 Test cell instrumentation 47
2.2.1 Calculation of output work 51
2.2.2 Heat release analysis 52
2.3 Fuel delivery and measurement 53
2.4 Energy balance measurement methodology 57
2.5 Temperature measurement 58
2.5.1 Coolant system differential thermocouples 58
2.5.2 Exhaust temperature measurements 62
2.6 Emissions measurement 69
2.6.1 Smoke measurement 70
2.7 Estimation of measurement uncertainty 71
2.8 Summary 75
3 Numerical simulations and methodology 76
3.1 First Law Energy balance model 76
3.1.1 Model inputs 79
3.1.2 Model outputs 84
3.2 Thermocouple modelling 87
3.3 Thermocouple dynamic error compensation 101
3.4 Chapter summary 106
4 Thermal studies using a first law analysis approach 107

4.1 Introduction 107
4.2 Evaluation of EGR techniques 110
4.2.1 Experimental methodology 111
4.2.2 Thermal stability 113
4.2.3 Energy balance results 114
4.2.4 Swirl flap effects 118
4.2.5 Constant lambda EGR strategy 125
4.2.6 Conclusions on EGR strategies study 129
4.3 Effect of piston material on energy flows 131
4.3.1 Experimental methodology 131
4.3.2 Results 133
4.3.3 Discussion 144
4.3.4 Conclusions on piston material study 149
4.4 Chapter summary 151
5 Modelling of thermocouple sensors 153
5.1 Introduction 153
5.2 Experimental methodology 155
5.3 Results and Discussion 156
5.3.1 Experimental results 156
5.3.2 Thermocouple modelling results 163
5.4 Chapter summary 173
6 Temperature reconstruction 175
6.1 Introduction 175
6.2 Temperature reconstruction – No conduction and radiation error 180
6.3 Temperature reconstruction – With conduction and radiation error 184
6.4 Mass-average exhaust enthalpy flow calculation 189
6.5 Summary 193
7 Conclusions and further work 194
7.1 Conclusions 194
7.2 Further work 197
7.2.1 Experimental equipment and methodology 197
7.2.2 Numerical simulations and methodology 198
7.2.3 Thermal studies 198
7.2.4 Temperature reconstruction 199
8 References 200

Contribution to the body of knowledge

This section summarises the contribution of this work towards the body of knowledge in the field of diesel engines.

- Modern emission reduction strategies and performance enhancing methods can result in marginal changes in efficiency. Being able to capture the effects of these strategies and assess the energy transfer process around the engine requires a high level of measurement fidelity, which only purpose build sensors can provide (Chapter 2 and 4).
- The effects of conduction error on the measurement of unsteady flows have been highlighted. Conduction along the body of the sensor is a parameter that was previously thought to be insignificant in the measurement of unsteady flows. The effects of conduction have also been shown to be more pronounced in sensors with a small thermal mass thus resulting in a lower temperature measurement compared to sensors with higher thermal mass (Chapter 5).
- A temperature reconstruction method has been introduced which can recover the true gas temperature when the signal of two different size sensors is used. This technique then removes both the dynamic and conduction errors in the measurement. The results of this technique showed a reduction in maximum temperature error of 12 % (Chapter 6).
- The results of the temperature reconstruction method can be used to estimate the mass-average exhaust enthalpy. Since the mass flow rate of the gases is taken into account this provides a better estimate of the exhaust energy. This resulted in an increase of 5 percentage points in the normalised exhaust enthalpy, thus improving the accuracy of the first law analysis method (Chapter 6).

List of publications

i. Papaioannou, N., Leach, F. C., Davy, M. H., Weall, A., & Cooper, B. (2018). *Evaluation of exhaust gas recirculation techniques on a high-speed direct injection diesel engine using first law analysis*. Proceedings of the Institution of Mechanical Engineers, Part D: Journal of Automobile Engineering. https://doi.org/10.1177/0954407017749110

ii. Papaioannou, N., Leach, F., and Davy, M., *"Effect of Thermocouple Size on the Measurement of Exhaust Gas Temperature in Internal Combustion Engines,"* SAE Technical Paper 2018-01-1765, 2018, https://doi:10.4271/2018-01-1765

iii. Papaioannou, N., Leach, F., and Davy, M., *"Thermal analysis of steel and aluminium pistons for a HSDI diesel engine"* SAE Technical Paper 2019-01-0546

Nomenclature

a	Number of moles of CO_2
A_{csa}	Cross-sectional area of thermocouple wire
A_s	Surface area of thermocouple junction
b	Number of moles of CO
Bi	Biot number
bMEP	Brake Mean Effective Pressure
bSFC	Brake Specific Fuel Consumption
c	Number of moles of H_2
CAD	Crank Angle Degrees
CA5	Point of 5% mass fraction burned
CA50	Point Of 50% Mass Fraction Burned
CA50	Point of 50% mass fraction burned
CA90	Point of 90% mass fraction burned
CI	Compression ignition
$c_{p,cool.(T)}$	Heat capacity of coolant
$c_{p,oil(T)}$	Heat capacity of oil
c_p	Heat capacity of thermocouple junction
cv_i	Specific heat capacity under constant volume
d	Number of moles of H_2O
e	Number of moles of O_2
EGR	Exhaust Gas Recirculation
EGT	Exhaust Gas Temperature
f	Number of moles of N_2
F_{lc}	Load cell signal
FSN	Filter smoke number
g	Number of moles of NO_x
h	Convective heat transfer coefficient
H_{abs}	Absolute humidity
ICE	Internal Combustion Engines
iSFC	Indicated Specific Fuel Consumption
j	Number of moles of $C_{7.2}H_{13.3}O_{0.035}$
k	Thermal conductivity
L	Conduction length
L_c	Characteristic length
L_l	Distance from load cell to the centre of crankshaft
m	Mass of thermocouple junction
m_{EGR}	Mass of EGR
$\overline{\dot{m}}_{exh}$	Time-average mass flow rate of exhaust gases
$\dot{m}_{exh}(\theta)$	Instantaneous mass flow rate of exhaust gases
$\dot{m}_f$	Mass flow rate of fuel
m_{fc}	Mass of fresh charge
m_i	Mass of species
M_i	Molar mass of species
$m_{O_2[\mathrm{EGR}]}$	Oxygen mass in EGR
$m_{O_2[fc]}$	Oxygen mass in fresh charge
n	Number of moles of air
N	Engine speed
n_{tot}	Total number of moles
nIMEP	Net Mean Effective Pressure
Nu	Nusselt number
Pr	Prandlt number
$\dot{Q}_{air}$	Energy transfer rate from inlet air
$\dot{Q}_{chem}$	Chemical energy transfer rate to exhaust gases
$\dot{Q}_{cool}$	Energy transfer rate to coolant
$\dot{Q}_{EGR}$	Energy transfer rate of EGR gases
$\dot{Q}_{exh}$	Energy transfer rate to exhaust

$\overline{\dot{Q}}_{exh}$	Time-average energy transfer rate to exhaust
$\hat{\dot{Q}}_{exh}$	Mass-average energy transfer rate to exhaust
$\dot{Q}_{ext}$	Extraneous energy transfer rate
$\dot{Q}_{htr}$	Energy transfer rate of oil heaters
q_{LHV}	Calorific value of fuel
$\dot{Q}_{oil}$	Energy transfer rate to oil
R	Universal gas constant
Re	Reynolds number
S_R	Swirl ratio
T_0	Ambient temperature
T_c	Temperature of reference junction
T_{diff}	Signal from differential thermocouple
$\overline{T}_{exh}$	Time-average temperature of exhaust gases
$\hat{T}_{exh}$	Mass-average temperature of exhaust gases
T_g	Instantaneous exhaust gas temperature
$T_{g(i)}$	Exhaust gas temperature at current time-step
T_h	Temperature of hot junction
T_{HPP}	Parasitic torque associated with high pressure fuel pump
T_{ref}	Temperature of 3 mm sheathed thermocouple
T_s	Thermocouple junction temperature
$T_{s(i)}$	Thermocouple junction temperature at current time-step
$T_{s(i+1)}$	Thermocouple junction temperature at next time-step
T_w	Exhaust pipe wall temperature
T2	Temperature of 50.8 µm thermocouple
T5	Temperature of 127 µm thermocouple
T10	Temperature of 254 µm thermocouple
TC	Thermocouple
$\dot{v}_{cool.}$	Volume flow rate of coolant
$\dot{v}_{(oil)}$	Volume flow rate of oil
VCV	Volume Control Valve
$\dot{W}_{HPP}$	Energy transfer rate to fuel pump
$\dot{W}_{shaft}$	Engine power output
$Y_{O_2[intake]}$	Intake oxygen mass fraction
γ	Polytropic coefficient
δ	Slope of fitted line
ε	Emissivity of thermocouple junction
ζ	Weight factor for exponential moving averaging
κ	Equilibrium gas constant
μ_0	Dynamic viscosity of air at free-stream conditions
μ_b	Dynamic viscosity of air at thermocouple surface
$\rho_{cool.(T)}$	Density of coolant
$\rho_{oil(T)}$	Density of oil
σ	Stefan-Boltzmann constant
σ_T	Standard deviation
τ	Time-constant

Acknowledgements

My biggest thanks, first, for giving me the opportunity to pursue this project, and also for his constant support and guidance go to my supervisor Dr. Martin Davy. I would also like to thank Dr. Felix Leach for his help and guidance. I would additionally like to thank Prof. Richard Stone for his immediate support when required.

Regarding project funding, I would like to thank Jaguar Land Rover for the project hardware and their financial support and on a personal level, Drs Antonis Michailidis and Adam Weall for their guidance. I would also like to thank EPSRC for their funding, without which I could not pursue this project.

Regarding the technical staff, I would like to thank Greg Maddock, David Ilsley, Stephen Skelton, Grzegorz Kornasiewicz, Graham Haynes and Maurice Keeble-Smith for their technical support and input when required. I would also like to thank Bob Yapp, Colin Smith and Darren Solden for their assistance throughout these years.

A big thank you goes to my colleagues, Joseph Camm, Safwan Hanis and Johannes Mutzke, of the Combustion group and Kun Liang and Ian Berryman of the Cryogenics group for their help, support and times of laughter. I would also like to thank everyone that I met through my involvement in the Greek society, as well as the football and the basketball teams, for taking my mind away from this challenge and allow me to have some fun. The list of names is too long but you know who you are.

Most importantly, I would like to thank Riyaz Ismail, Marc Perez Soriano, Xiaohang Fang, Blane Scott, Christina Palmou and Maika for the endless discussions we had about the future, on failure, success and life in general and the great times that we had in 58 Stratford Street. Your company and support helped me immensely.

Finally a big thank you goes to my family and friends back home whom all these years have continuously supported me in my endeavours and were the continuous recipients of my stress, anger and struggle.

1 Thesis Background

An introduction to diesel engines and the diesel combustion process will be presented along with the most important emissions and their formation mechanisms. Legislative measures will also be discussed along with the various test cycles used for emissions approval as set by the various governing bodies. A brief introduction to the various exhaust after-treatment systems used to reduce tailpipe emissions is also presented. Since these after-treatment systems can have a negative impact on the efficiency of the diesel engine, common methods to alleviate these penalties are also discussed. Finally, the energy balance approach is presented as a method of assessing various engine emissions and performance enhancing strategies, along with the operating principles of thermocouple sensors, which have been extensively used in this work.

1.1 Introduction

With approximately 380 million commercial vehicles on the road today [1] – 90% of heavy duty trucks are powered by compression ignition engines [2] – and the significant dieselisation of the light-duty sector (i.e. passenger cars) the use of diesel fuel has seen an eight-fold increase since 1970 [3]. Diesel passenger vehicles are primarily sold in Europe – with the European market accounting for 65% of global diesel car sales, and with India and South Korea being the other two regions where diesel passenger vehicles are a popular choice (12% and 6% respectively of global diesel car sales) [4].

Increased demand for diesel vehicles is due, for the most part, to the diesel's higher efficiency compared to their gasoline counterparts and their lower CO_2 emissions – CO_2, a direct product of hydrocarbon combustion, is a powerful greenhouse gas (GHG) that is believed to be the major anthropogenic contributor to recently reported rises in the earth's

surface temperature. However, the aftermath of the Dieselgate scandal has marked a significant change in market trends since for the first time since 2009 the gasoline vehicles sales are higher – on EU average terms – than diesels (50% versus 44%) [5]. Provisional reports from the European Environmental Agency (EEA) showed an increase of 1 g/km CO_2 in fleet average CO_2 emissions for 2017 [6]; a first ever increase in the previously declining trend since the introduction of the European Union's (EU) CO_2 emissions limits in 2008 [5]. This was attributed to the combination of reduced diesel vehicle sales as well as to a shift from small-size gasoline cars (with low CO_2 emissions) to medium-size and sports utility vehicles (SUVs) that are heavier and thus tend to emit more CO_2 [5, 7].

Despite this shift in market trends the advantages in fuel consumption associated with the diesel engine are still higher and are expected to help manufacturers reduce their fleet average CO_2 emissions targets [4]. Fleet electrification is also expected to help achieve these emissions limits, however, current limitations in battery technology and infrastructure prevents the widespread use of battery electric vehicles; rather, a hybrid powertrain—a combination of an ICE and an electric motor—can provide a better compromise between driving range and emissions, especially when emissions are considered on a well-to-wheel basis. Thus research and development in modern diesel engines is more important than ever. The next section will introduce the basic operating principles of diesel combustion along with major pollutants and the respective emission legislation.

1.2 Diesel combustion, emission formation and legislation

The most distinct difference between compression and spark ignition engines (apart from fuel composition) is the process of igniting the fuel/air mixture. Spark ignition engines

use a spark plug and an electric discharge across its electrodes (i.e. spark) initiates the combustion process. CI engines on the other hand, rely on the autoignition of the diesel fuel to initiate combustion. As the compression ratio (CR) of CI engines is significantly higher, CI engines generally present higher thermal efficiencies than SI engines – improvements are also due to the lower pumping losses of the CI engines as they generally do not operate an intake throttle. Moreover, as the properties of air approach those of an ideal gas, efficiency gains in diesels are also expected due to the lower heat losses during the compression stroke, compared to the gasoline engines where a fuel/air mix is compressed prior to combustion. The high pressure and temperature associated with high CR, combined with very high injection pressures (typical diesel injection pressures range from 800-2500 bar) result in a sequence of events that involves, fuel droplet breakup and atomisation, droplet vaporisation, fuel vapour/air mixing and eventually autoignition and start of combustion.

Combustion in diesel engines can be divided in two parts, a pre-mixed phase and a mixing controlled phase. Pre-mixed combustion initialises the combustion process at an area close to the vapour length of the jet where rich fuel/air vapour exists and is usually associated with high rates of heat release [8]. Once pre-mixed combustion is initiated, mixing controlled combustion takes over, forming a diffusion flame where – under lower heat release rates – fuel, air and combustion products are entrained in a thin reaction zone and burn stoichiometrically. Figure 1.1 illustrates a fully developed diffusion flame (its boundary is marked in orange) in terms of a single fuel jet, where the different emission formation zones and temperature distributions can be seen. Of course this illustration is an idealised case, as in real life applications, where multi-hole injectors and high levels of in-cylinder swirl are employed, jet-to-jet interactions are expected to occur, which can have an effect on emission fuel/air mixing and emission formation [9, 10].

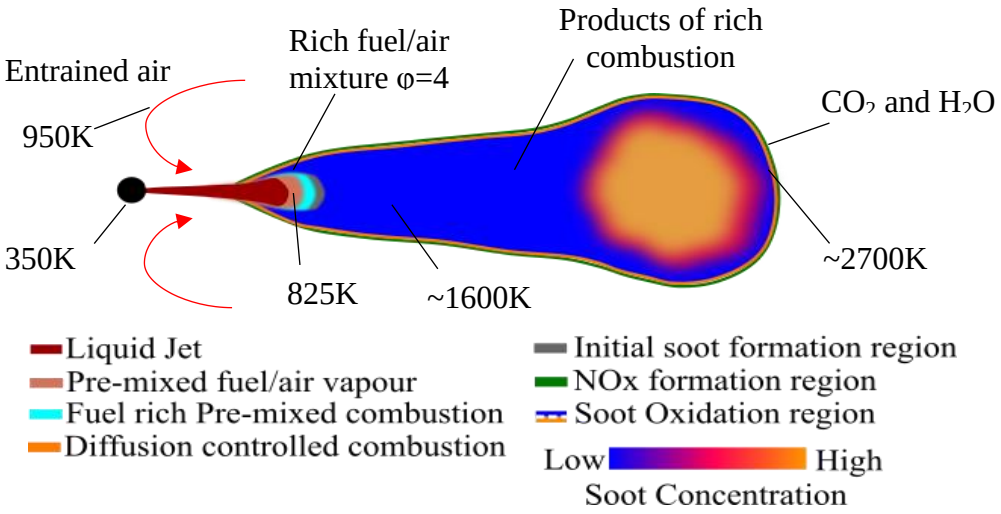

Figure 1.1: Schematic of fully developed diesel jet combustion. Adapted from [11]

Control over the diesel combustion process can be achieved by using several injection events during the cycle, namely; pilot, main and post depending on the timing of the injection event. In broad terms, pilot injections occur before Top Dead Centre (TDC) (i.e. -20 – 0 crank angle degrees (CAD)), main injections around TDC (i.e. 0 – 15 CAD) and post injections late in the cycle (i.e. 30 – 45 CAD). These can have an effect on combustion noise (pilot injection, [12-15]), the main combustion process, power output and tailpipe emissions (main injection, [16-23]) and emission reduction (post injection, [13, 18, 22]). Advancements in fuel injection equipment (FIE), both in terms of peak injection pressure and number of injections during the cycle [24], have significantly improved the level of control over the combustion process in modern diesel engines; leading to higher power output and reduced emissions due to improved fuel/air interaction [12, 18, 25].

However, despite the improvements, offered by advances in FIE, automotive manufacturers are still required to employ further emission reduction techniques and exhaust after-treatment systems to comply with legal emissions limits. The next section

will discuss the most common diesel emissions and their formation mechanisms along with the different legislative limits as introduced by different governing bodies.

1.2.1 Emissions formation

In the following section the most significant emissions from diesel engines will be presented along with a brief explanation of their formation reactions and mechanisms. The emissions that will be considered are nitrogen oxides ($NO+NO_2$), particulate matter (PM), carbon dioxide (CO_2), carbon monoxide (CO) and hydrocarbons (HC).

1.2.1.1 Nitrogen oxides

Mono-nitrogen oxides, comprising nitric oxide (NO) and nitrogen dioxide (NO_2) and jointly referred to as NO_x emissions, are major pollutant emissions of diesel engines. NO_x emissions from diesel engines are dominated by the in-cylinder production of NO, a fraction of which – 10-30% [26, 27] – may be oxidised to NO_2. NO_2 production, and the reduction of NO_2 to NO which may occur post-combustion in oxygen rich regions of the cylinder [27], is expressed by the following reactions [28]:

$$NO + HO_2 \leftrightarrow NO_2 + OH \tag{1.1}$$

NO_2 converts to NO through the following reaction:

$$NO_2 + O \leftrightarrow NO + O_2 \tag{1.2}$$

Emitted NO_2 may react in the atmosphere with the OH radical to produce acid rain and, in the presence of UV light, with volatile organic compounds to produce photochemical smog.

There are three accepted NO formation mechanisms during the combustion process; thermal NO production governed by the so-called extended Zel'Dovich mechanism,

"prompt" NO produced through the Fenimore mechanism, and the production of NO from fuel bound nitrogen. Since the composition of diesel fuel does not include significant amounts of nitrogen, this third mechanism will not be considered further.

1.2.1.2 "Thermal" NO

The governing equations for the extended Zel'Dovich mechanism are:

$$O + N_2 \leftrightarrow NO + N \tag{1.3}$$

$$N + O_2 \leftrightarrow NO + O \tag{1.4}$$

$$N + OH \leftrightarrow NO + H \tag{1.5}$$

Equations (1.3) and (1.4) were the reactions originally proposed by Zel'Dovich [1946], as found in Stone [29]. It is generally accepted that the first equilibrium equation, i.e. Equation (1.3), is limiting the formation rate of "thermal" NO_x due to its high activation energy (fast formation rates require high temperatures), associated with the strong triple bond in the N_2 molecule [30]. Equation (1.5) was introduced by Lavoie *et al.* [31] and has been shown to contribute significantly to the overall NO_x concentration, especially at lean, low temperature conditions.

Thermally bound NO is formed in the presence of high temperatures (T > 1800 K) in oxygen rich (lean) regions of the flame and when there is sufficient time for formation as the reaction rates are very slow compared to the combustion rates [29].

1.2.1.3 "Prompt" NO

The "prompt" mechanism is based on the rapid NO formation at fuel rich regions of the flame. This was postulated first by Fenimore [32], who suggested that the rate of nitric

oxide formation at fuel rich regions is not governed by the direct oxidation of the nitrogen molecules, as in the thermal mechanism.

Extended research has shown that "prompt" NO is formed by the rapid reaction of hydrocarbon radicals (most notably CH and CH_2 [33]) with cyano-compounds (e.g. NCN, HNC, NCO, CN, HCNO) or amines, which consequently form NO [34-38], as shown in Equation (1.6):

$$CH + N_2 \leftrightarrow NCN + H \tag{1.6}$$

which may lead to NO formation through the following reactions:

$$NCN + O \leftrightarrow CN + NO \tag{1.7}$$

$$NCN + OH \leftrightarrow NO + HNC \tag{1.8}$$

$$NCN + O_2 \leftrightarrow NO + NCO \tag{1.9}$$

Due to the lower activation energy of the "prompt" NO in contrast to the "thermal" NO, "prompt" NO will still be produced at low temperatures (~1000K) [30].

1.2.1.4 Particulate matter (PM)

Particulate matter is a complex form of aerosol emissions usually associated with the black smoke produced by diesel vehicles [39]. It primarily consists of two parts; solid carbon material (soot) and an organic part which consists of unburned hydrocarbons and other volatile chemical species that have been absorbed by the soot particles during combustion or expansion phase [40]. It has been shown that PM can be deposited onto the lungs after inhalation thus causing a health hazard. Soot particles start as spherules with size approximately 20-50nm [41]. As the soot formation process progresses, the spherules start to agglomerate into aggregates and form cluster or chain-like spherule structures

which are considered as soot particles [26]. It is generally accepted that soot particles are formed from unburned hydrocarbons, with the main precursors being acetylene and polycyclic aromatic hydrocarbons (PAH), following the pyrolysis of the fuel under highly rich conditions usually found in the core of the liquid fuel jet during injection [8].

Dec [8] presented a very comprehensive concept of the diesel flame ignition and propagation postulating that soot and NO_x emission formation occurs around and inside the flame envelope (Figure 1.1). As the injection event progresses, air is entrained into the core jet, soot particles which are formed in the fuel rich core are displaced out of the jet, towards the thin flame reaction zone, and begin to oxidize in the high temperature "thermal" NO_x production zone. Any soot particles that fail to oxidize in the later stages of combustion, eventually become particulate matter [25]. Heywood [26], states that soot production stops as soon as the injection finishes. That could be attributed to the fact that pyrolysis of the fuel has stopped, as the fuel rich jet is getting progressively leaner and the soot oxidization process has begun. The majority of the soot is oxidized before the exhaust gases are expelled through the exhaust valves.

1.2.1.5 Hydrocarbon emissions

Hydrocarbon emissions (HC) or organic emissions, are the product of incomplete combustion and thus directly connected to fuel consumption and combustion efficiency. Hydrocarbon emissions in general are not of great concern in diesel engines, since in contrast to conventional gasoline engines, the overall mixture strength is usually considerably leaner than stoichiometric. One contributor to HC emission in a conventional diesel engine is the dead volume created by the nozzle and the needle of the injector (sac-hole volume). After the termination of injection events, unburned fuel is trapped in this volume which later evaporates, thus increasing HC emissions [42].

The second significant source of HC in diesel engines is incorrect mixture preparation, i.e. the over mixing (over leaning) or under mixing of the charge. If the ignition delay is too long, this could lead to pockets of fuel that are excessively diluted. Ignition and combustion in these over-diluted regions is not possible. If the mixture is excessively rich, the lack of oxygen will similarly prevent self-ignition and combustion.

1.2.1.6 Carbon monoxide (CO)

Carbon monoxide is a product of incomplete combustion and is usually formed in fuel rich mixtures. Since the standard diesel cycle operates at very lean overall mixture strengths, CO emissions are usually not a concern.

However, in special operating regimes, like low temperature combustion (LTC), where temperatures are lower than usual and the mixtures tend to be richer, CO emissions tend to increase [43]. Note that the richer charge is due to the increased EGR rates employed in the majority of LTC strategies. EGR displaces oxygen molecules thus leading to decreased oxidation rates. As with HC emissions, mechanisms that lead to better air utilisation in the cylinder generally lead to a reduction of CO concentration at the exhaust—increased injection pressure, advanced injection timing and increased swirl all promote more complete combustion.

1.2.1.7 Carbon Dioxide (CO_2)

Carbon dioxide is a product of organic combustion and one of the main contributors to environmental pollution. The transport sector accounts for ~16% of the global carbon footprint produced by human activities, with road-going vehicles contributing the bulk of this amount [44, 45].

As a product of organic combustion CO_2 is directly linked to fuel consumption and engine efficiency. Considering that diesel engines have reduced pumping losses due to

the lack of a throttle plate and higher compression ratios which lead to higher cycle efficiencies, compared to their spark ignition counterparts, the fuel consumption and consequently CO_2 emissions will be significantly lower. More specifically, it is claimed that diesel engines have a ~3% CO_2 advantage over their gasoline counterparts (123 g/km vs 119 g/km) [7].

1.2.2 Legislation and emissions compliance

Following the various health and environmental concerns, agencies around the world have created different emission standards for internal combustion engines, which vary based on vehicle type (on-road, off-road, locomotive, etc.), vehicle weight (passenger car, heavy-duty vehicles, etc.) and fuel (gasoline or diesel). The major regulatory bodies for emissions control are: the California Air Resource Board (CARB) and the Environmental Protection Agency (EPA) in the US, the European Environmental Agency (EEA) and in Japan, a joint collaboration between government ministries and an advisory board called the Central Environment Council (CEC).

The regulatory bodies previously mentioned also specify testing procedures (i.e. driving cycles) in an attempt to simulate the driving conditions that vehicles are exposed to in their respective areas of operation. There are fundamental differences between the various driving cycles primarily due to their origin; the Federal Test Procedure (FTP) in the US is designed around motorway driving where the engine loads are higher, whereas the New European Driving Cycle (NEDC) in Europe mostly consists of constant cruising speeds and variable acceleration rates [42]. However, a growing body of evidence shows a significant divergence between official CO_2 and on-road, "real" CO_2 results from 2001 onwards, with the discrepancies being as high as 40% in 2016 (

Figure 1.2) [46]. Following this increasing trend, the European Commission introduced in 2017 the Worldwide Harmonized Light vehicles Test Procedures (WLTP) with the intent to replace the current NEDC approval test by using a more realistic laboratory test cycle [47].

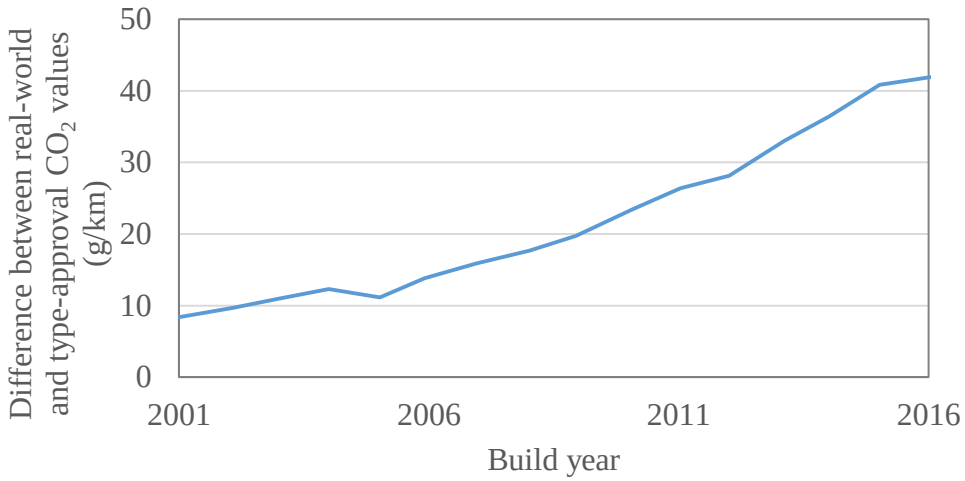

Figure 1.2: Average difference between real-world and type-approval CO_2 emission values for passenger vehicles in Europe [46].

Complimenting WLTP laboratory testing, the Real Driving Emissions (RDE) test procedure was also introduced by the European Commission. RDE is currently under a phase-in period (from 2017) and will be in full effect for all new vehicles from 2021 onwards [48]. RDE testing aims to measure vehicle emissions during on-road driving using an on-board Portable Emissions Monitoring Systems (PEMS) [49] and compare these results to laboratory approval tests – legally compliant Conformity Factors (CF) have been established that describe the ratio between RDE and laboratory results, with a temporary CF of 2.1, which from 2021 will be set to a CF of 1. The driver behind this policy was, similar to the observed CO_2 emission trends the increasing divergence between lab-based and on-road emissions. Recent studies have shown that EURO 6 approved type vehicles could result in 5-16 times higher NO_x emissions compared to the

legal limit when driven in RDE-compliant routes and 26-40 times higher under unregulated dynamic driving conditions [50].

This then goes to show the increasing need for emission reduction in IC engines, a process which can be achieved in two ways; at-source (i.e. by improving the combustion process) and at the tailpipe, using several after-treatment systems. The next section will introduce the most common emission reduction methods used in diesel powered vehicles.

1.2.3 Emission control and exhaust after-treatment

1.2.3.1 Emission reduction at source

A popular solution to the reduction of NO_x emissions at source is the introduction of recirculated gases from the exhaust cycle into the cylinder during the intake stroke – a process known as exhaust gas recirculation (EGR). Significant efforts have been made by researchers in order to understand the effects of EGR on the combustion process and how these affect emission formation [26], [43], [51]. Ladommatos *et al.* [51] carried out extensive experiments trying to pinpoint the exact effects of EGR on NO_x and soot formation. Ladommatos and co-workers suggested that five different factors can affect the inlet charge composition; the dilution effect (reduction of oxygen concentration), thermal throttling (reduced inlet charge mass), the chemical effect (introduction of combustion products into the charge), the thermal effect (rise in specific heat capacity of the charge) and the effect of inlet temperature (increase in the temperature of the inlet charge). From these five effects, they showed that the majority of the NO_x reduction was due to the dilution effect of EGR resulting in the displacement of available oxygen in the cylinder by carbon dioxide. This research also showed that the effect of increased heat capacity, due to the introduction of the CO_2, has an almost insignificant effect on the NO_x formation, contradicting the earlier work of Heywood [26].

Many researchers have shown that the use of EGR as a method of controlling NO_x emissions can have an adverse effect on soot emissions due to the reduced oxygen presence and lower in cylinder temperatures that tend to reduce the oxidation rates of soot particles. [52, 53]. This highlights the well-established NO_x-soot trade-off problem, seen in diesel engines, where an improvement in NO_x emissions is usually to the detriment of soot emissions and vice-versa. Figure 1.3 shows this trade-off on a φ-T map which indicates the local equivalence ratio against temperature. The red line indicates a possible path that the fuel element can follow during normal diesel combustion. The displacement of O_2 by EGR will lead to a higher equivalence ratio during the premixed part of combustion and consequently to a bigger excursion into the soot island as the combustion process evolves. Since combustion rates and peak cylinder temperatures will be reduced so will NO_x emissions. The displacement of oxygen is also expected to increase mixing times, resulting in slower combustion and to a deviation from a constant volume heat addition process, thus increasing heat transfer losses and decreasing efficiency.

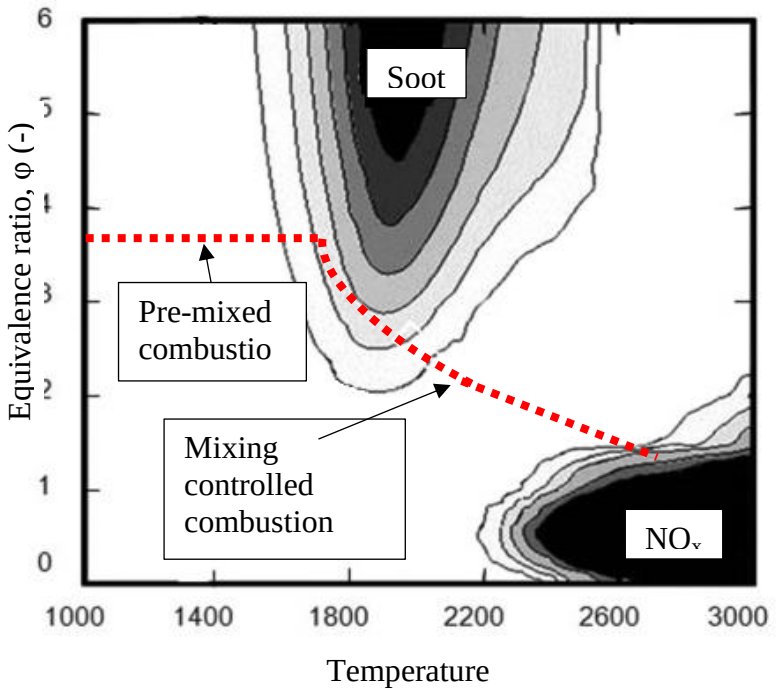

Figure 1.3: φ-T graph for normal diesel combustion. Adapted from [54], [55].

In order to improve this deterioration in fuel/air mixing due to lack of available oxygen, Ladommatos *et al.* [51] suggested the use of "additional" EGR, by which they described the introduction of EGR without oxygen displacement, in a similar fashion to an SI engine. This technique resulted in an increase in the total trapped mass in the cylinder and according to the authors led to a reduction in NO_x emissions, compared to no EGR introduction, and to an improvement in soot emission compared to standard EGR application. On a diesel "additional" EGR can be achieved by increasing the boost and exhaust back pressure simultaneously [56].

Recent developments in diesel fuel injection hardware have enabled further improvements in the engine out emission performance of the diesel. Since the introduction of the common rail system by Bosch in 1997 [57] the achievable operating pressure has significantly increased (Figure 1.4), independent of engine speed, along with the flexibility over the combustion process, since the injection duration became shorter and the allowable number of injections per cycle increased. The increase in injection pressure leads to better fuel vaporisation and hence better mixing and an increase of the air entrainment in the jet [25]. An improvement in air entrainment leads to better fuel/air mixing consequently leading to a reduction in soot emissions [12].

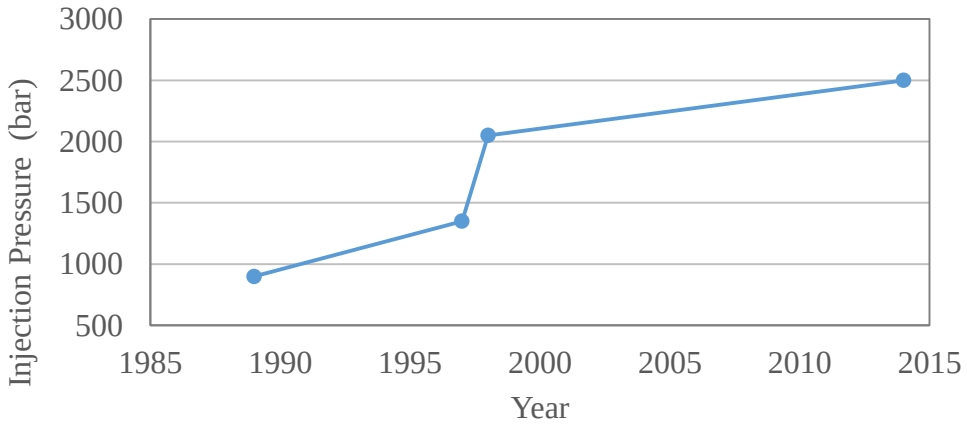

Figure 1.4: Evolution of maximum injection pressure limits in diesel FIE [24]

Another way of improving in-cylinder oxygen utilisation is by increasing in-cylinder swirl levels. Due to the nature of the diffusion combustion, swirl leads to improved mixing of the in-cylinder charge resulting in lower soot and CO emissions. Swirl enhanced mixing can thus allow for an increase in charge dilution (i.e. higher EGR rates), therefore reducing or keeping NO_x emissions at the same level [10]. The in-cylinder swirl levels can be altered with the use of a swirl flap, which is essentially a throttle device that acts to divert the induced air through an appropriately shaped port (i.e. swirl port) that is forcing the inlet flow in a rotating path about the cylinder axis. A typical configuration of a standard and a swirl port design is presented in Figure 1.5.

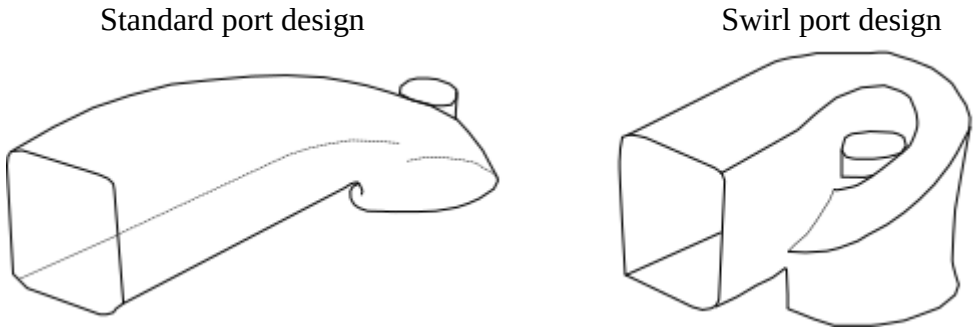

Figure 1.5: Standard and swirl port configuration. Adapted from [58]

Swirl has been shown to affect the fuel spray shape as well as the interaction of adjacent sprays [9]. The effect of swirl is to deform the fuel jet in the direction of swirl as can be seen in Figure 1.6. Miles [10] suggested that swirl can effectively transfer fuel and combustion products from the upstream side to the downstream side of the plume (with reference to the swirl direction), which could be the reason for the variations in the stoichiometry of the plumes under a pilot injection event reported by Sahoo *et al.* [59]. This deformation tends to shift the location of initial combustion away from the centreline of the jet, where fuel rich conditions exist, to a region of lower equivalence ratio.

Consequently, fuel replenishment of high temperature regions is avoided which in conjunction with the increased air entrainment tends to decrease soot formation.

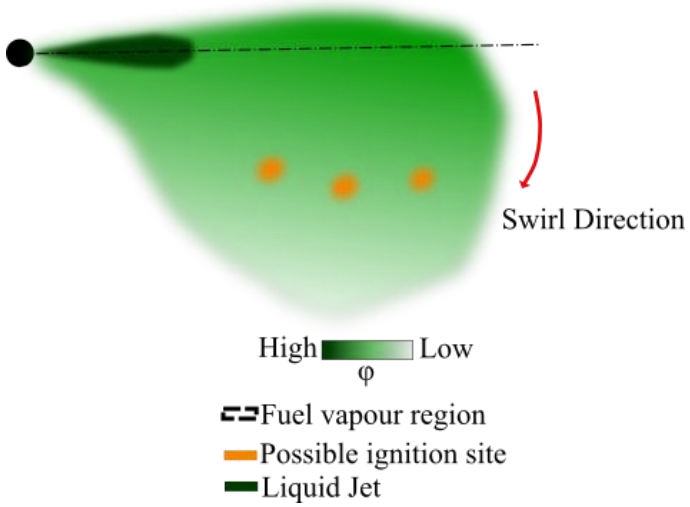

Figure 1.6: Fuel spray combustion due to swirl interactions. Adapted from [60]

1.2.3.2 Exhaust after-treatment

The most common after-treatment methods currently seen in modern diesel engines are, Diesel Oxidization Catalysts (DOCs), Nitric oxide reduction (De-NO_x) techniques such as Lean NO_x Traps (LNTs) and Selective Catalytic Reduction (SCR) systems and Diesel Particulate Filters (DPFs) [49]. DOCs are used to oxidize HC, CO and the Soluble Organic Fraction (SOF) absorbed by the soot particles thus reducing the PM emissions by up to 30% [61]. DOCs also increase the fraction of NO_2 in the exhaust to increase the conversion efficiency of the DPFs and the LNTs as they are usually located downstream from the DOCs' location (LNT systems are usually placed downstream from the DPFs [61]).

LNTs work under the principle of storing the NO_x molecules until the exhaust gas temperature is high enough to reduce them (regeneration mode) [62]. SCR systems on the other hand, utilise injections of urea-water mixture – Diesel Exhaust Fluid (DEF) – to reduce NO_x emissions into nitrogen. SCR systems have higher conversion efficiency than

LNTs (up to 95%) and are thus preferred on higher displacement engines (i.e. >2L) [49]. Lastly, DPFs are used to capture particulates in the exhaust stream. Their conversion efficiency is equally high, (95%) including ultra-fine particles (i.e. up to 100 nm diameter) [41].

Diesel after-treatment systems have a very discrete function; they are enablers for emissions compliance but do not enhance performance or efficiency (in fact, there are unavoidable performance and efficiency penalties associated with the operation of after-treatment systems [63]). This goes to show that emission reduction (either by reduction at source or by after-treatment systems) will come with a compromise in terms of engine efficiency and CO_2 emissions. In order for CI engines to keep their competitive advantage over their SI counterparts, several methods of improving engine efficiency have been implemented and continue to be developed. The next section will discuss some of these methods.

1.3 Improving the thermal efficiency of the diesel engine

An increase in thermal efficiency can be achieved (assuming that the pumping work and friction losses remains constant) by either improving the progression of the combustion process or by reducing the heat transfer to the surrounding surfaces during the combustion process, thus increasing the extracted work from the expanding gases. Numerous techniques have been developed over the years based upon these two principles however exhaustive coverage of those is outside the scope of this work. Only techniques used in the experimental studies presented later in this work are discussed.

A higher cylinder charge density is known to increase engine performance and efficiency. Turbochargers are nowadays an integral part of modern diesel engines, significantly increasing their power density and reducing the need for large displacement designs. This

in turn leads to reduced friction losses, due to downsizing, and consequently to higher thermal efficiencies. Higher charge density can also have a direct impact on the combustion process itself. Detailed spray studies have shown that as the ambient pressure in the cylinder chamber increases, spray atomisation is enhanced due to a higher rate of droplet breakup [25, 64]. This in turn increases the air entrainment in the spray and thus has the potential to reduce ignition delay and enhance combustion burn rates and efficiency. However, excessive boosting can have a negative effect on efficiency due to the higher back-pressure required to drive the EGR gases and also the higher heat capacity of the charge, which increases heat transfer losses [56].

The advantages of increased in-cylinder swirl on soot and CO emissions due to improved fuel/air mixing have already been discussed. Further to this, higher mixing rates lead to a reduction in ignition delay and faster burn rates, as fuel and air molecules interact more readily. Consequently this can result in increased thermal efficiency, as faster burn rates result in higher peak cylinder pressures and thus an increase in indicated work. However it should be noted that significant amounts of swirl can have an adverse effect on engine performance.

Different methods of measuring and defining the levels of swirl in the cylinder have been developed over the years. A common method of measuring the angular velocity of swirl is with the paddle wheel anemometer and by assuming a forced vortex structure for the flow. The angular velocity of the paddle wheel can then be considered equal to the angular velocity of the flow, assuming no slip between the flow and the vanes of the paddle wheel. As the magnitude of swirl is dependent on engine speed, some form of parametrisation would be useful. This is given by the swirl ratio which is defined by Stone [29] according to Equation (1.10).

$$S_R = \frac{\text{Speed of the swirl (RPM)}}{\text{Speed of the engine (RPM)}} \quad (1.10)$$

Miles [10] has shown that swirl affects the pre-mixed mass burned, with the highest mass burned seen under intermediate levels of swirl (i.e. S_R=2.5). Kook *et al.* [55] has also observed the effects of swirl on fuel conversion efficiency under a low temperature combustion regime. He concluded that very high values of swirl ratio (S_R>5) led to a deterioration of thermal efficiency due to increased heat transfer losses from the faster moving charge.

The way that swirl motion affects the combustion process is part of a complex interaction between the in-cylinder air motion and the piston bowl shape. As the piston is approaching TDC the swirl-driven air is forced into a toroidal shaped vortex which is guided by the bowl design and the squish generated flow – this is defined as the inward moving flow structure (w.r.t to the cylinder axis) resulting from the squeezing of the air located in the piston topland region by the upward motion of the piston (Figure 1.7). The interaction between the intake-generated swirl flow and the squish flow, results into a double vortex structure, which has been shown to affect oxygen utilisation, by bringing otherwise "unused" air closer to the spray plume region, thus improving performance and soot oxidation [65].

Figure 1.7 shows the interaction of the squish flow (red arrows) with the bulk flow structure (blue arrow) along with the centreline of the spray, usually directed in such a way as to maximise the fuel/air mixing process. A change in the piston topland region, is thus expected to have a direct impact on the effects of the squish flow penetration. In addition, under higher swirl numbers, the squish flow penetration is impeded by the

increased centrifugal forces, thus confining the lower vortex deeper into the bowl and reducing mixing rates [66].

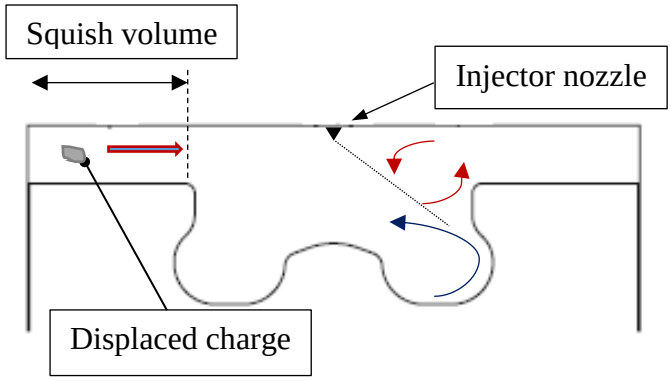

Figure 1.7: Flow structure interactions in a re-entrant bowl design piston. The red arrows represent the squish flow structure and the blue arrows the main flow structure. Adapted from [66]

The highly complicated nature of fuel/air interactions is thus a process that requires the optimisation of the combustion system as a whole, taking into account, the piston bowl design and fuel spray targeting. Depending on the bowl geometry, the fuel jet will impinge on the piston wall rim and follow the bowl radius, which will eventually divert its course back towards the centre of the cylinder (this will depend on the swirl magnitude). In general, spray impingement is undesirable, as it has been shown to increase soot emissions due to flame quenching upon contact with the piston walls [67]. This is one of the reasons for the increasing use of wide piston bowl designs (i.e. >60% of the bore diameter) in modern diesel engines [68]. At higher loads, where more fuel mass is injected, a wider bowl diameter tends to reduce the amount of spray impingement thus enhancing fuel/air mixing. This is especially important as peak power is limited by the mixing-controlled part of the diffusion combustion.

Spray impingement however, cannot always be avoided and wide bowl designs have been shown to increase emissions at lower load conditions [69, 70]. As a result, researchers

have investigated different ways of taking advantage of such fuel-jet/piston wall interactions to alleviate these negative effects. Dakhore *et al.* [71] tailored the fuel-jet/wall interaction in a medium-duty diesel engine to improve cylinder mixing by altering the piston lip geometry. This, combined with an optimised injection strategy such that the impinging jet was deliberately split in two parts using the piston lip (Figure 1.8), resulted in an improved utilisation of the air in both the squish and piston bowl regions which lowered soot emissions and increased combustion efficiency.

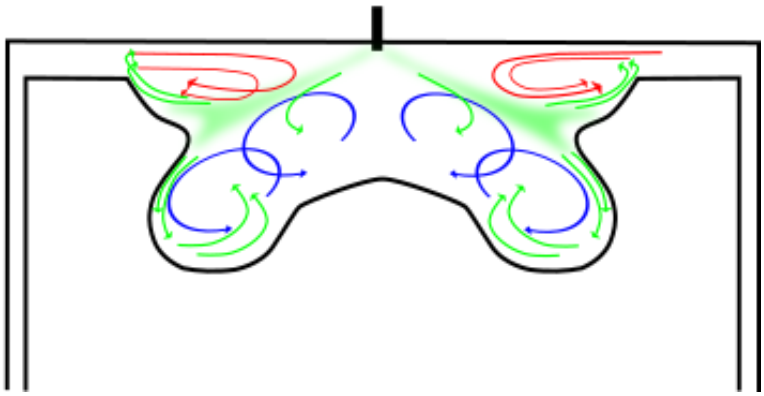

Figure 1.8**:** Fuel jet splitting utilising the piston lip design. Adapted from [71]

The concept of matching the combustion chamber design with the injection system characteristics was also investigated by Leach *et al.* [72, 73]. In their work they have shown that the protrusion length of the injector nozzle can have a significant effect on the progression of the combustion event (and consequently emissions) depending on the piston bowl shape. More specifically, comparing a stepped bowl piston to a standard bowl design they observed that the stepped bowl resulted in increased combustion duration, a finding that contradicts previous studies [71, 74]. Numerical simulations attributed this to a flame "hold-up" effect at the piston lip, slowing combustion progression. Despite this, their work concluded that a stepped piston bowl can have the potential to increase power output under full-load operation, as the slower combustion duration allowed for more

advanced injection timings, compared to the standard bowl, a parameter constrained by a maximum cylinder pressure limit.

The combustion chamber design also affects the resulting heat transfer to the piston. Since the piston surfaces are a moving boundary of the combustion chamber, potential improvements in piston heat transfer can have a direct impact on engine performance. The extended use of wider piston bowl designs despite the positive effects on spray impingement can lead to an increase in heat transfer losses due to a higher surface area-to-volume ratio (i.e. a bigger area exists to absorb the heat of combustion) [75]. When this is combined with a high compression ratio the heat losses are expected to increase further.

In order to fully utilise the benefits of a higher compression ratio on engine efficiency, the potential penalty in heat transfer must be minimised. With this in mind, Arato *et al.* [76] used numerical methods to optimise the piston bowl design of a high-compression ratio engine. The proposed design was a shallow dish-like bowl which reduced spray impingement and the amount of "re-entrancy" thus reducing turbulence levels. When this piston was installed on a single cylinder diesel engine, the reported improvements in indicated specific fuel consumption (isfc) were in the order of 3%, along with a reduction in heat transfer losses and an increase in exhaust enthalpy.

Several studies on reducing heat transfer in ICEs using ceramic coatings have also been carried out. The most common ceramic based coating used is yttria-stabilized zirconia (YSZ) which has been shown, when applied on a heavy-duty diesel engine piston, to reduce the instantaneous piston heat flux [77]. However this and similar studies [78, 79] were not conclusive with regards to thermal efficiency improvements, possibly due to the penalty observed in volumetric efficiency associated with the higher piston surface temperatures and consequently higher charge temperatures.

In order to overcome the aforementioned disadvantages, researchers have developed new coating materials (silica reinforced porous anodised aluminium – SiRPA) that allow the combustion chamber surfaces to follow the transient gas temperature during the cycle much closer [80-83]. Due to their low thermal conductivity and heat capacity, these coatings result in faster cooling during the exhaust and intake strokes, which reduces combustion chamber temperatures and thus does not impede volumetric efficiency. At the same time, higher surface temperatures at the point of peak gas temperature are achieved, thus lowering the temperature gradient between the wall and the gases, and consequently reducing convective heat losses. The on-engine application of this coating on a diesel piston led to an improvement in fuel consumption (2%) and indicated work (~1.5%) while reducing heat transfer losses and increasing exhaust enthalpy [83]. These results have been shown to be independent of EGR rate and injection timing [82].

Another method that results in reduced heat transfer to the combustion chamber surfaces is by employing steel pistons. The lower thermal conductivity of steel compared to aluminium, which is commonly employed in light-duty diesel pistons, results in lower heat conduction through the piston and consequently to higher piston surface temperatures; resulting in lower heat transfer from the combustion chamber to the piston. Steel pistons have a wide use in heavy-duty applications with their first introduction in the early nineties [84], both as a full steel or an articulated steel-aluminium design, due to their higher durability and strength dictated by the higher cylinder pressures imposed by the heavy-duty sector [85, 86]. In addition, due to their higher stiffness, steel pistons require smaller wall thicknesses consequently leading to a lower piston assembly mass and hence to a lighter powertrain unit.

Recently, steel pistons have found their way into light-duty diesel applications, and apart from their structural benefits over the aluminium pistons, researchers have also reported improvements in fuel efficiency – both in terms of brake and indicated specific values [87, 88]. The improvements in net isfc were reportedly due to both the higher piston surface temperatures – and consequently reduced heat transfer to the oil and coolant – as well as the higher compression ratio due to the smaller topland volume of the piston design employed. In addition to this, the lower thermal expansion rate of steel, allowed for smaller clearances between the liner and piston which resulted in reduced blow-by; a parameter known to affect indicated work [89].

In terms of brake specific fuel consumption (bsfc) the additional benefits observed for the steel piston design were attributed to a reduction in frictional losses, due to a shorter piston skirt and due to a reduction of piston side forces due to an increased conrod length. These results are important as they highlight the potential for wider application of steel pistons in light-duty applications. As the effects of steel piston on the performance of light-duty diesel engines are not widely reported in the literature, the results presented in Chapter 4 seeks to expand upon this body of knowledge.

The following section will discuss the breakdown of the fuel energy flows in ICE engines along with the most common heat transfer paths during engine operation.

1.4 Transfer of heat and energy in IC engines

Internal combustion engines convert the chemical energy of the fuel into mechanical work. As already mentioned, the efficacy of the conversion of fuel energy into useful work is dependent on a multitude of factors, from the mixing and combustion of the fuel/air mixture which affects combustion efficiency, to heat transfer and pumping losses that reduce the useful work on the crankshaft (i.e. brake work). On top of that the relative

motion between mechanical parts (e.g. piston/cylinder or valves/camshaft) induces frictional losses further reducing the work output of the engine. Furthermore, many ancillary components of modern vehicles (i.e. water pump, high-pressure fuel pump, air-conditioning pump etc.) are driven by the engine, thus consuming work to complete their function. An accurate knowledge of each of these energy transfer terms therefore provides critical information to engine designers.

Figure 1.9 shows a typical breakdown of the fuel energy in an IC engine. The chemical energy released from the combustion of the fuel can be split mainly in three energy terms; potential piston work (i.e. indicated work), overall heat transfer (including the energy transfer to the cooling and lubricating medium and the radiative heat loss from engine surfaces) and the thermal energy of the exhaust gases. Combustion inefficiency can be considered as an extra energy term in the exhaust stream, (i.e. the chemical energy associated with unburned fuel found in the exhaust) however, this is usually very small, especially for diesels where the fuel/air mixture is predominantly lean, and as such can be ignored.

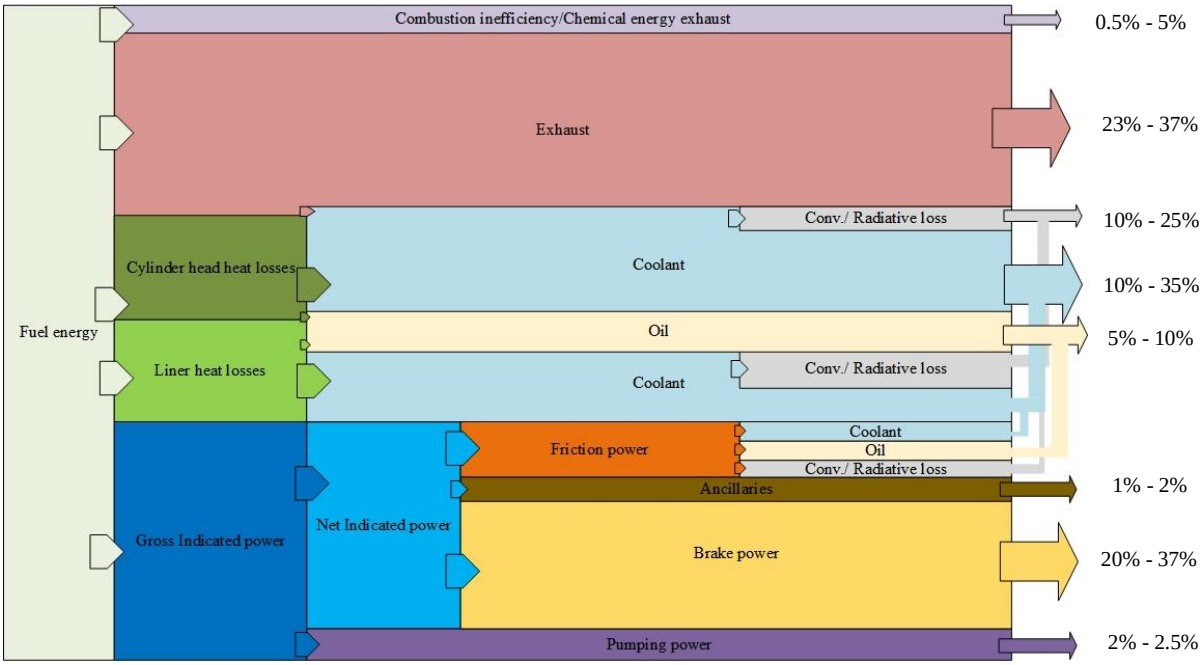

Figure 1.9**:** Typical fuel energy breakdown for an internal combustion engine. Values are shown as a percentage of fuel energy and are only indicative.

As a rule of thumb, the heat transfer losses and exhaust enthalpy in diesel engines account for approximately ~40-75% of the total fuel energy depending on operating conditions [26]. Consequently, following the principle of conservation of energy, a reduction in heat transfer has the potential to increase indicated work and/or the exhaust enthalpy. An increase in exhaust enthalpy can improve the efficiency of the turbocharger and the cold-start performance of the after-treatment systems, however this work will only focus on the in-cylinder processes and how these can increase the useful work to the piston. Before introducing the various heat transfer paths in the combustion chamber it is worth first presenting the different mechanisms through which heat is being transferred.

The second law of thermodynamics states that heat will flow from a hotter to a colder body and this process can be achieved via three mechanisms; namely, conduction, convection and radiation. The conduction of heat describes the transfer of energy within a substance from highly energetic molecules to less energetic molecules due to molecular

interactions (i.e. collisions) [90]. The energy transfer via conduction is expressed mathematically using Fourier's law according to Equation (1.11).

$$Q_{cnd} = -kA_{csa}\frac{dT}{dx} \tag{1.11}$$

Where k is the thermal conductivity of the material, A_{csa} is the cross-sectional area and $\frac{dT}{dx}$ is the temperature gradient across a distance x. The negative sign is used to indicate the transfer of heat from the hotter to the colder region of the substance.

Apart from molecular interactions, transfer of heat can also occur due to the movement of molecules within a fluid or a when a solid comes in contact with a fluid. This process is called convection and can occur either naturally, due to the buoyancy forces resulting from density variations within the fluid, or by an external force such as a pump. The transfer of heat between a moving fluid and a surface is an important field of study in ICEs, especially under forced convection conditions. In order to describe this energy transfer process, the heat transfer coefficient h is used. Assuming that the fluid will be at a lower temperature than the surface in contact, the energy transfer due to forced convection is then given by Equation (1.12) according to Newton's law of cooling.

$$Q_{cnv} = hA_s(T_s - T_f) \tag{1.12}$$

where A_s is the surface area exposed to the flow, T_s is the temperature of the surface and T_f is the fluid temperature. It is therefore clear that estimation of the heat transfer coefficient is paramount in these types of problems; however this is far from a trivial task.

It is known that when that when a fluid comes into contact with a surface the particles at the interface will assume the velocity of the surface due to the no-slip condition. The viscosity of the fluid and the resulting shear stress between adjacent fluid particles will

then lead to a velocity gradient between the surface and the bulk flow which is known as the velocity boundary layer. Similarly, a temperature gradient between a fluid and a surface will lead to the creation of a thermal boundary layer. The two boundary layers can be seen in Figure 1.10**.**

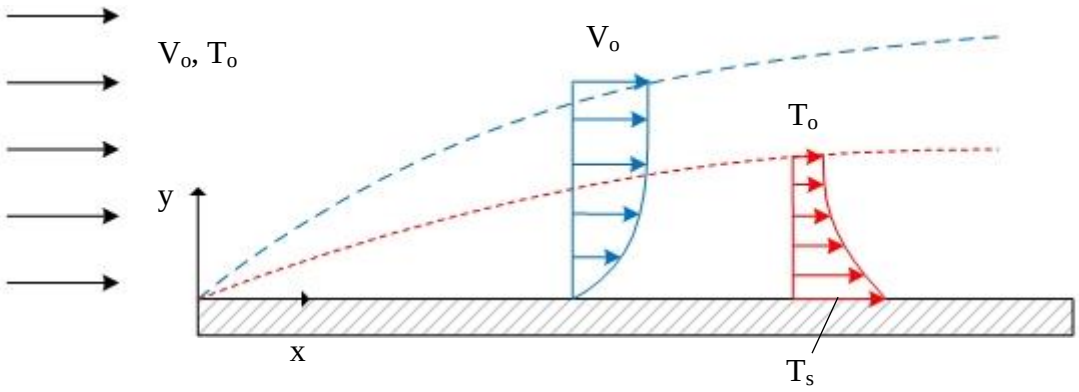

Figure 1.10: Velocity and thermal boundary layers on a flat plate. The blue colour represents the velocity boundary layer and the red colour the thermal boundary layer.

Considering that the relative motion between the surface and the fluid at the boundary will be zero (i.e. at height y=0), the local surface heat flux, will be purely due to conduction, according to Equation (1.13). It should be noted that k_f is the thermal conductivity of the fluid since heat transfer will be occurring through the boundary layer.

$$\dot{q}_s = -k_f \left.\frac{dT}{dy}\right|_{y=0} \tag{1.13}$$

Conservation of energy suggests that the total energy convected to the surface should be equal to the energy conducted through the boundary layer. Therefore, combining Equations (1.12) and (1.13) provides an expression for the heat transfer coefficient. This is shown below.

$$h = \frac{-k_f \left.\frac{dT}{dy}\right|_{y=0}}{\left(T_s - T_f\right)} \tag{1.14}$$

Equation (1.14) shows that the heat transfer coefficient is then highly dependent on the flow conditions – the temperate gradient will change based on the boundary flow conditions (i.e. laminar or turbulent) – as well as the fluid properties. Further to this, the geometric properties of the surface will also affect the heat transfer coefficient. It should also be noted that Equation (1.14) refers to local conditions only, as the boundary layer will build up along the length of the surface shown in Figure 1.10. Therefore, integration over the surface area would be necessary in order to evaluate the total energy transfer.

All of the above make the experimental determination of the heat transfer coefficient a significant challenge. Instead, experiments over a range of geometries and fluid velocities have been carried out in order to provide an indication of the *average* heat transfer coefficient $\bar{h}$. One such correlation developed by Whitaker [91], has been used in this work to model the heat transfer process to a thermocouple junction (refer to Chapter 3). From this point onwards any reference to the heat transfer coefficient will imply an average value over the surface area of the body and for simplicity this will be indicated by h.

The third mode of heat transfer is thermal radiation. Thermal radiation manifests as the emission of energy, by oscillation or transition of the electrons of a substance, through electromagnetic waves [90]. This mode of heat transfer is important as it does not require the presence of a temperature gradient within a form of matter like in the convection and conduction modes. Therefore the transfer of energy is dependent on how effectively the body of interest can emit this energy. An indication of this ability is the emissivity ε, of a substance and it can take values from 0 to 1, where a value of 1 represents an ideal

emitter (i.e. a black body). The energy transfer due to thermal radiation can be estimated using the Stefan-Boltzmann law according to Equation (1.15).

$$Q_{rad} = \sigma \varepsilon A_s \left({T_s}^4 - {T_w}^4 \right) \tag{1.15}$$

Where σ is the Stefan-Boltzmann constant, ε is the emissivity of the body, A_s is the surface area of the body, T_s is the surface temperature of the body and T_w is the temperature of the surrounding surfaces. It should be noted that Equation (1.15) assumes that no energy is absorbed by the transferring medium.

In-cylinder heat transfer is a very complicated process affected by a multitude of factors. The hot combustion gases convect heat to the cooler combustion chamber walls, a process driven by the peak cylinder temperature, the levels of swirl in the cylinder and the temperature and material properties of the surrounding surfaces. In diesels, radiation of soot particles can further increase the heat transfer to the surrounding surfaces. This residual heat will then be transferred to the cooling medium, the lubricating oil and the various engine components via different heat transfer modes. A schematic of this process can be seen in Figure 1.11, with the different arrow types indicating the three heat transfer modes; the solid arrows represent the convective heat transfer, the single chevrons represent the conductive heat transfer and the double chevrons represent the radiative heat transfer.

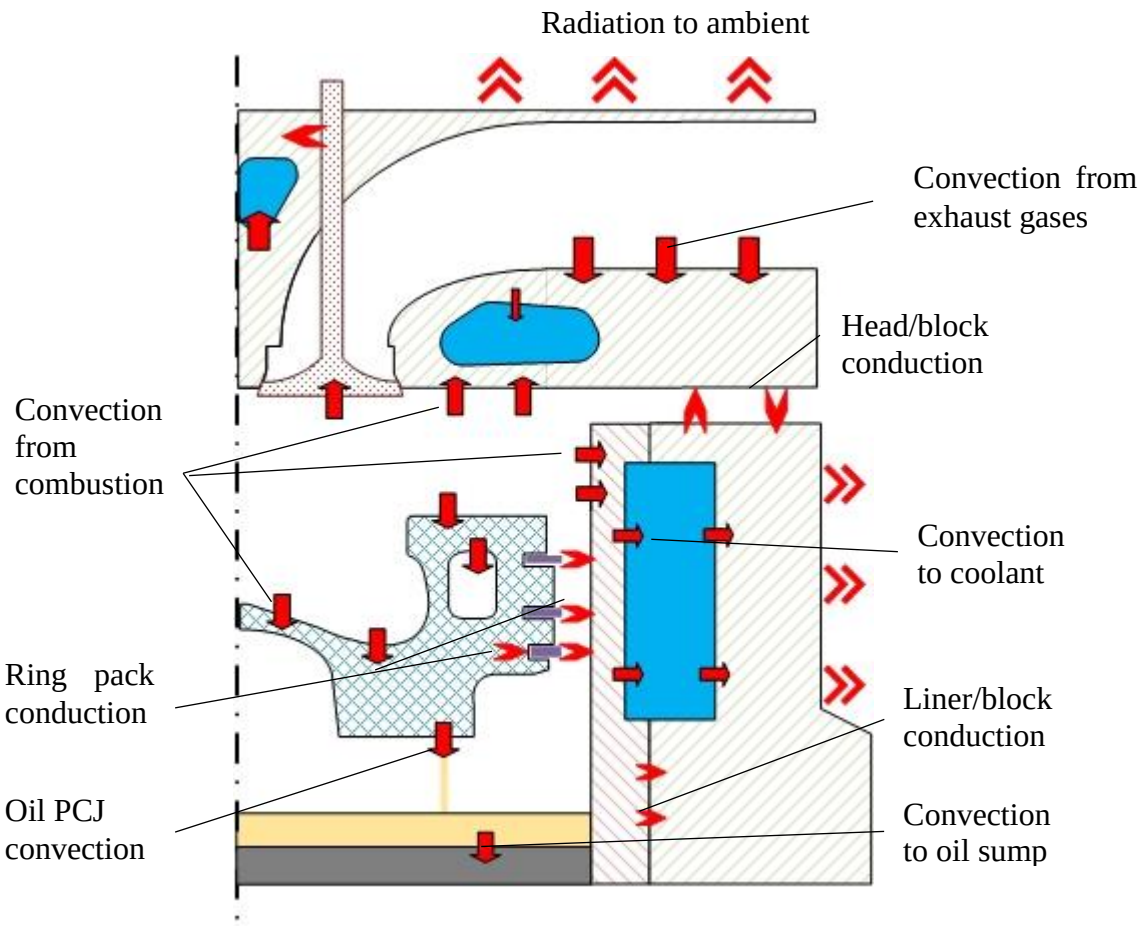

Figure 1.11: Typical heat transfer process in an IC engine. The arrows indicate the convective heat transfer, the single chevrons the conductive heat transfer and the double chevrons the radiative heat transfer.

The main sources of heat transfer to the coolant are the cylinder walls and the exhaust port surfaces, which convect heat from the combustion gases during the cycle and engine friction, with the piston-crank assembly presenting the biggest contribution to the total friction losses (e.g. ~45%) [26]. It has also been shown that heat conducted from the piston to the cylinder walls, can contribute significantly to the energy transferred to the coolant. Studies carried out by MAHLE have shown that, depending on the piston cooling approach, approximately 30-65% of the heat flow through the piston crown can be transferred to the cylinder wall via the piston ring pack and the piston skirt.

The main purpose of the engine oil is to lubricate surfaces that are in relative motion thus reducing component friction and wear. Undoubtedly, friction will lead to heat being transferred to the lubrication oil, as it is circulated around the engine, thus acting as an extra source of cooling (or heating if the engine is operating under low load conditions). Indeed, modern engines utilise oil cooling at the underside of the piston, to reduce thermal loading and prolong piston service life. The thin lubricating film on the cylinder walls will also receive some heat before returning to the oil sump.

Thermal contact of engine components (e.g. cylinder head and cylinder block, valves and cylinder head) will result in the conduction of heat between the individual parts depending on the established temperature gradient, and heat conduction through the walls of the engine can result in radiative heat transfer to the ambient as engine surfaces get hotter. It is obvious that tracking all the different energy transfer paths, with competing or cumulative effects, quickly becomes a very challenging task. Knowledge of local velocity and temperature conditions to correctly evaluate the heat transfer process further builds into this complexity. A more practical approach considers the engine as a black box and the various energy transfer terms are estimated using an energy balance approach.

Energy balance studies apply the first law of thermodynamics across an imaginary boundary around the engine (i.e. a control volume). This control volume is considered as an open system where mass and heat can be transferred across its boundaries, with the calculation of the various energy transfer terms carried out under steady state conditions. This implies that the engine speed and load are constant and the system has reached thermodynamic equilibrium, i.e. thermal gradients across its boundaries are constant. Depending on the goal of the study, the boundary can be adjusted to included specific engine components (e.g. a turbocharger) and exclude others (e.g. the after-treatment

systems). Equation (1.16) shows mathematically a typical energy balance on an IC engine.

$$\overbrace{\dot{m}_f q_{LHV} + \dot{Q}_{air}}^{\text{Inputs}} = \overbrace{\dot{W}_{shaft} + \dot{Q}_{cool} + \dot{Q}_{oil} + \dot{Q}_{exh} + \dot{Q}_{ext}}^{\text{Outputs}} \tag{1.16}$$

where $\dot{m}_f q_{LHV}$ is the rate of chemical energy from the fuel and $\dot{Q}_{air}$ is the rate of thermal energy from the induced air. $\dot{W}_{shaft}$, $\dot{Q}_{cool}$, $\dot{Q}_{oil}$, $\dot{Q}_{exh}$ and $\dot{Q}_{ext}$ are the brake power, and the energy transfer rates to the coolant and oil, the rate of thermal energy in the exhaust and the extraneous losses respectively.

The extraneous term accounts for all of the energy transfer that cannot be measured during an energy balance study, primarily heat transfer across the control volume boundary, in the form of radiation and convection losses from the engine itself. A detailed description of how each term is calculated is presented in Chapter 3.

The application of first law analysis on IC engines is not new and has been applied widely due to its simplicity [26, 74, 92-101]. However, depending on the level of detail required and the accuracy of the measurement, this analysis can quickly become non-trivial. For instance, if the energy dissipation to the coolant and oil is to be estimated separately, the test facility must accommodate two conditioning systems, one for each medium. Similarly, if a piston cooling jet is employed, a separate oil conditioning system is required to establish the contribution of heat from piston cooling [87]. Attempts have also been made in the past to accurately measure the extraneous energy term; rather than inferring its magnitude from subtracting the total energy losses from the total energy input into the control volume. This was achieved by employing an ‘adiabatic’ enclosure around the engine and a suction fan to provide a flow of air around the engine [99]. The

extraneous losses where then simply calculated as the change of enthalpy across the boundaries of the enclosure. However, it should be noted that depending on the configuration of the test facility, space limitations might prevent the use of such an approach.

Complications associated with the accurate measurement of temperature also apply. In an attempt to reduce the uncertainty associated with the extraneous losses, researchers have measured the energy flow to the coolant, by measuring directly the temperature at the cylinder head cooling galleries [74]. Improving upon this logic, multiple temperature measurements of the cylinder liner and head have also been employed [100-102], although this process requires careful modification of the engine components to accommodate the installation of the temperature sensors as well as to provide a robust method for extracting the sensors' wires from the engine's components.

Estimation of exhaust enthalpy requires knowledge of temperature and mass flow rate in the exhaust manifold; where commonly time-average values for both of these parameters are used. Equation (1.17) shows this mathematically, where c_p is the heat capacity of the exhaust gases (this is usually assumed to be independent of temperature), $\overline{\dot{m}}_{exh}$ is the time-average mass flow rate of the exhaust stream, $\overline{T}_{exh}$ is the time-average exhaust temperature and T_0 is the ambient temperature.

$$\overline{\dot{Q}}_{exh} = \overline{\dot{m}}_{exh} c_p \left(\overline{T}_{exh} - T_0\right) \tag{1.17}$$

The time-average exhaust temperature ($\overline{T}_{exh}$) and mass flow rate ($\overline{\dot{m}}_{exh}$) are calculated according to the following equations.

$$\overline{T}_{exh} = \int_{0}^{720} T_{exh}\, d\theta \Big/ \int_{0}^{720} d\theta \tag{1.18}$$

$$\overline{\dot{m}}_{exh} = \int_{0}^{720} \dot{m}_{exh}\, d\theta \Big/ \int_{0}^{720} d\theta \tag{1.19}$$

where the limits of the integrals represent the crank-angle degrees.

However, the expulsion of exhaust gases during the cycle is a highly dynamic event and Caton *et al.* [103] have shown that time-average exhaust temperature can lead to significant under-prediction of the "true" exhaust enthalpy. Instead, he argued, a better method for estimating the exhaust enthalpy would be to use the instantaneous values for temperature and mass flow rate (i.e. $\dot{m}_{exh}(\theta)$). The *mass-averaged* exhaust enthalpy would then be calculated as follows:

$$\hat{\dot{Q}}_{exh} = \dot{m}_{exh}(\theta) c_p \left(\hat{T}_{exh} - T_0\right) \tag{1.20}$$

where θ indicates the crank angle, and ($\hat{T}_{exh}$) the mass-average exhaust temperature. The latter is calculated according to Equation (1.21). It should be noted that the integration in this case is only carried out for the period that the exhaust valves are open.

$$\widehat{T_{exh}} = \int_{EVO}^{EVC} \dot{m}_{exh}(\theta) T_{exh}\, d\theta \Big/ \int_{EVO}^{EVC} \dot{m}_{exh}(\theta) d\theta \tag{1.21}$$

Comparing the mass-average exhaust temperature ($\hat{T}_{exh}$) to the time-average exhaust temperature ($\overline{T}_{exh}$) have been shown to result in significant discrepancies, with the mass-average values being as much as 100 K higher [103], which highlights the need for instantaneous exhaust gas temperature measurements. Further to this, an indication of instantaneous mass flow rate is also necessary according to Equation (1.21).

Knowledge of instantaneous exhaust mass flow rate can be inferred by measurement of the gas velocity. Temperature measurements can then be used to calculate the density of the gases. The most common method for measuring air velocity is with the use of a hot-wire anemometer, however, this technique is limited to ambient temperatures of ~150 °C [104]; a point much lower than diesel exhaust temperatures. Consequently, numerical simulations are usually employed to provide an indication of the velocity profiles in the exhaust manifold, with the prerequisite that the flow characteristics of the exhaust system are known. The same approach has been used in this work (Chapter 3).

Temperature measurement of unsteady flows (e.g. exhaust gas flow), has also been shown to be a significant challenge. The measurement of exhaust gas temperature (EGT) in internal combustion engines is commonly carried out with sheathed thermocouples due to their low cost, simplicity and robustness. However, despite their reliable nature, the physical presence of the sensor induces undesired dynamic errors – the dynamic error in this context is referring to the inability of the sensor to follow a fluctuation in temperature – which are directly proportional to the thermal mass of the sensor and the local flow conditions. Consequently, the estimation of mass-average exhaust enthalpy as shown in Equation (1.21), is not feasible due to the inherent dynamic error of the temperature sensors.

Considering that the exhaust enthalpy and the heat transfer to the coolant are one of the major energy transfer terms (Figure 1.9), an accurate calculation of these terms will provide a better insight into the performance potential of IC engines. As a result, this work focuses on the development of measurement techniques and methodologies that would allow for a more accurate measure of temperature, whether under unsteady flow or stead-state flow conditions. Throughout this work, the primary temperature sensors used

were thermocouples and as such the following section will introduce their theory of operation as well as compensation techniques that can reduce the dynamic error of the sensor in an unsteady flow environment.

1.5 Measurement of temperature using thermocouples

Thermocouples operate on the principle of thermoelectricity. This is a phenomenon first observed by Thomas Seebeck, where if two dissimilar metals are connected in a loop forming two junctions, an electromotive force (E) will be created, provided that the two junctions are kept at different temperatures. More significantly, this electromotive force was found to be dependent on the temperature difference between the two junctions. Figure 1.12 shows a schematic representation of the Seebeck effect.

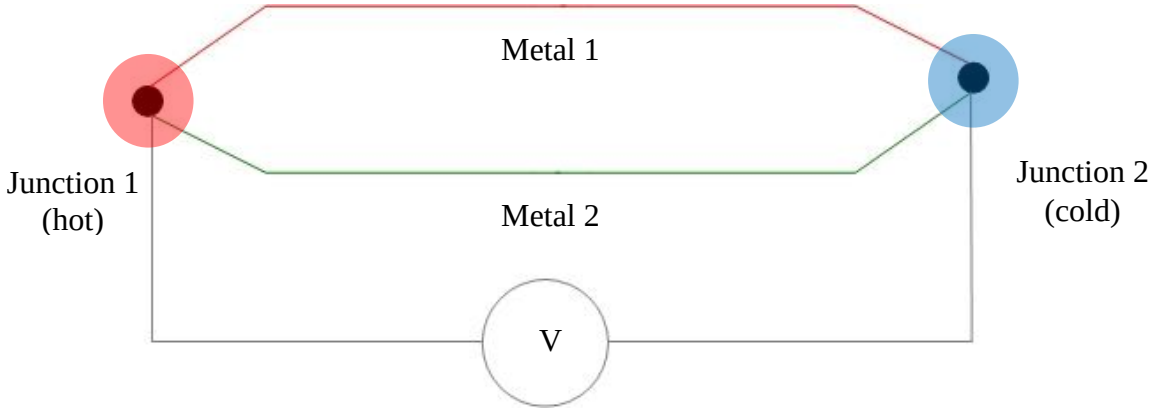

Figure 1.12: Schematic representation of the Seebeck effect.

However, the configuration presented in Figure 1.12 is not practical for real-life applications. Breaking the loop at the cold junction and measuring the voltage across the two legs of the thermocouple will provide the same measurement, if the temperature at the cold junction is known.

Cold junction compensation (i.e. knowledge of the temperature at the cold junction) is most commonly provided using an ice bath, thus keeping the reference temperature at 0

°C. As this configuration is bulky and unpractical the use of an isotherm of known temperature can also provide the same results. Figure 1.13 shows such a measurement configuration for a K-type thermocouple.

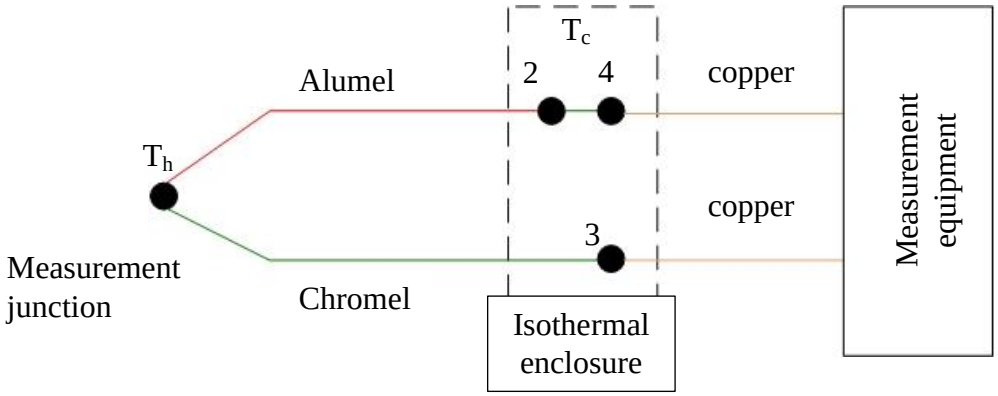

Figure 1.13: Typical thermocouple measurement configuration for a K-type thermocouple.

It is worth noting that the different material of the measurement instrument leads (usually copper) can result in unwanted junctions between the different thermocouple legs. This can create an extra emf which is not representative of the temperature difference between the measurement and the cold junction. However, according to the law of intermediate metals, if such junctions (i.e. junction 3 and 4 in Figure 1.13) are kept to the same temperature, the resulting emf will be of equal magnitude and opposite direction and will thus cancel out. Consequently the emf produced by the configuration presented in Figure 1.13, will be given by Equation (1.22).

$$E_{23} = e_{s,23}(T_h - T_c) \tag{1.22}$$

Where $E_{23}$is the resulting emf, $e_{s,23}$ is the Seebeck coefficient which is dependent on the thermocouple materials and $(T_h - T_c)$ is the temperature difference between the measurement and reference junctions. The National Institute of Standards and Technology (NIST) has tabulated voltage values for different thermocouple types under a

range of temperatures, which can be used to identify the temperature of the measurement junction without knowledge of the Seebeck coefficient of the thermocouple. It should be noted that, the emf produced by the thermocouples is very small (~41 μV/K for K-type thermocouples) and as such an amplifier circuit is necessary.

Considering that the thermocouples are providing an indication of the temperature difference between the measurement (hot) and reference (cold) junctions, this principle can be used to improve the measurement uncertainty associated with the estimation of the heat rejected to the cooling medium. The energy transfer to the coolant can be estimated by using an equivalent form of Equation (1.17). Therefore the combined uncertainty of this calculation will be dependent on the uncertainties associated with three temperature sensors, namely; coolant feed, coolant outlet and reference junction.

On the other hand, if the reference junction is used to measure the coolant feed temperature and the measurement junction is installed onto the coolant outlet line, then the resulting configuration will be measuring directly the temperature differential between the two lines. As this differential thermocouple does not infer the temperature difference between two sensors but directly measures it, the associated uncertainty will be reduced. Following this, such a differential thermocouple system has been designed and used in this work to provide a more accurate estimation of the energy rejection to the coolant. More details on this can be found in Chapter 2.

1.5.1 Dynamic error using temperature sensors

Temperature measurement in ICEs is usually carried out with intrusive methods by exposing the sensor to the flow of interest (non-intrusive methods involve laser diagnostic techniques which are beyond the scope of this thesis). As a result, intrusive temperature measurements (such as thermocouples) rely on the transfer of heat from the fluid to the

sensor. This process has two caveats; first, the sensor indicates the temperature of the sensor's body and not the fluid's temperature and second, the heat transfer rate to the sensor is finite which means that the sensor will indicate changes in temperature with some delay. This is the cause of the dynamic error under unsteady temperature measurements.

As already mentioned, the dynamic error is dependent on the physical characteristics of the sensors and the local flow conditions, driving the heat transfer process. More specifically, the dynamic error of a sensor is governed by its time-constant (τ) defined as:

$$\tau = \frac{mc_p}{hA_s} \tag{1.23}$$

Where m and c_p are the mass and the heat capacity of the sensor and h and A_s the heat transfer coefficient and the surface area of the thermocouple junction. Equation (1.23) then shows that the dynamic error increases with the sensor's thermal mass (i.e. mc_p) for given flow conditions. Research specific applications have tried to reduce this dynamic error by employing fine-wire thermocouples which vary in size from 25.4 μm - 812μm. However, recent studies have shown that even these sensors result in significant dynamic errors [105].

Figure 1.14 shows the effect of the increasing dynamic error as the thermal mass of temperature sensor is increased on the measurement of a typical diesel exhaust temperature profile (T_g) during an operating cycle. The blue, red and green lines indicate the temperature of three bare-wire thermocouples, with their respective numbers indicating their junction size in thousands of an inch. The purple line is typical of a standard 3 mm sheathed thermocouple (T_{ref}) usually employed in such measurements. As it can be seen, a smaller junction size follows the gas temperature profile much closer,

however, there is still a significant under-prediction of the peak temperature. Further to that, the time-average temperature values of the bare-wire thermocouples can be seen to be lower than that of the time-average exhaust gas temperature. This is attributed to the small thermal mass of such sensors combined with heat transfer losses from the measurement junction to the colder surroundings. On the other hand, the sheathed thermocouple shows no variation in the logged temperature during the cycle and also under predicts time-average exhaust temperature, although not to the same degree that the bare-wire thermocouples do. Thus, being able to correct these sources of errors can significantly improve the estimation of the true exhaust enthalpy. Details on this work are covered extensively in Chapter 5.

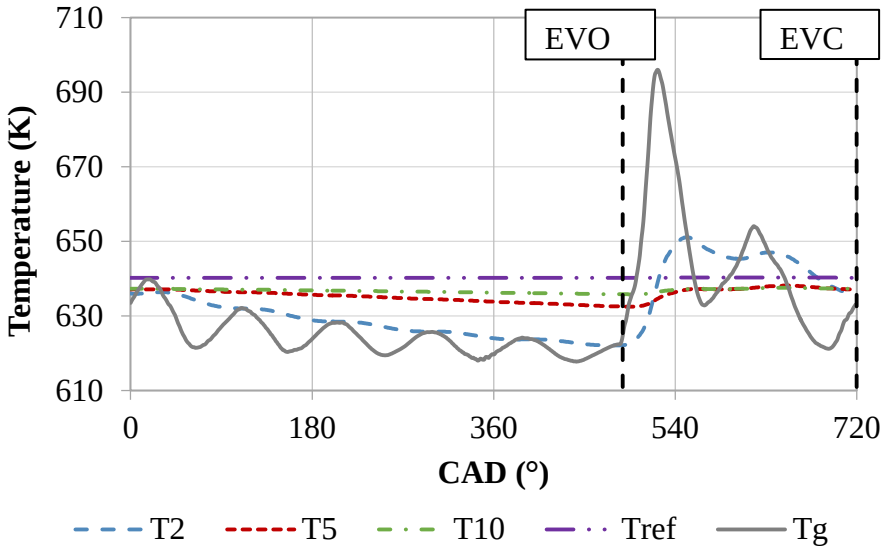

Figure 1.14: Effect of time-constant on unsteady temperature measurements. T2: temperature of 2tau TC, T5: temperature of 5tau TC, T10: temperature of 10tau TC, Tref: temperature of reference TC, Tg: modelled exhaust gas temperature.

1.6 Conclusions

The diesel engine still offers significant efficiency benefits over gasoline. However, in order to meet the upcoming legislative emission limits, diesel efficiency needs to improve further. A common tool used to measure the thermal efficiency of IC engines, along with

the various energy transfer terms, is the first law analysis. Typical results of this analysis show that the biggest energy transfer terms in IC engines are associated with the cooling medium and the exhaust gases. Therefore, managing the magnitude of these terms to successfully increase the useful piston work has the potential to improve engine efficiency. Similarly, accurate estimation of these energy terms can lead to significant insights regarding the thermal efficiency of the diesel engine.

This work focuses on the development of the necessary instrumentation and required methodology to accurately estimate the fuel energy breakdown using a first law analysis approach. Specific focus is given in the accurate estimation of the energy transferred to the cooling medium and the exhaust by developing application specific instrumentation. The instrumentation used in this work is presented in Chapter 2. An energy balance model has been developed for this work which was used to assess different EGR strategies, as well as compare the performance of different piston designs. Further to this, a thermocouple model has been developed to study the various parameters affecting the temperature measurement of unsteady flows (e.g. exhaust flow in IC engines). The development and theory of these models is discussed in Chapter 3. Chapter 4 and 5 present the results of the experimental and numerical studies carried out for this thesis. Finally, Chapter 6 presents a method of correcting the measurement errors associated with unsteady temperature measurements thus allowing for the estimation of mass average exhaust enthalpy. A comparison between, mass-average and time-average exhaust enthalpy is also shown. The following chapter will discuss the instrumentation set-up used in this work.

2 Experimental equipment and methodology

2.1 Single-cylinder diesel engine

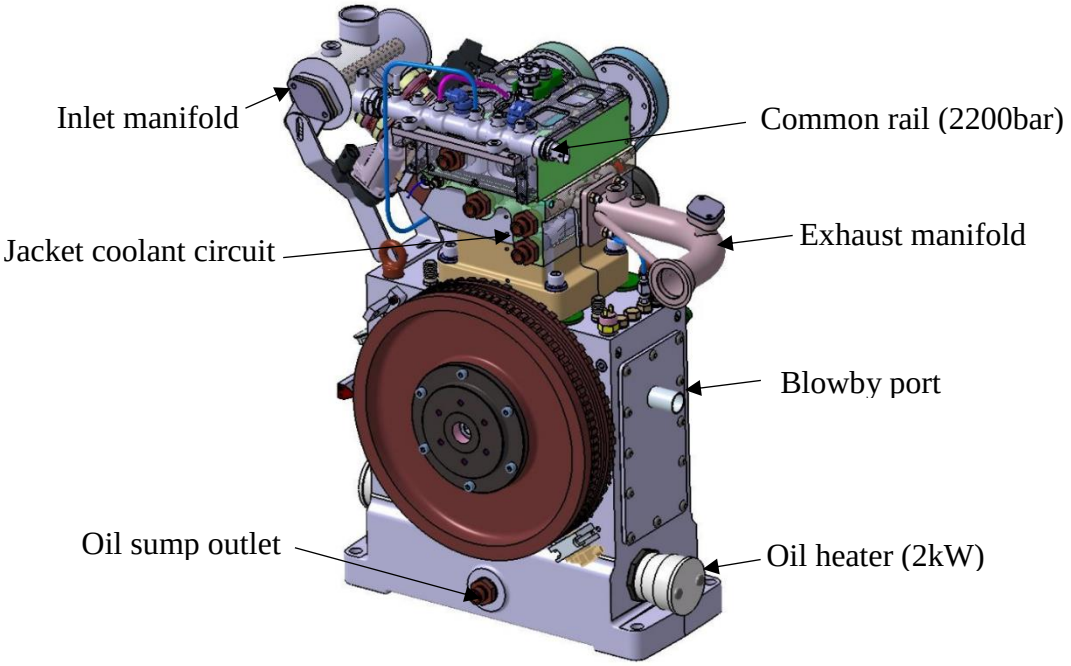

Figure 2.1: AJ200D single-cylinder diesel engine

This work was performed on a single-cylinder diesel engine supplied by Jaguar Land Rover where the cylinder head, valve-train, crank-piston assembly and cylinder block are based on the AJ200D “Ingenium” engine [106]. The bottom end is a Ricardo Hydra unit. Single cylinder engines are commonly used for research purposes as they provide a cost-effective option for testing new hardware – the fuel consumption and cost of some new hardware is reduced by approximately a factor of four. Their ease of accessibility also reduces downtime during major hardware changes. Another advantage of the single-cylinder configuration is that cylinder to cylinder interactions are eliminated, along with the associated effects on cylinder scavenging and trapped mass [29]. This is particularly useful when the effects of fuel air mixing or EGR application on engine performance are studied.

As this engine is not equipped with a balancer shaft and the vibrations associated with a single-cylinder engine can be significant, the engine unit as a whole is mounted on a seismic mass which is resting on four dampers to reduce the induced stress on the various engine and peripheral components. A production standard fuel injection system is used, capable of reaching pressures of up to 2200 bar along with a production multi-hole injector. Fuel is delivered to the common rail system via a high-pressure fuel pump from the production AJ200D engine. High-pressure pumps are equipped with volume control valves (VCVs) that can bypass excess fuel and thus reduce the amount of fuel to be pressurised at the injection pressures required. Consequently, as this pump is designed for multi-cylinder engine applications, the ancillary losses (associated with the work required to pressurise the fuel) are expected to be much higher. The ancillary losses associated with the high-pressure pump are presented in Chapter 3. The specifications of the engine can be seen in Table 2.1.

Table 2.1 : Engine and injection system specifications

Parameter	Specification
Bore × Stroke	83 × 92.4 mm
Displacement	500 cm3
Valves per Cylinder	2 intake, 2 exhaust
Compression Ratio	15.4 : 1
Injection system	Common rail
Fuel Pressure	400-2200 bar
Injector holes	8

The engine is equipped with a split cooling system, allowing for independent cooling of the cylinder head and the jacket. This allows for a more detailed insight into the energy flows under various engine conditions. However, independent temperature control of the

cylinder head and the jacket is not possible in the current test cell configuration. This would require separate heat exchangers and heaters for each circuit and due to the space limitations of the facility this was not possible. Diesel engines commonly utilise oil cooling to keep the temperature of the piston within specified limits without compromising power output [107] – oil is directed to the underside of the piston with the use of a piston cooling jet (PCJ). This prevents excessive piston surface temperatures and reduces piston thermal loading.

Different piston materials have been tested in this work, aluminium and alloy steel (Chromoly). Due to the lower thermal conductivity of steel (almost half that of aluminium [108]) the steel piston temperatures are expected to be significantly higher than the aluminium –increases of 50-100 K depending on piston location have been reported [86]. Accordingly, the single-cylinder engine used in this work uses two different PCJ configurations depending on the piston material; a single PCJ for the aluminium piston and a double PCJ for the steel piston. Figure 2.2 shows the PCJ location along with typical oil cooling galleries for the aluminium piston employed. It should be noted that there are no separate oil circuits for lubrication and piston cooling.

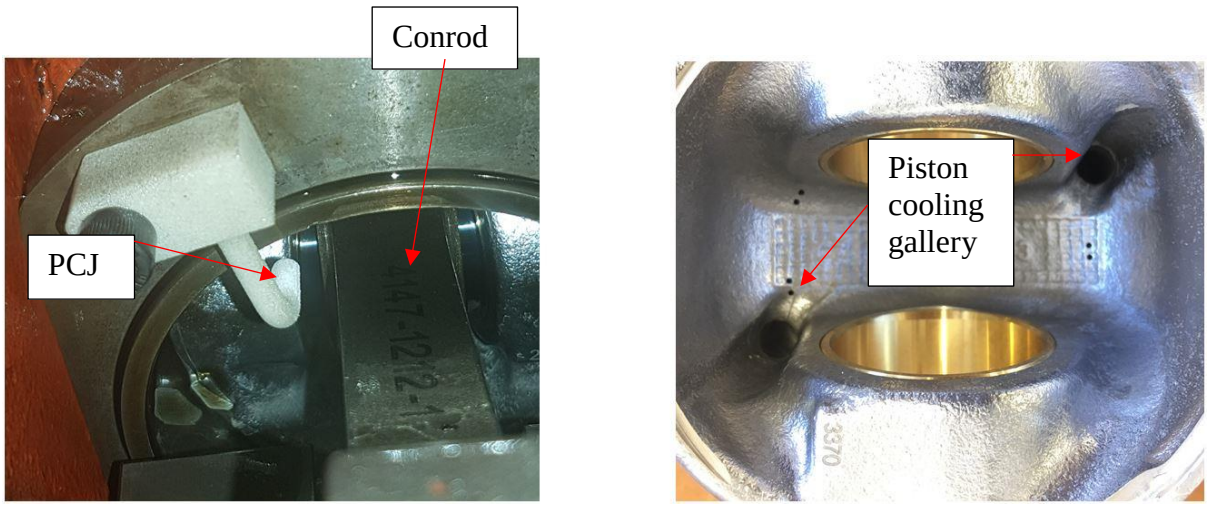

(a) (b)

Figure 2.2: (a) Piston cooling jet installed on the engine. (b) Typical piston oil cooling galleries

Application of EGR is achieved only via a high pressure EGR loop. The EGR valve used is a production unit from the Ford V6 Lion engine. Fresh charge and EGR gases are mixed into an inlet manifold, with the EGR gases coming into the manifold via a perforated tube in order to assist mixing. Direct control over the temperature of the EGR gases is not possible and is rather limited within a temperature range depending on the temperature and flow rate of the coolant.

Finally, the bulk rotation motion of the cylinder charge is only adjusted in terms of swirl; the rotating motion around the cylinder's centreline. In order to alter the flow characteristics of the intake charge, the cylinder head is equipped with two types of inlet port designs; a standard filling port and a swirl port. The amount of induced swirl is controlled with the use of a VDO throttle which is fitted in the filling port approximately 15 cm upstream of the intake valve. Closing the swirl flap will divert more flow through the swirl port, forcing the induced flow into a rotating motion. When the swirl flap is fully closed the swirl ratio is almost doubled, compared to a fully-open swirl flap case.

2.2 Test cell instrumentation

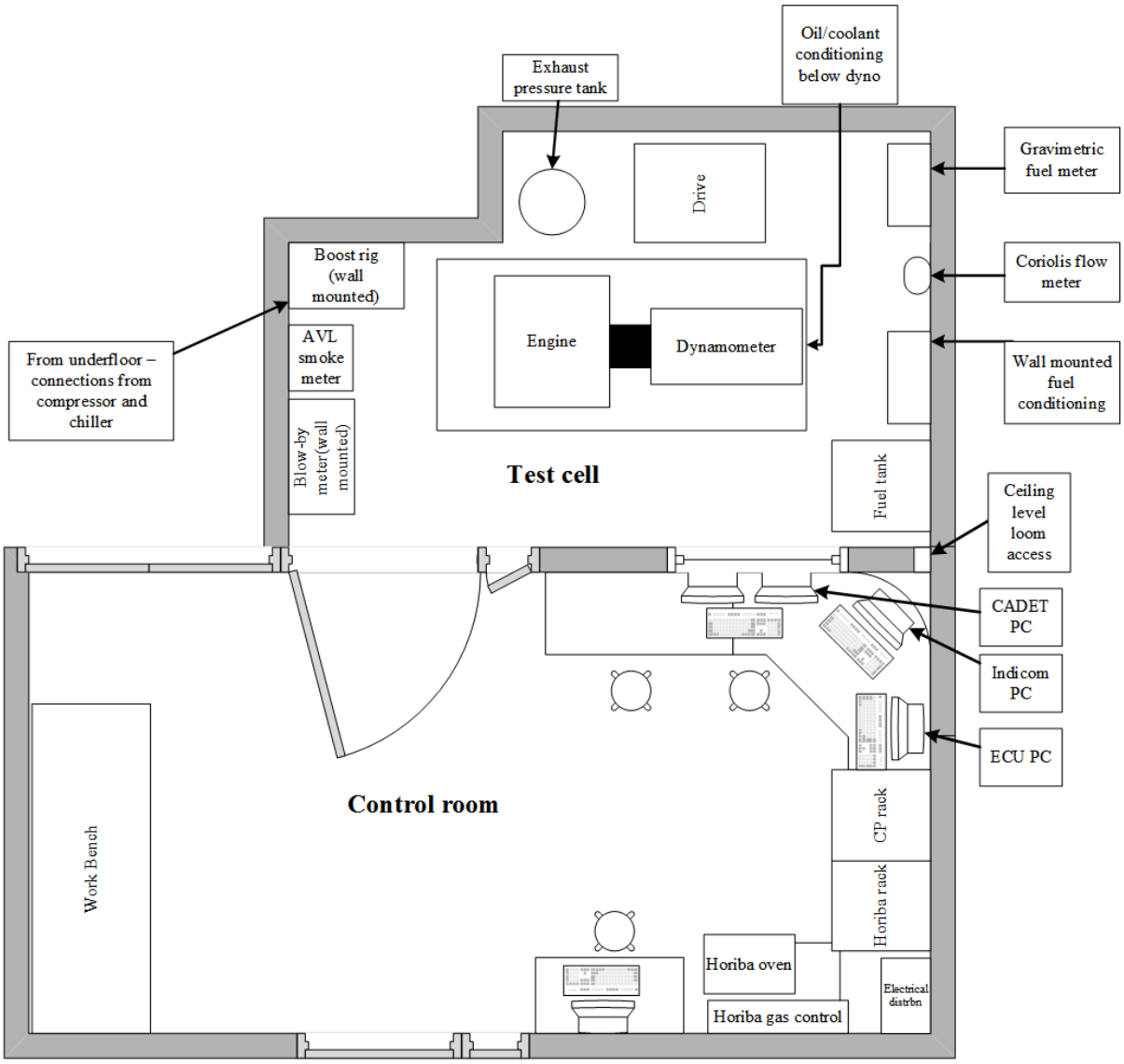

Figure 2.3: Overview of test cell facility

Figure 2.3 shows a plan view of the test facility. The majority of the measurement equipment along with the engine and the dynamometer are located in the test cell. Due to space and temperature limitations the emissions analyser tower was installed into the control room (cell temperatures could be as high as 45 °C depending on engine test and ambient conditions). According to health and safety requirements the engine and the test

cell equipment were controlled and data was logged remotely from the control room using three computers, each responsible for different operations.

The engine is connected to a 57 kW VASCAT AC dynamometer which can be used both to brake the engine under normal engine operation and motor (i.e. turn) the engine when no fuel is injected. As such a conventional starter motor is not required for initial firing of the engine. Considering that the maximum power output from the engine is 55 kW the dynamometer is not expected to limit the testing operating range of the engine. Finally, the speed and load of the dynamometer is controlled via an ABB Power Electronics drive unit.

The engine operating conditions are controlled via a Pi Innovo M670 OpenECU, which is based on a Jaguar Land Rover (JLR) Simulink model. This provides full control over the fuel delivery system (i.e. injected quantity, fuel rail pressure, number of injections, etc.) as well as control of the EGR and swirl valve positions. Power output is controlled by demanding an injection quantity via the ECU and, in order to achieve a high repeatability and accuracy of the test conditions, closed loop control is used to control the net indicated mean effective pressure (NIMEP). Control over combustion phasing – here defined by the point of 50% mass fraction burned (CA50) – is achieved through closed loop control of the CA50 values thus further enhancing testing fidelity.

Two data acquisition systems have been employed. The majority of the signals are logged at a frequency of 1 Hz via a Sierra-CP CADET control system. Temperature, flow rates, inlet and exhaust pressures, EGR and emissions were all logged as this frequency. In order to provide a large enough sample size while avoiding large test file sizes every test condition was logged for a three minute period. Crank-angle resolved data – in-cylinder pressure, flow and swirl port pressures, exhaust pressure and the injector current clamp

signal – are logged by an AVL Indicom fast-data acquisition system. Different signal resolutions are available, however for this work all signals are logged at a 0.1 CAD interval unless stated otherwise.

Dedicated conditioning rigs control the coolant and oil supply temperatures to the engine to ± 1K and are installed below the dynamometer. Heat is rejected from each circuit into a Bowman heat exchanger with a cooling capacity rated for a 120 kW engine. Considering that the single-cylinder engine has a maximum power output of 55 kW the cooling capacity of the heat exchangers will always be within their design limits. When the engine is operated under low load conditions or during warm-up the heat rejected to the oil and coolant circuits is not enough to reach the specified operating temperature of 90 °C. As a result, two 3 kW immersion heaters are installed in the coolant circuit and for the oil circuit, two 2 kW heaters are installed in the oil sump along with an additional 3 kW heater upstream of the oil heat exchanger.

Energy balance calculations for the coolant and oil also requires accurate knowledge of the respective flow rates for each medium. The individual coolant volume flow rates for the cylinder head, cylinder jacket and EGR engine cooling circuits are measured using three turbine flowmeters by TITAN Enterprises. The specified flow rates for the cylinder head, cylinder jacket and EGR, as specified by the engine manufacturer, are 11.5, 11.2 and 4 L/min respectively and are controlled with a set of ball valves. As the volume flow rate is dependent on the temperature of the medium, the coolant flow rates were set once the coolant temperature reached the target value of 90 °C. Due to the higher viscosity of the lubricating oil, the oil volume flow rate was measured using a FLOMEC oval gear flowmeter. In contrast to the coolant circuit, the flow rate of oil cannot be adjusted and it is rather dictated by the supply pressure of the oil pump (4-5 bar).

Measurement of temperature around the test cell is done using a combination of standard K-type thermocouples and platinum-resistance thermometers (PRTs). Considering their linear response across a wide range of operation and their robustness, K-type thermocouples are used as a cost-effective option for the majority of the temperature measurements. When a higher accuracy is required – temperature signals control the operating status of the fluid conditioning units in the cell – such as the outlet temperature of the engine's coolant, PRT's are employed. Further to that, energy balance studies in this work required the use of purpose built temperature sensors and these will be discussed in detail in a later section of this chapter.

Boosted intake conditions are provided by a set of external compressors capable of providing a total of 4.5 bar absolute pressure at full speed conditions. The intake pressure is regulated with an accuracy of ± 0.5% by a PID controlled dump valve system. An external 10 kW heater (OSRAM Sylvania) and a 15 kW chiller (International Celsius) provide intake air temperature control with ± 1 K accuracy. Monitoring of inlet air flow was carried out using two methods, a hot-wire anemometer and the use of emission data to derive the air fuel ratio. These two methods provide consistent results with deviations of <5%, a limit deemed acceptable by the industrial partner. It should be noted that uncertainties associated with the inlet flow rate are not expected to have a direct impact on the accuracy of the energy balance model, as the contribution of the air enthalpy in the total energy into the engine was found to be relatively small (~0.04% of the fuel energy).

Due to the significant pressure pulsations found in a single cylinder engine, the exhaust and inlet systems are equipped with 25 L smoothing tank in order to dampen out such pulsations and reduce their effect on pressure and temperature measurements. In order to drive the exhaust gases into the engine, a back pressure valve (BPV) is required. This

valve is installed downstream of the smoothing tank and is close-loop controlled via CADET in order to provide as constant backpressure as possible during testing.

2.2.1 Calculation of output work

Internal combustion engines convert the chemical energy of the fuel to useful work at the flywheel. Depending on the where this work is calculated it can be termed as indicated or brake work. Therefore accurate measurement of either term is important. Modern engine applications utilise pressure transducers and crank shaft encoders to provide information on the indicated work and load cells to provide information on brake work.

2.2.1.1 Indicated work calculation

The cylinder pressure transducer used in this work is a Kistler piezoelectric transducer. Piezoelectricity is the effect during which a crystalline structure creates an electric charge when exposed to an external mechanical load [40]. Due to the small magnitude of the output charge – the sensor's sensitivity is ~35 pC/bar – a charge amplifier is also necessary to first amplify and then convert the output charge into a voltage signal for the data acquisition system (DAQ). An accurate measurement of the angular position of the crank-shaft is provided by an AVL angle-encoder with a resolution of 0.1 CAD. In order to ensure an accurate and consistent measurement of TDC position an AVL428 probe accurate to ± 0.1 CAD was also used. A TDC check was carried out following a major rebuilding event as a 1% error on the determination of the TDC location translates to ~8% error in IMEP [109].

2.2.1.2 Brake work calculation

The brake work is calculated using the signal of an Interface load cell rated to 1 kN. The load cell is installed onto the dynamometer's swing arm and is measuring the reaction force exerted on the dyno by the engine. When this reaction force is multiplied by the

normal distance to the centre of rotation, the brake torque is derived. The load cell signal was logged at a frequency of 1 Hz by the CADET system.

2.2.2 Heat release analysis

The heat release and mass fraction burn results presented in this work is calculated using the AVL Concerto software [110], using the signals from the in-cylinder pressure transducer and that of the shaft encoder. Equation (2.1) is then used for the estimation of heat release at each crank angle interval, i.

$$Q_i = \frac{100}{\gamma_i - 1} V_{i+1} \left[P_{i+1} - P_{i-1} \left(\frac{V_{i-1}}{V_{i+1}} \right)^{\gamma_i} \right] (x_i + 1) \tag{2.1}$$

where γ is the polytropic coefficient, V is the instantaneous cylinder volume and P the cylinder pressure. x_i is an empirically derived constant, which for diesels, is equal to 1 [110]. This constant takes into account the changes in mixture properties due to the presence of fuel. The polytropic coefficient (γ) is calculated from Equation (2.2) as shown below.

$$\gamma = \frac{0.288}{cv_i} + 1 \tag{2.2}$$

where cv_i is the specific heat under constant volume, which is taken to vary with temperature according to the following equation.

$$cv_i = 0.7 + T_i(0.155 + 2x_i)10^{-3} \tag{2.3}$$

where T_i is the bulk gas temperature calculated according to the ideal gas law at each crank angle interval. The cylinder trapped mass is calculated by specifying the intake temperature and pressure during the cycle and by assuming that volumetric efficiency is

90%. Finally, the heat release calculation is carried out for the interval between -25 – 135 CAD at a 0.1 CAD resolution.

2.3 Fuel delivery and measurement

The high-pressure (HP) fuel delivery to the injector is accomplished with a high-pressure pump from the production 4-cylinder AJ200D engine. More specifically, the high-pressure pump is manufactured by Bosch and is using a single plunger design. The fuel is delivered to the high pressure pump at a pressure of ~1 bar via a delivery pump. The HP-pump is comprised of an eccentric cam which is connected to the engine's crankshaft, via the timing belt, and drives the pump plunger used to compress the fuel to pressures above those achieved with the delivery pump. The high-pressure fuel is then fed to the fuel rail where the injection pressure is controlled via a pressure control valve. A metering unit is also used to control the amount of fuel entering the HP-pump depending on operating conditions, thus minimizing the work associated with running the HP-pump.

The accurate metering of a small fuel quantity (due to the low fuel consumption of the single-cylinder engine) under the high fuel flow rate conditions provided by a fuel pump sized for a 4-cylidner engine is a significant challenge, especially under low load conditions. Considering that the fuel flow rate is the most important input into the energy balance calculations the measurement of fuel flow is provided by two independent instruments, based on different operating principles, thus allowing more robust measurements.

The first instrument is a Sierra-CP FuelTrak 1000 gravimetric fuel weigher. Its principle of operation is based on the monitoring of the weight of a fuel container – using a load cell – while fuel is being drawn from it. Therefore for a given time-step, the rate of change of the container weight can be estimated and is equal to the fuel flow rate into the

engine. It should be noted that diesel injectors are equipped with a return fuel line for the excess fuel that was not injected during the cycle. This avoids injector damage from excessive pressure build-up. The "return line" fuel is accounted for in the calculation of the fuel flow rate by connecting the return line downstream of the meter. The schematic of the gravimetric fuel flowmeter system can be seen in Figure 2.4. Considering that the mass of fuel retained in the metering system will affect the accuracy of the reading (e.g. erroneous readings resulting from higher fuel return temperatures) the temperature of the feed and return lines was closely controlled. This was achieved by passing the fuel through a heat exchanger – two heat exchangers were used, one for the feed and one for the return line – upstream of the fuel weigher unit. The temperature of the heat exchangers' coolant was controlled via a fuel conditioning unit, which was connected to the mains water supply. The pressure and temperature of the fuel lines was also monitored. These points are marked in Figure 2.4; P and T symbols are used to indicate pressure and temperature measurements respectively.

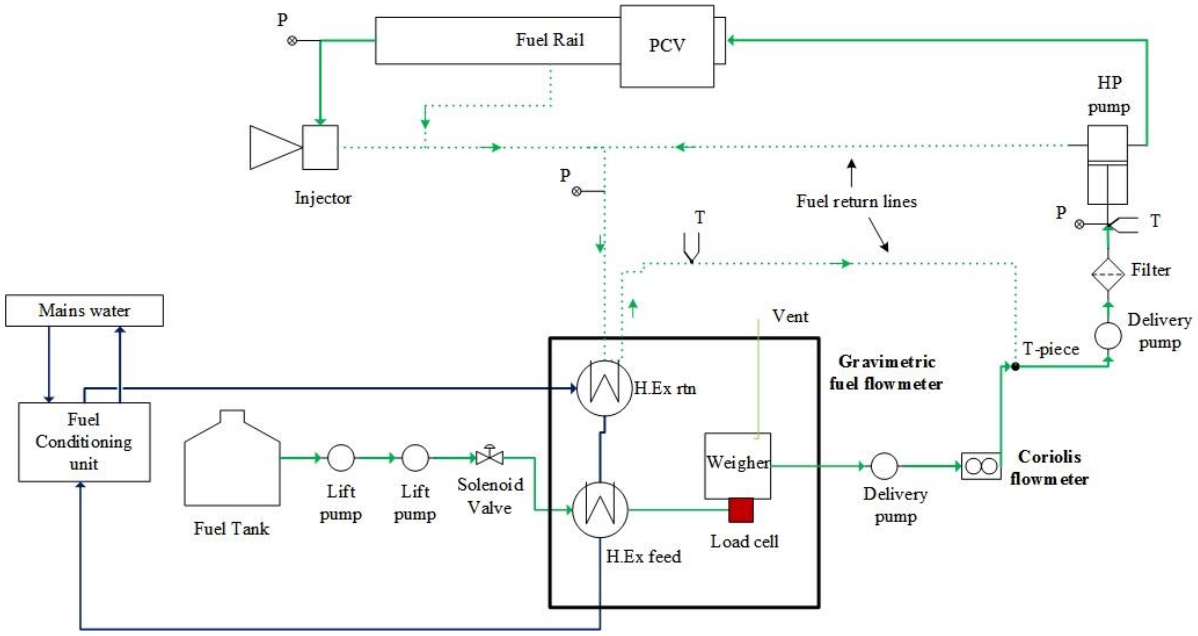

Figure 2.4: Schematic of fuel metering configuration

The second device used for fuel flow measurements is a Siemens Sitrans Coriolis flow meter. Similarly to the gravimetric unit, the Coriolis meter is installed upstream of the fuel return line, in order to account for the unused fuel during the cycle. Coriolis flowmeters pass the medium of interest through a vibrating U-shaped tube and are comprised of a flow-tube and a transmitter. The flow-tube (i.e. a u-shaped tube) is oscillated by the transmitter at its resonant frequency; which is dependent on the mass and the geometry of the tube [111]. The frequency is recorded with appropriately positioned sensors on each side of the flow-tube. When flow is introduced, the Coriolis force will cause the tube to twist as the fluid travels around the bend of the tube (i.e. the Coriolis force reverses direction) and a phase shift will be observed between the two position sensors signals. This phase shift is proportional to the amount of flow passing through the flow-tube.

As the mass and volume of the flow tube is constant, the density of the fuel can also be calculated, since different density fluids will have a different phase shift. Considering that the measurement principle of the Coriolis flowmeter allows for a direct measurement of the mass flow rate – as opposed to the measurement of a force exerted by a container onto a load cell – this device is expected to provide more accurate results compared to the gravimetric flowmeter.

A typical measurement between the two instruments can be seen in Figure 2.5. As it can be seen, the Coriolis meter can provide fuel flow measurement at a frequency of 1Hz – the actual frequency response of the Coriolis meter is in the order of kHz with the temporal resolution of the readings shown here being limited by the data acquisition system – whereas the gravimetric meter is only capable of providing a single measurement over the duration of the logging period (i.e. the slope of the line). This

would then mean that a longer logging period would provide more accurate measurements for the gravimetric meter, albeit resulting in longer testing times and potentially higher testing costs. A logging period of three minutes was found to provide a good comprise between measurement accuracy and testing time. As the Coriolis meter is not prone to such constraints, it provides a more versatile solution. However the difference between the two meters is less than 1% which highlights the confidence associated with the fuel flow measurement.

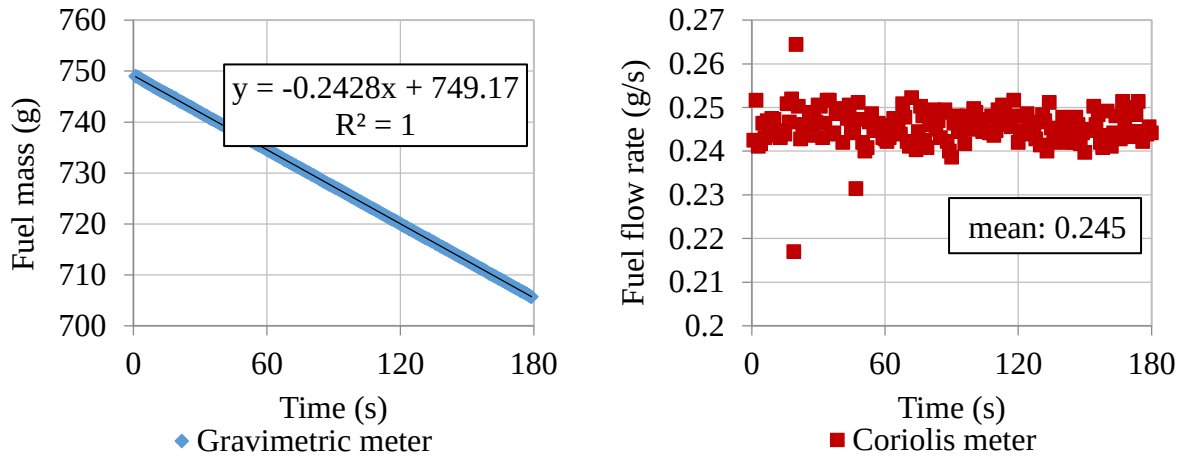

Figure 2.5: Typical measurement results of the two fuel metering methods

2.4 Energy balance measurement methodology

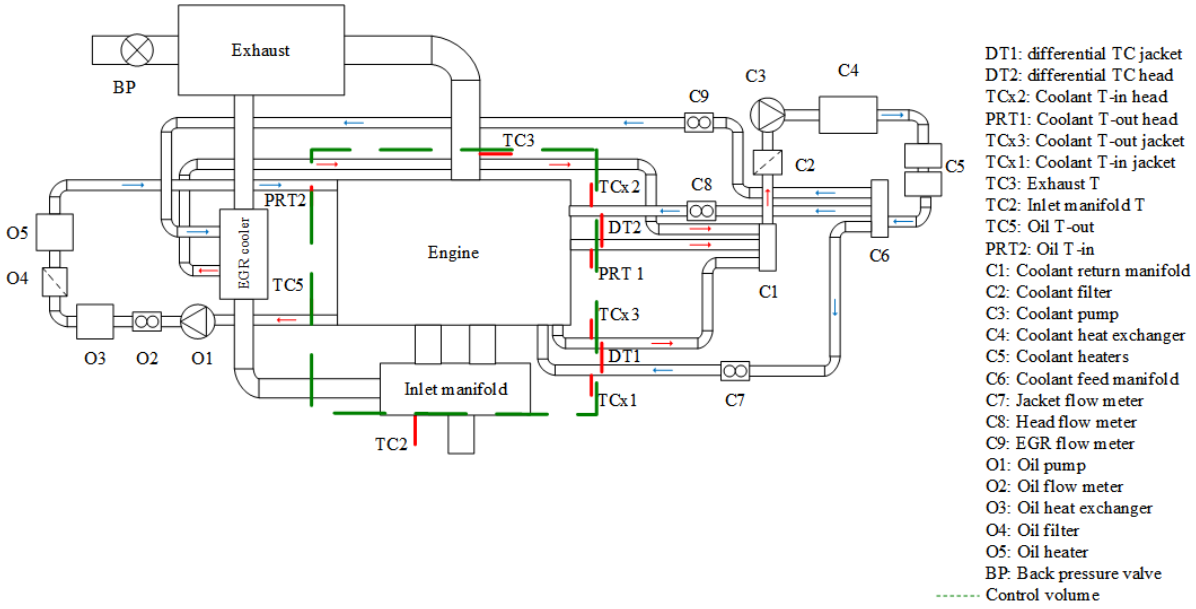

Figure 2.6: Engine schematic indicating measurement locations and instrumentation for energy balance studies.

Depending on the requirements of the study, the controlled volume can be set to include various components of interest such as turbocharger, intercooler, EGR cooler etc. In this study the control volume excluded the EGR cooler and external heaters/coolers associated with the oil and cooling conditioning units. However, the energy input from the oil sump heaters was considered in the calculations. Excluding the EGR loop from the controlled volume required the estimation of the exact composition of the EGR stream which increased the complexity of the energy balance calculation. However, the added complexity was deemed justifiable in order to keep the controlled volume as small as possible. This was done in an attempt to reduce the unaccounted energy losses across the system (e.g. the extraneous losses). The extraneous term accounts for all of the energy transfer that cannot be measured with the currently installed instrumentation, primarily heat transfer across the control volume boundary, in the form of radiation and convection

losses from the engine surfaces. In addition to this, as the engine is mounted on a seismic mass of a considerable heat capacity, heat conduction from the oil sump is also expected to increase the extraneous losses. The engine schematic along with the necessary measurements to carry out the energy balance calculations can be seen in Figure 2.6. The green dotted line approximates the assumed controlled volume.

Thermodynamic equilibrium suggests that the rate of temperature change across the system boundary would be equal to zero during the energy balance calculations. In order to achieve this, once the engine reached the required test conditions it was allowed to settle, usually for 10 minutes, depending on operating conditions. Temperature differences across the engine, and consequently energy transfer terms, depending on engine operating conditions could result in very small values. Therefore, to provide statistically significant results, every test point was repeated for a minimum of three times. Further information on the assumptions and the working principles of the energy balance model can be found in Chapter 3.

2.5 Temperature measurement

2.5.1 Coolant system differential thermocouples

Calculation of energy flows around the engine requires highly accurate inputs, especially at conditions when the magnitude of energy inputs is small and the measurement error is high. More specifically, it was observed that when the engine is operated under low load conditions the temperature differences across the engine coolant were very small ($\sim \Delta T = 0.2$ K) and approaching the measurement limit of the sensors – this was true even for calibrated thermocouples (refer to Table 2.2). Consequently, the resulting compounded error did not allow statistically significant differences to be measured. To alleviate this problem two differential thermocouples were designed, built and then installed onto the

coolant circuit lines; the first on the cylinder head circuit and the second on the cylinder jacket circuit. The reference thermocouples (i.e. the cold junction) were installed into the feed lines. Figure 2.7 shows the installation configuration.

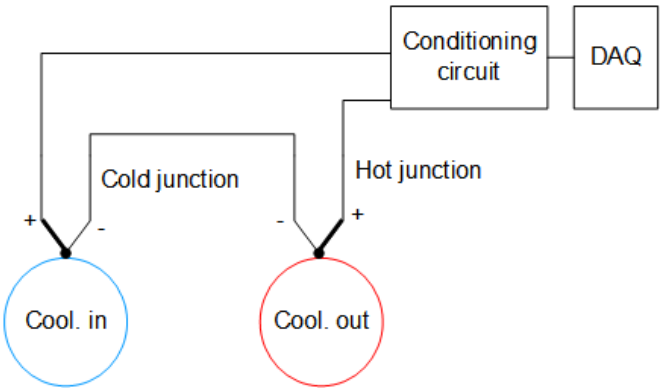

Figure 2.7: On-engine configuration of differential thermocouples

The differential thermocouple design is based on K-type thermocouples. As the output voltage of these thermocouple is very small (~40 μV/K), a conditioning circuit was required in order to amplify the signals to a voltage that will be compatible with the data acquisition card (0–10 V range). In order to utilize the full range of the input card and reduce the signal to noise ratio, two stages of amplification were used, the first one was an instrumentation amplifier by Analog devices (AD8422) and the second an operational amplifier by Texas Instruments (LM741). Combined, the two amplifiers provided a total gain of 11900V/V. During the first stages of development, engine measurements have shown that a negative temperature difference could be realised across the engine as the hotter coolant was transferring heat to the colder engine under low load conditions or during warm-up. Furthermore, the originally designed temperature range was found to be insufficient under full load condition (amplifier was saturating at 7.5 K temperature difference). Recognising that such conditions will be part of the future test schedule, a DC offset was added to the output signal (~20 mV) in order to allow the measurement of

these negative temperatures and the supply voltage to the amplifiers was increased from 8 to 12 V. These changes allowed the measurement range to be extended to -4 – 12 K.

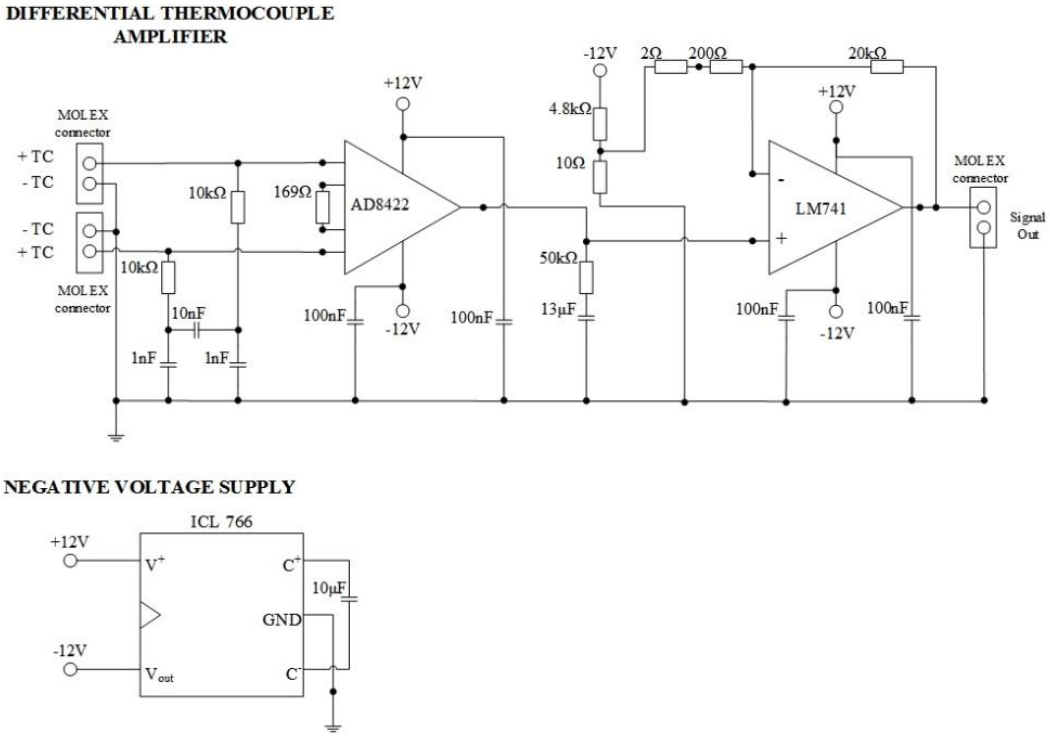

Figure 2.8: Conditioning circuit for the differential thermocouples.

The negative voltage supply was provided by a voltage converter integrated circuit made by Intersil (ICL 662). Considering the very small voltages used and that high power electronics found into the test cell could lead to potential noise being picked up by the thermocouples, two stages of low pass filtering were used, one before each amplification stage. Decoupling capacitors connected to the supply inputs of the amplifiers also ensured a stable power supply thus resulting in a stable signal output. The wiring diagram of the conditioning circuit for the differential thermocouples can be seen in Figure 2.8.

2.5.1.1 Calibration of differential thermocouples

The differential thermocouples were calibrated "offline" using two stirred water baths; one was at the reference temperature and the second at the set-point temperature. A total

of fifteen points were logged from -4 to 12 K temperature difference in one degree intervals. The reference bath was held at a constant temperature of 90 °C to simulate the operating conditions of the engine, with the second bath having a varying temperature to achieve the required temperature difference. Once the desired temperature difference was set, the two baths were allowed to settle and the output voltage from the differential thermocouples was logged. By applying a least square criterion to the measurements the calibration curve was derived. The residuals from the calibration (i.e. the difference between the measured and the fitted values) for the two differential thermocouples can be seen in Figure 9.

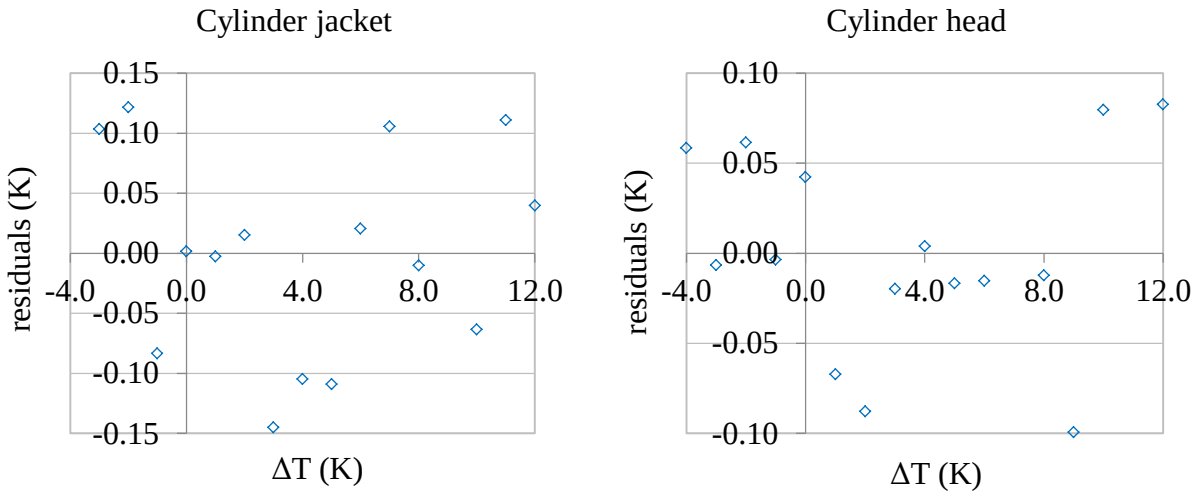

Figure 2.9: Residuals results from the differential thermocouple calibration.

The results presented in Figure 2.9 show a very small scatter which is overall below 0.15 K across all measurements. When using these calibration results, the calculated residuals can give an indication on the associated uncertainty of the measurement. The standard deviation of the logged value will be given by Equation (2.4) according to [112]:

$$\sigma_T = \sqrt{\frac{residuals^2}{\delta^2}} \tag{2.4}$$

Where δ indicates the slope of the fitted line using the least squares method (i.e. the sensitivity of the sensor). The resulting uncertainty of the sensitivity for the two differential thermocouples in the 95% confidence interval limits is ± 0.05 K and ± 0.03 K for the cylinder jacket and cylinder head circuits respectively. It should be noted that these values do not take into account the additional errors associated with the data acquisition system (i.e. digitisation errors).

2.5.2 Exhaust temperature measurements

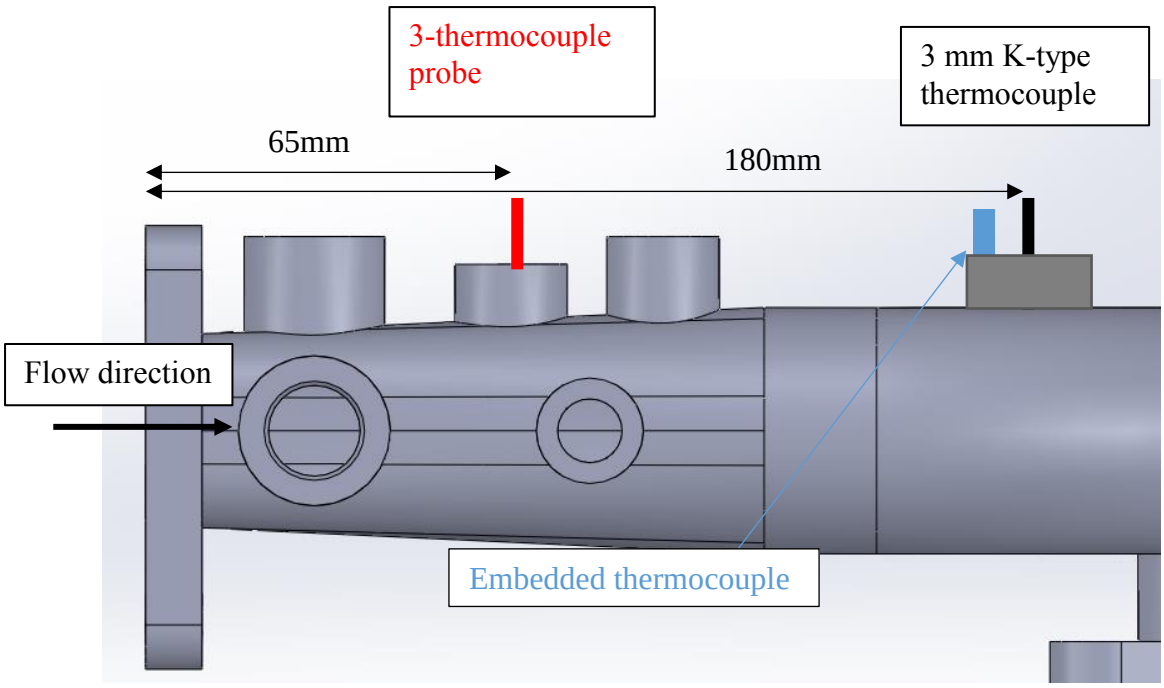

Figure 2.10: Installation position of various exhaust temperature sensors on exhaust manifold

Exhaust enthalpy is one of the major energy transfer terms in internal combustion engines. As such, accurate knowledge of this term significantly improves the overall accuracy of the energy balance calculation. Time-average exhaust temperature

measurements were carried out with a standard 3 mm K-type thermocouple, commonly used in engine testing applications. This sensor was used as a reference for all exhaust temperature measurements and was installed 180 mm from the engine. In order to provide an indication of the radiative and conduction error on these measurements, the temperature of the manifold wall was monitored using a 1.5 mm K-type thermocouple, which was embedded onto the manifold at a very close distance to the reference thermocouple.

2.5.2.1 Three-thermocouple probe

Mass average exhaust enthalpy requires the knowledge of the instantaneous exhaust gas temperature; a parameter that can be determined using the two-thermocouple reconstruction techniques discussed in Chapter 6. Consequently, a three-thermocouple probe was manufactured and installed on the exhaust manifold, as close as physically possible to the exhaust ports. This probe was located at 65 mm distance from the engine and 115 mm upstream of the reference sensor. It was assumed that the metal temperature of the exhaust manifold– once it reached a steady state temperature– would not vary between the locations of the two sensors and as such the wall temperatures measured could also be used for the correction of the three-thermocouple probe signal. A schematic of the measurement configuration can be seen in Figure 2.10.

The two-thermocouple reconstruction techniques require the use of thermocouple sensors with a significantly different junction size and thus thermal mass and time-constant, in order to successfully recover the dynamic error of the sensor. Following this a thermocouple probe comprised of three different size, bare-wire, K-type thermocouples was constructed based on the design of Kar [113]. Its main components are the probe's body (stainless-steel and ceramic tubes), the LEMO connector (for thermocouple

soldering) and the thermocouple extension cable (to transfer the thermocouple signal to the amplifier). A picture of the probe can be seen in Figure 2.11.

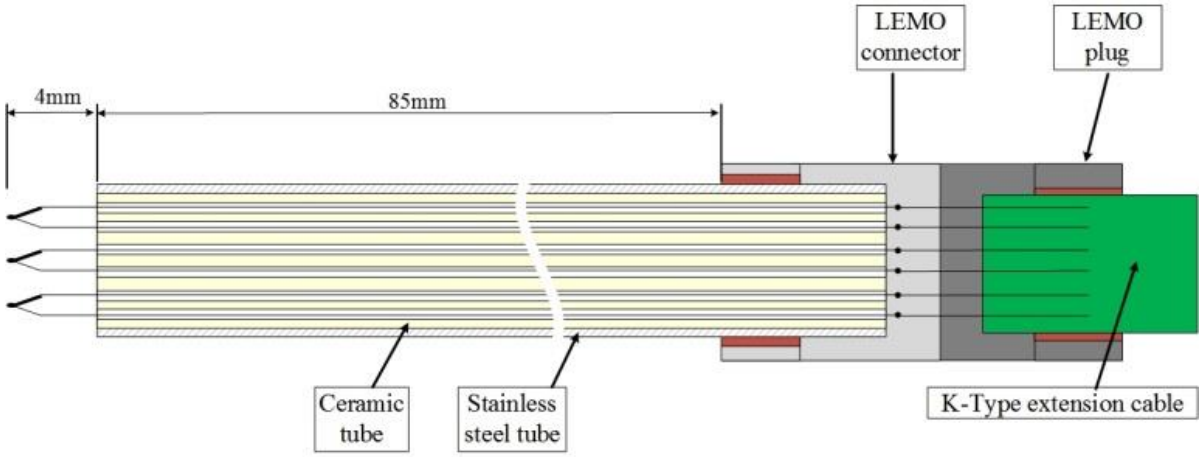

Figure 2.11: Three-thermocouple probe for temperature reconstruction technique (not to scale).

The three thermocouples sizes were 50.8, 127 and 254 μm, with the 127 and 254 μm junctions being butt-welded to allow for a faster response during measurement. The 50.8 μm junction is not commercially available in a butt-welded configuration. The thermocouples were installed into a six-hole alumina tube with the exposed length to the gas flow being ~4 mm. Due to the brittle nature of ceramics, the alumina tube was bonded to a 3 mm stainless steel tube to withstand the engine vibrations using a high temperature ceramic-metal paste, capable of reaching temperatures up to 650 °C. Diesel exhaust temperatures can reach an excess of 800 °C which prohibits the use of the thermocouple probe at these temperatures. However, the fragile nature of the bare-wire thermocouples (along with the melting point of solder), present a bigger limitation to the operating range of the probe. It was found that the probe could be safely operated at ~450 °C for a total testing time of ~ 2 hours before thermocouple breakage would occur.

A LEMO connector was used to solder the thermocouples wires and connect to a K-type extension cable to amplify their signal. Two types of thermocouple cables exist, extension

cables and compensating cable. Extension cables are using thermocouple alloys to transfer the measured signal and do not present any accuracy limitations. Compensating cables on the other hand are made of cheaper alloys that have similar emf characteristics to the measurement junction in a limited temperature range. Despite their cost benefits, compensating cables can lead to erroneous readings if used outside ambient temperature conditions [108, 114]. Consequently, an extension type thermocouple wire was used to ensure that no measurement errors will arise from the signal transmission. The total loop resistance is not considered to be an issue in this application as the total length of the extension wire remained below the specified limit of 30 meters for a minimum diameter of 20 AWG [115] – the total length of the extension wire was 10 meters and 28 AWG gauge. Further to that, according to the law of intermediate metals, the copper pins of the LEMO connector are not expected to introduce any measurement errors due to unwanted junctions.

The thermocouple signals were amplified by an instrumentation amplifier commonly used in the Combustion and Engines group for fast-temperature and heat flux measurements [113]. The amplifier is an INA110 integrated circuit with the option of different gain settings; 50, 100, 200, 500 V/V. The cold junction compensation was carried out with a K-type thermocouple and thermocouple reader, both calibrated in a stirred water bath to remove any bias error. The error associated with the cold junction was ±0.2 K for the 95% confidence limits. The cold junction thermocouple was connected at the point where the thermocouple probe signals were connected to the instrumentation amplifier. Once conditioned, the thermocouple signals where simultaneously logged by the fast-DAQ system at a resolution of 1 crank angle degree. A schematic of the measurement configuration can be seen in Figure 2.12.

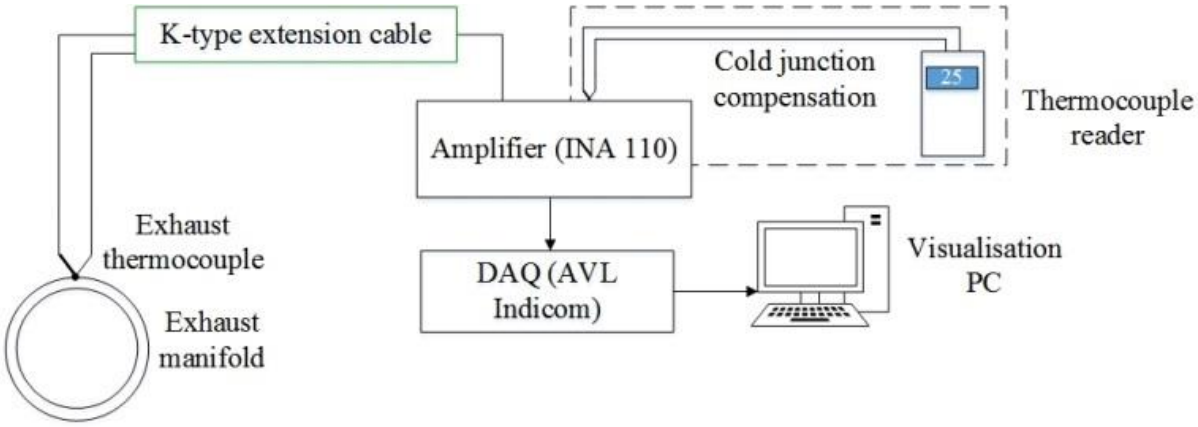

Figure 2.12: Measurement configuration for the three-thermocouple probe

Once the probe's signals were logged, the measured voltage was converted into a temperature measurement, "offline", using a *MATLAB* script following Equation (2.5).

$$T = d_0 + d_1 E + d_2 E^2 + \cdots + d_n E^n \tag{2.5}$$

where d_i indicates the thermocouple coefficient and E the electromotive force measured. The K-type thermocouple coefficients are based on the ITS-90 scale and are accurate to within -0.05–0.04 K [116].

2.5.2.2 Three- thermocouple probe calibration

Calibration of the probe to the expected operating range (300 –750 °C) is beyond the capabilities of a water or an oil bath as the maximum allowed temperatures are limited to ~120 °C. High temperature salt baths can reach temperatures up to 550 °C [117]; however concerns with regards to the possible failure of the fine-wire thermocouples due to the higher viscosity of the liquid medium (and consequently the resulting stress), prevented further investigation of this option. Instead, prior to engine installation, the correct operation of the probe was ensured by comparing its readings to a standard 3 mm K-type thermocouple, used for exhaust gas temperature measurements on the single-cylinder diesel engine. For that reason a brass oven was designed and made, which was

capable of simultaneously accommodating both temperature sensors. A cross-sectional view of the brass oven can be seen in Figure 2.13.

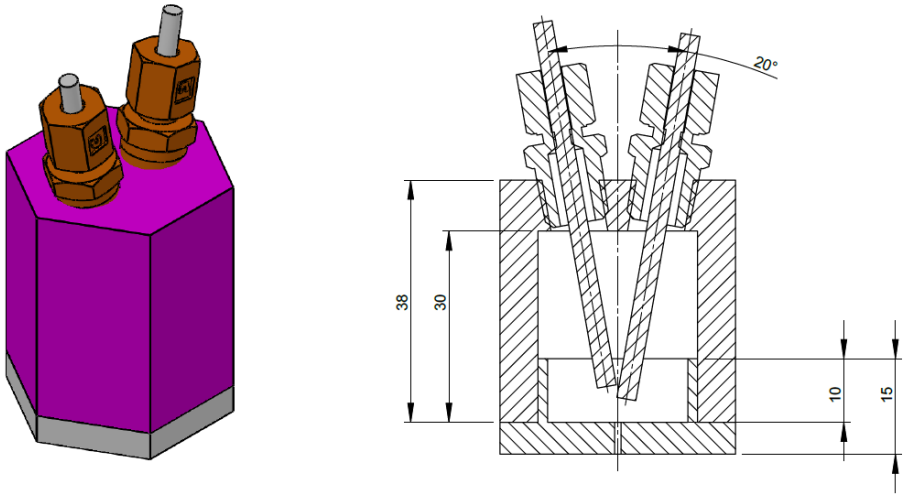

Figure 2.13: Brass oven used for calibration of three-thermocouple probe.

The size of the oven was chosen to be a compromise between long heating/cooling times and conduction error along the length of the probe. A higher oven volume would increase the mass of metal and air that require heating and as such the time required to reach a test point would increase. Equally, a small oven volume would reduce testing times but limit the immersion depth of the sensor increasing the conduction error along the sensors' body, as the temperature gradient between the measurement junction and the environment would increase. NPL suggests an immersion depth of 20 times the diameter of the sensor in order to minimise such errors [118], so the height of the oven was set according to the recommended immersion depth of the 3 mm thermocouple (i.e. 60 mm). In order to ensure that both sensors were exposed to the same temperature field, they were installed at an angle; thus any errors associated with natural convection are expected to be minimised.

The temperature range tested was between 200-550 °C which was well above the expected exhaust gas temperatures on the single cylinder engine. A propane torch was use to raise the temperature of the oven to the require set-point temperature, with the 3 mm K-type thermocouple acting as the reference sensor. Once the target temperature was reached, the readings were logged when all thermocouple readings were stable. An oscilloscope was used to log the signals of the three-thermocouple probe, whereas the reference thermocouple was logged using a standard thermocouple reader. The measurements were repeated three times to provide an indication of measurement repeatability.

The results can be seen in Figure 2.14, where the error bars indicate the 95% confidence limits. The black line represents the unity slope line of the reference sensor. It can be seen that there is a very good agreement between the thermocouples up to 450 °C, which shows that the probe is expected to work satisfactorily within the engine operating condition of interest. Beyond this point significant discrepancies start to appear, where the bare-wire thermocouples indicate a significantly higher temperature than the reference thermocouple. This is thought to be caused by limitations associated with the measurement rig rather the sensors themselves. At these higher temperatures, the rate of temperature rise for the reference sensor reduced, which would imply that energy is transferred away from the measurement junction. Radiative heating (the oven walls will be at a higher temperature than the sensor) is expected to be more pronounced for the reference sensor, due to its bigger surface area, thus leading to the opposite trend observed. The results are thus probably attributed to the increased conduction losses along the length of the reference sensor, perhaps due to insufficient immersion depth. In order to validate this assumption, an oven with a bigger immersion depth would be

required. However, as this phenomenon occurs outside the range of the conditions tested the reasons behind this were not investigated further.

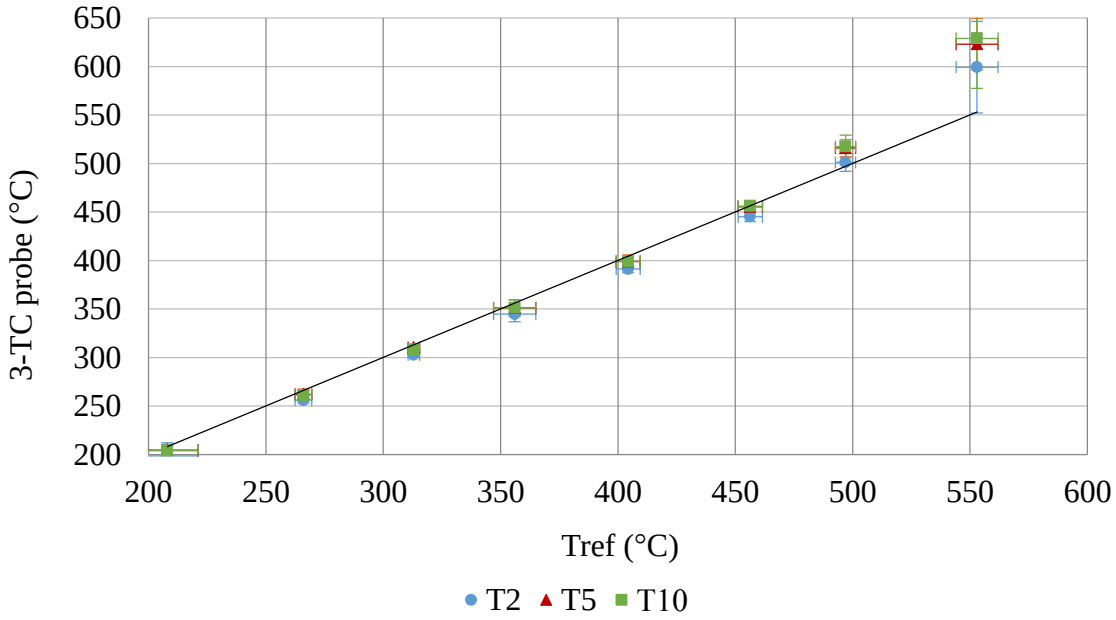

Figure 2.14: Three-thermocouple probe measurement comparison to 3 mm K-type thermocouple (Tref). The black line represents the unity slope line of the reference sensor.

2.6 Emissions measurement

A Horiba MEXA-One emissions analyser provides the majority of the facility's emissions measurement capabilities. The MEXA-One provides simultaneous measurements of CO, CO_2, NO_x, THC and O_2. The measurement of CO and CO_2 concentration is using the principle of Non-Dispersive Infra-Red absorption (NDIR). Nitric oxide emissions are measured using a chemiluminescence detector and total hydrocarbons with the use of a flame ionization detector (FID). Finally, the oxygen measurements are done with the use of a magneto-pneumatic detector [119].

The sample gas is drawn through a two meter heated line into a heated filtering unit in order to remove particulates and avoid clogging of the equipment. The sample gas is then drawn, via another heated line, into an oven unit of constant temperature (~191°C)

situated in the control room, with integrated NO_x and HC analysers. The heating of the sample gas is done to prevent H_2O and HC condensation. Finally, the sample gas exits the oven unit where it is drawn into the main cabinet unit where two CO/CO_2 analysers reside, one for the exhaust line and one for the EGR line. The O_2 analyser is also located in the main cabinet. Figure 2.15 presents a schematic of the emissions' measurement configuration.

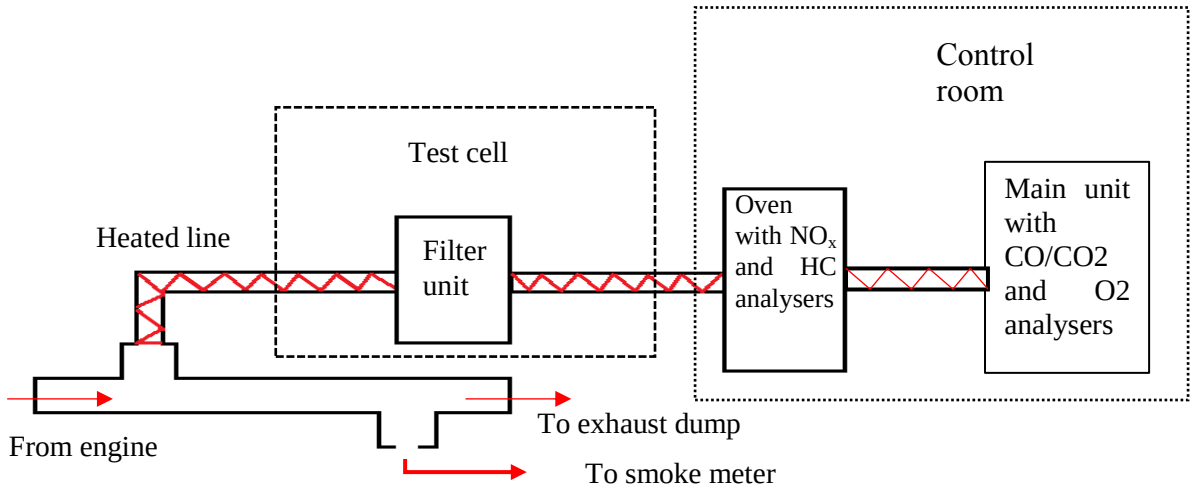

Figure 2.15: Emissions measurement configuration

2.6.1 Smoke measurement

Smoke measurements were obtained with an AVL 415 filter-type device. Exhaust gas is passed through a filter paper via a heated line, blackening the paper. Smoke concentration, given in terms of filter smoke number (FSN), is then established by measuring the reflectivity of the blackened filter paper using a reflectometer. A zero value shows a clean filter whereas a value of ten indicates no light reflection [120]. At conditions where smoke concentration is low, the amount of filter obscuration will be correspondingly lower for a fixed sampling volume. This may lead to potential increase in measurement inaccuracy. Consequently, three samples were drawn at each test condition and an average smoke number was provided.

2.7 Estimation of measurement uncertainty

Despite all the efforts made for the measurement process – which includes the combined uncertainties of sensors, environmental conditions and measurement method used [112] – to be a well-defined and controlled task, some form of scatter or variance in the measured values is expected assuming that the experiment is repeated more than once. This variance observed on the number of samples taken, is due to either; unexpected sources of error, random in nature, or inaccuracies associated with the measurement equipment. These sources of error are referred to as, random and bias errors respectively.

Bias or systematic error indicates a constant deviation from the true value and is usually attributed to manufacturer's tolerances [121]. Sensor's characteristics such as, linearity and hysteresis are a form of bias error. Systematic errors can be removed from the measurement by calibrating the sensor against a reference device. It is therefore obvious that the accuracy of the calibration will be dependent on the accuracy of this reference device. Ideally, sensor calibration should be carried out *in situ*, in order to take into account all sources of bias error in the measurement chain (i.e. sensor, amplifier gain, DAQ resolution etc.). However, this is not always practical, in which case calibration is carried out "offline" and any systematic errors associated with the conditioning electronics must be considered separately.

The sensors used in this work, to carry out the energy balance analyses, were calibrated either "offline" or the calibration certificate provided by the manufacturer was used. The errors associated with the analog to digital conversion were considered negligible and thus not included in the overall uncertainty calculations. The resolution of an analog to digital converter (ADC) is directly dependent to the number of bits it can handle and it is expressed mathematically as 2^n, for an n-bit ADC. In this work, the DAQ cards used by

the CADET system have a 16 bit resolution which, over the full input range of 10 V, corresponds to a resolution of:

$$Resolution = \frac{10}{2^{16}} = 0.15\ mV \tag{2.6}$$

If the quantisation error is assumed to be no more than half of the least significant bit (LSB) then the error associated with the ADC is $\pm\frac{0.15}{2} = \pm 0.07\ mV$. For example, this error is three orders of magnitude smaller than the uncertainty associated with the differential thermocouple sensitivity and thus ignoring its contribution is not expected to affect the overall calculation of uncertainty.

However, there are other sources of error that are not constant in nature and can be dependent on environmental conditions or even down to the diligence of the operator. The errors associated with these uncertainties are called random errors and cannot be accounted for with calibration.

An indication of the random error associated with a measurement can be given by the standard deviation of the sample. It is well accepted that random errors in engineering applications are assumed to be normally distributed [112, 121, 122] and this assumption was also carried into this work. Since, time and cost usually prohibits a large number of samples to be taken (large sample size is commonly accepted as n >30), the Student t-distribution is used to quantify random errors [122], with the Student t-distribution approaching the normal distribution for large sample sizes [123]. In this work the uncertainty associated with random errors was calculated at the 95% confidence interval following Equation (2.7).

$$U_{rand} = \pm t_{0.95} \frac{s}{\sqrt{n}} \tag{2.7}$$

Where *s* is the standard deviation of the sample, *n* the number of samples logged and $t_{0.95}$is the 95th percentile point for the two-tailed Student t-distribution [124]. From Equation (2.7, one can conclude that all things being equal, increasing the sample size would lead to a reduction in the uncertainty associated with random errors.

Finally, since a measurement system is comprised of a number of components it is of interest to know the overall uncertainty, provided that the individual component uncertainties are known. The most widely accepted method for combining uncertainties and used throughout this work, is to calculate the square root of the sum of squares (RSS) of the individual uncertainties [121]. Equation (2.8) shows this calculation.

$$U_{total} = \pm\sqrt{{U_{rand}}^2 + {U_{cal.}}^2} \tag{2.8}$$

where U_{rand} shows the uncertainty associated with random errors during the measurement and $U_{cal.}$ is the uncertainty associated with using the calibration results. It should be noted that the uncertainties presented in Equation (2.8) are due to random and not systematic errors.

Table 2.2 shows the uncertainty associated with the parameters used for the energy balance calculation. Sensors that have been calibrated are presented under the *Calibration uncertainty* column. Most of the uncertainties provided in Table 2 by the manufacturers are specified in terms of full scale output (FSO or FS) which shows the maximum expected error over the operating range of the sensor. In terms of the emissions analyser, the results show the full scale uncertainty of the analyser's linear response (this was the biggest uncertainty observed compared to analyser's repeatability and drift). Since the

calculation of the air fuel ratio is based on the combined uncertainties of the emissions analysers presented in Section 2.6, the uncertainty associated with the air flow calculation, from emissions data, is calculated following Equation (2.8) and results in a value of ± 0.9%.

Table 2.2: Uncertainties associated with the sensors used for energy balance calculations

	Measurement	**Sensor**	**Manufacturer's specified uncertainty**	**Calibration uncertainty (U_{cal})**
Intake system	Air flow rate (kg/h)	Hot wire anemometer	±1% of full scale above 10% full scale ± 3 kg/h	-
	Inlet Pressure (barG)	Pressure transducer	± 0.04% FS (± 0.28 bar)	-
	Inlet Temperature (°C)	K-type thermocouple	±2.2°C or ±0.75% (Whichever is greater)	-
Exhaust system	Exhaust port P (barG)	Pressure transducer	± 0.04% FS (± 0.28 bar)	-
	Exhaust port T (°C)	K-type thermocouple	±2.2°C or ±0.75% (Whichever is greater)	-
Fuel system	Fuel mass flow rate	Gravimetric flow meter	± 0.1 %	-
		Coriolis flow meter		-
Lubrication system	Oil T in (°C)	PRT	-	± 0.4 K - 95% confidence limits
	Oil T return (°C)	K-type thermocouple	-	± 0.35 K - 95% confidence limits
	Oil flow rate (L/m)	Gear flow meter	± 0.22 L/m	-
Coolant system	Cylinder head temperature difference (K)	Differential thermocoulpe	-	± 0.03 K - 95% confidence limits
	Cylinder head flow rate (L/m)	Flow meter	± 0.08 L/m	-

	Cylinder jacket temperature difference (K)	Differential thermocoulpe	-	± 0.05 K - 95% confidence limits
	Cylinder jacket flow rate (L/m)	Flow meter	± 0.08 L/m	-
Work output	Cylinder Pressure (bar)	Pressure transducer	-	± 0.9 mbar - 95% confidence limits
	Engine Load (N)	Load cell	±0.05% FS, ±0.1 N	-
	Engine position (CAD)	AVL shaft encoder	± 0.004%	-
Emissions	Air flow rate (kg/h)	CO	0.52% FS (linearity)	-
		CO_2	0.5% FS (linearity)	-
		NO	0.28% FS (linearity)	-
		NO_x	0.19% FS (linearity)	-
		THC	0.43% FS (linearity)	-
		O_2	0.07% FS (linearity)	-

2.8 Summary

In this section the instrumentation used in this work was presented. The single cylinder engine used is based on the AJ200D engine by Jaguar Land Rover using a production fuel injection system. An overview of the test cell instrumentation was presented along with purpose built measuring devices that allowed a more accurate estimation of energy transfer terms across the engine. Finally, the methodology for estimating the uncertainty associated with the experimental measurements was presented along with the uncertainties of the sensors used for the energy balance calculations. The following section will present the model developed to carry out the first law analysis studies as well as the thermocouple model along with the temperature reconstruction method used to correct for the measurement errors arising during the temperature measurement of unsteady flows.

3 Numerical simulations and methodology

This chapter details the theory of the modelling work carried out in this thesis and whose results are presented in Chapters 4-6. Two models were developed and used; the first, is an energy balance model, which applies the first law of thermodynamics around the engine, thus estimating the fuel energy breakdown (Chapter 4). The second model, simulates the response of the thermocouple sensors used in the experimental work carried out, under unsteady flow conditions. This model is based on the lumped capacitance method and it was developed after the unexpected findings during the measurement of exhaust temperature using the three-thermocouple probe and a standard 3 mm K-type thermocouple (Chapter 5). Finally, a temperature reconstruction method was used – based on the work of Tagawa *et al.* [14] – to recover the true gas temperature from a thermocouple signal. This method removes dynamic errors introduced by the physical presence of the sensor in the measurement environment and allows for a more accurate estimation of exhaust enthalpy. The method is presented initially for convective heat transfer and is subsequently expanded further to account for conduction and radiation errors associated with the use of temperature sensors. The results of this technique are presented in Chapter 6.

3.1 First Law Energy balance model

A first law energy balance model was coded in MATLAB considering four energy input terms and six energy output terms. The energy input terms in rate form are: the chemical energy of the fuel ($\dot{m}_f q_{LHV}$), the enthalpy of the inlet air ($\dot{Q}_{air}$), the enthalpy of the EGR gases $\left(\dot{Q}_{EGR}\right)$ and the energy input from the electric heaters $\left(\dot{Q}_{htr}\right)$, found in the oil sump (refer to Chapter 2). The corresponding energy output terms, in rate form are: the brake

work ($\dot{W}_{shaft}$) measured at the flywheel, the energy transferred to the coolant ($\dot{Q}_{cool}$), the energy transferred to the oil ($\dot{Q}_{oil}$), the exhaust enthalpy ($\dot{Q}_{exh}$), the exhaust chemical energy ($\dot{Q}_{chem}$), the high pressure fuel pump work ($\dot{W}_{HPP}$) and the extraneous losses ($\dot{Q}_{ext}$). It should be noted that the heat taken by the piston oil jet could not be estimated separately due to the engine/dynamometer configuration and is thus included in the $\dot{Q}_{oil}$ term. The energy balance model is expressed mathematically according to Equation (3.1).

$$\dot{m}_f \cdot q_{LHV} + \dot{Q}_{air} + \dot{Q}_{EGR} + \dot{Q}_{htr} = \dot{W}_{shaft} + \dot{Q}_{cool} + \dot{Q}_{oil} + \dot{Q}_{exh} + \dot{Q}_{chem} + \dot{W}_{HPP} + \dot{Q}_{ext} \quad (3.1)$$

In terms of model implementation the only parameter that was not calculated, rather directly imported into the model, was the brake power ($\dot{W}_{shaft}$) which was calculated by the CADET system. As such it is presented in the *Model inputs* section.

The boundary of the control volume was kept to a minimum by installing the temperature sensors used as close as possible to the engine. For the coolant circuits, the differential thermocouples, described in Chapter 2, have been installed 20 cm away from the engine, considering the space limitations imposed by the various engine components. Similarly, the exhaust and inlet gas temperatures were measured 20 cm from the engine. The oil inlet and outlet temperatures were measured 10 cm from the engine. The locations of these sensors can be seen in Figures 3.1-3.3.

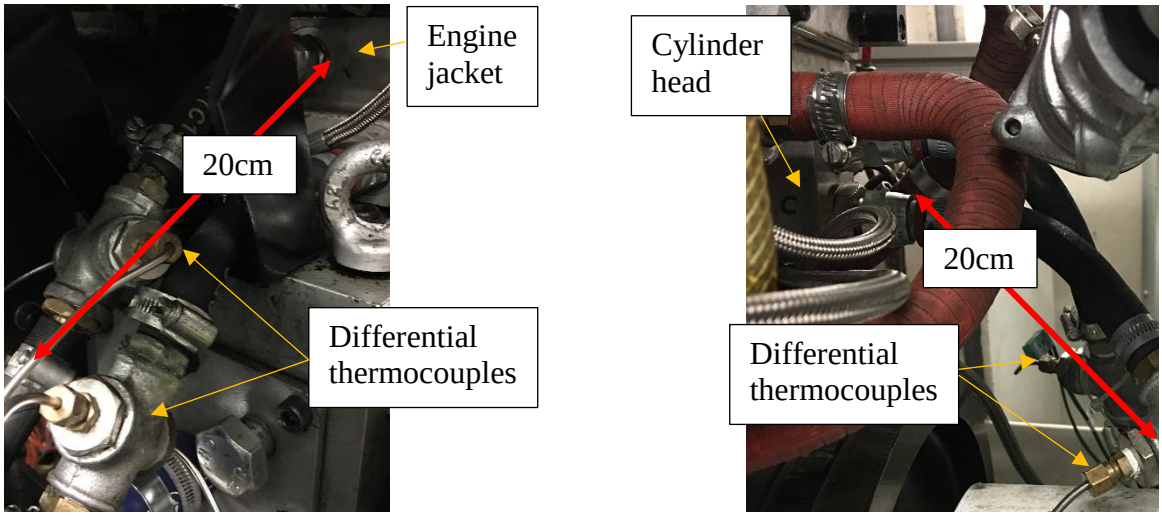

Figure 3.1: Location of differential thermocouples on engine coolant lines

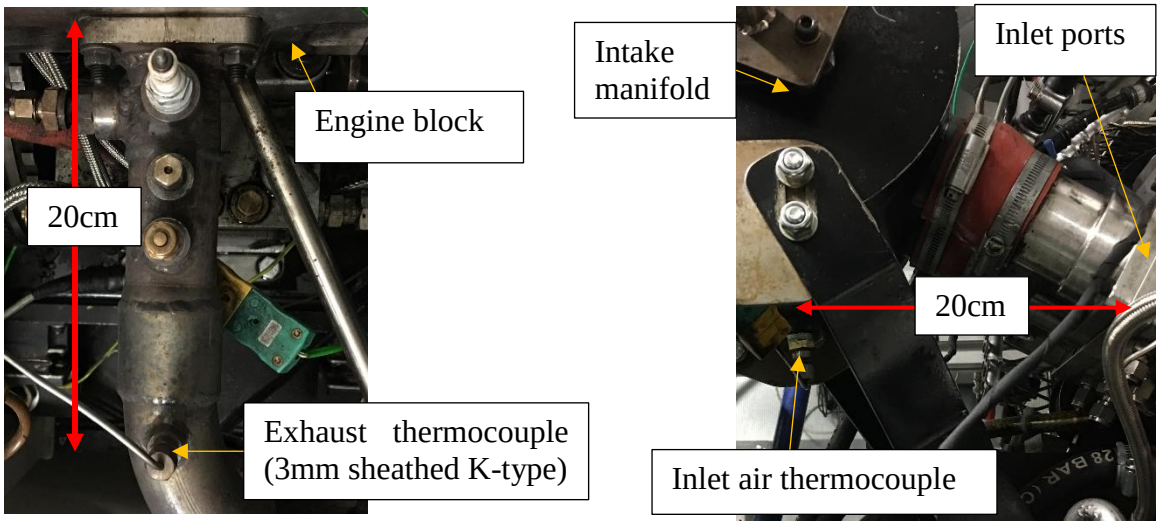

Figure 3.2: Location of thermocouple sensors on exhaust and inlet

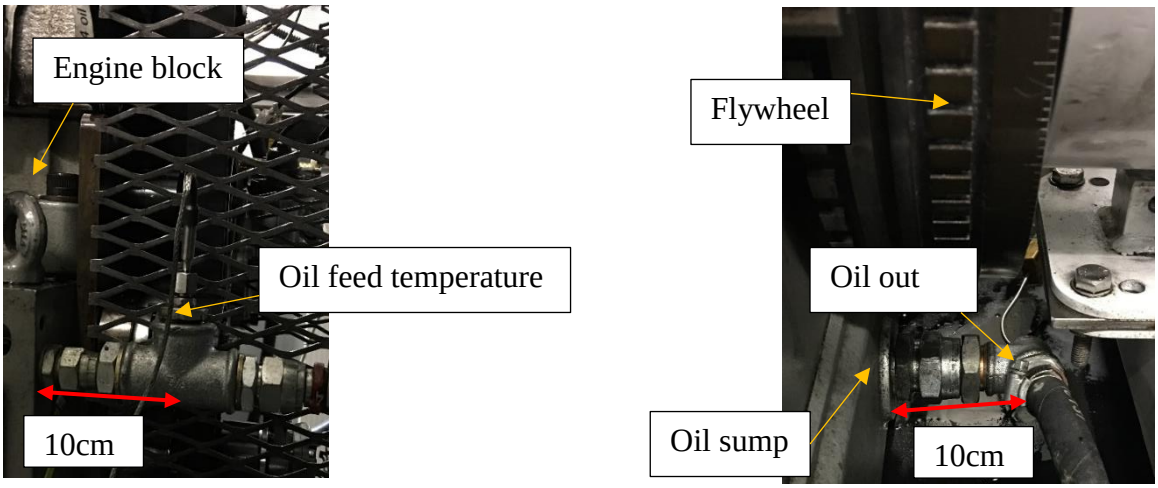

Figure 3.3: Location of temperature sensors on oil lines

3.1.1 Model inputs

As already mentioned in Chapter 2, two independent methods of fuel metering were used in order to increase experimental accuracy. Consequently, an average value of fuel flow rate between the two methods was used as an input to the energy balance model. The calorific value for the fuel was assumed to take a value of 42.7 kJ/g according to Stone [29]. Correspondence with the fuel supplier confirmed that the fuel used in the experiments has a very similar calorific value to the one presented above.

The intake charge was considered to be comprised of two streams; the freshly induced air and the EGR stream. The total energy rate input from the intake charge was calculated based on Equation (3.2). This calculation takes into account the enthalpy of each chemical species found in the intake charge, based on the intake manifold conditions, rather than using the properties of air, as is commonly done [99].

$$\dot{Q}_{\text{in,charge}} = \overbrace{\left[\left(\sum_{i=1}^{n}\frac{\dot{m}_i}{M_i}\cdot h_{i,\,man} - \sum_{i=1}^{n}\frac{\dot{m}_i}{M_i}\cdot h_{i,\,ref}\right)_{\text{air}}\right.}^{\dot{Q}_{\text{air}}} + \underbrace{\left.\left(\sum_{i=1}^{n}\frac{\dot{m}_i}{M_i}\cdot h_{i,\,man} - \sum_{i=1}^{n}\frac{\dot{m}_i}{M_i}\cdot h_{i,\,ref}\right)_{\text{EGR}}\right]}_{\dot{Q}_{EGR}} \tag{3.2}$$

The enthalpy of species i at inlet and reference conditions is denoted by $h_{i,\,man}$ and $h_{i,\,ref}$ respectively, with the reference conditions taken at 298.15 K. The mass flow rate of species i is denoted by, $\dot{m}_i$ and the molar mass by M_i. The values used for the molar mass of the species were taken from Heywood [26].

Enthalpy values were calculated using tabulated least-squares coefficients associated with fourth-order polynomials that fit the thermodynamic properties of each species, based on data by McBride *et al.* [125]. The dimensionless form below was coded as a MATLAB script and was called when required.

$$\frac{H°(T)}{RT} = \alpha_1 + \alpha_2\frac{T}{2} + \alpha_3\frac{T^2}{3} + \alpha_4\frac{T^3}{4} + \alpha_5\frac{T^4}{5} + \frac{b_1}{T} \tag{3.3}$$

Where $\alpha_{1\text{-}5}$ and b_1 are the tabulated coefficients for each species and R is the universal gas constant.

The number of moles for each species and consequently the mass flow rate $\dot{m}_i$, was calculated from the chemical equilibrium equation of fuel and air, assuming incomplete combustion and eight different species as the by-products of combustion, based on the work of Silvis [126]. Additionally, the EGR stream was also included. This is shown in Equation (3.4) below:

$$\begin{aligned} &\mathrm{C_{7.2}H_{13.3}}O_{0.035} + n(\mathrm{O_2} + 3.77\mathrm{N_2} + 0.16\mathrm{CO_2} + 0.0076H_{abs}H_2O) \\ &\quad + \frac{EGR}{100}(a\mathrm{CO_2} + b\mathrm{CO} + c\mathrm{H_2} + d\mathrm{H_2O} + e\mathrm{O_2} + f\mathrm{N_2} \\ &\quad + g\mathrm{NO_x} + \mathrm{j}\mathrm{C_{7.2}H_{13.3}}O_{0.035}) \leftrightarrow \\ &\quad \leftrightarrow a\mathrm{CO_2} + b\mathrm{CO} + c\mathrm{H_2} + d\mathrm{H_2O} + e\mathrm{O_2} + f\mathrm{N_2} \\ &\quad + g\mathrm{NO_x} + j\mathrm{C_{7.2}H_{13.3}}O_{0.035} \end{aligned} \tag{3.4}$$

The constants shown for the species comprising the intake air are calculated by normalising the concentration of each species with respect to the concentration of oxygen in ambient air (i.e. 0.2099%) according to [126]. The term H_{abs} indicates the absolute humidity of ambient air in grams of water per kilogram of air.

The mole fraction (i.e. concentration) of CO_2, CO, THC, O_2 and NO_x was provided by the emissions analyser. It is recalled that the THC and NO_x measurements were taken on a wet basis (i.e. the water found in the exhaust was not removed prior to the measurement) and that the CO_2, CO, and O_2 measurements were carried out on a dry basis. Consequently, for a wet basis measurement, the moles of water should be taken into account when estimating the moles of species in the exhaust. An example of this calculation is shown in Equation (3.5) for the NO_x species.

$$g = \frac{[NO_x]}{(n_{tot} + d)} \tag{3.5}$$

where n_{tot} represents the total number of moles in the exhaust.

It should be noted that the emissions analyser is converting the NO_2 found in the exhaust to NO and then the total amount of nitrogen oxides is presented as NO_x.

For the dry species, a cooler is used to condense the water. However, some water still escapes the cooler and it should thus be taken into account. Therefore, the number of moles for the dry species were calculated according to Equation (3.6), using as an example the CO species.

$$b = \frac{[CO]n_{tot}}{(1 - [H_2O]_{cooler})} \tag{3.6}$$

where $[H_2O]_{cooler}$ is the mole fraction of water escaping the condenser.

The number of moles of oxygen (n), hydrogen (c), water (d) and nitrogen (f) were then calculated from the iterative solution of six simultaneous equations, namely; the 4 atomic balances, C, H, O and N balance, the total mole balance, n_{tot}, and finally an expression for the number of moles of water. It should be noted that any unburned hydrocarbons

found in the exhaust were considered to have the same composition as the fuel. The first 5 equations can be seen below:

Carbon balance

$$7.2 + 0.16n = (1 - \frac{EGR}{100})(a + b + 7.2j) \tag{3.7}$$

Hydrogen balance

$$13.3 + 2 \cdot 0.0076H_{abs}n = (1 - \frac{EGR}{100})(2c + 2d + 7.2j) \tag{3.8}$$

Oxygen balance

$$0.013 + n(2 + 2 \cdot 0.16 + 0.0076H_{abs}) = (1 - \frac{EGR}{100})(2a + b + d + 2e + g + 7.2j) \tag{3.9}$$

Nitrogen balance

$$2 \cdot 3.76n = (1 - \frac{EGR}{100})(2f + g) \tag{3.10}$$

Total number of moles

$$n_{tot} = a + b + c + e + f + g + j \tag{3.11}$$

The sixth equation used to calculate the number of moles of water (d), was provided by the water/gas equilibrium equation (Equation (3.12)).

$$\mathrm{CO_2 + H_2 \leftrightarrow CO + H_2O} \tag{3.12}$$

This reaction is used to describe the dissociation of H_2O and CO_2 at rich fuel/air mixtures during combustion. An equilibrium gas constant κ is used to describe the rate at which the

gases reach equilibrium, a parameter that is dependent on peak combustion temperatures. Literature indicates a range between 3.5-3.8 for the value of κ [126] and for this work κ was set to 3.5. Equation (3.13) shows the expression for the equilibrium gas constant, κ.

$$\kappa = \frac{bd}{ac} \tag{3.13}$$

To solve these equations, an initial value for n was assumed and the calculation was iterated until the change in the value of n was insignificant (i.e. $<10^{-7}$). Finally, the quality of the solution was assessed by comparing the calculated oxygen concentration to the assumed value of oxygen concentration at the beginning of the calculation (i.e. 0.2099%) [126].

The energy input from the in-sump heaters $(\dot{Q}_{htr})$, was calculated based on the current drawn for a given oil heater demand. The oil heater demand is determined on the temperature difference between the set-point temperature and the oil feed temperature. An 8-point measurement was carried out for different oil heater demands, ranging from 0-100%, and the current values were logged using a current clamp signal at each point. This measurement was repeated five times. An average value for each point was then calculated and a polynomial was fitted to the results and imported to the energy balance model. The polynomial fit can be seen in Figure 3.4 with the error bars indicating the 95% confidence limits. Thus, by knowing the oil heater demand, the current through the heaters was estimated and by multiplying with the mains voltage supply, the rate of energy input from the heaters was calculated.

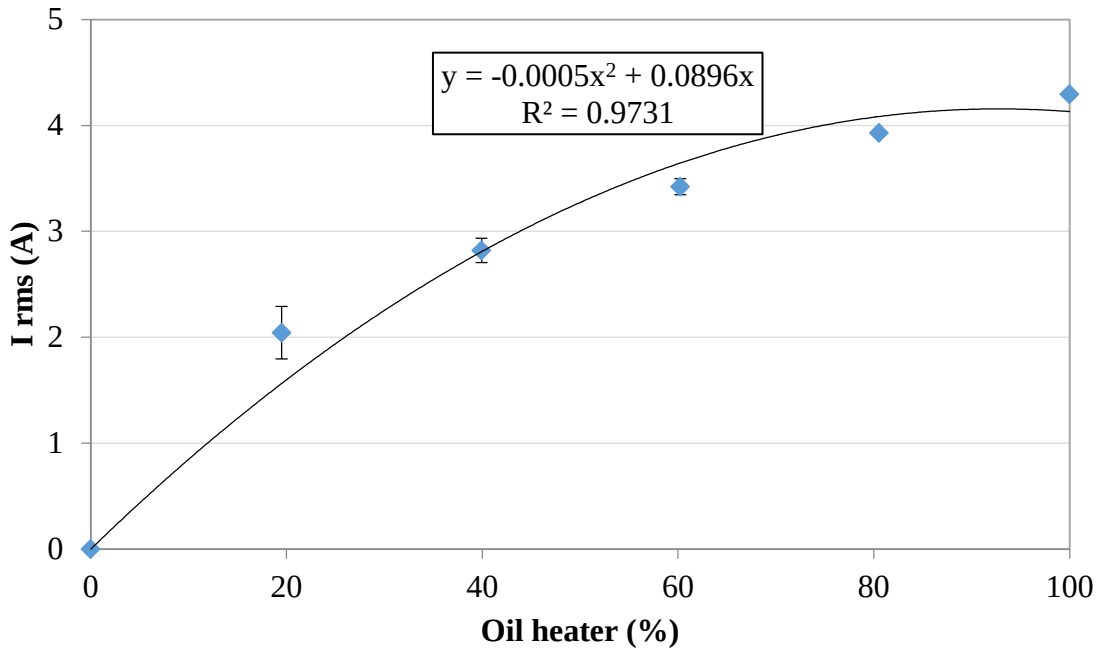

Figure 3.4: Characterization of the oil heater demand. The values presented are averaged over five samples and the error bars indicate the 95% confidence limits. The fitted 2nd order polynomial is imported into the energy balance model to estimate the rate of energy input from the heaters

Finally, as the brake power ($\dot{W}_{shaft}$) is calculated by the CADET system using the load cell signal, it was directly imported into the energy balance model. Equation (3.14) shows this calculation.

$$\dot{W}_{shaft} = \frac{2\pi \cdot N \cdot F_{lc} \cdot L_l}{60} \tag{3.14}$$

where N is the engine speed in RPM, F_{lc}, is the load cell signal and L_l is the distance of the load cell from the centre of the crankshaft.

3.1.2 Model outputs

The rate of heat transferred to the coolant, for a coolant line x (either cylinder head or cooling jacket) was calculated from Equation (3.15):

$$\dot{Q}_{cool} = c_{p,cool.(T)} \cdot T_{diff(x)} \cdot \dot{v}_{cool.(x)} \cdot \rho_{cool.(T)} \quad (3.15)$$

where $T_{diff(x)}$ is the differential thermocouple signal, $\dot{v}_{cool.(x)}$ the measured volume flow rate of the coolant and $c_{p,cool.(T)}$ and $\rho_{cool.(T)}$ are the specific heat capacity and density of the ethylene glycol-water mixture for a 50% v/v concentration. Both of these properties were calculated based on the time-average temperature of the feed coolant line using a standard K-type thermocouple.

The thermophysical properties of the glycol mixture were provided by the industrial partner and can be seen in Figure 3.5. The fitted polynomials were then imported into MATLAB and called when required.

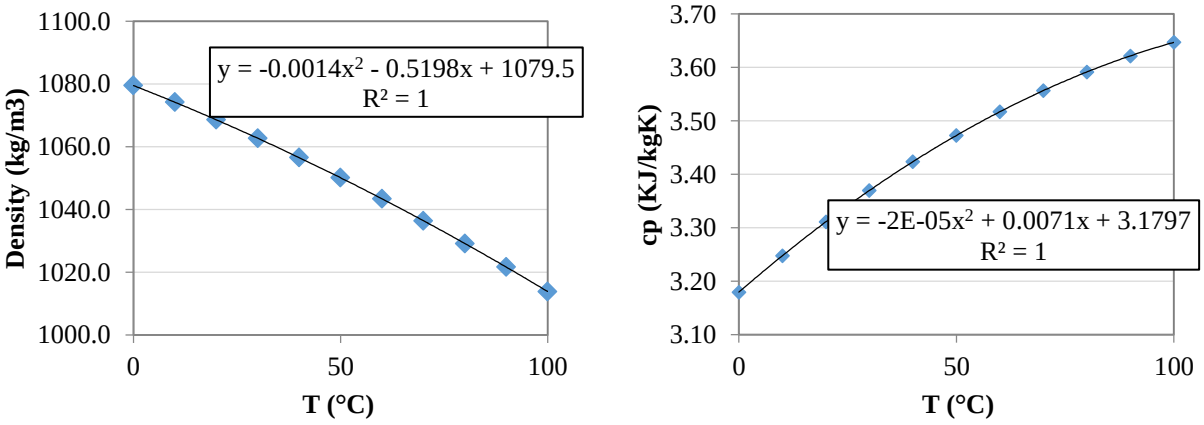

Figure 3.5: Thermophysical properties of ethylene glycol/water mixture for a 50% v/v concentration. The fitted polynomials are imported into MATLAB to estimate the energy transfer to the coolant

Similarly, the energy rate transferred to the oil was calculated according to Equation (3.16)

$$\dot{Q}_{oil} = c_{p,oil(T)} \cdot (T_{out} - T_{in}) \cdot \dot{v}_{(oil)} \cdot \rho_{oil(T)} \quad (3.16)$$

The thermophysical properties of the lubricant were calculated from empirical correlations derived by Larsson *et al.* [127] for a variety of lubricant types. The correlations used were based on the results of polyalphaolefin which is a synthetic base oil and has very similar density (810.2 kg/m^3) to the SAE 10W40 oil (819 kg/m^3) used in this work. In order to assess the effects of this density discrepancy, the model was tested with both density values; this resulted in a 0.03% difference in the energy transferred to the lubricant. This difference was deemed negligible and thus the discrepancy in density was considered acceptable.

The exhaust thermal energy was calculated from the enthalpy of the exhaust species using Equation (3.17) following the same principles presented above, for the enthalpy calculation of the intake air.

$$\dot{Q}_{exh} = \left(\sum_{i=1}^{n} \frac{\dot{m}_i}{M_i} \cdot h_{i.\,exh} - \sum_{i=1}^{n} \frac{\dot{m}_i}{M_i} \cdot h_{i.\,ref} \right) \tag{3.17}$$

The chemical energy rate in the exhaust ($\dot{Q}_{chem}$) was calculated from the oxidation energy of CO, H_2 and THC, where the number of moles of each species was calculated from Equation 3.4.The equilibrium equations for the oxidation of the CO and H_2 species used, can be seen in Equations (3.18) and (3.19). The energy from the unburned hydrocarbons was calculated from the calorific value of the fuel (q_{LHV}).

$$\mathrm{CO} + 0.5\mathrm{O_2} \leftrightarrow \mathrm{CO_2} \tag{3.18}$$

$$\mathrm{H_2} + 0.5\mathrm{O_2} \leftrightarrow \mathrm{H_2O} \tag{3.19}$$

Apart from the frictional losses that tend to reduce the brake work output, energy is also consumed by the various ancillary components of the engine. This energy is eventually dissipated as heat into the coolant, oil or the ambient air. In this work, the only ancillary

component driven by the timing belt of the engine is the high pressure fuel pump. Consequently, the fuel pump power ($\dot{W}_{HPP}$) indicates the energy required to pressurise the fuel at a given operating pressure. It is worth noting that in this work the fuel pump work will be higher than normal, as the high pressure pump employed here is from a 4-cylinder engine. The parasitic torque (T_{HPP}) used in the calculations was 8.5 Nm, based on published data of a high pressure diesel pump [128]. The data were corrected to account for the differences in pump types between the two studies. It should be noted that the volume control valve of the high-pressure pump was not operational during these studies and consequently the parasitic torque (T_{HPP}) would be constant independent of fuel rail pressure. The ancillary losses were then calculated from Equation (3.20):

$$\dot{W}_{HPP} = 2\pi \cdot N \cdot T_{HPP} \tag{3.20}$$

As already discussed, adiabatic enclosures have been used in literature to quantify the extraneous term ($\dot{Q}_{ext}$). Due to the difficulty of implementing such a configuration in the existing facility, the extraneous term was calculated by solving Equation (3.1) once all energy transfer terms were known.

3.2 Thermocouple modelling

The heat transfer process is a three dimensional phenomenon and depending on the complexity of the geometry, modelling it accurately can be a significant challenge. In this section, the model used to assess the effect of different size thermocouple junction on transient temperature measurements will be presented. It is recalled from Chapter 2 that four K-type thermocouples were used for exhaust gas temperature measurement; three bare-wire thermocouples, comprising a thermocouple probe, and a 3 mm sheathed thermocouple which is commonly used in such applications. The model is based on a transient 1-D lumped system analysis.

The main assumption of this method is that when a body is exposed to a transient thermal event, no temperature gradients within the body occur. This means that the body will have a uniform temperature at any point of this transient event. Consequently, according to Fourier's Law, conduction through the solid is instant assuming an infinite thermal conductivity. It is obvious that this is not feasible in real life, however the assumption of the lumped capacitance method is valid if the conductive resistance of the body is significantly smaller than the convective resistance between the fluid and the body [90]. A measure of this, is a parameter called the Biot number.

The Biot number is a dimensionless index that describes the ratio of convective heat transfer to the heat conducted within a body, when the body is exposed to a thermal gradient and can be expressed as:

$$Bi = \frac{L_c h}{k} \tag{3.21}$$

where L_c is the characteristic length (usually defined as $\frac{\text{volume}}{\text{surface area}}$), h is the convective heat transfer coefficient and k is the thermal conductivity of the body.

Another way to express this is the ratio of surface thermal resistivity (dependent on h) to the internal thermal resistivity (dependent on k). Figure 3.6 shows the effect of Biot number on the internal temperature gradient of a body when exposed to a fluid temperature of $T2$. It is widely accepted that the lumped capacitance approach is justified when $Bi << 0.1$ [90]. A small Biot number thus does not require the use of numerical methods (e.g. finite difference method) to solve the 1-D transient heat equation, rather the system can be considered, "thermally", as a single finite volume (lumped model).

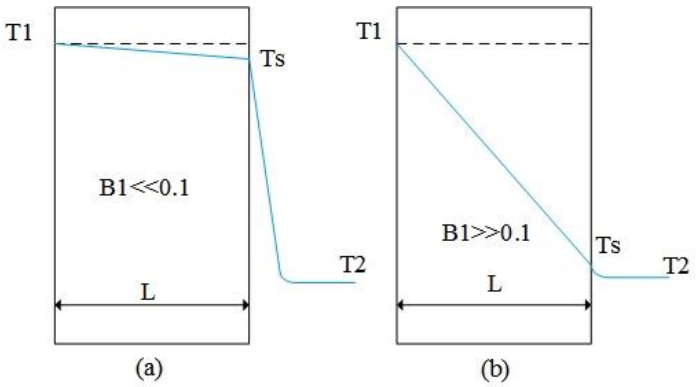

Figure 3.6: Effect of Biot number on internal temperature gradient when exposed to a fluid of temperature T2

Different junction types for the bare-wire thermocouples were employed with the goal of keeping their temporal response as high as possible. Consequently, a bead-type junction was used for the 50.8 μm thermocouple and a butt-welded type junction for the 127 and 254 μm thermocouples respectively. Generally, butt-welded junctions offer a faster response as the junction size is smaller, however, due to manufacturing constraints the 50.8 μm thermocouple is only offered with a bead-type junction. The small size of these thermocouples makes the assumption of the lumped capacitance method valid, as can be seen in Table 3.

Due to the small size of the junctions used and limitations in manufacturing tolerances, the exact size of each junction was examined using photomicrography. Despite the magnification offered by photomicrography, the exact thermocouple junction size was still very difficult to determine. Consequently, the junction diameter as specified by the manufacturer was used in the model. However, the geometry of each junctions was well captured which allowed the modelling of the bead-type junction as a sphere and the butt-welded junction as a tube of finite length.

During the fusion welding process of the butt-welded K-type thermocouples, the Alumel leg is melted into the Chromel leg [129] and due to the fact that the exact penetration depth is not clear, an accurate estimation of the sensing junction length is quite difficult. Accordingly, the junction length of the butt-welded thermocouples was corrected to match the experimental data logged with the thermocouple probe (refer to Chapter 5).

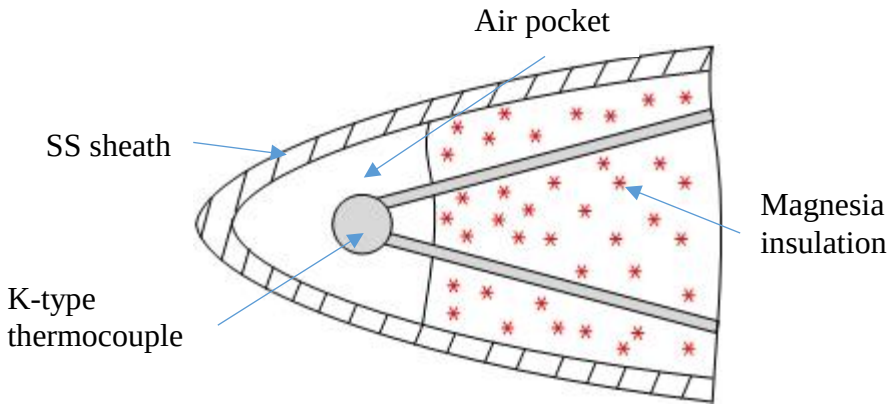

Figure 3.7: Cross-sectional representation of sheathed thermocouple. Adapted from [130].

The construction of a sheathed thermocouple is somewhat different to the bare-wire thermocouples as it incorporates a ceramic insulation layer along with a protective sheath, to increase the corrosion resistance of the junction. More specifically, the 3 mm reference thermocouple used in this work is comprised of a stainless steel sheath and a mineral based insulation in powder form (Magnesia - MgO), packed inside the sheath.

Manufacturing inconsistencies have been shown to result in a non-uniform distribution of the mineral insulation, resulting in air pockets around the sensing junction [130]; this could lead to temperature non-uniformities within the thermocouple sheath, consequently, invalidating the lumped capacitance assumption. Figure 3.7 shows a typical cross-sectional representation of a sheathed thermocouple [130].

Since machining of the reference thermocouple was not possible in order to identify the actual construction of the sheath and considering that the aim of this modelling work was to identify the effects of thermocouple size under transient temperature measurements, the reference thermocouple was modelled ignoring the sheathed construction. Instead, the junction was treated as a sphere with a diameter of 3 mm, assuming a uniform Nickel construction. Table 3 presents the junction geometry of the thermocouples used along with their respective Nusselt number correlations.

Table 3: Characteristics of modelled thermocouples

Thermocouple diameter	**Nusselt correlation**	**Junction geometry**	**Biot number**
0.0508mm	Sphere	Bead	0.000165
0.127mm	Tube	Butt-welded	0.000325
0.254 mm	Tube	Butt-welded	0.000396
3 mm	Sphere	Bead	0.000528

The indicated temperature of the sensing junction in the exhaust stream will be dependent on the thermal equilibrium of the different heat transfer terms – these are: conduction losses along the thermocouple leads, radiative cooling to the cooler surroundings and heat convected from the hot gases. These terms are shown in Figure 3.8. The thermocouple model is thus based on an energy balance approach around the thermocouple junction following the equation below:

$$\underbrace{hA_s(T_g - T_s)}_{\text{Convectio}} - \underbrace{\sigma\varepsilon A_s(T_s^4 - T_w^4)}_{\text{Radiation}} - \underbrace{kA_{csa}\frac{d^2T_s}{dx^2}}_{\text{Conduction}} = \underbrace{mc_p\frac{dT_s}{dt}}_{\text{Energy change}} \quad (3.22)$$

where h is the convective heat transfer coefficient, σ is the Stefan-Boltzmann constant, ε the emissivity of the thermocouple material and k, m and c_p are the thermal conductivity, mass and heat capacity of the thermocouple material respectively. A_s is the junction surface area and A_{csa} denotes the cross-sectional area of the thermocouple wire. The gas temperature is given by T_g, the thermocouple measured temperature is given by T_s and the exhaust manifold wall temperature is given by T_w.

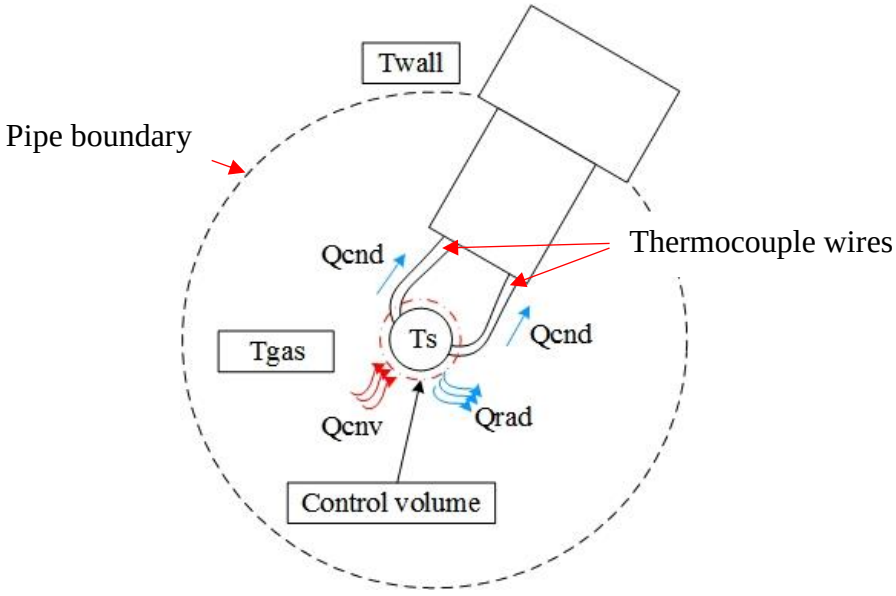

Figure 3.8: Heat transfer on a thermocouple junction installed in a pipe with internal flow.

The exhaust wall temperature was measured by an embedded K-type thermocouple, installed at a very close proximity to the K-type thermocouple probe (refer to Chapter 2). Experimental measurements have shown that upon thermal equilibrium of the engine, the exhaust wall temperature did not show any appreciable variations, therefore, for the purpose of model simplification, this value was assumed to be constant for the duration of the engine cycle.

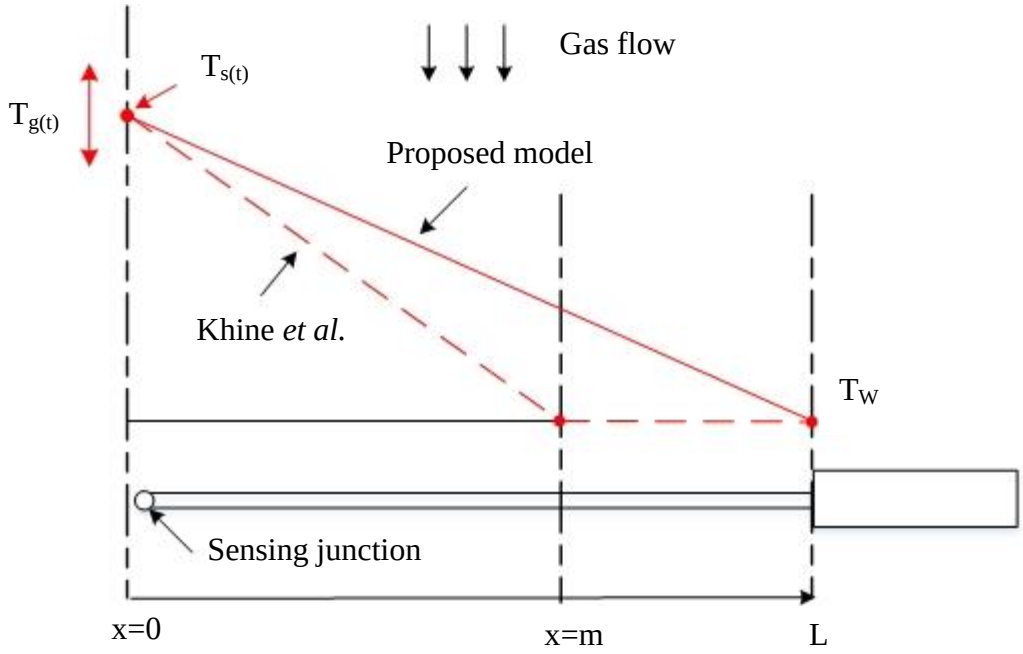

Figure 3.9: Theoretical model for conduction error estimation. The solid red line indicates the assumed temperature distribution used in the thermocouple model.

Estimating the steady state conduction error is commonly carried out by treating the thermocouple as a thin rod and applying the analytical solutions available for fins [131]. However, the effect of conduction error on unsteady temperature measurements is usually ignored. Exceptionally Khine *et al.* [132], measured the unsteady temperature at the wake of a heated cylinder exposed to an external flow and corrected for the conduction error along the body of the sensor by assuming the temperature distribution shown in Figure 3.9 (red dashed line). The length m was introduced by Khine and his co-workers to account for the construction of the sensor – they employed a prong design to hold the fine-wire thermocouple in constant tension with m being the distance from the thermocouple junction to the start of the prong.

However, considering the construction of the thermocouple probe used in this work and the measurement environment (i.e. internal flow in pipe and not external flow), a more suitable conduction model is indicated by the solid red line. A linear temperature

variation along the length of the probe is expected to lead to inaccuracies as the effects of the thermal boundary layer are not taken into account, however considering the aim of this study, this simplification was deemed acceptable.

As the conduction term is dependent on the driving thermal potential between the junction temperature and the wall temperature, and assuming that the wall temperature will be constant throughout the cycle duration, the conduction term in Equation (3.22) can be estimated at every time-step from an expression of the form $A\frac{\Delta T}{L}$, where L indicates the conduction length. In this case, L is the exposed length of the thermocouple probe to the exhaust flow. The energy balance for the hot junction then becomes:

$$\underbrace{hA_s\left(T_g - T_s\right)}_{\text{Convectio}} - \underbrace{\sigma\varepsilon A_s(T_s^4 - T_w^4)}_{\text{Radiation}} - \underbrace{2kA_{csa}\frac{(T_s - T_w)}{L}}_{\text{Conduction}} = \underbrace{mc_p\frac{dT_s}{dt}}_{\text{Energy change}} \tag{3.23}$$

Using the finite difference approximation for the time derivative, Equation (3.24) becomes:

$$\overbrace{\frac{hA_S}{mc_p}\left(\left(T_{g(i)} - T_{s(i)}\right)\right)}^{\text{Convectio}} - \overbrace{\frac{\sigma\varepsilon A_s}{mc_p}\left(T_{s(i)}^4 - T_{w(i)}^4\right)}^{\text{Radiation}} - \overbrace{\frac{2kA_{csa}}{mc_p}\frac{(T_{s(i)} - T_w)}{L}}^{\text{Conduction}} = \underbrace{\frac{T_{s(i+1)} - T_{s(i)}}{\delta t}}_{\text{Temperature}} \tag{3.24}$$

Where δt indicates the time-step size (i.e. 1 CAD) and i the current time step. Solving for $T_{s(i+1)}$ we get the temperature history of the thermocouple, according to Equation (3.25).

$$T_{s(i+1)} = T_{s(i)} + \frac{\delta t}{mc_p}\left[hA_S\left(T_{g(i)} - T_{s(i)}\right) - \sigma\varepsilon A_s\left(T_{s(i)}^4 - T_w^4\right) - 2A_{csa}k\frac{\left(T_{s(i)} - T_w\right)}{L}\right] \quad (3.25)$$

The above equation was coded into MATLAB and an initial temperature for the thermocouple junction $T_{s(i)}$ was assumed based on the experimental conditions.

The emissivity (ε) of a material is a parameter that is very much dependent on surface characteristics such as surface roughness, surface coating and surface oxidation [133]. Therefore, soot deposition is expected to alter the emissivity of the thermocouple sensors used. Experimental work [134] supports this observation, reporting an increase in the emissivity of soot-deposited Nickel substrate (~0.895) compared to the emissivity of a deposit-free, oxidised Nickel substrate of (~0.58) at 470 °C. This then implies that a soot-deposited thermocouple junction is expected to experience higher radiative heat transfer – the overall heat transfer process however, will also depend on the thermal conductivity of the soot deposited layer and the resulting convective heat transfer, since recent studies have shown that soot deposition can act as an insulator and thus affect the resulting temperature measurement [135]. In this work, the emissivity values presented by Ran Fu *et al.* [134] for a soot-deposited substrate have been used.

K-type thermocouples are comprised of nickel based alloys – the positive leg is made of Chromel and the negative leg of Alumel [12] – accordingly, the material properties used for the thermocouple simulations, were taken to be those of nickel. Table 4 details the thermo-physical properties of nickel, which were assumed to be independent of temperature.

Table 4: Thermo-physical properties of nickel

Property	**Value**	**Units**
Density (ρ)	8908	kg/m^3
Heat capacity (c_p)	440	J/kgK
Thermal conductivity (k)	90	W/mK
Emissivity (ε)	0.895	-

The heat transfer characteristics of the thermocouple junctions were calculated using Nusselt number correlations presented by Whitaker [91], according to Equation (3.26):

$$Nu = 2 + \left(0.4\, Re^{\frac{1}{2}} + 0.06\, Re^{\frac{2}{3}}\right) Pr^{0.4} \left(\frac{\mu_b}{\mu_0}\right)^{\frac{1}{4}} \tag{3.26}$$

where Re is the Reynolds number, Pr is the Prandtl number, and $\frac{\mu_b}{\mu_0}$ is the ratio of the dynamic viscosity at the surface of the body to the dynamic viscosity at free stream conditions.

Note that the viscosity ratio has been calculated at every time-step to account for the change in thermocouple surface and gas bulk temperatures and has been shown to remain within the specified limits defined by Whitaker (e.g. 0.25-5.2 for a cylinder and 1.0-3.2 for a sphere). Consequently, this correlation is used to describe both spherical geometries and tubes in a crossflow.

In these simulations the properties of the gas were taken as those of air, assuming a transparent medium (i.e. the working fluid will not absorb or emit any radiation to and from the surroundings). The thermo-physical properties ($k_{air}, c_{P,air}\ and\ \mu_{air}$) of air were

calculated based on published data and the corresponding exhaust gas temperature $T_{g(i)}$ at each time-step.

Data from a one-dimensional engine model provided by the project's industry partner was used to provide an indication of the exhaust gas temperature along with flow velocity profiles necessary for the calculation of the Reynolds and Nusselt numbers. The necessary boundary conditions (i.e. crank angle resolved intake and exhaust pressures) were set using the experimental signals from the fast-response pressure transducers (Chapter 2). In order to reduce the modelling effort, the model was limited to the length of the exhaust manifold between the exhaust ports and up to the location of the reference thermocouple sensor.

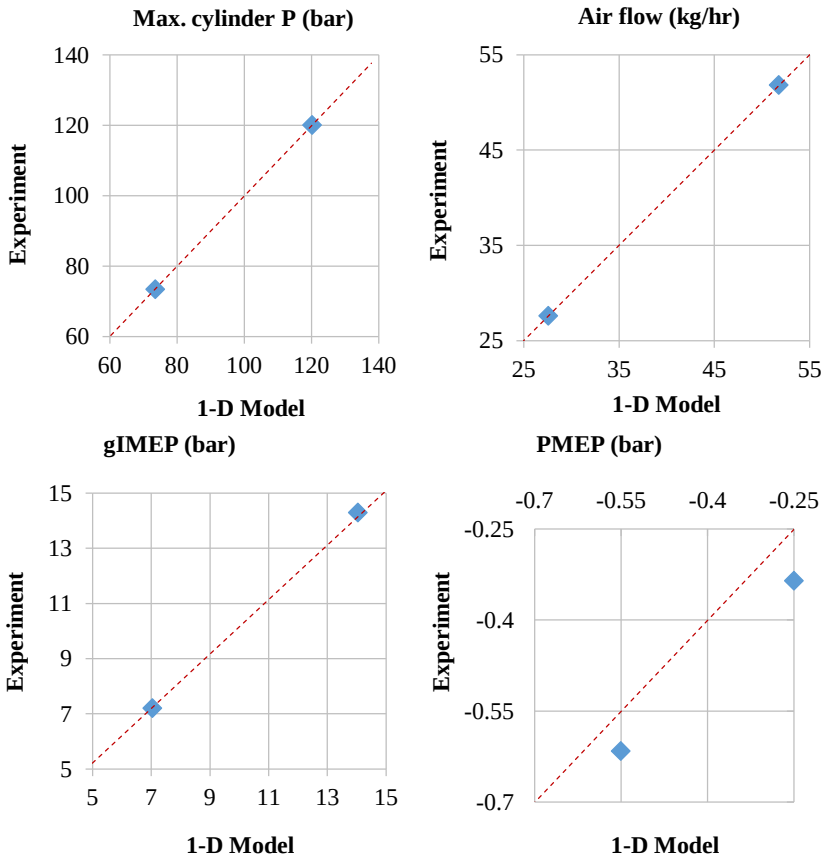

Figure 3.10: Validation results for the 1-D engine model. The blue dots show the experimental results and the red dotted line represents the unity slope line for the modelled results.

The validation of the one-dimensional model was carried out against several experimental parameters; these include: maximum cylinder pressure, intake flow rate, average cylinder pressure and pumping mean effective pressure (pmep). The results of the validation can be seen in Figure 3.10, with the blue dots indicating the experimental data. In general there is a very good agreement with the experiment, with some deviation arising for the pmep values (~0.05 bar and ~0.1 bar for the higher and lower load cases respectively). These deviations are a result of the intake pressure boundary conditions used in the model in order to match the experimental engine flow rates. However, it is not expected that these discrepancies will have an effect on the simulated exhaust gas temperature although they could affect the exhaust gas velocity profile. However, for the purpose of this work these discrepancies were considered acceptable. Considering that accurate knowledge of the errors associated with the measurement of the exhaust gas temperature was not available, validation of the modelled exhaust gas temperature was not possible.

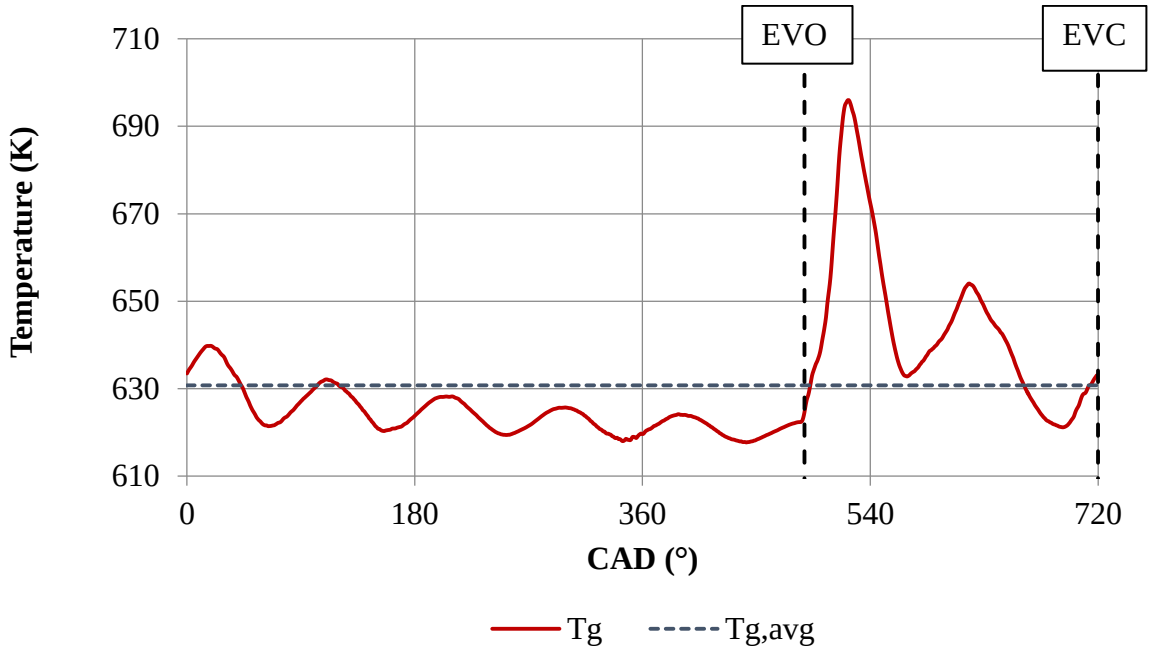

Figure 3.11: Typical "true" exhaust gas temperature signal from the 1-D engine model. The dotted line indicates the time-average value of the signal presented.

A typical, exhaust gas temperature signal from the 1-D model, can be seen in Figure 3.11. The observed undulations on the generated signal are a result of the pressure pulses travelling along the length of the exhaust manifold and are captured by the pressure transducer signal (i.e. the boundary conditions used). The horizontal dotted line indicates the time-average exhaust temperature which is representative of the measurements taken with a standard 3 mm sheathed thermocouple. This suggests that the exhaust enthalpy will be under-predicted if this value is used, especially during the exhaust valve opening period. This is discussed in more detail in Chapter 6. Finally the modelled exhaust temperature signal was imported into the thermocouple model, with the value at CAD=0° being the initial condition for all thermocouple junctions. Figure 3.12 shows the flowchart of the thermocouple model.

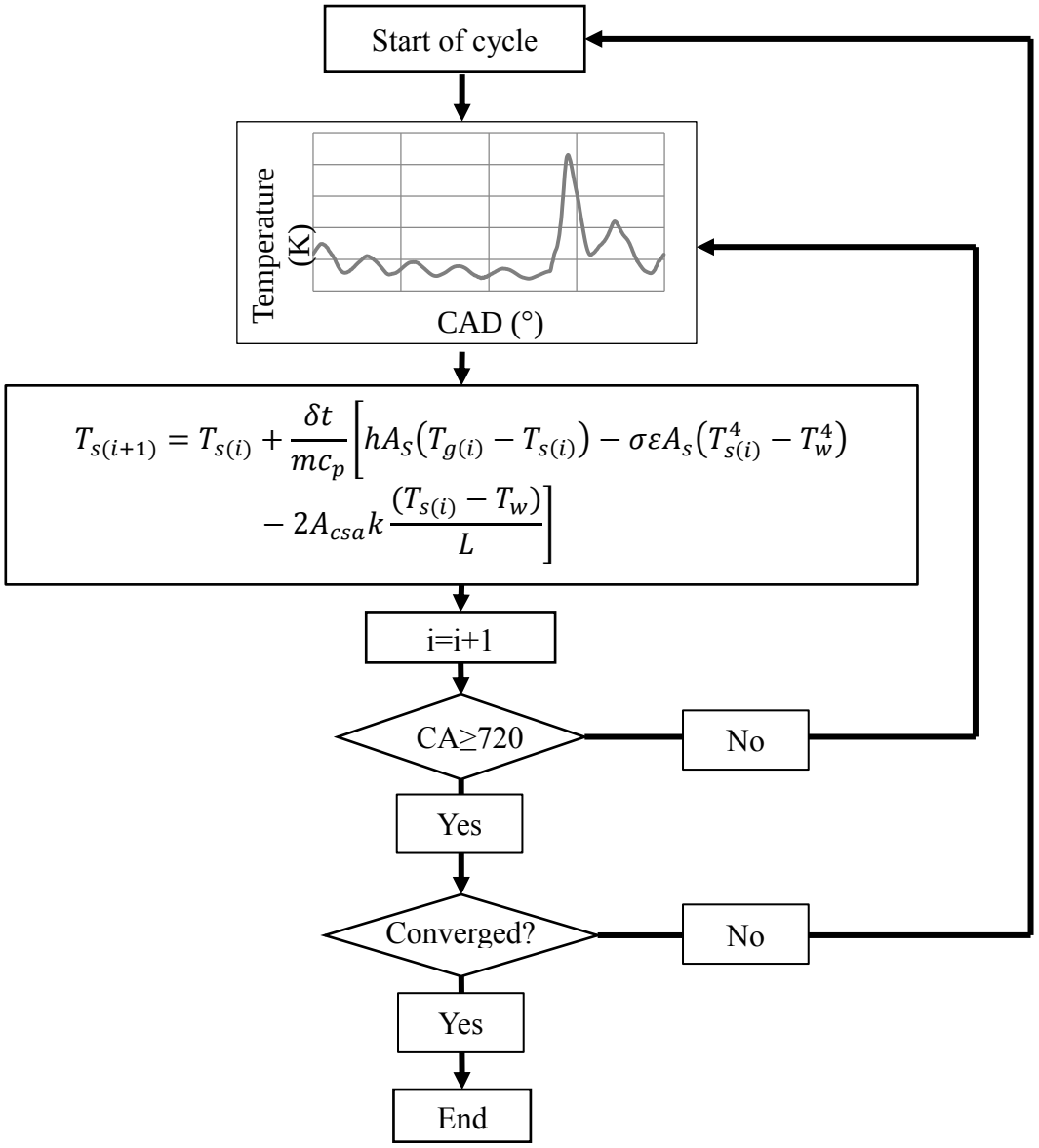

Figure 3.12: Flowchart of thermocouple modelling algorithm

3.3 Thermocouple dynamic error compensation

Chapter 1 has already introduced the effects of a sensor's time-constant in the measurement of unsteady temperature fields. It is recalled that due to the finite thermal mass of temperature sensors, some form of dynamic error will be introduced, which is manifested both as a phase lag and as an underprediction of the "true" gas temperature. This dynamic error is directly linked to the time-constant of the sensor and is present irrespective of junction size. Thus, temperature reconstruction involves the process of recovering the high-frequency temperature components that have been lost due to the thermal inertia of the thermocouple by estimating the thermocouple's time-constant.

Testing under known flow conditions – and consequently a known value of heat transfer coefficient – is a method commonly used to identify a sensor's time-constant [136-138]. Despite their simplicity, these techniques are very restrictive since in practice the flow conditions are usually not known. A more versatile method to correct the dynamic error is the use of dual probe techiques, where the signals of two different size thermocouples is used to estimate their time-constant *in situ* [113, 139-141]. This approach does not require knowledge of the local flow conditions.

Dual probe techniques assume that both thermocouples will be exposed to the same temperature and velocity fields, such that the gas temperature at the thermocouples' location can be assumed the same. The time-constants for each thermocouple can then be estimated by solving a simultaneous system of equations, based on an energy balance approach. In this work, the compensation method introduced by Tagawa *et al*. [14] is used. Through their work Tagawa and co-workers argued that the local gas temperature experienced by the two thermocouples will not be identical and thus put forward a

compensation method which minimises the time-average difference between the two thermocouples. The minimisation criterion used was the least-squares method.

Recalling Equation (3.22) and ignoring conduction and radiation for the two thermocouples we have the following system of equations:

$$\left.\begin{aligned} T_{g1} &= T_{s1} + \tau_1 \frac{dT_{s1}}{dt}, \\ T_{g2} &= T_{s2} + \tau_2 \frac{dT_{s2}}{dt}, \end{aligned}\right\} \tag{3.27}$$

Minimizing the time-averaged temperature difference between the two local gas temperatures (i.e. T_{g1} and T_{g2}) results in the time-constants τ_1 and τ_2 presented below:

$$\left.\begin{aligned} \tau_1 &= \frac{(\sum G_2^2)(\sum G_1 \Delta T) - (\sum G_2 \Delta T)(\sum G_1 G_2)}{(\sum G_2^2)(\sum G_1^2) - (\sum G_1 G_2)^2}, \\ \tau_2 &= \frac{(\sum G_1 G_2)(\sum G_1 \Delta T) - (\sum G_2 \Delta T)(\sum G_1^2)}{(\sum G_2^2)(\sum G_1^2) - (\sum G_1 G_2)^2}, \end{aligned}\right\} \tag{3.28}$$

where Σ indicates a moving average filter processes and G is the rate of change of the thermocouple signal, $\frac{dT_s}{dt}$.

The results of Equation (3.28) are highly sensitive to the averaging process since thermocouple signals are subject to measurement noise. The derivative term shown in Equation (3.27) will magnify the noise which can result in erroneous time-constants. Tagawa *et al*. [14] employed a central sliding moving average window to remove signal noise, with the choice of window size providing a compromise between temporal resolution and non-physical values from the resulting time-constants (i.e. negative values for τ). Reducing the window size will increase the temporal resolution of the time-constants, approaching the instantaneous value, however, if the window size is too small, it could only include high frequency temperature components. Consequently, the

minimisation criterion will try to compensate for these temperature fluctuations by providing a negative time constant. On the other hand, as the window size is increased, the effect of averaging is more pronounced and the resulting time-constants approach their time-average ($\bar{\tau}$), rather their instantaneous values (τ).

The amount of averaging should thus be adjusted considering the prevailing flow characteristics during the cycle. During the period that the exhaust valves are closed, it is expected that the velocity of the gases in the manifold will be almost negligible. It is noted that pressure waves – created during the valve opening period – travelling the length of the exhaust pipe will prevent the ambient gas from being completely stagnant. On the other hand during the valve opening event, flow velocities are extremely high with the area around the valves approaching choked conditions depending on operating conditions. This can be seen more clearly in Figure 3.13, where a 1D simulated exhaust gas velocity profile of the single cylinder diesel engine used in this study is shown.

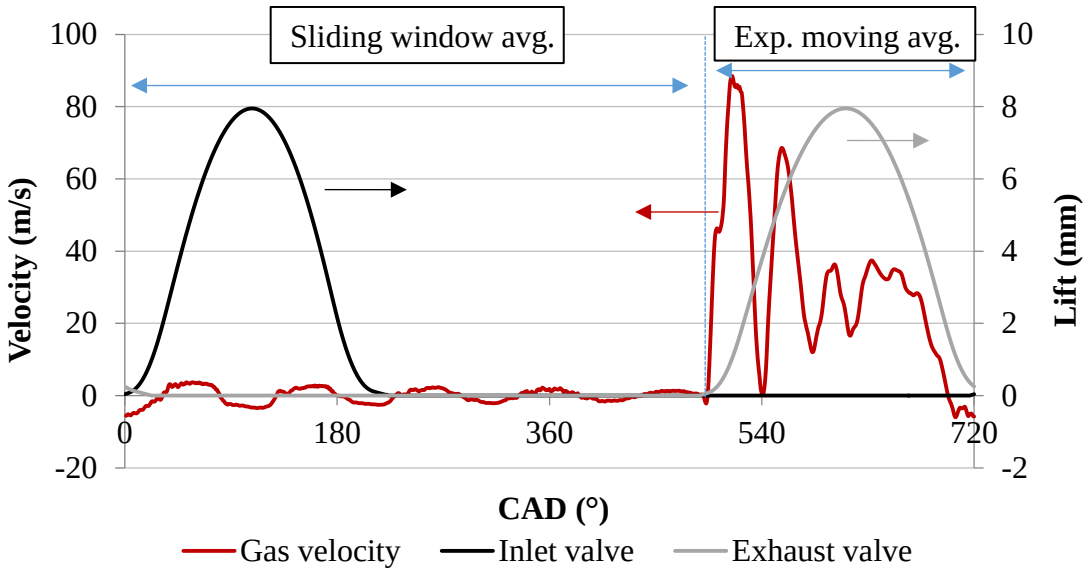

Figure 3.13: Simulated gas velocity profile for the single cylinder diesel engine. The different averaging method used are also shown for the two valve events

As such, these two valve opening periods were considered separately in order to reduce the effect of averaging on the instantaneous values of τ, especially during the blowdown period that is of highest interest. In addition, different averaging methods were used for the EVC and the EVO durations (Figure 3.13). Since the gas dynamics during the EVC period are not expected to be significant (i.e. no flow condition) an average time-constant was calculated during this event – the window size during the EVC period was set to half the number of data points during this time.

Considering the inherent dynamic error of temperature sensors, the indicated value at a given time will be a result of the flow conditions that the sensor has already been exposed to in the past. Therefore, during the EVO period, the time-constant was estimated at each time-step using an exponential moving average window following Equation (3.29) [123].

$$f(t) = \zeta g(t) + (1 - \zeta) f(t - 1) \tag{3.29}$$

where $f(t)$ is the filtered output, $g(t)$ is the input value and ζ is the weight factor.

This weight factor determines the importance of the past values on the filtered output, with a value of 1 implying that the same weight is given to all past data (i.e. simple moving average). Predictive models utilise exponential moving average methods over simple moving average as they can better predict rapidly changing values. In the period that the exhaust valve is open, and particularly close to the blowdown period, the time-constant will be rapidly changing and thus the exponential moving average method is appropriate. In this work, the value of ζ was set to $\zeta = 0.08$.

It is noted that the method presented by Tagawa *et al.* [14] was used as a baseline case and was then expanded to include the effects of radiation and conduction—modelling

work carried out in Chapter 5 shows that conduction is an important source of error in unsteady temperature measurements, commonly ignored in literature.

By taking an energy balance approach around the thermocouple junction, according to Equation (3.24), and by solving for the gas temperature, Equation (3.27) then becomes:

$$\left.\begin{aligned} T_{g1} &= T_{s1} + \tau_1 C_1, \\ T_{g2} &= T_{s2} + \tau_2 C_2, \end{aligned}\right\} \tag{3.30}$$

Where the parameter C is equal to:

$$C = \beta(T_s^4 - T_w^4) + \gamma(T_s - T_w) + \frac{dT_s}{dt} \tag{3.31}$$

and the parameters β and γ are equal to:

$$\beta = \frac{\sigma \varepsilon A_s}{m c_p} \tag{3.32}$$

$$\gamma = \frac{2 A_{csa} k}{m c_p L} \tag{3.33}$$

It should be noted that the conduction error was modelled by assuming a linear temperature distribution along the thermocouple wire (Figure 3.9). Finally the thermocouple time-constants while taking into account the conduction and the radiation error were calculated similarly to Equation (3.28) as shown below:

$$\left.\begin{aligned} \tau_1 &= \frac{(\sum C_2^2)(\sum C_1 \Delta T) - (\sum C_2 \Delta T)(\sum C_1 C_2)}{(\sum C_2^2)(\sum C_1^2) - (\sum C_1 C_2)^2}, \\ \tau_2 &= \frac{(\sum C_1 C_2)(\sum C_1 \Delta T) - (\sum C_2 \Delta T)(\sum C_1^2)}{(\sum C_2^2)(\sum C_1^2) - (\sum C_1 C_2)^2}, \end{aligned}\right\} \tag{3.34}$$

3.4 Chapter summary

This chapter introduced the modelling methods used for this thesis. The energy balance model is comprised of four inputs and six energy output terms. A modified method, based on published work, was used to calculate the number of species in the intake and exhaust streams and thus calculate their respective enthalpies. For this model the exhaust enthalpy calculation is based on a time-average exhaust temperature measurement. Experimental results using this model are presented in Chapter 4.

Subsequent work on the accurate estimation of the exhaust enthalpy resulted in building a thermocouple model based on the lumped capacitance method. The thermocouples used were modelled as spheres or tubes depending on their junction geometry. Due to manufacturing tolerances and to reduced modelling complexity, the sheathed thermocouple was also modelled as an exposed junction thermocouple with the assumption that the junction is comprised solely of Nickel. A one-dimensional code was used to provide an exhaust temperature profile, based on the experimental conditions presented in Chapter 5, which was then used as an input to the thermocouple model.

Finally, a temperature reconstruction method was presented, which is used to recover the true gas temperature measured by temperature sensors as this is usually not possible due to the dynamic errors introduced by their physical presence. These methods are noted to be highly sensitive to the averaging process employed. Accordingly the widely different flow characteristics seen during the EVC and EVO periods on engine, dictate that these two events are considered separately. This method was then expanded further to include the effects of radiation and conduction errors on temperature measurement. The results of this method are presented in Chapter 6. The next chapter presents the experimental results of two engine studies by applying the first law analysis.

4 Thermal studies using a first law analysis approach

This section presents the experimental results of energy balance studies carried out on a single cylinder diesel engine. The negative effects of EGR on smoke emissions have already been discussed in Chapter 1, along with various strategies which when employed can somewhat alleviate these penalties. Consequently, the first study looked into the effects of different high-pressure EGR application techniques and how these can affect the engine efficiency and the tailpipe emissions under two load/speed conditions. However, EGR application can result in a reduction in engine efficiency, due to the lower burn rates associated with the displacement of oxygen. Changing the thermal properties of the piston has the potential to remove the negative effects on efficiency by reducing the heat transfer to the piston thus increasing the potential work during the cycle. Following this, the second study looked to compare the performance of two pistons with the same bowl design but constructed from different materials; one aluminium and one steel.

4.1 Introduction

The use of EGR in diesel engines as a method of NO_x reduction, by displacing fresh intake charge, is widely covered in the literature [43, 51, 53, 142-144]. Thermal NO_x emissions are reduced due to the reduced oxygen concentration in the cylinder and the presence of inert gases with higher heat capacity both of which act to lower combustion temperatures. However some care is required, since reduced oxygen concentrations and lower in-cylinder temperatures may also reduce oxidation rates to the point that soot, CO, and THC emissions are increased—a tendency that may be offset by increasing mixing rates. Higher levels of in-cylinder swirl have been shown to reduce the emissions penalty traditionally associated with EGR, leading to improved emissions oxidation [10], albeit

with potential penalties in NO_x emissions and volumetric efficiency [67, 72]. Increased levels of swirl have also been shown to improve combustion efficiency thus having the potential to improve thermal efficiency. However, excessive levels of swirl can have the opposite effect due to increased convection loses, slowing combustion and increasing CO and THC emissions [9, 10, 68, 72].

Another method of improving thermal efficiency is by reducing the convective losses to the combustion chamber surfaces. Studies have shown that between 10 to 25% of the fuel energy released in-cylinder is transferred to the cylinder walls (depending on load conditions) – and then to the engine coolant and oil [56, 99]. Reducing this heat transfer thus has great potential for delivering significant improvements in thermal efficiency.

Ceramic-based coatings, usually of yttria-stabilized zirconia (YSZ), have been explored as a means of insulating the combustion chamber surfaces. Applied on a heavy duty diesel engine piston, these coatings have been demonstrated to reduce the instantaneous piston heat flux [77]. However, the expected benefits on thermal efficiency were not seen likely due to a penalty in volumetric efficiency resulting from the higher cylinder surface temperatures throughout the cycle [78, 79].

In order to overcome this disadvantage, researchers have recently developed new coating materials using silica reinforced porous anodised aluminium (SiRPA) that allow the combustion chamber surfaces to follow the transient gas temperature during the cycle [80-83]. The low thermal conductivity and heat capacity of these so-called “Temperature Swing Coatings” allows for fast surface cooling during the exhaust and intake strokes, thus maintaining volumetric efficiency, while also providing high surface temperatures in the late compression and early expansion strokes, thus leading to lower heat transfer losses from the hot gases to the walls. Application of SiRPA coating on the piston of a

diesel engine resulted in an improvement of 2% in fuel consumption and ~1.5% in indicated work along with a reduction in heat losses and an increase in exhaust enthalpy [83]. The effects of this new coating on indicated work, heat losses and exhaust enthalpy have been shown to be independent of EGR rate and injection timing [82].

An alternative approach to managing in-cylinder heat transfer, as opposed to the application of surface coatings, is to change the material of the piston itself. Alloy steel pistons have been widely used in heavy-duty applications since their first introduction in the early nineties [84], both as full steel or articulated steel-aluminium designs. Initially, the use of steel pistons in the heavy-duty sector was motivated by the need to provide high durability and strength in face of high peak cylinder pressures [85, 86]. The higher stiffness of the alloy steel also allowed for the reduction of piston wall thickness, consequently leading to a lower reciprocating mass and reduced engine stresses.

Recently, steel pistons have found their way into light-duty diesel applications, and apart from their structural benefits over the aluminium pistons, researchers have reported improvements in both brake and indicated fuel efficiency [87, 88].

The improvements in net indicated specific fuel consumption (nisfc) reported in these two studies were attributed to:

- Higher piston surface temperatures due to the lower thermal conductivity of steel compared to aluminium, and consequently reduced heat transfer to the oil and coolant
- Higher compression ratio due to smaller topland volume of the particular piston design that was considered

- The lower thermal expansion rate of steel, which then allowed for smaller clearances between the liner and piston thus reducing blow-by.

In terms of brake specific fuel consumption (bsfc), the additional benefits observed for the particular steel piston design tested in the literature [87, 88] were attributed to a reduction in frictional losses, due to:

- A shorter piston skirt
- A reduction of piston side forces due to increased conrod length

The above results thus highlight the potential benefits of alloy steel pistons.

Following the above discussion, enhancing the emission performance of the diesel engine without compromising its efficiency is desirable. Thus two thermal studies have been carried out, using the first law analysis (FLA) modelling tool introduced in Chapter 3, one looking into the effect of different HP EGR application techniques on emission performance and engine efficiency, and the second compared the performance of different piston materials on engine efficiency and the resulting energy flows. The results of these studies follow below.

4.2 Evaluation of EGR techniques

In this study, three different cooled HP EGR methods at two different operating conditions (1500 rpm/6.8 bar nIMEP and 1750 rpm/13.5 bar nIMEP) were tested. The three EGR methods examined were; a baseline HP EGR case, HP EGR with increased swirl, and HP EGR under constant λ conditions. Note that while FLAs on internal combustion engines are not new, with many examples available in the literature [26, 74, 92-97, 99, 100], the application of FLA to EGR application methods is novel and the results of this work are expected to guide the development of future EGR strategies.

4.2.1 Experimental methodology

In total three EGR strategies have been tested, each comprised of a three-point EGR sweep, and repeated for two load conditions. The EGR rates tested were; 0%, 17%, and 22% or 35%, depending on load condition where the maximum EGR rate for each load point was limited by a smoke value of $FSN = 3$.

The first strategy involved the application of high-pressure EGR, under higher in-cylinder swirl levels which was achieved by fully closing the swirl flap (SF closed). The second strategy was based on the "additional" EGR concept, introduced in Chapter 1, which essentially involved the application of EGR under constant λ conditions (Constant λ). Since the engine used is not equipped with an intake throttle, as in gasoline engines, constant λ conditions were achieved by the simultaneous increase in boost and exhaust back pressures with increasing rates of EGR. This ensured that the amount of oxygen present in the cylinder stayed constant. It should be noted that "internal" EGR (i.e. the exhaust gases not leaving the cylinder at the end of the cycle) was not calculated for these tests.

Control of the air flow rate into the engine was achieved by fixing the inlet and exhaust pressures, with the EGR rate being controlled independently using an EGR valve. For the constant λ EGR points, it was necessary to increase the inlet and exhaust pressures above the baseline conditions so as to maintain the target λ value at a given EGR rate. Finally, the intake temperature was held constant at 40 °C for all test points, in order to remove any thermal throttling effects (i.e. the reduction of volumetric efficiency due to lower charge density) typically associated with the use of EGR.

The operating conditions tested were 1500rpm/6.8bar nIMEP and 1750rpm/13.5bar nIMEP; points that are part of the standard testing sequence followed by the industrial

partner. The start of injection timings was held constant (only a pilot and a main injection were used) across all test points in order separate the effects of the different EGR strategies and injection timing on combustion progression. For the Baseline and SF closed cases, main injection fuelling was adjusted to maintain a constant nIMEP at each load condition. However, for the constant λ cases, the fuelling was kept constant at the baseline level (0% EGR) as EGR rate was increased. This inadvertently, resulted in a reduction in nIMEP at the higher EGR rates, with the maximum deviation being in the order of ~4%.

Table 4.1 shows the operating conditions for each EGR strategy along with the load/speed condition. The combustion related metrics for temperature, heat release and mass fraction burned (MFB) presented were calculated from in-cylinder pressure data using the combustion analysis package, AVL Concerto, as presented in Chapter 2. It is should be noted that the values of MFB are presented with respect to the start of pilot injection.

Table 4.1: Operating conditions for the two load cases.

Test point	1500 rpm/6.8 bar			1750 rpm/13.5 bar		
Engine speed (rpm)	1500			1750		
Fuel rail pressure (MPa)	55			90		
Inlet air temperature (°C)	40			40		
Coolant temperature (°C)	90			90		
EGR strategy – Baseline/Swirl flap closed						
Intake pressure (barG)	0.25			1.0		
Exhaust pressure (barG)	0.45			1.4		
nIMEP (bar)	6.8			13.5		
Intake $\boldsymbol{Y_{O_2}}$ (EGR %v/v)	0.23 (0%)	0.21 (17%)	0.18 (35%)	0.23 (0%)	0.20 (17%)	0.19 (22%)
EGR strategy – Constant λ						
Intake pressure (barG)	0.25	0.40	0.70	1.0	1.4	1.5
Exhaust pressure (barG)	0.45	0.70	1.2	1.4	1.8	2.1
nIMEP (bar)	6.8	6.7	6.5	13.5	13.5	13.4
Intake $\boldsymbol{Y_{O_2}}$ (EGR %v/v)	0.23 (0%)	0.22 (17%)	0.19 (35%)	0.23 (0%)	0.21 (17%)	0.20 (22%)

In order to compare between the different EGR strategies, energy flows are presented graphically against the intake charge composition expressed in terms of intake oxygen mass fraction (Equation (4.1)).

$$Y_{O_2[intake]} = \frac{m_{O_2[fc]} + m_{O_2[EGR]}}{m_{fc} + m_{EGR}} \quad (4.1)$$

where $m_{O_2[fc]}$ is the oxygen mass of the fresh charge, $m_{O_2[\mathrm{EGR}]}$ is the oxygen mass in the EGR gases and m_{fc} and m_{EGR} is the mass of the fresh charge and the mass of EGR respectively. The relationship between EGR rate and Y_{O_2} for the conditions tested is shown in

Table 4.1.

4.2.2 Thermal stability

For each engine test point the engine was run at the target speed and load until thermal equilibrium was established. Once this was achieved, low-speed (1 Hz) data were logged for a period of three minutes – all the channels used as inputs into the energy balance model were logged at 1 Hz. High-speed (0.1 CAD) combustion data were logged for 300 consecutive cycles. A minimum of three independent experiments was performed at each test point and a mean data set was generated for each condition.

Thus all figures presented here show the mean logged values over three runs. In all cases error bars show the 95% confidence limits of the mean data. Where error bars are not visible, the 95% confidence limit is sufficiently small as to be hidden by the data marker. Finally, all emission results are presented as normalised values unless otherwise stated.

4.2.3 Energy balance results

Figure 4.1 and Figure 4.2 present sample energy balance results for both load/speed conditions at their respective highest EGR rates (i.e. 35% and 22%, as shown in Table 4.1). Similar trends were observed between the different EGR strategies for all EGR rates and load conditions and are thus not presented for clarity. The results indicate that the two major energy transfers terms, independent of EGR strategy, are brake work and exhaust thermal energy, with the third biggest energy transfer term being the energy transfer to the coolant – the HP fuel pump work is not representative of this engine as the pump is sized for a four-cylinder engine and the pump's metering control unit was disabled during these tests.

Note that the pumping work (quantified for each test point in Figure 4.3) is included in the brake work term as the output from the dynamometer load cell represents the net effect of the useful work during the power stroke and the work consumed during the gas exchange process. Thus, these results highlight the need for the accurate determination of energy transfer to the cooling medium and the exhaust; which a significant part of this work is dealing with.

A comparison between the two load cases indicates that the extraneous losses are reduced at higher load conditions independent of EGR strategy. This is due to the larger injected fuel mass at higher load, which reduces the relative proportion of extraneous losses with respect to the total energy input despite an increase in engine surface temperature.

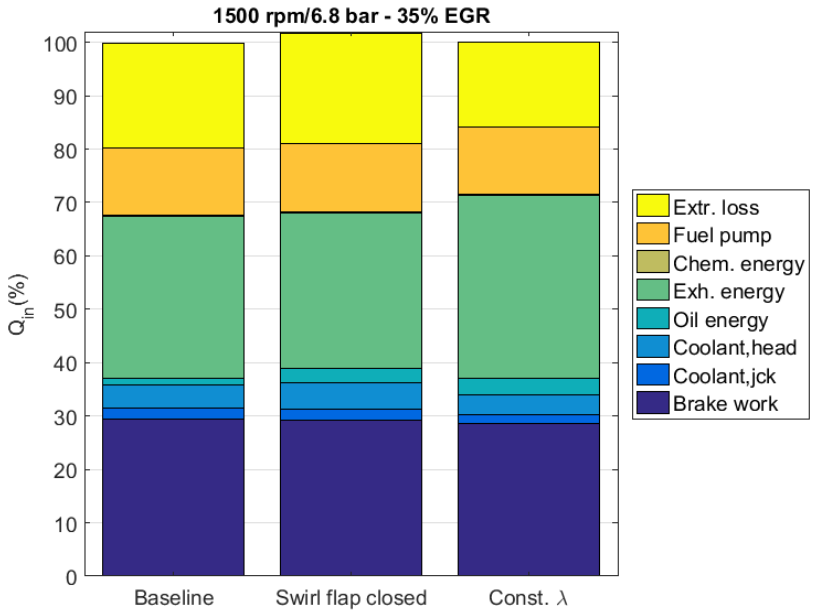

Figure 4.1: Energy balance results (normalised with respect to the total energy input to Baseline) for the different EGR strategies under 1500 rpm/6.8 bar nIMEP, 35% EGR rate conditions.

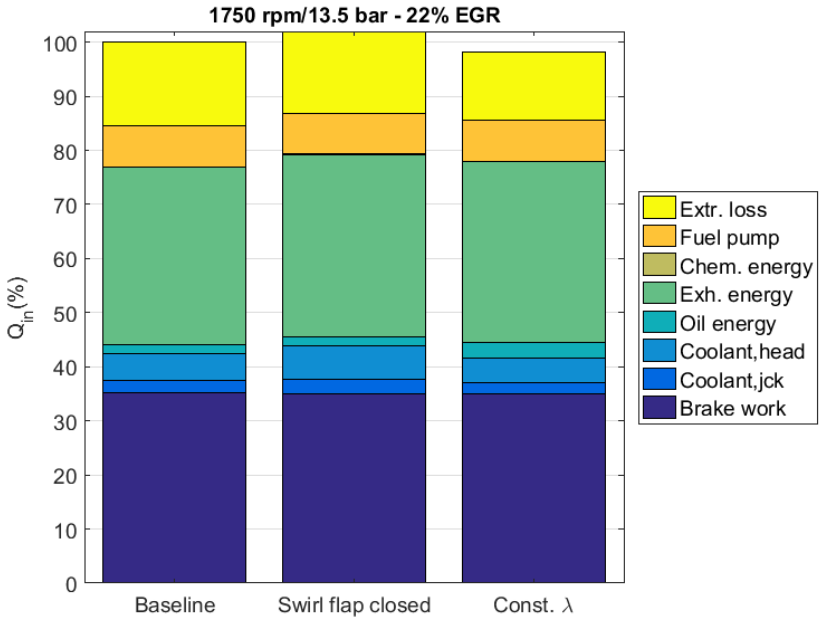

Figure 4.2: Energy balance results (normalised with respect to the total energy input to Baseline) for the different EGR strategies under 1750 rpm/13.5 bar nIMEP, 22% EGR rate conditions.

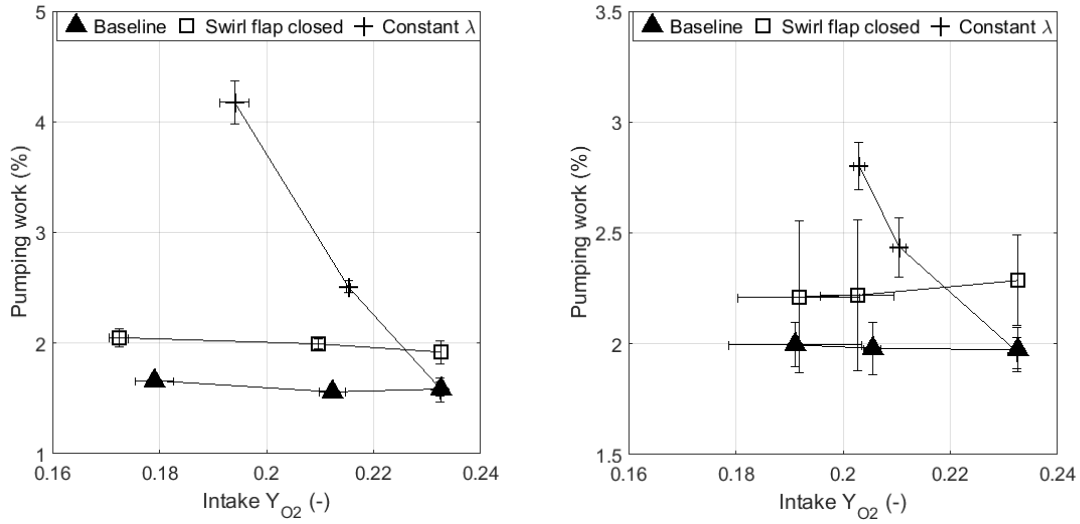

Figure 4.3: Pumping work as a percentage of input energy vs. intake oxygen mass fraction for the different EGR strategies at (a) 1500 rpm/6.8 bar nIMEP and (b) 1750 rpm/13.5 bar nIMEP load conditions.

Figure 4.4 presents the variation of brake work output with intake oxygen mass fraction under the different operating conditions. It is clear that under 1500 rpm/6.8 bar nIMEP conditions, the brake work is decreased significantly (~4-7%) compared to the 1750 rpm/13.5 bar nIMEP case with this decrease being attributed to the relatively increased fuel pump work (the sole ancillary loss on this engine), shown in Figure 4.5.

Figure 4.6 presents the cumulative energy transfer to the coolant lines for all three EGR strategies. Increasing the EGR rate (reducing intake oxygen mass fraction) reduces the heat transferred to the cooling system at both speed/load conditions regardless of EGR strategy. However, this reduction is small and not statistically significant at the 95% confidence interval. Nonetheless the trends are consistent and are attributed by the author to the reduction of bulk gas temperature at higher EGR conditions (as shown in Figure 4.13).

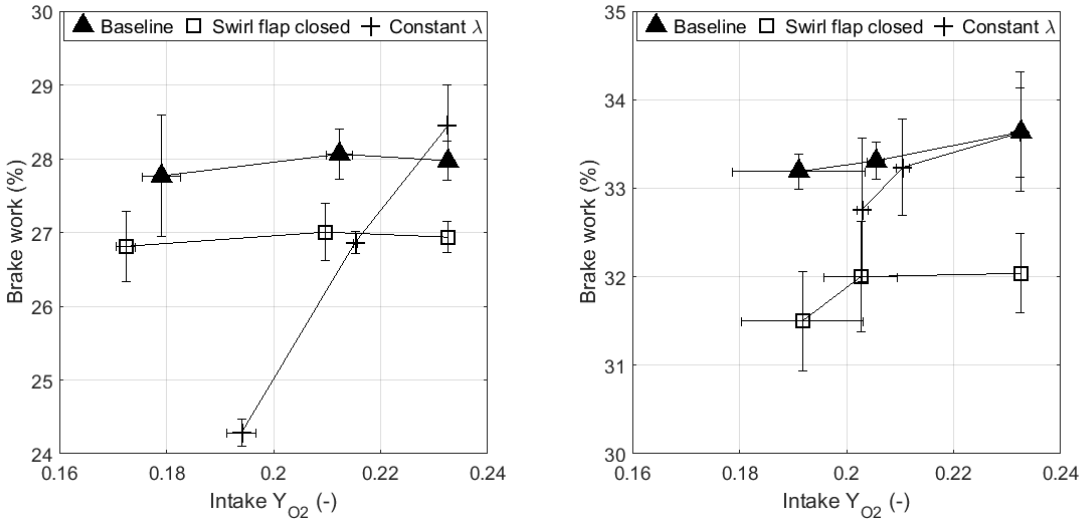

Figure 4.4: Brake work out vs. intake oxygen mass fraction for the different EGR strategies at (a) 1500 rpm/6.8 bar nIMEP and (b) 1750 rpm/13.5 bar nIMEP load conditions.

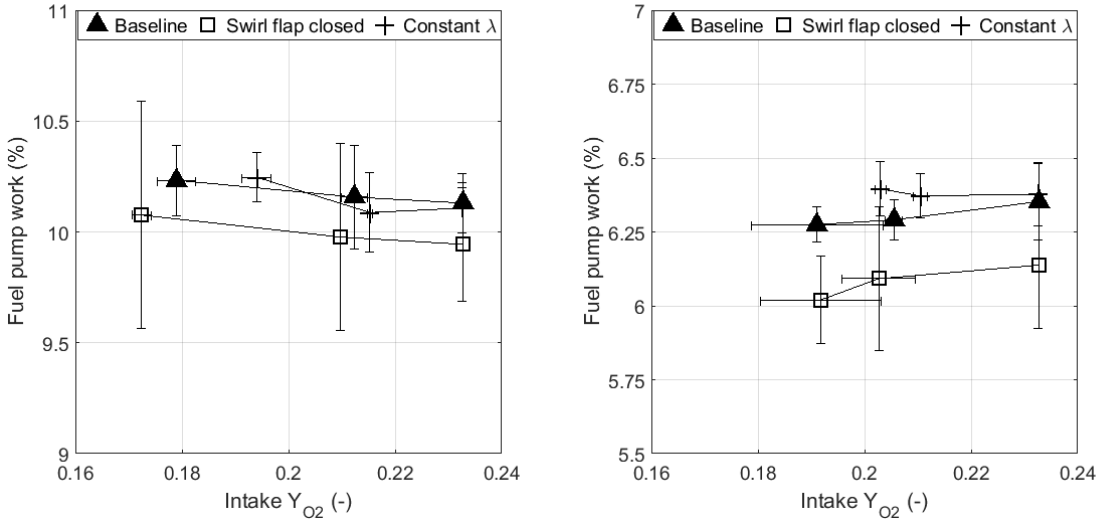

Figure 4.5: Fuel pump work as a percentage of input energy vs. intake oxygen mass fraction for the different EGR strategies at (a) 1500 rpm/6.8 bar nIMEP and (b) 1750 rpm/13.5 bar nIMEP load conditions.

The difficulty in accurately measuring the coolant energy transfer in a single cylinder engine is clearly highlighted by the magnitude of the error bars shown in Figure 4.6. Under low load conditions, the typical rise in coolant temperature across the engine is approximately 0.8 K. Thus, even with the use of purpose built differential thermocouple, presented in Chapter 2, calibrated to a high level of accuracy – the associated measurement uncertainty is as low as ± 0.07 K – the percentage error in the temperature measurements is approximately 9%. Comparatively, if standard sheathed K-type thermocouples, calibrated to an accuracy of ± 0.25 K, were to be used for these measurements then the resulting uncertainty in the measured temperature differential across the engine would approach 45%. Recalling the equation for standard error (Equation (2.7)) and by assuming that the standard deviation of the current work is representative of a larger sample, then a further 23 tests using the high-accuracy differential thermocouple system would be required to provide statistical certainty to the low-load measurements at the 95% confidence level. Equally, assuming a standard deviation of 0.6 K for a standard sheathed K-type thermocouple, Equation (2.7) shows that to achieve statistically meaningful results at the 95% confidence interval, hundreds of individual tests are required.

4.2.4 Swirl flap effects

It is well understood from the literature, e.g. [67, 72], that the throttling effect of closing a swirl flap will increase pumping work, as seen in Figure 4.3, and reduce brake efficiency (Figure 4.4). It is also expected that efficiency will be affected by swirl flap induced changes to the mixing, combustion and heat transfer characteristics of the engine.

Figure 4.6 shows that closing the swirl flap increases the total heat flow to the coolant independent of load. This result is consistent with current understanding of swirl flap

effects; closing a swirl flap increases in-cylinder swirl mixing, leading to faster burning and higher in-cylinder temperatures [55, 68]. In addition, the increased mean flow velocity and turbulent intensity associated with swirl flap use increases convective heat transfer [9, 10, 55]. Both of these effects are expected to increase the heat flux to the cylinder wall and thus the heat transferred to the coolant. Detailed examination of emissions and heat release results provides further insight into the causes of the increased heat transfer to the coolant when the swirl flap is closed. Figure 4.7 shows the NOx-smoke results for the different operating conditions.

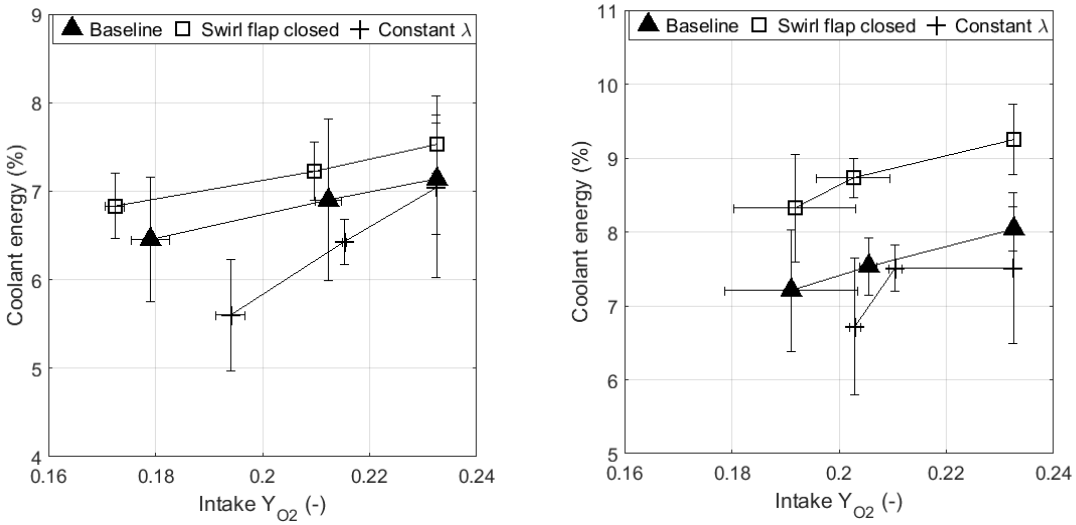

Figure 4.6: Total heat transferred to the coolant as a percentage of input energy vs. intake oxygen mass fraction for the different EGR strategies at (a) 1500 rpm/6.8 bar nIMEP and (b) 1750 rpm/13.5 bar nIMEP load conditions.

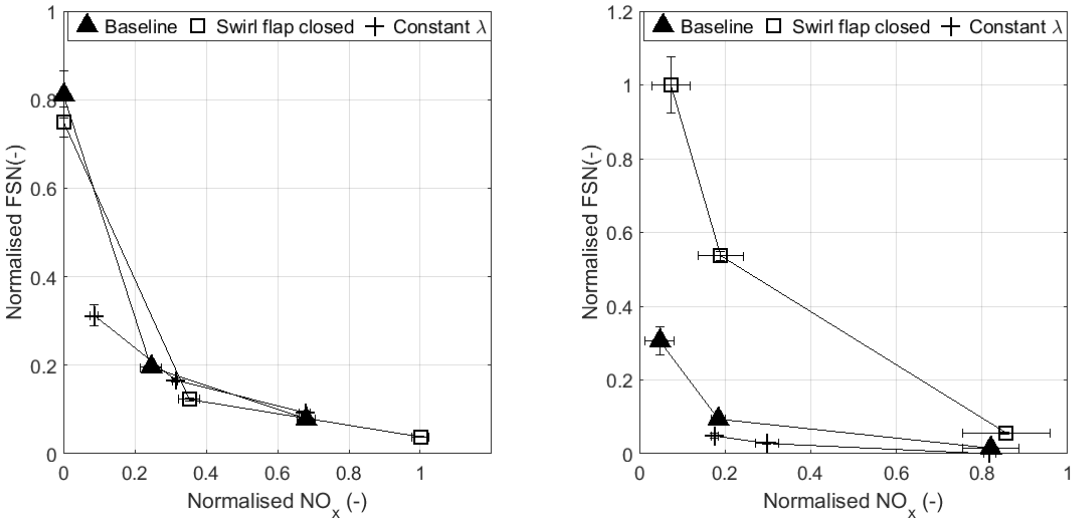

Figure 4.7: Normalised NO_x vs normalised filter smoke number (FSN) for the different EGR strategies at (a) 1500 rpm/6.8 bar nIMEP and (b) 1750 rpm/13.5 bar nIMEP load conditions.

At the low-load 1500 rpm/6.8 nIMEP condition, higher NO_x emissions with the closed swirl flap at 0% and 17% EGR suggest higher combustion temperatures relative to the baseline case, consistent with the literature [9, 10]. For the 35% EGR case, the NO_x results are essentially independent of swirl flap position – perhaps indicating that the in-cylinder temperature in both of these high EGR cases is sufficiently low as to inhibit any significant 'thermal' NO_x production. Closing the swirl flap is shown to increase ignition delay, approximated throughout this work by the crank angle duration between start of pilot injection (SOI.P) and the angle of 5% mass fraction burned (CA5), for all EGR rates as seen in Figure 4.8(a). The corresponding data for combustion phasing and duration, presented in Figure 4.9(a) and Figure 4.10(a) respectively, show that the combustion event is advanced and overall combustion duration is decreased compared to the baseline case—indicating a beneficial increase in post-ignition fuel-air mixing resulting in reduced smoke, CO, and THC emissions as shown in Figure 4.7(a), Figure 4.11(a), and Figure 4.12(a) respectively.

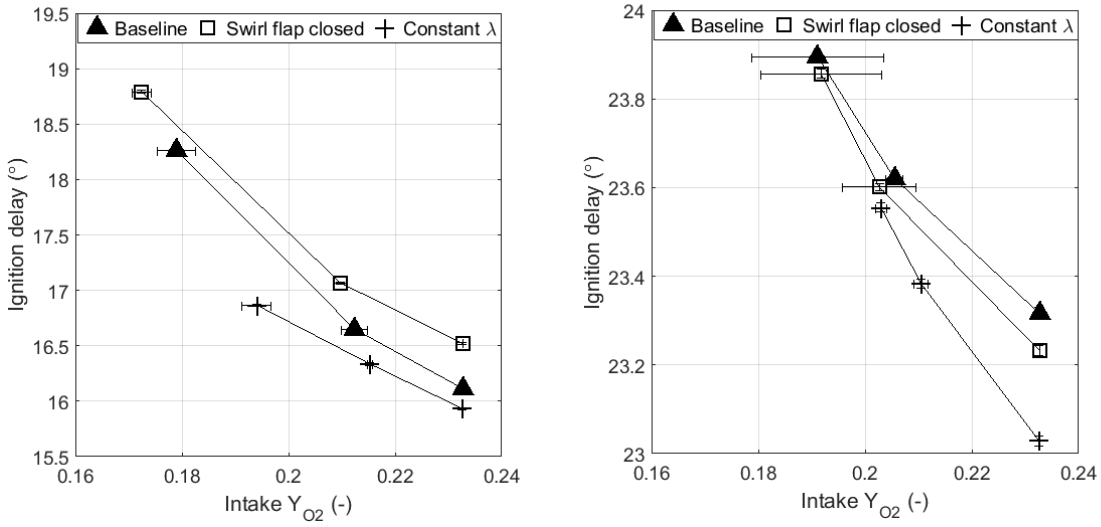

(a) (b)

Figure 4.8: Ignition delay (CA5 – SOI.P) vs. intake oxygen mass fraction for the different EGR strategies at (a) 1500 rpm/6.8 bar nIMEP and (b) 1750 rpm/13.5 bar nIMEP load conditions.

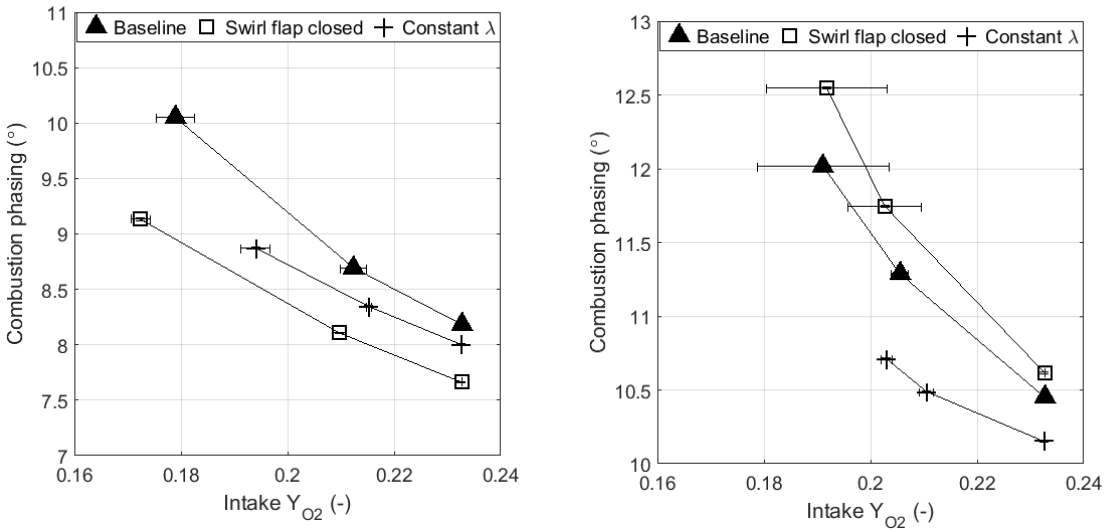

(a) (b)

Figure 4.9: Combustion phasing (CA50 – TDC) vs. intake oxygen mass fraction for the different EGR strategies at (a) 1500 rpm/6.8 bar nIMEP and (b) 1750 rpm/13.5 bar nIMEP load conditions.

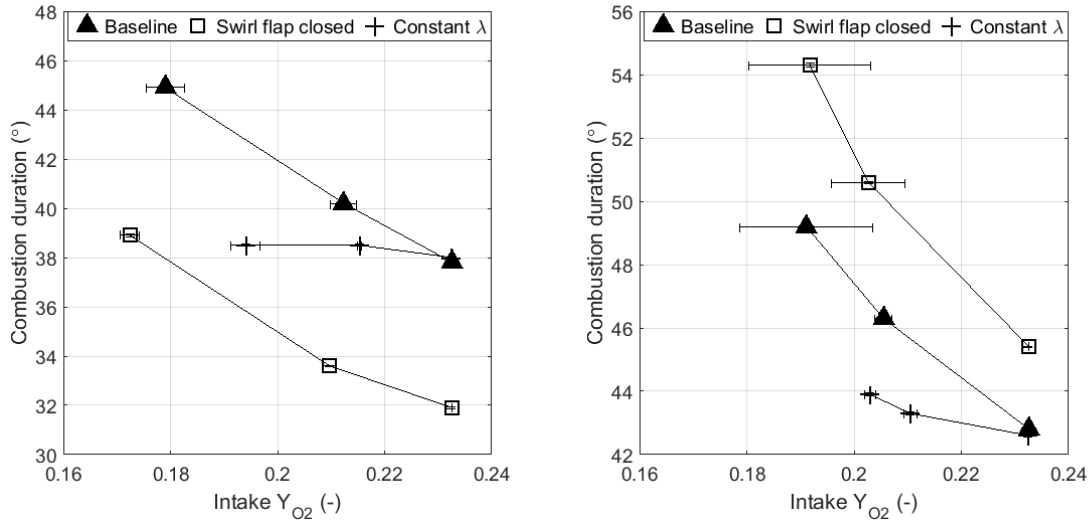

Figure 4.10: Combustion duration (CA90 - SOI.P) vs. intake oxygen mass fraction for the different EGR strategies at (a) 1500 rpm/6.8 bar nIMEP and (b) 1750 rpm/13.5 bar nIMEP load conditions.

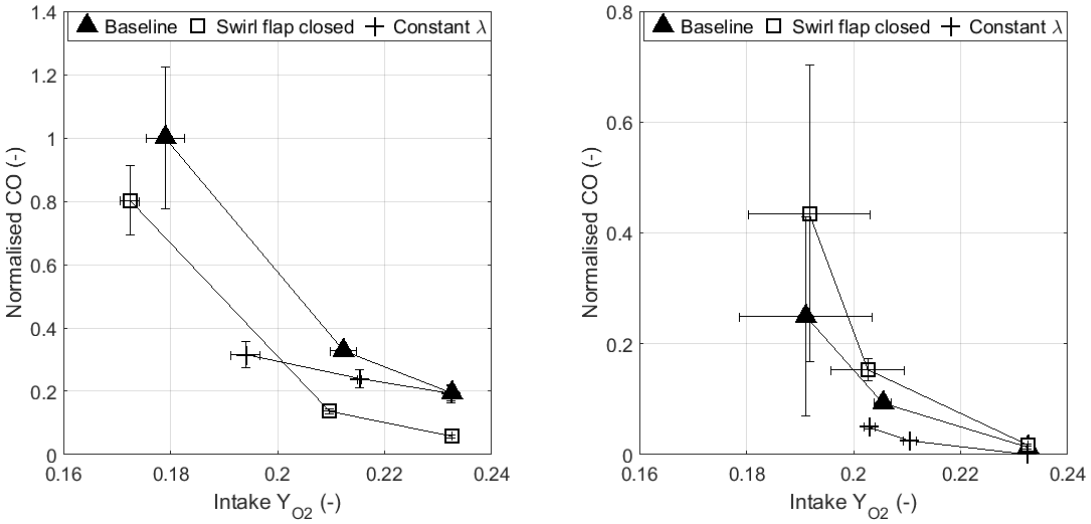

Figure 4.11: Normalised CO emissions vs. intake oxygen mass fraction for the different EGR strategies at (a) 1500 rpm/6.8 bar nIMEP and (b) 1750 rpm/13.5 bar nIMEP load conditions.

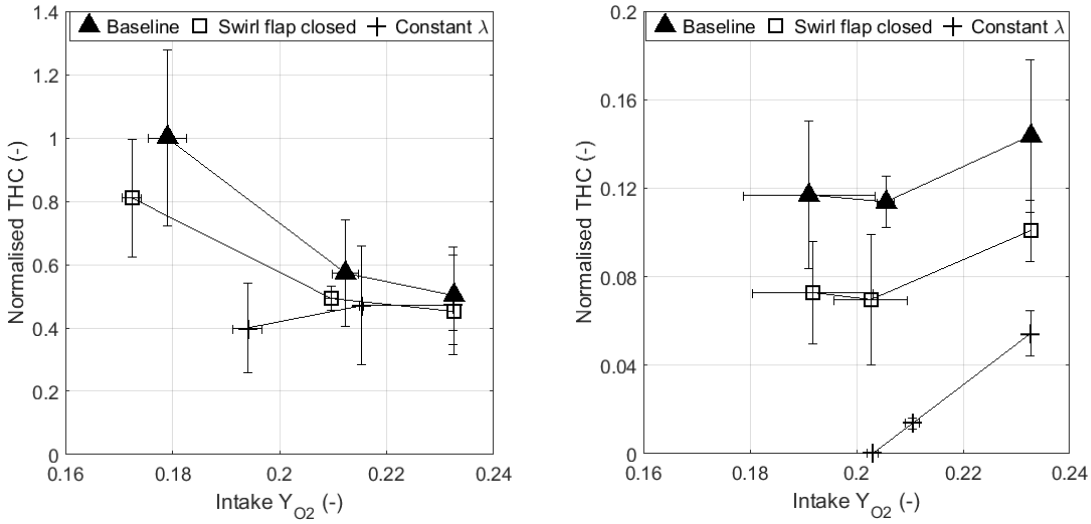

Figure 4.12: Normalised THC emissions vs. intake oxygen mass fraction for the different EGR strategies at (a) 1500 rpm/6.8 bar nIMEP and (b) 1750 rpm/13.5 bar nIMEP load conditions.

At the higher speed/load condition however, we see a different situation. In-cylinder swirl is known to scale with engine speed [29]. Therefore, the baseline swirl level is expected to be higher at the 1750 rpm/13.5 bar nIMEP condition than at 1500 rpm/6.8 bar nIMEP operating point. Closing the swirl flap will increase this swirl level still further. Excessive levels of swirl have been reported to increase heat convection, which can lead to lower cylinder temperatures and longer combustion durations [29, 66, 69]. This extended combustion duration can lead to incomplete combustion due to flame quenching – increasing soot, CO and THC emissions [55, 69, 145]. High levels of cylinder swirl can also lead to fuel jet-jet interactions increasing local equivalence ratio and consequently CO and THC emissions [9, 145]. Finally, excessive swirl levels have been shown to result in over-leaning of the fuel/air mixture (i.e. pockets of fuel that escape combustion) thus increasing CO and THC emissions [59].

The results presented in Figure 4.9(b) and Figure 4.10(b) do show an increase in combustion duration when the swirl flap is closed at the higher load condition. Soot and

CO emissions also increase (Figure 4.7(b) and Figure 4.11(b)) consistent with a reduction in soot oxidation and incomplete oxidation of fuel due to flame quenching. However, THC emissions at this load point are relatively insensitive to both swirl flap position and EGR rate (Figure 4.12(b)). One possible explanation for these seemingly contradictory results could be that the CO emissions at this load point are dominated by the late cycle bulk quenching effects, associated with the longer combustion duration, which result in reduced CO oxidation rates. On the other hand THC emissions are, to a significant degree, due to the improved mixing at these higher speed conditions, a mixing which is further enhanced by the increased combustion duration when the swirl flap is closed.

Considering the ignition delay, Figure 4.8(b) indicates a reduced sensitivity to EGR compared to the lower speed/load condition. This is consistent with the increased swirl motion associated with higher engine speed improving fuel-air mixing and hence offsetting the oxygen displacement effect of increasing EGR. A notable feature of the ignition delay data at the 1750 rpm/13.5 bar nIMEP condition (Figure 4.8(b)) is its relative insensitivity to the swirl flap position, which is reflected in the THC results.

Taken as a whole, the emissions trends presented in Figure 4.7, Figure 4.11 and Figure 4.12 indicate that the increases in coolant heat flow relative to the baseline condition shown in Figure 4.6 when the swirl flap closed are the result of significantly different physical phenomena for the two speed/load conditions. For the lower speed/load case, the emissions results suggest that the increased heat flow to the coolant is predominantly due to higher in-cylinder temperatures. For the higher speed/load case, the emissions results suggest that the cause is likely an increase in the convective heat transfer coefficient compensating for a reduction in the in-cylinder gas temperature. Note that the calculated peak bulk gas temperatures presented in Figure 4.13 do show an increase from the

baseline value with swirl flap operation for the 1500 rpm/6.8 bar nIMEP low load case and a decrease for the higher speed/load (1750 rpm/13.5 bar nIMEP) case. However, it should be noted also that the results presented in Figure 4.13 indicate the combined effects of varying charge properties and in-cylinder motion along with the effects of variable combustion phasing for the different EGR strategies and EGR rates.

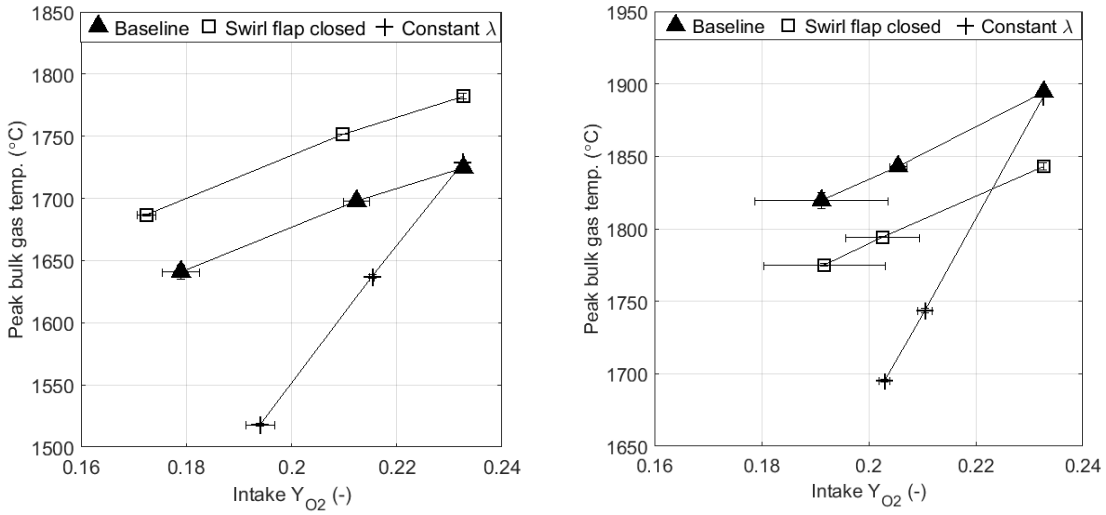

Figure 4.13: Peak gas bulk temperature (based on cylinder pressure signal assuming ideal gas behaviour) vs. intake oxygen mass fraction for the different EGR strategies at (a) 1500 rpm/6.8 bar nIMEP and (b) 1750 rpm/13.5 bar nIMEP load conditions.

4.2.5 Constant lambda EGR strategy

Maintaining a constant λ value as EGR is increased would indicate that a constant mass of oxygen is maintained in the cylinder relative to the fuelling regardless of EGR rate thus alleviating the negative effects of oxygen displacement during EGR application. Note that in a real (multi-cylinder) engine running with a fixed turbine geometry, the boost pressure would vary with EGR level so that for these engines 'real' EGR would be somewhere between the constant lambda and displacement EGR strategies examined in this work. However, where the engine uses a variable geometry turbine, as is the case in many

modern vehicles, the boost pressure can be held constant and the EGR rate adjusted with the EGR valve. The constant lambda scenario is representative of this strategy.

Clearly, for a given load and speed condition, the ‘additional’ EGR approach necessitates an increase in intake mass flow rate and hence a higher intake pressure. For EGR to be driven against this pressure, the exhaust backpressure must also increase. This can be seen in

Table 4.1, which describes the intake and exhaust backpressure conditions used to drive the EGR for the constant λ tests. The increase in pumping work associated with the ‘additional’ EGR strategy is in the range of 0.5% to 2.5% (Figure 4.3), contributing to the reduced brake efficiency shown in Figure 4.4. It is not certain however that these penalties in efficiency will be as profound for multi-cylinder engines where the intake and exhaust mass flow rates are proportionally increased.

The results presented in Figure 4.6, indicating the heat flow to the coolant, show increased sensitivity to EGR for the constant λ case compared with both the baseline and swirl flap cases, particularly at the lower speed/load condition (1500rpm/6.8bar nIMEP). It is thought that this increased sensitivity is caused by the increased charge density associated with the ‘additional’ EGR increasing the total heat capacity of the charge. Increasing the heat capacity will cause an additional reduction in the peak bulk gas temperature on top of that expected from EGR alone. This hypothesis is supported by the results presented in Figure 4.13. For all conditions, the calculated peak gas bulk temperature is seen to decrease with increasing EGR, as expected. However, the results for the constant λ case show a much more significant decrease in peak gas bulk temperature with EGR than either of the baseline and closed swirl flap cases.

The significant reduction in peak bulk gas temperature observed under constant λ operation as EGR levels are increased is interesting in light of the NO_x emissions results shown in Figure 4.14, which presents normalised brake specific NO_x emissions for the baseline and constant λ cases, plotted against the total intake oxygen mass and the peak bulk gas temperature. It is noted that NO_x emissions are given relative to the highest value measured across the full test matrix. Increasing EGR rates under constant λ operation leads to a comparative increase in NO_x emissions with respect to the baseline case that is attributed by the author to the greater oxygen content of the charge (it is assumed that despite the reduction of peak gas temperature shown in Figure 4.13, the local reaction zone temperatures remain sufficiently high as to generate thermal NO_x). Since no oxygen is displaced under constant λ operation, local oxygen availability is increased.

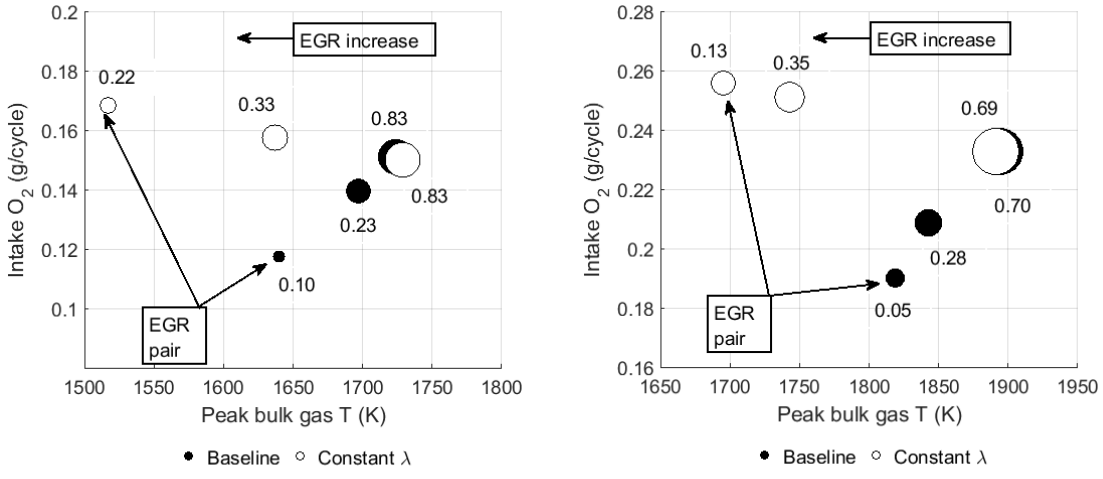

(a) (b)

Figure 4.14: Intake oxygen mass vs. peak bulk gas temperature for the baseline and constant λ cases at (a) 1500 rpm/6.8 bar nIMEP and (b) 1750 rpm/13.5 bar nIMEP load conditions. The circle size indicates relative NOx emissions and the arrows indicate constant EGR 'pairs'.

Operating at constant λ also increases charge density compared to the 'conventional' EGR approach (as shown in

Table 4.1 Table 4.1). Increasing charge density has been shown to improve fuel–air mixing and reduce ignition delay due to improved spray atomisation [64, 145]. This agrees well with the reduction in ignition delay that is seen for the constant λ strategy 1500 rpm/6.8 bar nIMEP case compared with the baseline case (Figure 4.8). Interestingly, the results presented in Figure 4.10 show that combustion duration for the constant λ EGR strategy is relatively insensitive to EGR rate. This contrasts sharply with the baseline and swirl flap strategy results where combustion duration was substantially increased by the addition of EGR, particularly at low load and speed. These results then suggest that the increased oxygen availability and charge density provided by the constant λ strategy is enabling a more sustained and complete combustion event for a given EGR rate. Note that reduced sensitivity of the CO and THC emissions to EGR for the constant λ case, presented in Figure 4.11 and Figure 4.12 respectively, and the significant reduction in soot emissions at high levels of EGR compared to the baseline and swirl flap cases (Figure 4.7) also support this interpretation of the results and are in good agreement with the earlier work of Ladommatos *et al.* [51].

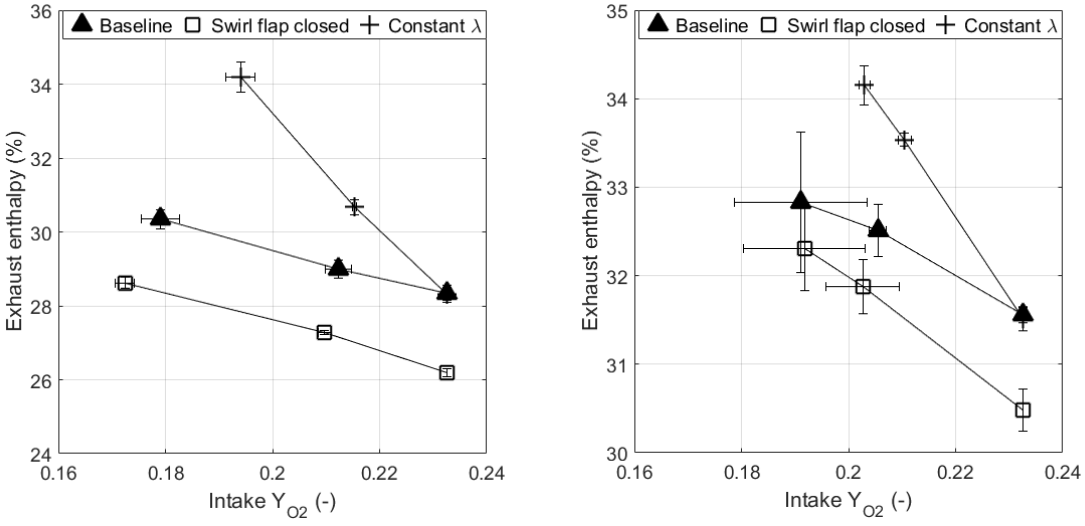

Figure 4.15: Exhaust enthalpy as a percentage of input energy vs. intake oxygen mass fraction for the different EGR strategies at (a) 1500 rpm/6.8 bar nIMEP and (b) 1750 rpm/13.5 bar nIMEP load conditions.

Figure 4.15 shows the exhaust enthalpy as a percentage of input energy against intake oxygen mass fraction for the different EGR strategies. Given approximately constant values of efficiency, pumping work, ancillary work and extraneous losses, the energy transferred to the exhaust will follow an opposite trend to the coolant heat transfer. Increasing levels of EGR are seen to increase the energy transferred to the exhaust. It is interesting to note that the exhaust enthalpy is increased under constant λ operation despite a substantial (~50 K) reduction in exhaust temperature. This is due to the fact that the total energy transferred to the exhaust is a function of both the specific enthalpy and the mass flow rate of the exhaust gases. The higher intake mass flow rate under constant λ operation, leads to an increase in the exhaust mass flow rate relative to the baseline case.

Finally, the author notes that the Ricardo Hydra engine used in this work is atypical in many respects, not least in that as an unbalanced engine it is attached to a very large seismic mass, which acts as a very effective heat sink. Accordingly, the overall magnitudes of the energy flows that are determined on this engine are not expected to be representative of a production multi-cylinder. In particular, heat losses to the coolant circuit are lower than would be expected of a multi-cylinder engine and extraneous losses are substantially increased. Nonetheless, the changes in energy flow induced by variations of EGR strategy, speed and load observed in this work are expected to be indicative of real engine behaviour.

4.2.6 Conclusions on EGR strategies study

The effects of three different cooled high-pressure EGR strategies (baseline, closed swirl flap, and constant λ) on engine efficiency and the resulting energy flows have been

studied at two speed/load conditions using a first law analysis approach on a single-cylinder high-speed Diesel engine.

The results for the baseline EGR strategy with constant boost pressure and reducing lambda with increasing EGR were found to be in good agreement with the literature such that increasing EGR rate was shown to increase ignition delay and combustion duration. Bulk gas temperature and NO_x emissions were reduced, as was heat transfer to the coolant. Exhaust thermal energy was increased, as were smoke and CO emissions.

Introducing EGR under higher swirl conditions induced by closing the swirl flap:

- Increased pumping work and reduced brake efficiency
- Increased heat flow to the coolant
- Reduced exhaust thermal energy

Some differences were noted between the two load conditions; for the low-load low-speed condition (1500 rpm/6.8 bar), the closed swirl flap results indicate an increase in post-ignition fuel-air mixing such that:

- Combustion duration, and smoke, CO, and THC emissions are reduced
- Peak bulk gas temperatures and NOx emissions are increased

For the mid-load, higher-speed (1750 rpm/13.5 bar) condition, the closed swirl flap results indicate an increase in combustion duration attributed to excessive swirl levels increasing heat convection from the reaction zone leading to:

- A reduction in peak bulk gas temperature and increased smoke and CO emissions
- Increased exhaust gas temperature

The addition of EGR under conditions of constant λ increases, for any given EGR rate, the intake mass flow rate and therefore charge density, the specific heat of the charge, and the oxygen content of the charge. These changes lead to the following changes with respect to the baseline EGR strategy:

- Pumping work and exhaust thermal energy being increased
- Peak bulk gas temperature, exhaust gas temperature, and heat transfer to the coolant being reduced
- Soot, CO, and THC emissions being decreased, as was combustion duration
- NO_x emissions are higher for the same EGR rate
- Brake efficiency was reduced at low load

4.3 Effect of piston material on energy flows

With the notable exception of the referenced works [87, 88], the effects of moving from conventional aluminium piston designs to similar alloy steel pistons in light-duty diesel engines are not widely reported within the open literature. This study seeks to expand on the knowledge by reporting observations from an experimental comparison between similar aluminium and steel pistons on a single cylinder high-speed direct injection diesel research engine at two speed/load conditions both with and without EGR.

4.3.1 Experimental methodology

Figure 4.16 shows the geometries of the two piston designs used. It can be seen that, although the alloy steel piston shares the same combustion bowl geometry (and compression ratio) as the baseline aluminium piston, there are notable differences between the designs that have been facilitated by the change to a stronger, more rigid material. The total length of the piston (Lp) has been reduced by ~23% and the top land (TL) by ~55%. Compression height is also reduced, necessitating an increase of

approximately 5% in conrod length for the steel piston. Wall thicknesses have been reduced leading to a ~50% increase in the cooling gallery volume. Note here that the ring pack design was the same for both pistons and that two piston cooling jets (PCJs) were used for the steel piston design as opposed to a single PCJ for the baseline aluminium piston. All other engine components remained constant across all tests.

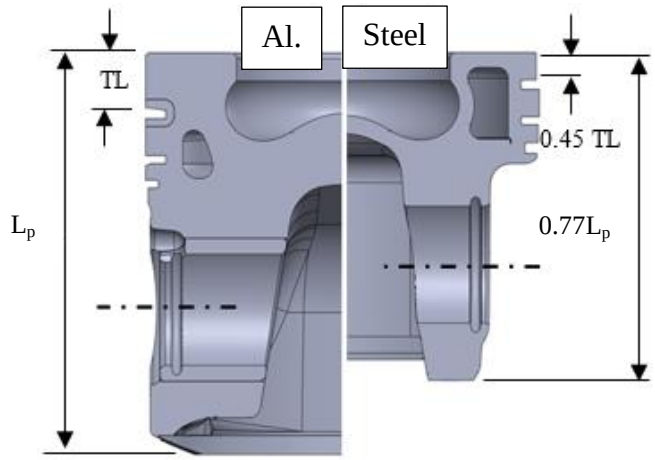

Figure 4.16: Comparison of aluminium (left) and alloy steel piston (right) designs (not to scale).

The engine was operated at two different speed and load conditions in order to assess the performance of the two piston designs. The intake temperature was held constant at 40 °C and the coolant and oil inlet temperatures were controlled to 90 °C. Two EGR set points were run at each engine speed, one at zero EGR and a second point with EGR (where the EGR rate varied according to the load condition). Table 4.2 presents the operating conditions for the two test cases. Combustion phasing was fixed by controlling the CA50 to a constant value via closed loop control on the ECU.

Thermal stability and data logging followed the same approach to the aforementioned energy balance study. Similarly, all values presented here are an average of three runs and the error bars indicate the 95% confidence interval.

Table 4.2: Engine operating conditions for the Al./Steel piston study

Test point	**1**	**2**
Engine speed (rpm)	2000	1500
nIMEP (bar)	25.7	6.92
CA50 (CAD bTDC)	13.3	7.2
T_{intake} (°C)	40	40
$T_{coolant}$ (°C)	90	90
T_{oil} (°C)	90	90
EGR (%) (0, max)	0, 8	0, 32

4.3.2 Results

In this section the experimental results comparing the performance of the steel and aluminum pistons are presented. The results of the first law model are presented first and then further supported by analysis of heat release data. The effect of trapped mass on engine performance is also discussed.

Figure 4.17 - Figure 4.20 show the results of the energy balance model for the conditions presented in Table 4.2. For each case, all values are presented as a percentage of the total energy input. The 95% confidence intervals are not included in the figures so as to aid clarity, however the statistical results for each case are included in the table following each graph. The total energy input in kW is also included to assist in the comparison between each test point.

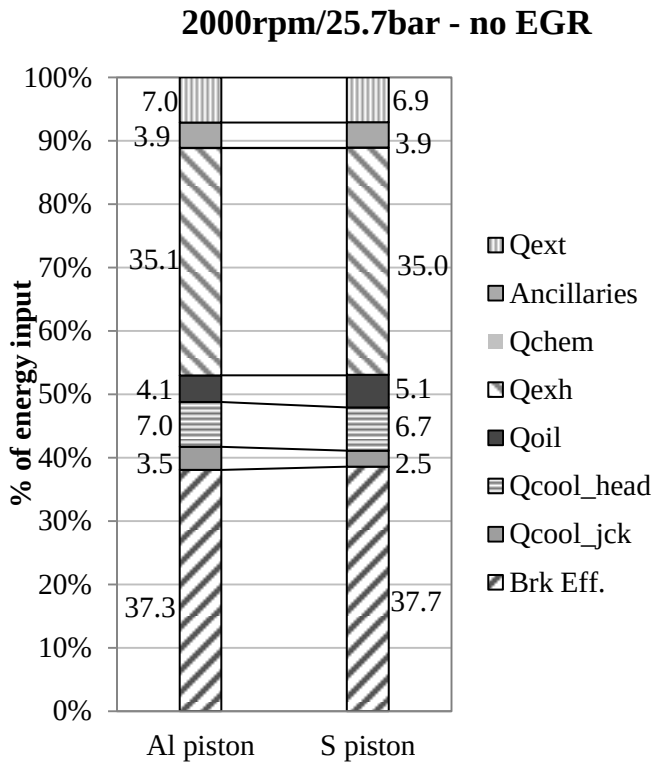

Figure 4.17: First law analysis results for aluminium and steel pistons for the 2000 rpm /25.7 bar nIMEP - no EGR case. Results presented as percentage of total energy input.

Table 4.3: Energy balance results for the 2000 rpm/ 25.7 bar nIMEP 0% EGR case (presented in Figure 4.17). The total energy input in kW is also included for each case. Results include the 95% confidence intervals.

2000 rpm /25.7 bar nIMEP 0% EGR		
	Al piston	**Steel piston**
Qin (kW)	**50.9±0.2**	**50.7±0.1**
Brk Eff.	37.3±0.2	37.7±0.2
Qcool_jck	3.5±0.1	2.5±0.1
Qcool_head	7.0±0.1	6.7±0.1
Qoil	4.1±0.2	5.1±0.2
Qexh	35.1±0.1	35.0±0.2
Qchem	0.0±0.0	0.0±0.0
Ancillaries	3.9±0.0	3.9±0.0
Qext	7.0±0.3	6.9±0.4

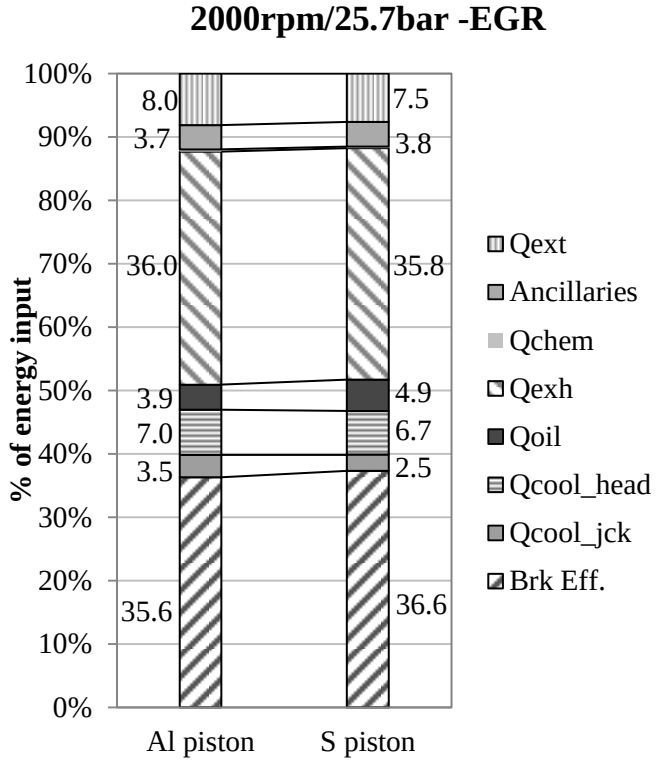

Figure 4.18: First law analysis results for aluminium and steel pistons for the 2000 rpm /25.7 bar nIMEP - EGR case. Results presented as percentage of total energy input.

Table 4.4: Energy balance results for the 2000 rpm / 25.7 bar nIMEP EGR case (presented in Figure 4.18). The total energy input in kW is also included for each case. Results include the 95% confidence intervals.

2000 rpm/ 25.7 bar nIMEP EGR		
	Al piston	**Steel piston**
Qin (kW)	**53.2±0.3**	**52.6±0.6**
Brk Eff.	35.6±0.3	36.6±0.4
Qcool_jck	3.5±0.0	2.5±0.0
Qcool_head	7.0±0.1	6.7±0.1
Qoil	3.9±0.1	4.9±0.2
Qexh	36.0±0.1	35.8±0.3
Qchem	0.4±0.0	0.3±0.1
Ancillaries	3.7±0.0	3.8±0.0
Qext	8.0±0.3	7.5±0.4

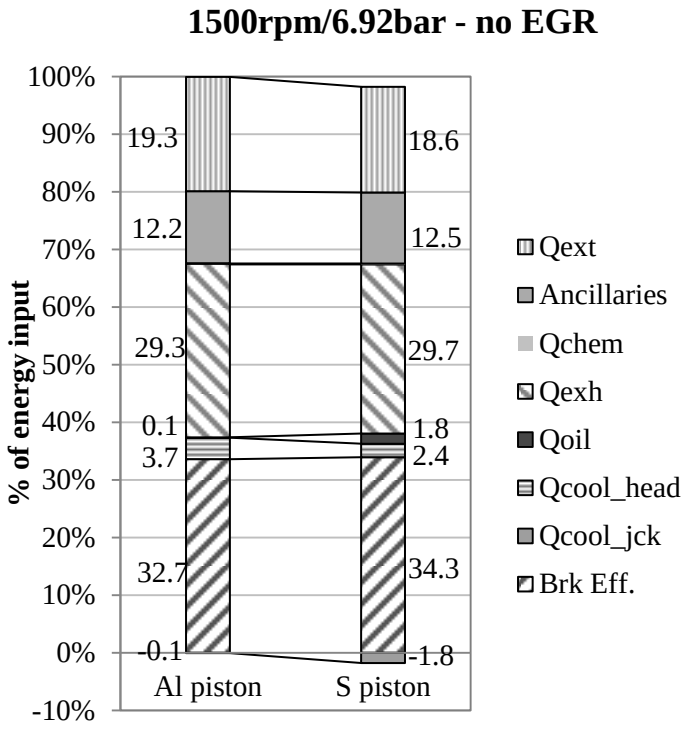

Figure 4.19: First law analysis results for aluminium and steel pistons for the 1500 rpm/ 6.92bar nIMEP - no EGR case. Results presented as percentage of total energy input.

Table 6: Energy balance results for the 1500 rpm / 6.92 bar nIMEP 0% EGR case (presented in Figure 4.19). The total energy input in kW is also included for each case. Results include the 95% confidence intervals.

1500 rpm / 6.92 bar nIMEP 0% EGR		
	Al piston	**Steel piston**
Qin (kW)	**10.7±0.2**	**10.4±**
Brk Eff.	32.7±0.4	34.3±0.4
Qcool_jck	-0.1±0.3	-1.8±0.1
Qcool_head	3.7±0.2	2.4±0.2
Qoil	0.1±0.4	1.8±0.1
Qexh	29.3±0.5	29.7±0.3
Qchem	0.1±0.0	0.2±0.0
Ancillaries	12.2±0.2	12.5±0.1
Qext	19.3±1.2	18.6±1.0

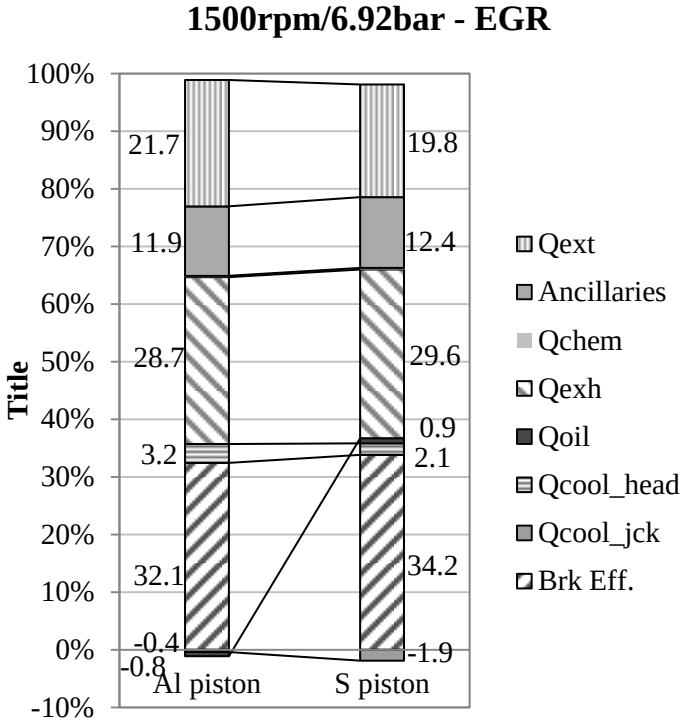

Figure 4.20: First law analysis results for aluminium and steel pistons for the 1500 rpm /6.92 bar nIMEP - EGR case. Results presented as percentage of total energy input.

Table 7: Energy balance results for the 1500 rpm / 6.92 bar nIMEP EGR case (presented in Figure 4.20). The total energy input in kW is also included for each case. Results include the 95% confidence intervals.

1500 rpm / 6.92 bar nIMEP EGR		
	Al piston	**Steel piston**
Qin (kW)	**10.9±0.1**	**10.5±0.2**
Brk Eff.	32.1±0.4	34.2±0.5
Qcool_jck	-0.4±0.3	-1.9±0.1
Qcool_head	3.2±0.2	2.1±0.2
Qoil	-0.8±0.3	0.9±0.2
Qexh	28.7±0.3	29.6±0.4
Qchem	0.2±0.0	0.3±0.0
Ancillaries	11.9±0.2	12.4±0.2
Qext	21.7±0.7	19.8±1.2

The results show statistically significant increases in brake efficiency for all four test points when switching from the baseline aluminium piston to the steel piston design. The observed benefits are relatively small at high load (2000 rpm/25.7 bar nIMEP, Figure 4.17 and Figure 4.18). A benefit of ~0.6% is observed for the 0% EGR condition and ~1% with 8% EGR. The benefits are more pronounced for the low speed/load case (1500 rpm /6.92 bar nIMEP, Figure 4.19 and Figure 4.20) where improvements of ~2.2 and ~1.6% are seen for the 0% and 32% EGR conditions respectively.

The results also show a consistent reduction in energy transfer to the coolant both in the jacket and the head with the steel piston. More specifically, the energy to the coolant in the jacket is reduced by 1 percentage point (which corresponds to an equivalent temperature drop across the engine of 0.8 K) for the 2000rpm /25.7bar nIMEP 0% EGR case. Similar magnitude reductions were noted with EGR. As the speed and load are reduced, the energy transfer to the cooling jacket is negative, indicating that the coolant is transferring energy to the cylinder walls (the inlet coolant temperature was controlled to the same set point). A higher negative value is seen for the steel piston design indicating a reduction in the energy transferred from the cylinder to the jacket coolant circuit compared with the aluminium piston.

The energy transferred to the coolant in the head is comparatively higher than the transfer to the jacket (by as much as ~4 percentage points) irrespective of piston design and operating condition. Here, steel piston operation resulted in a reduction of ~0.3 percentage points independent of EGR for the 2000 rpm/25.7bar nIMEP case, and a reduction of ~1.2 percentage points under the 1500 rpm/6.92bar nIMEP condition, to the energy transferred to the jacket coolant circuit.

The proportion of the input energy transferred to the oil circuit was increased by approximately 1 percentage point, across all test conditions, for the steel piston design.

With regards to the exhaust gas enthalpy, the observed changes between the aluminium and steel piston designs were within the 95% confidence limits and therefore not statistically significant. Similarly, no appreciable differences in ancillary or extraneous losses were observed between the aluminium and steel pistons designs under the same speed/load conditions with the exception of the 1500 rpm/6.92bar EGR condition where a small increase in ancillary losses is seen with the steel piston.

Figure 4.21 shows the experimental data for Friction Mean Effective Pressure (FMEP), where FMEP = IMEP – BMEP. It is shown that moving from the aluminium to the steel piston design resulted in a reduction in FMEP of the order of 6-10% for all test conditions. It is also seen (as might be expected) that FMEP is independent of EGR rate.

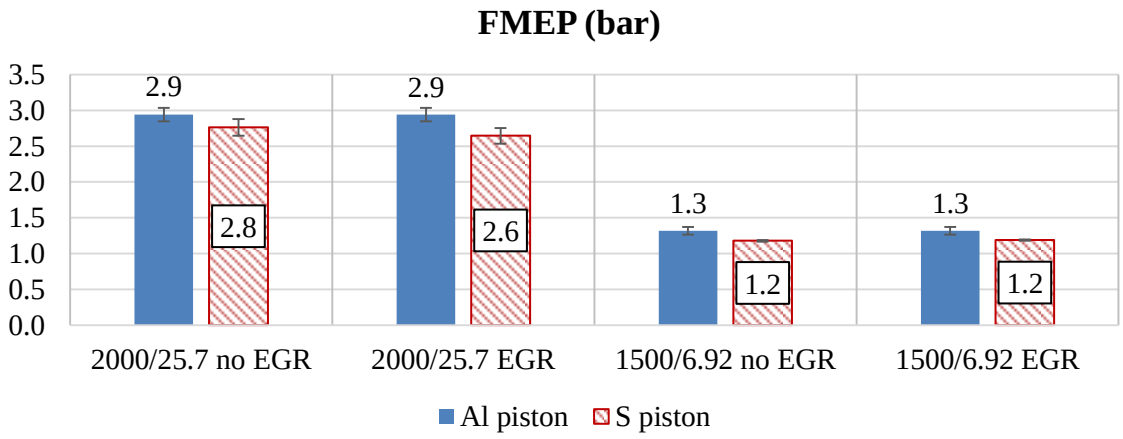

Figure 4.21: FMEP comparison for the conditions tested. The error bars indicate the 95% confidence limits.

Figure 4.22 and Figure 4.23 show, respectively, the normalised net indicated specific and the brake specific fuel consumption. In all cases, the fuel consumption was reduced for

the steel piston design. The differences are uniformly statistically significant for BSFC, but are less clear-cut for nISFC where they are noted to be statistically insignificant for the higher speed/load case. BSFC was reduced by ~1.2 to 2.5% for the higher speed/load condition, and ~3.5% for the lower speed/load case. The reductions in nISFC were of the order 0.5% for the 2000 rpm/ 27.5 bar nIMEP conditions and between 0.9 and 1.3% at the 1500 rpm/6.9 bar nIMEP condition depending on EGR rate.

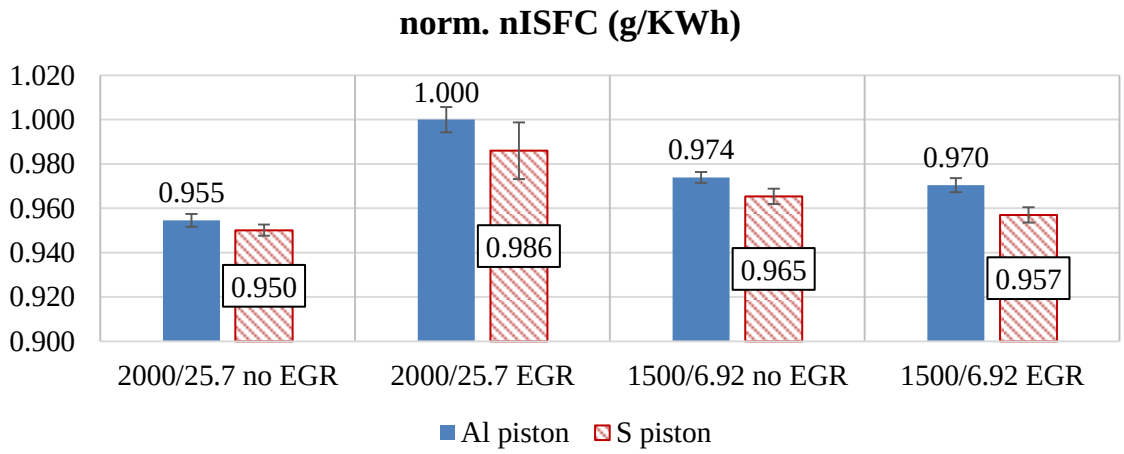

Figure 4.22: Normalised NISFC comparison for the conditions tested. The error bars indicate the 95% confidence limits.

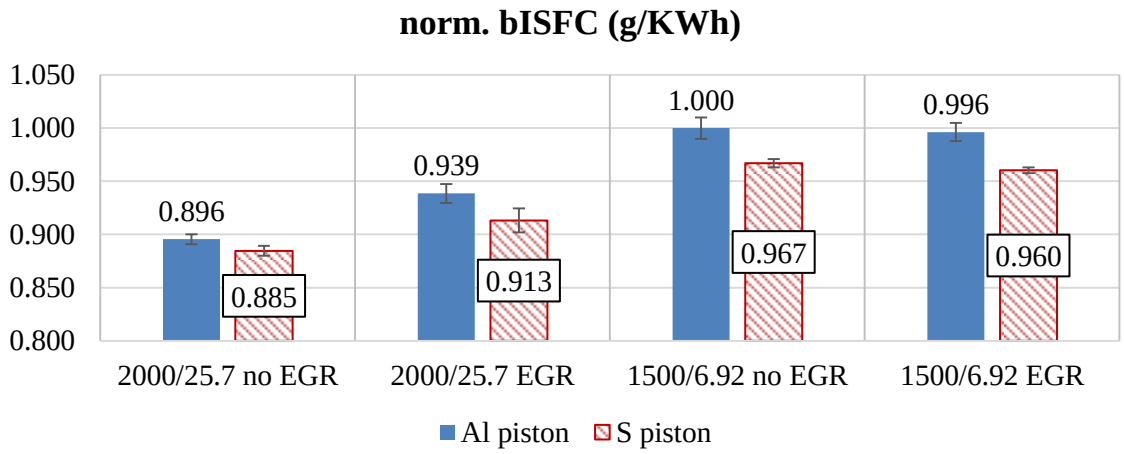

Figure 4.23: Normalised BSFC comparison for the conditions tested. The error bars indicate the 95% confidence limits.

Figure 4.24 shows the measured time-average mean exhaust temperatures for all conditions and pistons examined. It is seen that the use of the steel piston design results in consistent, small (~1.3 to 2.5%), but statistically significant decreases in mean exhaust gas temperature. A note on the detail of these exhaust temperature measurements is included in [105].

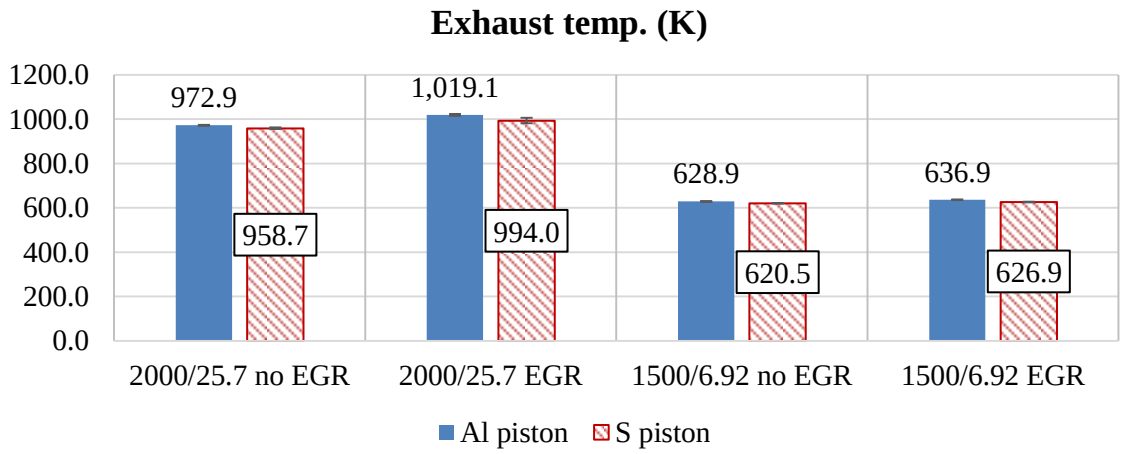

Figure 4.24: Mean time-averaged exhaust gas temperature for all conditions and pistons tested. The error bars indicate the 95% confidence limits of the data.

Figure 4.25 shows the ignition delay results, averaged over 3000 cycles, measured over 10 experimental runs each 300 cycles long. In this work, the ignition delay is defined as the interval between the start of the main injection (MSOI) and the point of 10% mass fraction burned (MFB). The results show that ignition delay is reduced under steel piston operation, independent of engine load and EGR rate.

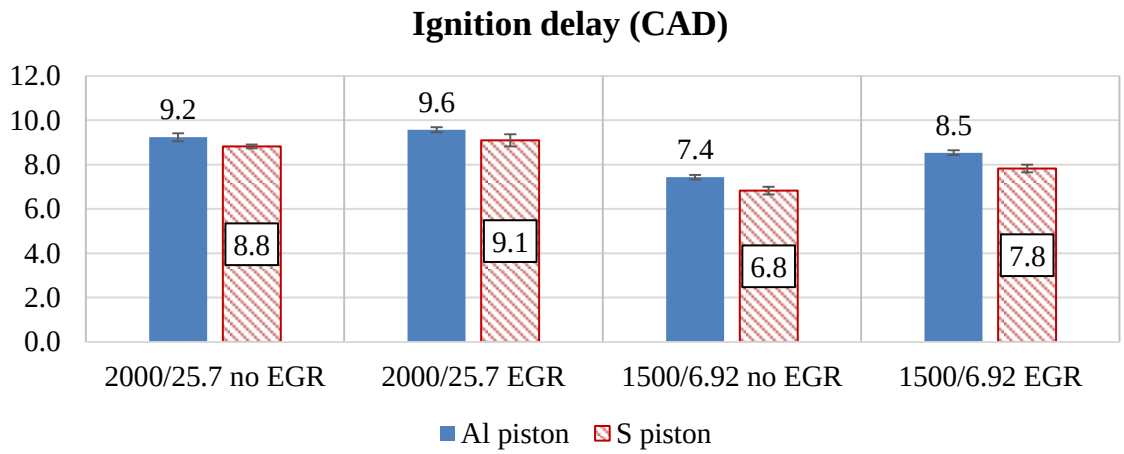

Figure 4.25: Ignition delay results for the conditions tested. Results are averaged over 10 experimental runs comprised of 300 cycles each. Ignition delay is defined as MSOI-MFB10%.

Figure 4.26 and Figure 4.27 show, representative cumulative heat release rate data, for the 2000 rpm /25.7 bar nIMEP and the 1500 rpm/6.92 bar nIMEP respectively. The dashed lines in these figures indicate the conditions of 0% EGR rate. Table 3 details the changes in ignition delay, early phase combustion duration (10 – 50% MFB), late phase combustion duration (50 – 90% MFB) and the overall combustion duration (10 – 90% MFB) for the steel piston relative to the aluminium. Although the differences are small, there is a clear trend in that the use of steel piston results in a reduction of the ignition delay, a similar burn rate between 10 to 50% MFB and a faster burn rate between 50 to 90% MFB.

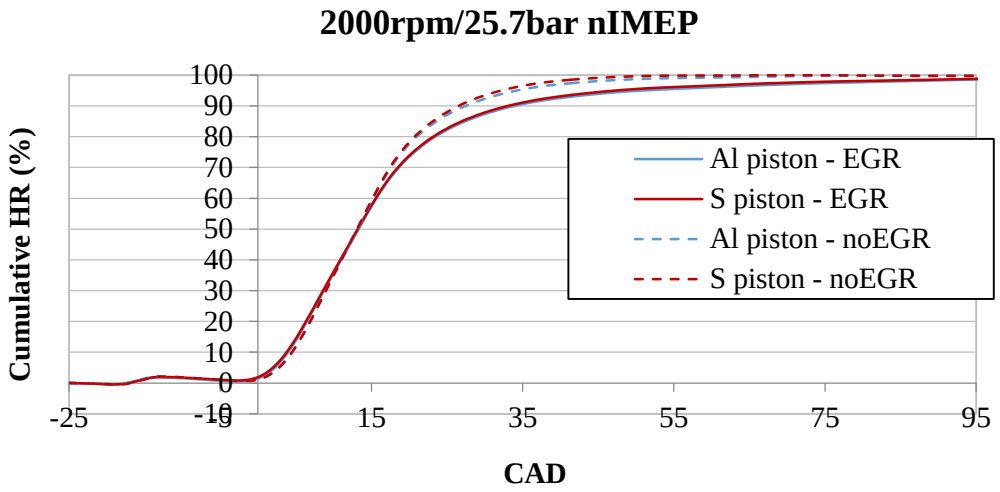

Figure 4.26: Representative cumulative heat release results for 2000 rpm/25.7 bar nIMEP case. The dashed lines indicate the 0% EGR cases.

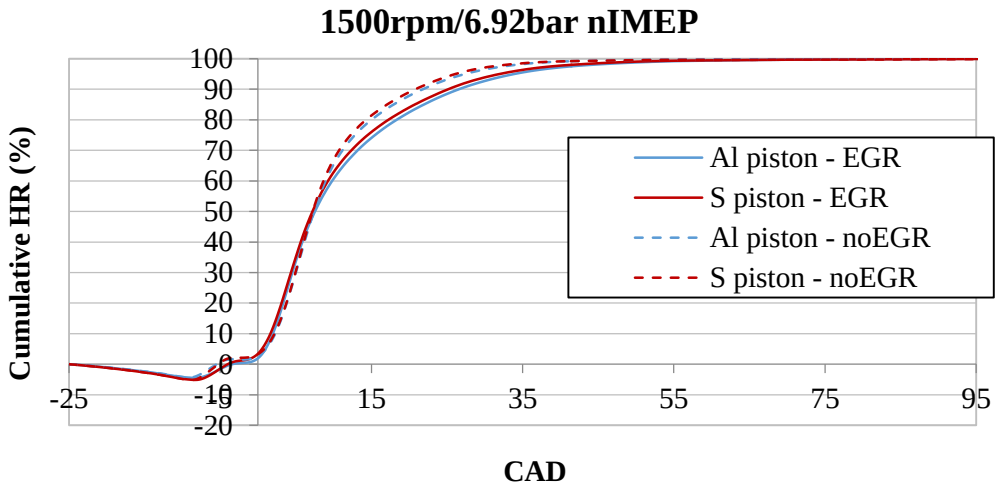

Figure 4.27: Representative cumulative heat release results for 1500 rpm/6.92 bar nIMEP case. The dashed lines indicate the 0% EGR cases.

Table 4.5: Change in ignition delay and combustion duration values between aluminium and steel pistons. Negative values indicate reductions for the steel piston.

	Ign. Delay (CAD)	**10-50% MFB (CAD)**	**50-90% MFB (CAD)**	**10-90% MFB (CAD)**
2000/25.7	-0.54	0.05	-0.81	-0.76
2000/25.7 EGR	-0.84	0.07	-0.75	-0.68
1500/6.92	-0.32	-0.07	-0.84	-0.91
1500/6.92 EGR	-0.65	-0.01	-1.08	-1.09

Figure 4.28 presents the blow-by measurements for the two pistons design under the four test conditions. Higher levels of blow-by are seen for the higher speed/load conditions. Differences due to EGR rate are not statistically significant. The results show that blow-by is significantly reduced with the steel piston design.

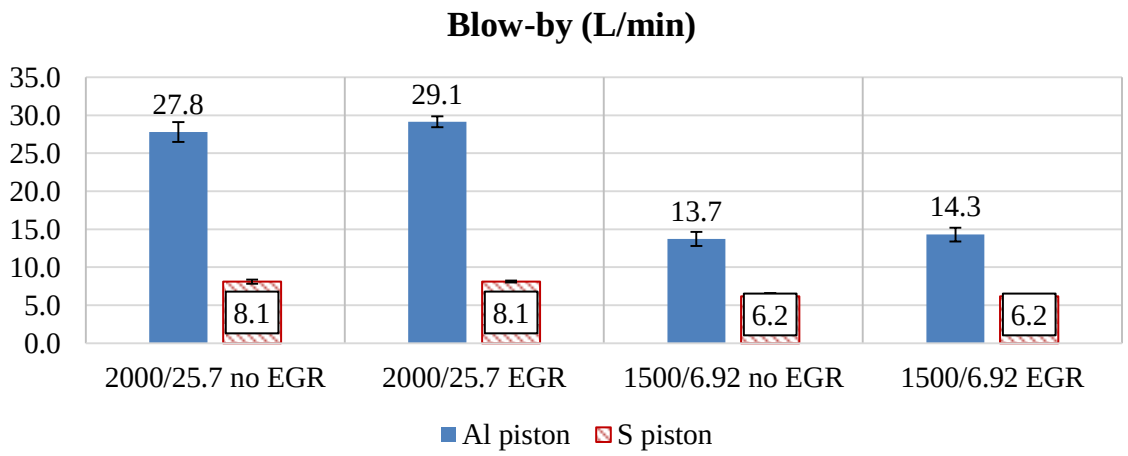

Figure 4.28: Blow-by measurements for the conditions tested. The error bars indicate the 95% confidence limits.

4.3.3 Discussion

Equation (4.2) details the relationship between brake work output, indicated work and the friction and ancillary losses of the engine.

$$Brake\ work = ind.work - (friction + ancillaries) \tag{4.2}$$

Brake and indicated work are calculated in this work by using a load cell and the in-cylinder pressure trace respectively with their difference indicating the total losses due to friction and work required to drive ancillary components. In the current work, ancillary losses are restricted to the parasitic torque of the high pressure pump–this calculation is detailed in a previous study [56]. As described in this earlier work, the fuel pump is sourced from a production four-cylinder engine. Accordingly, the percentage of fuel

pump work that is reported herein is noted to be much higher than would be expected on a production engine. Note also that these ancillary losses are constant at fixed injection pressure/speed/load conditions and that since nIMEP was held constant during testing in this work, any improvements that are observed in brake work between piston designs must relate directly to reductions in friction.

Heywood [26] reports that almost a third of the total energy to the coolant is due to friction between the piston and the liner. Thus, the reduced energy transfer to the coolant in the jacket—for all operating conditions and EGR rates—when operating with the steel piston is consistent with the reduced frictional losses associated with the design as shown in Figure 4.21. It is also consistent with the expected effects of the reduced skirt length and longer con-rod length associated with the steel piston, and in full agreement with the literature [87, 88]. It should be recognized however that the energy transfer to coolant in the jacket is also affected by heat conduction through the piston ring pack and that the observed changes may not be due to frictional effects alone.

Mahle [146] state that, for a spray jet cooled aluminium piston, approximately 30% of the heat flow through the piston crown is dissipated through the ring pack (with approximately 50% going to the oil flow through the cooling galleries and the remaining 20% dissipated via the inner contour and the bottom part of the piston skirt). Thus, it is entirely possible that the observed reduction in energy transfer to the jacket coolant with the steel piston is the result of reduced conduction through the piston ring pack.

Exploring this thought further, there are clearly significant differences in the thermal properties of the two piston materials with the thermal conductivity of aluminium being approximately four times greater than that of steel. However, with reference to Figure 4.16, it is also clear that the effects of reduced thermal conductivity will be offset to some degree by the thinner wall thickness and greater cooling gallery surface area of the steel

piston design—to the extent that a preliminary analysis indicates that the thermal resistance of the heat transfer path from the piston bowl and crown to the cooling galleries of the steel piston is similar or lower than for the aluminium piston.

The oil flow rate through the piston cooling galleries was neither controlled nor known in the present work, being governed by the oil supply to the engine and the flow resistance of the piston cooling circuit. As described previously, in addition to having an approximately 50% larger cooling gallery volume, the steel piston design utilises a twin PCJ arrangement compared to the single PCJ of the aluminium piston. These physical differences suggest that there should be less flow resistance for the steel piston cooling circuit—and therefore a greater volume flow rate of cooling oil through the steel piston—for a fixed constant pump speed, and indeed an increase in the total flow rate of oil to the engine of ~7% was measured for the steel piston design (Figure 4.29 refers).

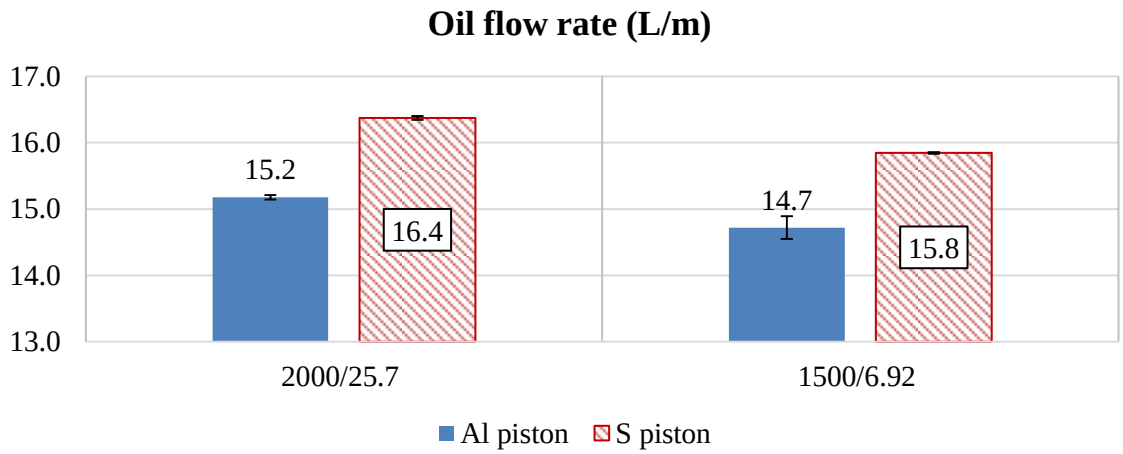

Figure 4.29: Total oil flow rate measurements for the conditions tested. The error bars indicate the 95% confidence limits.

An increase in oil gallery surface area and volume flow of rate oil would increase piston cooling, thereby reducing conduction from the ring pack to the coolant jacket, and increase the energy transfer to the cooling oil. Both of these trends are consistent with the

experimental data. Note here that the increase in energy transferred to the oil with the steel piston (Figure 4.17 to Figure 4.20 inclusive) observed in the current work is contrary to previously reported studies within the literature [87, 88]. This apparent disagreement is attributed to differences in piston cooling arrangements between the current study and the referenced works. The previous studies employed an independent oil supply and conditioning system for piston cooling. As a result, the temperature and flow rate of the cooling oil to the piston could be varied independently from the lubricating oil to control piston temperature to set target values.

Whereas friction work and ring pack conduction are expected to influence the energy transfer to the coolant in the jacket directly, their influence on the coolant in the cylinder head is less clear. There is clearly some level of thermal contact between the liner and head. However, it is to be expected that this will be a minor effect and that dominant source of energy into the cylinder head coolant will be heat transfer from the combustion and exhaust gases. The reduced energy transfer to the cylinder head cooling circuit that is seen with the steel piston is then consistent with the reduction of exhaust gas temperature (EGT) that is noted for the steel piston design in Figure 4.24. This might also indicate that the change from the aluminium to steel piston has in some way caused a change in the combustion process.

The literature suggests that the lower thermal conductivity of steel will lead to higher piston surface temperatures [88], which would result in reduced heat flux between the hot combustion gases and the piston bowl and crown. Without direct measurement in the current work it is not possible to confirm or quantify changes in piston surface temperature, however the observations of reduced ignition delay in the present work (Figure 4.25) are consistent with the effects of increased piston surface temperature reported in the literature [147]. Similarly, the small increase in the mixing controlled burn

rate – reducing the overall combustion duration by ~0.8-0.9 CAD – that is presented in Figure 4.26 and Figure 4.27, and Table 4.5 for the steel piston may also indicate a higher piston surface temperature as the increase in burn rate is consistent with the expected effects of reduced heat loss [83]. In turn, the slightly earlier heat release could be responsible for a minor reduction in exhaust gas temperature shown in Figure 4.24.

The reduction in blow-by with the steel piston, as reported in Figure 4.28, may also be significant with respect to the reduced ignition delay, piston temperature and in-cylinder heat transfer. As a fraction of the total intake mass, the measured blow-by ranged from ~1-3% independent of operating conditions, which is consistent with values reported in literature [26, 148]. This would give approximately 1.3% more trapped mass for the steel piston than for the baseline aluminium case. A simple isentropic compression calculation, assuming a polytropic coefficient of 1.4, indicates that an increase of 1.3% in trapped mass would give a corresponding increase in peak cylinder pressure of ~1.4 bar and indeed increases in peak cylinder pressure of this order were observed for the steel piston in the experimental results (Figure 4.30).

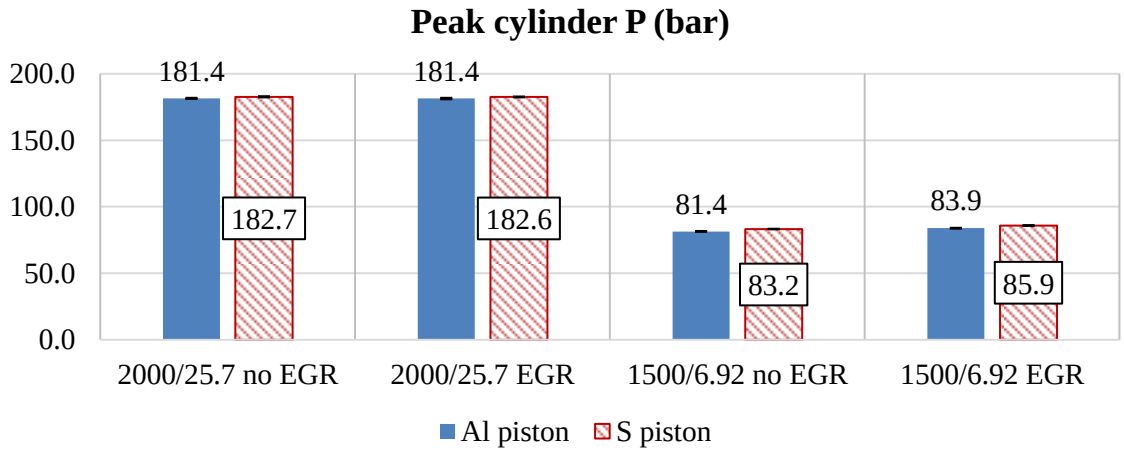

Figure 4.30: Peak cylinder pressure measurements for the conditions tested. The error bars indicate the 95% confidence limits.

The increased trapped mass and resultant higher in-cylinder pressures are expected to lead to higher bulk gas temperatures and higher indicated work for the steel piston design for a given energy input. However, the measured changes to the peak gas temperatures are small and although a constant trend of increasing temperature with the steel piston was seen the differences between the different piston materials were not statistically significant. Nevertheless, the improvements in nISFC shown in Figure 4.22 for the steel piston does indicate a positive effect on the indicated work, particularly at lower load, i.e. less fuel is required to achieve the target value of nIMEP. The results suggest that the indicated work for a given fuel input is increased by the combination of a small increase in trapped mass due to reduced blow-by and a similarly small increase in mixing-controlled burn rate. It can be seen in Figure 4.23 that the benefits of improved fuel usage combine with the reduction in frictional (and ancillary) losses shown in Figure 4.21 to yield substantial benefits in brake specific fuel consumption. However, as the friction, thermal, and parasitic characteristics of a single cylinder engine are significantly different to its multi-cylinder equivalent, the author suggests that it is the indicated values that are of practical interest.

4.3.4 Conclusions on piston material study

This study has compared the effects of different piston materials on the performance of a single-cylinder direct injection diesel engine. Two pistons design were tested, aluminium and steel, at two speed/load conditions and their performance was assessed using a first law analysis approach; all other engine parameters were held constant. This analysis was further supplemented by heat release analysis data. It was found that switching from the baseline aluminium piston to the steel piston design resulted in:

- A reduction of between 6 and 10% in frictional losses for all test conditions. This was attributed to the reduced total and topland heights of the steel piston design.
- A reduction of ~1 percentage point across all test conditions in the energy transferred to the jacket coolant. This reduction was attributed to the combination of reduced frictional losses and lower levels of heat conduction through the ring pack.
- A reduction of ~1 percentage point across all test conditions in the energy transferred to the cylinder head coolant circuit. The author attributes this reduction to changes in the combustion characteristics as evidenced by the reduced ignition delay, faster mixing controlled burn rate and decreased exhaust gas temperature seen for the steel piston.
- Reduced piston blow-by, consistent with the literature, which results in an increase in trapped mass of order 1%.
- A reduction of between 0.5 and 1.3% in nISFC—where the larger increases were seen at the low speed/load condition—due to the combination of an increase in trapped mass and the increased mixing-controlled burn rate.
- An increase of ~1 percentage point in the energy transferred to the oil as a result of the increased cooling gallery volume of the steel piston design and an increased volume flow of cooling oil associated with the steel piston design and its twin cooling jet configuration.
- An increase in brake efficiency at all four conditions tested. The observed benefits are relatively small at high load. The benefits were more pronounced for the low speed/load case where improvements in the order of 2% were achieved.

4.4 Chapter summary

This chapter presented the results of two thermal studies, using the first law modelling tool introduced in Chapter 3. The first study compared different high-pressure EGR strategies; these being standard application of HP-EGR, HP-EGR application under increased swirl levels (e.g. by utilising a swirl flap) and the application of HP-EGR without O_2 displacement (i.e. under constant λ conditions). The results of this study showed that both of these alternative methods result in a penalty in brake efficiency, due to an increase in pumping work; with exception of the SF case under low speed/load conditions where an improvement in brake efficiency, due to increased burn rates, was observed. Furthermore, both strategies resulted in higher NO_x emissions but in a reduction in CO, THC and smoke. The second study looked into the effects of different piston materials, these being alloy steel and aluminium, on the resulting energy flows and engine efficiency. Steel piston operation has resulted in an improvement in nisfc (~0.5-1.3%) due to a faster burn rate combined with a reduction in blow-by. A reduction in the energy transfer to the coolant was also observed with the steel piston which was attributed to the combined effects of the lower thermal conductivity of steel and the reduced friction due to the shorter piston skirt of the steel design.

Finally, this work has demonstrated the extreme difficulty of obtaining accurate measurements of energy transfer to the engine coolant system at low-load. The results indicate that twenty-three repeat tests would be necessary to provide statistical certainty to these measurements at 95% confidence even when using purpose-built differential thermocouples accurate to ± 0.07 K.

The results of both of these studies indicate that the energy transfer to the exhaust is more than 30% of the total energy input into the engine. However it is recalled, that the

exhaust enthalpy values presented above were calculated on a time-average basis, due to errors associated with unsteady flow temperature measurements, which have the potential to underestimate the energy found in the exhaust. Thus improving the accuracy of these measurement has the scope to provide a better insight into exhaust energy transfer. The following chapter will discuss the resulting errors arising during the exhaust gas temperature measurement process using both numerical and experimental results.

5 Modelling of thermocouple sensors

The previous chapter has highlighted the significant proportion of the input fuel energy that is contained in the exhaust of an ICE; almost 40%. An accurate measurement of the exhaust temperature is clearly essential for estimating the exhaust enthalpy. Typically exhaust gas temperature measurements are made with thermocouples, which may vary in size from 0.05 mm (for fast response applications) to a few millimetres. These sensors are subject to both dynamic errors, due to their thermal inertia, and conduction and radiation errors due to temperature gradients between the sensor and the surrounding environment. Thus the goal of this study was to assess the performance of different size temperature sensors under various temperature fields and identify the major sources of measurement error. In this chapter, the results of instrumenting the exhaust of the single cylinder diesel engine, both with a three thermocouple probe (comprised of a 50.8 μm, a 127 μm and a 254 μm fine wire thermocouple) and a standard 3 mm sheathed thermocouple, are presented. The experimental results were also supported numerically, using the lumped capacitance thermocouple model introduced in Chapter 3.

5.1 Introduction

Energy balance studies on internal combustion engines highlight the need for accurate exhaust gas temperature (EGT) measurements, especially when investigating the effects of different combustion strategies [56, 74, 97, 99, 103]. In addition, accurate knowledge of EGT is important for heat transfer modelling of exhaust systems and CFD model development and validation [149]. Furthermore, accurate measurement of EGT in internal combustion engines is important for a wide range of monitoring and design purposes. Unreliable EGT measurements can lead to component damage from excessive thermal

loading [150], or to the underutilisation or inefficient use of turbocharger and after-treatment systems [151-153]. For instance, the conversion efficiency of diesel oxidation catalysts and selective catalytic reduction (SCR) systems is dependent on their operating temperature and consequently on the exhaust gas temperature. The regeneration of diesel particulate filters (DPFs) is achieved by retarding the post-injection timing thus increasing the temperature of the exhaust gases [29]. Accurate monitoring of the EGT, and thus being able to optimise the regeneration event, has the potential to improve fuel efficiency.

The measurement of EGT in internal combustion engines usually involves the use of thermocouples due to their low cost, simplicity and robustness at elevated temperatures. In order to capture the transient behaviour of the EGT in specialised research applications, fine-wire thermocouples, which can vary in size from 0.001" to 0.032", are commonly employed [103, 113, 115, 141]. However, larger, more robust thermocouples (e.g. 3 mm sheathed probes) are typically used for conventional test-bed applications, to the detriment of the measurement system's dynamic response.

It is recalled that the dynamic response of a thermocouple to temperature fluctuations is governed by its time-constant (τ) and that several techniques have been developed to identify this time-constant *in situ* and thus correct for this dynamic error (Chapter 3). In addition to the potential errors associated with an uncertain dynamic response, thermocouple temperature measurements are commonly subject to additional potential sources of error; conduction and radiation, which are dependent on the geometrical properties of the sensor, the characteristics of the flow to be measured and the installation of the sensor relative to the flow (as well as potential errors relating to the catalysis of the thermocouple metals which are typically very small and hence will be disregarded).

Measurement errors introduced due to radiative heat transfer [133, 154, 155], and slow dynamic response [113, 139, 141, 156, 157] of thermocouple sensors in temperature measurement have been widely covered in the literature. On the other hand, thermocouple conduction error is less commonly studied and the published work is mostly limited to temperature measurements in steady flows [132, 154, 155, 158]. Conduction error is a consequence of the temperature gradient along the axis of the sensor, resulting in a heat flow away from the measurement location, and thus to a discrepancy between the fluid and the sensor's apparent temperature. It has been shown that this error can be reduced by either, increasing the sensor's immersion length, or by reducing its diameter (and hence its conduction area) [132, 155]. However, these conduction error reduction techniques are not always applicable, usually limited by the sensor's service life and the diameter of the pipe that is to be instrumented, and therefore an understanding of the conduction error is required in order to achieve an accurate measurement.

This work combines experimental and numerical studies to assess the performance of different size thermocouples on the measurement of EGT in internal combustion engines and to quantify the relative importance of the different sources of error, namely; conduction, radiation and dynamic response.

5.2 Experimental methodology

Two types of thermocouples have been used; fast response and mineral sheathed thermocouples. Three bare-wire K-type thermocouples, of varying junction diameters (50.8 μm (T2), 127 μm (T5) and 254 μm (T10)), were combined in a single thermocouple probe (hereafter called 3-TC probe) (refer to Chapter 2). A 3 mm mineral sheathed K-type thermocouple, representing conventional engine instrumentation, was used as a reference EGT sensor. The manifold wall temperature, required for the estimation of

radiation and conduction losses, was measured by an embedded K-type thermocouple. The relative location of each of the sensors along with the signal conditioning details are discussed in Chapter 2.

The engine was operated at two different speed/load conditions in order to assess the response of the different thermocouple sensors. The engine operating conditions can be seen in Table 5.1. Once the engine reached stable operation, judged as being when the reference 3 mm thermocouple reading had achieved a steady state, the exhaust temperature signals were logged for 300 consecutive cycles. An ensemble average for each thermocouple signal was then calculated using the AVL Concerto software and converted to temperature using the process described in Chapter 2. For the bench testing the thermocouple signals were logged using an oscilloscope.

Table 5.1: Engine operating conditions

Test point	**1500 rpm/6.8 bar nIMEP**	**1750 rpm/13.5 bar nIMEP**
Engine speed (rpm)	1500	1750
nIMEP (bar)	6.8	13.5
Approximate exhaust temperature (K)	623	753
Wall Temperature (K)	509	589

5.3 Results and Discussion

5.3.1 Experimental results

In this section the experimental data from the 3-TC probe and the 3 mm sheathed reference thermocouple are presented and compared at the two different speed/load points. Figure 5.1 shows the measured exhaust gas temperature at the 1500 rpm/6.8 bar nIMEP condition. The two dashed lines indicate the time of exhaust valve opening (EVO)

and exhaust valve closing (EVC) events. As expected, the T2 thermocouple – having the smallest time constant – is able to capture the blowdown event more clearly thus resulting in a higher temperature reading compared to the other two fine-wire thermocouples. It is also interesting to note that due to its lower time constant, the T2 thermocouple cools more rapidly, during the period that the exhaust valves are closed, thus resulting in the lowest apparent temperature at the end of the cycle. These effects are lessened as the size of the junction is increased.

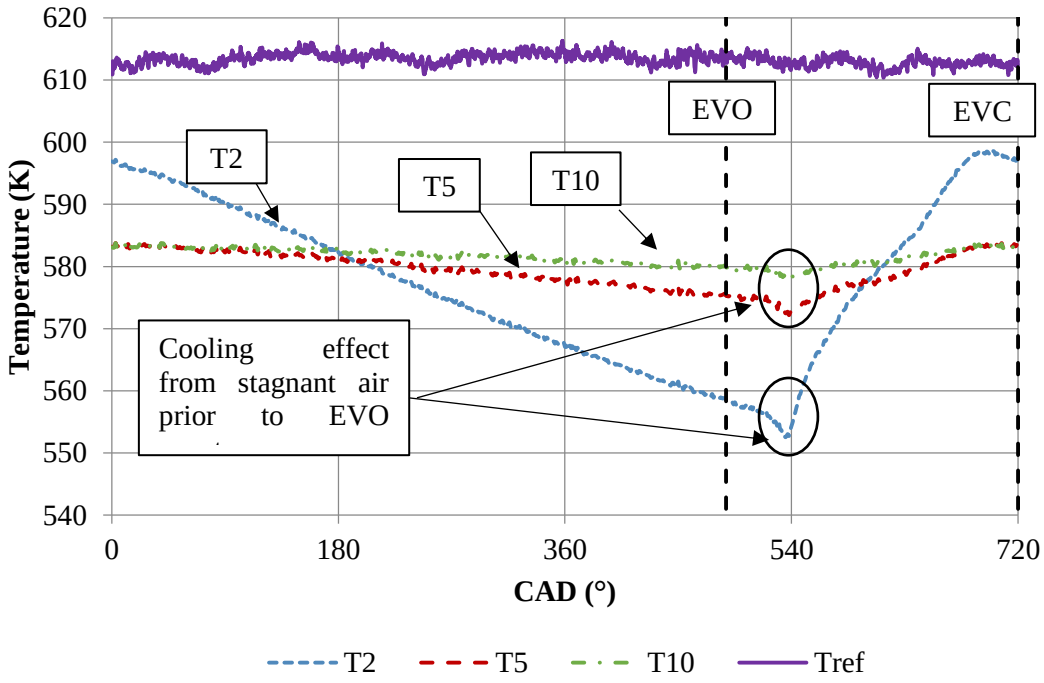

Figure 5.1: Experimental exhaust temperature measurements for the 3-TC probe and the reference thermocouple at 1500 rpm/6.8 bar nIMEP point.

Worthy of note is the sudden cooling period prior to the rapid increase in temperature that is captured by all thermocouples of the 3-TC probe at approximately 540 CAD. Kar *et al.* [113] also observed this cooling trend suggesting that it is caused by a combination of two phenomena: a) prior to EVO the column of air between the sensor and the valves is exchanging heat with the surroundings and when the EVO event occurs this “cooler” gas

precedes the hot gases exiting the cylinder thus resulting in the measured cooling spike, and b) while the valves are closed they will exchange heat with the cylinder head and during the EVO period, where the flow is choked and the heat transfer very high, the first hot gases leaving the cylinder will exchange heat with the colder valves, resulting in a lower temperature. These trends discussed are the same at the 1750 rpm/13.5 bar nIMEP conditions and so are omitted for brevity.

The results present in Figure 5.1 show an unexpected behaviour in terms of the response of the different thermocouple sensors. The reference thermocouple indicates an apparent temperature of 613 K, a reading that is significantly higher than both the instantaneous and the time-averaged temperatures measured with the 3-TC probe. Since conduction and radiation errors in temperature measurement are dependent on sensor size (the immersion length for both probes is the same) the opposite trend might reasonably be expected. Repeated experiments with a second 3-TC probe confirmed the result. The position of the two probes was also swapped to ensure that these observations were not a result of the probe location. Figure 5.2 presents the measured time-average temperatures for the 3-TC probe and the reference thermocouples for the two speed/load conditions. Note that at the higher speed and load condition the magnitude of the discrepancy between the fine-wire and sheathed thermocouples is of the order of 80 K.

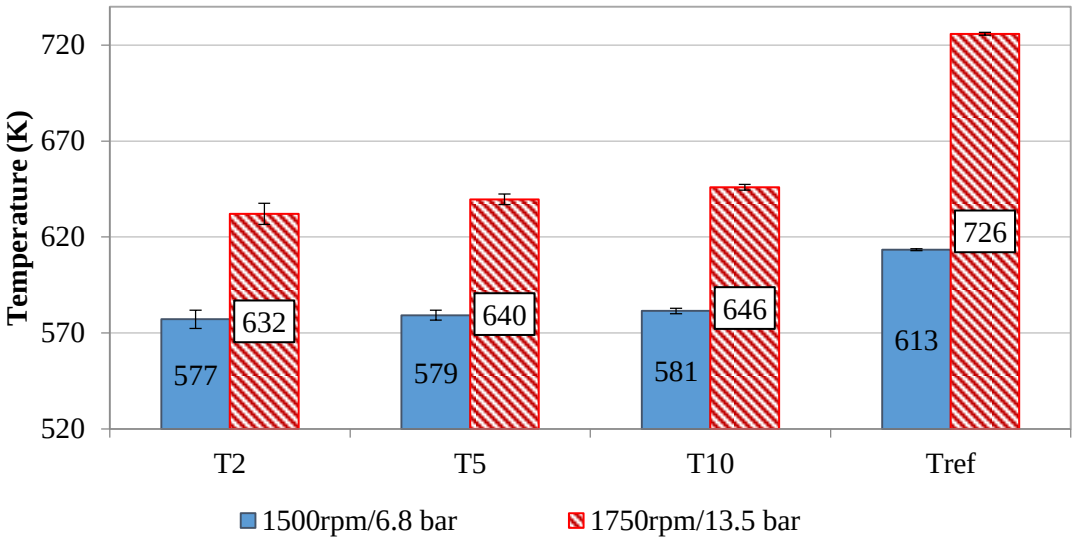

Figure 5.2: Experimental time-average exhaust temperatures for the different thermocouple sizes for both speed/load conditions. The blue colour indicates the 1500 rpm/6.8 bar nIMEP and the red colour the 1750 rpm/13.5 bar nIMEP conditions. The error bars indicate the 95 % confidence limits.

At this point it is worth recalling the miniature oven results presented in Chapter 2. Figure 2.14 clearly indicates no such discrepancies between the different thermocouples under the steady-state heating conditions provided by a propane torch, thus indicating no obvious fault of the sensors. In order to test the correct operation of the sensors further, these were installed on a spare exhaust manifold on a test bench, identical to the on-engine installation, where a heat gun was used to replicate the exhaust gas stream. The use of heat gun provided a steady flow of gas thus removing any effects associated with the pulsating nature of the exhaust gases found on the engine. This installation can be seen in Figure 5.3.

Figure 5.3: Test bench installation using the exhaust manifold and a heat gun as a heat source. The installation of the 3TC-probe and the reference thermocouple are identical to the engine installation.

The maximum temperature achieved for these tests was ~563 K (based on the reference thermocouple reading), a point significantly lower than the exhaust conditions on the engine, however, the resulting trends are expected to be the same. A temperature sweep of 7 points was carried out, with the measurements repeated on different days. Figure 5.4 shows these results for the T5 thermocouple, with the black line representing the unity slope line for the reference thermocouple. It is noted that due to wiring issues with the 3-TC probe only the T5 thermocouple signal was available for these tests.

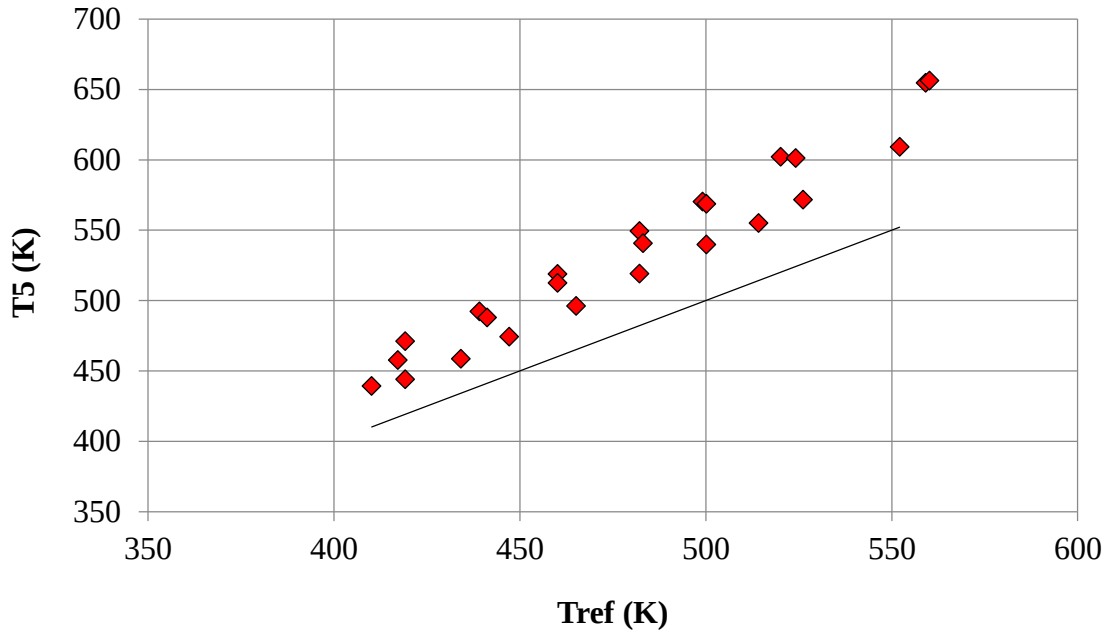

Figure 5.4: Temperature measurement comparison using the exhaust manifold test-bench installation. The black line represents the unity slope line for the reference thermocouple.

The results clearly indicate that the T5 fine-wire thermocouple is indicating a higher value throughout the temperature range tested. This is expected as the 3-TC probe is installed closer to the heat gun and heat transfer losses to the manifold walls are expected to reduce the thermal energy that the reference sensor is exposed to. Due to the construction of the 3-TC probe, and the exposed length of the thermocouple junctions (~4 mm from the tip of the probe), aerodynamic effects might arise depending on the circumferential orientation of the probe such that, a junction located at the wake of another junction might not be fully exposed to the prevailing flow conditions and thus indicate a lower temperature. Further to this, manufacturing inaccuracies associated with the thermocouple junction might affect the sensitivity of the sensor to temperature changes depending on junction orientation relative to the gas flow. Consequently, the 3-TC probe was also tested under different circumferential orientations to test such effects. The orientations tested were 0°, 90°, 180° and 270° relative to the flow direction. The results of this test can be seen in Figure 5.5. The annotation shows the orientation of the

three thermocouple junctions relative to the flow direction and the black line the unity slope line of the reference sensor.

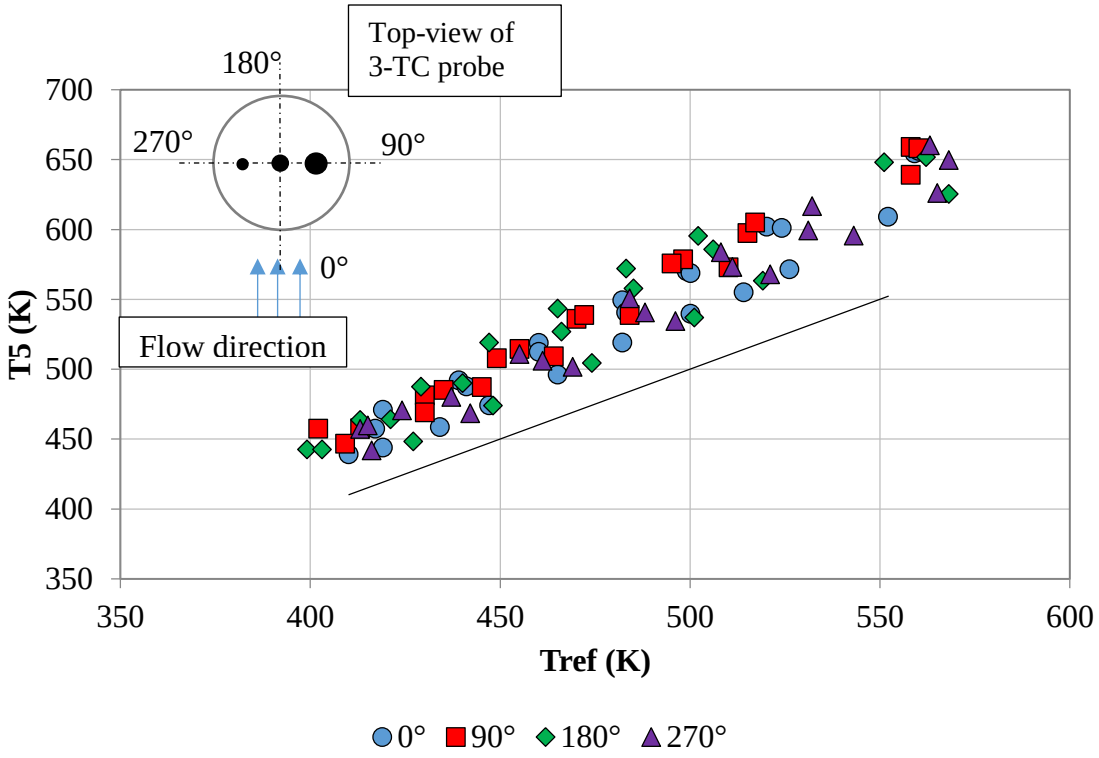

Figure 5.5: Effect of probe orientation relative to the flow direction on temperature measurement for the T5 thermocouple. The annotation indicates the approximate orientation of the three junctions at each installation angle. The black line indicates the unity slope line for the reference sensor.

Figure 5.5 shows that the orientation of the probe does not have a significant effect on the logged temperatures considering the scatter of the measurements. Furthermore, the temperature measured by the T5 thermocouple is consistently higher than that of the reference sensor, independent of probe orientation, which is in agreement with the results presented in Figure 5.4. When these observation are combined with the calibration results presented in Chapter 2, one can conclude that the 3-TC probe's operation is correct and that the results presented in Figure 5.2 must be due to the resulting flow conditions found in the exhaust stream during engine operation. The following section discusses the results

of the numerical simulations carried out, in an attempt to explain the results shown in Figure 5.1 and Figure 5.2.

5.3.2 Thermocouple modelling results

In this section, the author presents the results of lumped capacitance modelling of the three different size thermocouples of the 3-TC probe and also for the reference thermocouple. The simulations were carried out in three stages in order to better understand the observed experimental data: firstly, the thermocouple transient response to a time varying input gas temperature (T_g) and flow velocity from 1-D engine simulation was predicted in the absence of radiation and conduction. Secondly, the simulation was expanded to include the radiation term, and finally the model was expanded to include radiation and conduction. In each case, the model was run until the temperature at the start of the cycle converged to the temperature at the end of the cycle. All data presented are converged values.

No radiation or conduction terms

Ignoring the radiation and conduction terms, Equation (3.22) is discretised as:

$$T_s(t+1) = T_g(t) + \left[T_s(t) - T_g(t)\right]e^{-\frac{\Delta t}{\tau}} \tag{5.1}$$

where the time constant (τ) is given by Equation (3.23) and Δt is the size of the time-step [131].

The model results of Equation (5.1) for the different thermocouples at the 1500 rpm/6.8 bar nIMEP are shown in Figure 5.6 where the solid line indicates the modelled gas temperature from the 1-D engine model. The observed undulations are a result of the pressure pulses travelling along the length of the manifold – these undulations are captured by the fast response pressure transducers that are used as an input into the 1-D

model – a detailed discussion of the exhaust pressure fluctuations from this engine is included in [159]. The results clearly indicate that as the size of the thermocouple, and consequently the time-constant, increases the temperature signal is significantly attenuated, as expected. As an example, the model results for the T2 thermocouple indicate an average time constant of $\bar{\tau} = 19\,ms$ over the cycle duration, which corresponds to a frequency response of ~55 Hz. Consequently, the T2 thermocouple is not able to capture the temperature fluctuations associated with the pressure pulsations occurring at ~100 Hz. Similarly the maximum temperature is also significantly under predicted, with the T2 thermocouple indicating a peak temperature of ~645 K compared to the "true" peak temperature value of ~695 K.

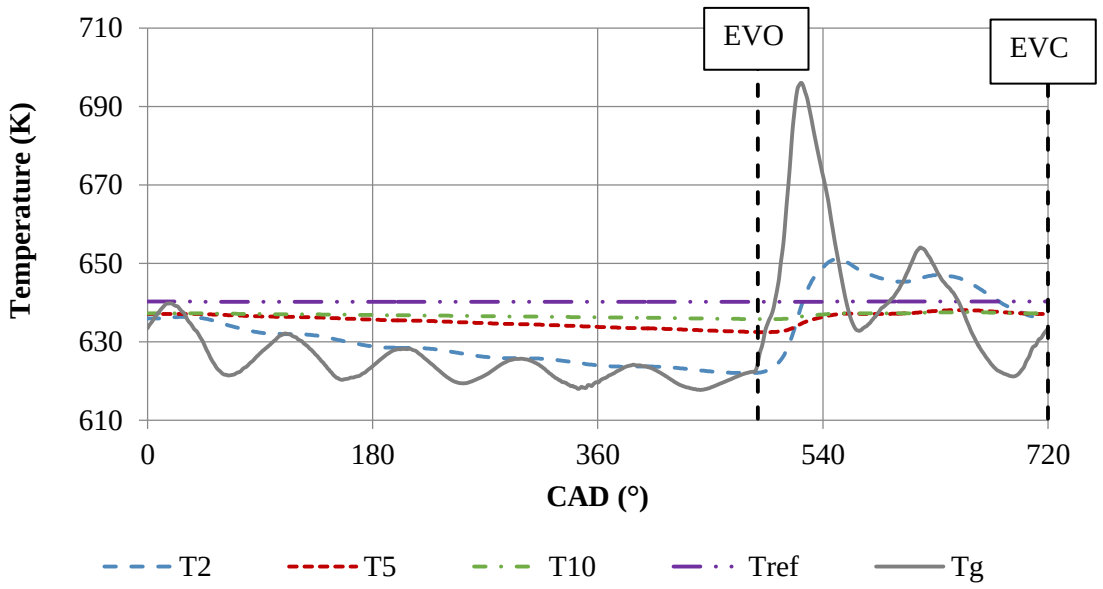

Figure 5.6: Simulated thermocouple results for the 1500 rpm/6.8 bar nIMEP case (Equation (5.1)). Effects of radiation and conduction are not included.

These observations highlight the dynamic error that is induced by thermocouple measurements of unsteady temperature flows; this dynamic error is expected to be pronounced in exhaust gas temperature measurements as the fragility of fine-wire thermocouples and the harshness of the environment, forces a compromise between

frequency response and robust measurements, dictating a minimum junction diameter of 0.254-0.508 mm [156].

In agreement with the experimental results presented in Figure 5.2, the 3-TC probe thermocouples are predicted to result in lower time-average temperatures compared to the reference thermocouple. However although this trend is correct, the absolute differences between the modelled and experimental values are quite different. More specifically, the results of Equation (5.1), for all thermocouples, result in an overestimate of the time-average temperature ($\bar{T}_s$) compared to the time-averaged gas temperature ($\bar{T}_g$) that is input. These differences can be seen in Table 5.2 for both speed/load conditions modelled.

Table 5.2: Modelled time-average temperature results: No radiation or conduction terms (Equation (5.1)) for the two speed/load conditions

Conditions	$\overline{T}_g$	$\overline{T}_2$	$\overline{T}_5$	$\overline{T}_{10}$	$\overline{T}_{ref}$
1500 rpm/6.8 bar IMEP	630 K	632 K	635 K	637 K	639 K
1750 rpm/13.5 bar IMEP	706 K	712 K	716 K	718 K	722 K

The discrepancies observed between the input and predicted time-averaged temperatures shown in Table 5.2 are an artefact of the thermocouples' thermal inertia. By definition, as the thermal inertia of a body increases the slower it can respond to temperature changes and thus the longer it takes to reach equilibrium. Similarly, upon equilibrium, a larger thermal inertia implies a higher amount of thermal energy stored within the body and consequently a higher apparent body temperature. Therefore, as the T2 thermocouple has the smallest inertia is able to follow the temperature fluctuations during the cycle much closer and reach a steady state condition much quicker. However, since its thermal mass is not zero, once equilibrium is reached (i.e. the temperature at the beginning and the end

of the cycle is the same), its apparent temperature ($\bar{T}_2$) will be higher than the gas temperature ($\bar{T}_g$) with the difference indicating the extra energy required to heat its thermal mass.

Radiation terms included

Equation (5.2) shows the discretised solution of Equation (3.32) for T_s with the radiation term included and the conduction term ignored.

$$T_s(t+1) = T_s(t) + \frac{\Delta t}{mc_p}\left[hA_S\left(T_g(t) - T_s(t)\right) - \sigma\varepsilon A_S(T_s^4(t) - T_w^4)\right] \tag{5.2}$$

From Equation (5.2) it is clear that the radiative term will be dependent on the exposed surface area of the body (assuming a constant wall temperature). The flow conditions will not have an effect on the energy transferred by radiation and it is also recalled that for these simulations the fluid is considered to be transparent. Figure 5.7 shows the effect of radiation (Equation (5.2)) in terms of time-average values for the modelled thermocouples for the 1500 rpm/6.8 bar nIMEP case. The wall temperature was fixed at $T_w = 509\,K$. Under the 1750 rpm/13.5 bar nIMEP case the radiation errors for each thermocouple were of the same order of magnitude as those presented in Figure 10 and have thus been omitted.

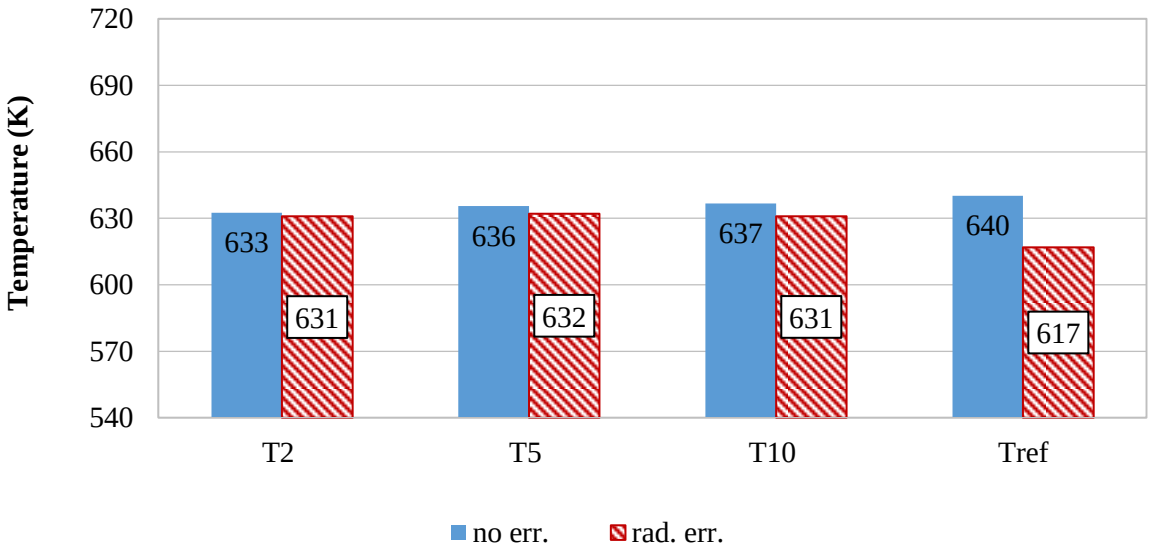

Figure 5.7: Effect of radiation error (rad err.) on time-averaged temperatures for all thermocouple sizes at the 1500 rpm/6.8 bar nIMEP condition. Constant wall temperature, $T_w = 509\ K$.

The results clearly indicate that radiation has a small effect on the fine-wire thermocouples for the conditions modelled here. On the other hand, due to its relatively larger size, the error due to radiative heat transfer on the reference thermocouple is ~23 K. The effects of thermal inertia discussed in the previous section are still apparent for the 3-TC probe thermocouples, with the T5 thermocouple indicating the highest temperature, but it is interesting to note though that the 3-TC thermocouples are now indicating higher time-average temperatures than the reference thermocouple.

Due both to the relatively minor effect of radiation on the time-averaged temperature and to the fact that the results in Figure 5.7 now follow an opposite trend to those shown in Figure 5.2, i.e. the reference thermocouple reports a lower time-average temperature than the 3-TC probe values, it is concluded that the substantial differences in the experimental time-averaged temperatures reported by the 3-TC and reference thermocouples are not due to the effects of radiative heat transfer.

Radiation and conduction terms included

It is recalled that the discretised solution for the temperature history of the thermocouple junction, including conduction and radiation error, was introduced in Chapter 3 and is shown below to assist the reader.

$$T_s(t+1) = T_s(t) + \frac{\Delta t}{mc_p}\left[hA_S\left(T_g(t) - T_s(t)\right) - \sigma\varepsilon A_S(T_s^4(t) - T_w^4) - \frac{2kA_{csa}}{L}(T_s(t) - T_w)\right] \quad (5.3)$$

The results of Equation (5.3) for the 1500 rpm/6.8 bar nIMEP case can be seen in Figure 5.8. Comparing against the results presented in Figure 5.6 it is clear that heat transfer along the sensor's body has a significant impact on the resulting temperature measurement for all thermocouples, with the conduction error having a more profound effect on the fine-wire thermocouples than the reference sensor. More specifically, the results presented in Figure 5.8 indicate similar trends to the experimental results presented in Figure 5.1 and Figure 5.2; namely the time-average temperature of the fine-wire thermocouples is lower than the reference thermocouple.

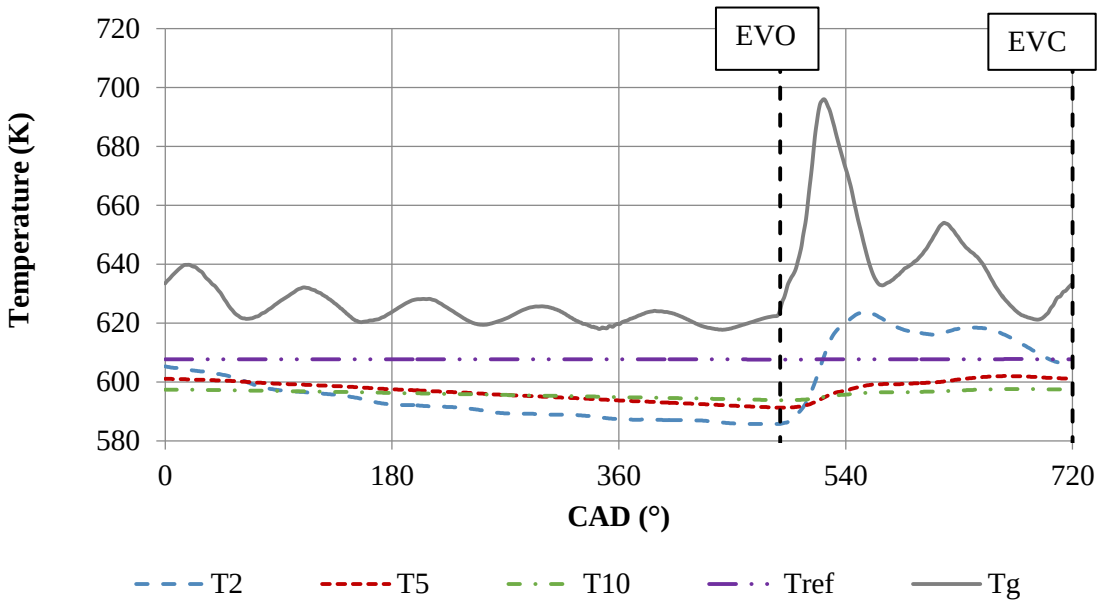

Figure 5.8: Thermocouple modelling results including conduction and radiation losses for the 1500 rpm/6.8 bar nIMEP conditions (Equation (5.3)). The wall temperature was constant at $T_w = 509\ K$.

The relative magnitudes of the conduction effects on the fine-wire and reference thermocouples observed in these simulations is in sharp contrast to the literature where conduction effects in unsteady flows with fine-wire thermocouples is usually ignored due to the small diameter to length ratio of these sensors [113, 156]. On first sight, according to Equation (5.3) one would expect the opposite trend, as the conduction error is directly proportional to the cross-sectional area of the thermocouple wires (assuming constant thermal properties) [132, 160]. However, each term in Equation (5.3) is also dependent on the thermal mass (mc_p) of the thermocouple junction. Looking into the relative contribution of each heat transfer term in Equation (5.3) to the total energy of the thermocouple junction can assist in understanding the observed thermocouple behaviour. Figure 5.9 shows this relative contribution in percentage terms for the reference thermocouple. Following Equation (5.3), a positive sign for the radiation and conduction

terms will indicate the energy transferred from the control volume (Figure 3.8) whereas a positive sign for the convective term shows the energy flow into the control volume.

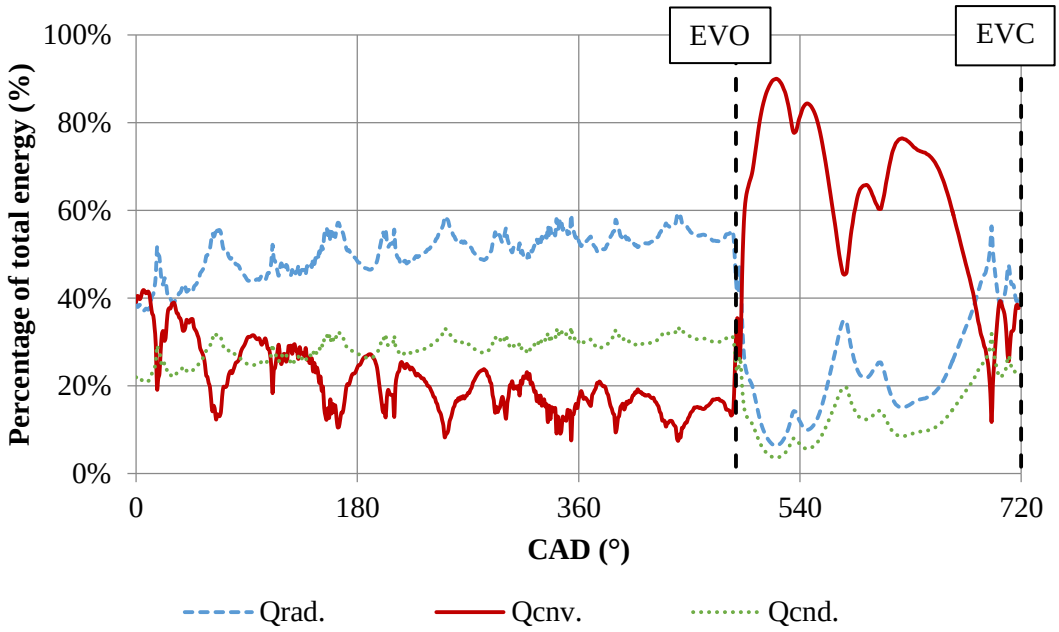

Figure 5.9: Relative contributions of heat transfer modes on the total energy of the reference thermocouple junction during one cycle.

As expected, the dominant heat transfer mode during the time that the exhaust valves are open is heat convection from the hot gases to the thermocouple surface. During this period heat conduction and radiation have a very small contribution in the total energy transferred. However, once the valves are closed, the conductive and radiative terms are significantly increased, with the convective term progressively decreasing to ~15% – this is in agreement with observations made by Cambel and Jennings [161] where they concluded that as the flow velocity is reduced the temperature measurement error is dominated by radiative and conductive heat transfer. Under these conditions, the effect of radiation is much more pronounced compared to the heat conducted along the length of the probe, with the maximum values approaching ~55% and ~30% of the instantaneous energy transfer for the radiation and conduction terms respectively.

The results for the relative contribution of heat transfer modes for T2 thermocouple are presented in Figure 5.10. An interesting observation here is the opposite trend that the conduction and convection terms follow during the EVC period for the two thermocouples – conduction is increasing during the EVC event for the reference thermocouple and decreasing for the T2 thermocouple and vice-versa for the convection term. The radiation term is constant irrespective of junction size for this period. During the EVC event the temperature of the gas will keep decreasing as it exchanges heat with its cooler surrounding, a phenomenon that is observed experimentally in Figure 5.1.

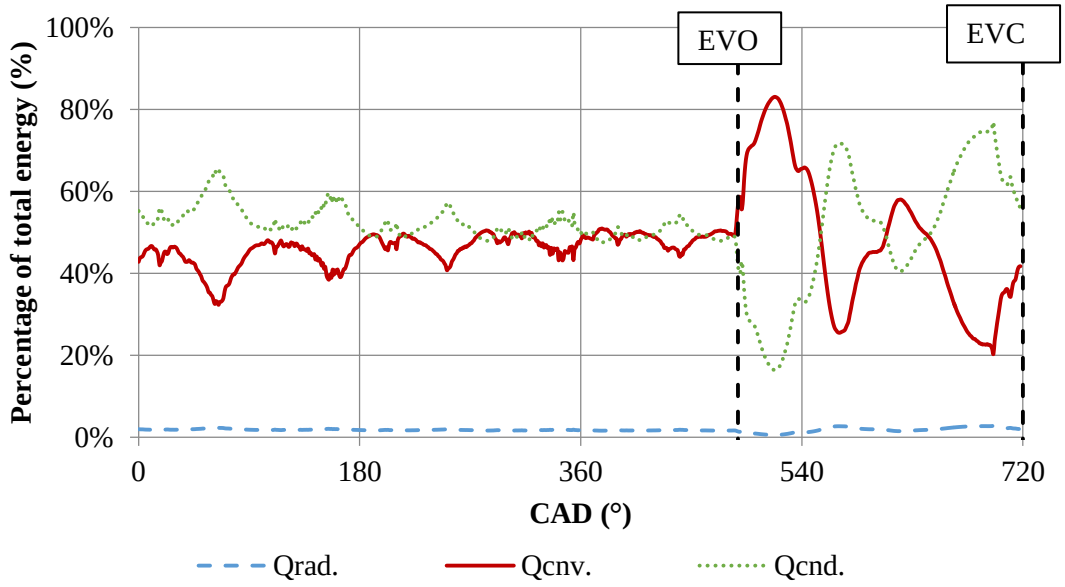

Figure 5.10: Relative contributions of heat transfer modes on the total energy of the T2 thermocouple junction during one cycle.

With respect to the sensor operation and the reported gas temperature three scenarios now exist:

1. the gas and sensor cool at the same rate
2. the gas cools faster than the sensor, in which case these gas and sensor temperatures will converge – which will tend to reduce the magnitude of the

convection term and relatively increase the magnitude of the conduction and radiation term as is seen in Figure 5.9 to be the case for the reference thermocouple

3. the sensor cools faster than the gas – increasing the magnitude of the convection term and reducing the relative magnitude of the conduction term as is shown to be the case for the T2 thermocouple in Figure 5.10.

Referring back to Figure 5.8, it is clear that the temperature of the T2 thermocouple is reducing at a faster rate than the gas temperature during the EVC period. This indicates that the T2 thermocouple loses heat more readily (despite the conduction term being of similar magnitude to the reference thermocouple during EVC) due to its lower thermal mass. The compounded effects of lower thermal inertia and conduction losses then explain the lower time-average temperature of the fine-wire thermocouples, summarised in Figure 5.11, compared to the reference thermocouple that has been observed experimentally (Figure 5.1 and Figure 5.2).

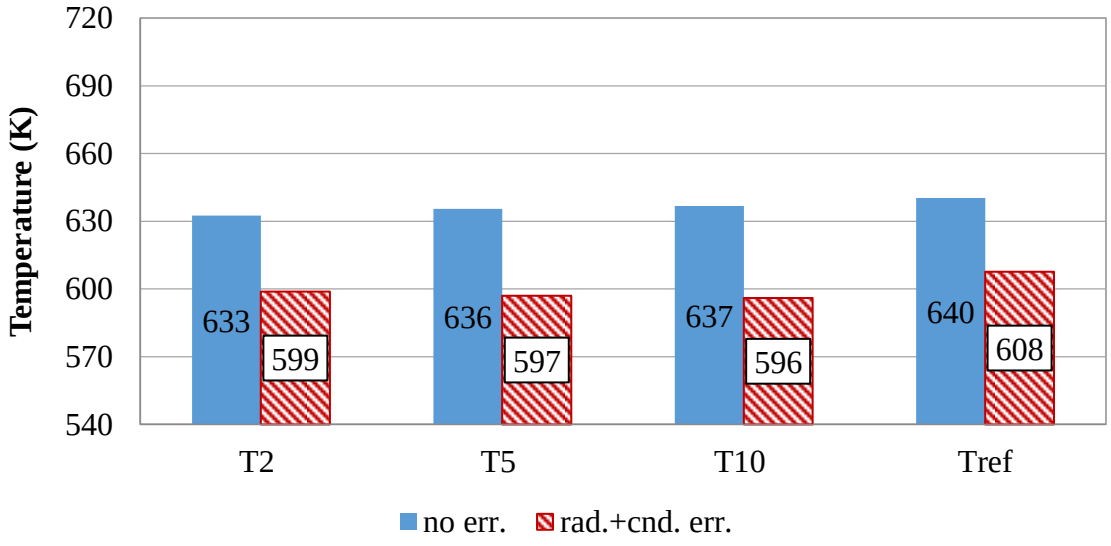

Figure 5.11: Simulation results of conduction and radiation error effects on time-average temperatures for all thermocouple sizes at the 1500 rpm/6.8bar nIMEP condition. Constant wall temperature, $T_w = 509$ K.

5.4 Chapter summary

Detailed experimental and modelling work have been carried out to identify the response of different thermocouple sizes on the temperature measurement of unsteady flows, along with their resulting measurement errors. As such, a standard 3 mm sheathed thermocouple used as a reference sensor, was installed on the exhaust manifold of an ICE along with three fine-wire thermocouples of varying diameter and tested under two different speed/load conditions.

The experimental results show that the measured time-average exhaust temperature is dependent on the sensor size, with the smaller thermocouples indicating a lower average temperature for the two speed/load conditions tested. Subject to operating conditions, measurement discrepancies of up to ~80 K have been observed between the different thermocouples used. Thermocouple modelling supports the experimental trends and shows that the effect of conduction is inversely proportional to the thermocouple junction size–an effect attributed to changes in the thermal inertia of the device. This conduction error is not typically considered in the literature for exhaust gas temperature measurement. Modelling results also show that radiative heat transfer is small compared to the effect of conduction with radiation errors being more pronounced for the 3 mm thermocouple. More specifically, the model results show that:

1. Radiation error is not important for EGT when using fine-wire thermocouples based on the conditions tested here
2. Conduction error has a significant effect on the measurement of unsteady temperatures
3. The effect of conduction error has a more pronounced effect on the fine-wire thermocouples due to their lower thermal mass as they can lose heat more readily.

4. When fine-wire thermocouples are used for time-average temperature measurements of unsteady flows they will indicate a lower temperature compared to a sheathed thermocouple due to the compounded effects of conduction error and lower thermal mass.

Nevertheless, it is recognised that the faster transient response of the fine-wire devices does offer the potential of recovering the instantaneous exhaust gas temperature and hence, the correct mass-averaged exhaust enthalpy. Consequently, any technique employed to recover the instantaneous exhaust gas temperature, should also be taking into account the effects of conduction. The following chapter presents the results of the temperature reconstruction technique introduced in Chapter 3, and highlights the differences between the time-average and mass-average exhaust enthalpy on the energy balance analysis.

6 Temperature reconstruction

The results presented in the previous chapter indicate clearly that even the smallest thermocouple will introduce some dynamic error due to its thermal inertia. Further to this, conduction and radiation effects were also shown to introduce further measurements errors. Chapter 3 has already introduced a dual probe technique that can recover the "true" gas temperature, using the signal of two different size thermocouple sensors. When the "true" gas temperature signal is used in combination with the instantaneous exhaust mass flow rate the mass-average exhaust enthalpy can be estimated. This has been shown to be much higher than the widely used time-average enthalpy measured with standard sheathed thermocouples. Consequently, mass-average enthalpy has the scope to improve the accuracy of the first law analysis. This chapter presents the results of the temperature reconstruction method and the effect of mass-average exhaust enthalpy on the energy balance results.

6.1 Introduction

The equations behind the temperature reconstruction method used in this work have already been presented in Chapter 3. Considering that the "true" exhaust temperature is unknown, the effectiveness of the reconstruction method presented here was measured against an exhaust temperature profile, which has been modelled in a 1-D numerical simulation. The reconstructed thermocouple time-constants were evaluated against the results of the lumped capacitance model, which were treated as a reference. The accuracy of the reconstruction method and the effects of the averaging methods have been assessed by taking the thermocouple signals, comprising the fine-wire thermocouple probe (i.e. T2,

T5 and T10 thermocouples), modelled by Equation (3.25) and attempting to reconstruct the gas temperature provided by the 1-D model.

Prior results have shown that the reconstruction method requires the dynamic response of the thermocouple pair used to be sufficiently different, so that at least one thermocouple can capture the necessary flow information. Tagawa *et al.* [141] recommended a diameter ratio, for the thermocouple pair, between 2-3 for a successful reconstruction since this provides sufficiently different response without a significant compromise on temporal resolution. It is also expected that thermocouples with higher temporal resolution, due to their lower thermal mass, are expected to provide a more accurate reconstruction as they can follow the temperature fluctuations much closer.

It is recalled that the thermocouple probe is comprised of three thermocouples – the diameter ratio for every combination of thermocouple pairs is within the range specified by Tagawa *et al.* [141] – where the reconstruction results from the combination of the different junction pairs could be used as a way to validate the temperature reconstruction method when the true gas temperature is not known. The reconstruction method was validated under two test cases, with the simulated exhaust temperature profiles used corresponding to the engine conditions shown in Table 5.1.

Figure 6.1 shows the reconstructed time-constants for the 1500rpm/6.8bar nIMEP conditions, where each thermocouple time-constant is calculated twice, since these are the possible thermocouple combinations with the thermocouple probe employed. The dark grey line indicates the true time-constants as calculated in the lumped capacitance model. The error bands on the true-time constant are associated with the uncertainties in the Nusselt number correlation which in this case are ~25% [91]. The numbers in brackets indicate the thermocouple pair combination, with the number indicating the junction size

in thousands of an inch. The observed undulations on the true time-constants are linked to the pressure pulses found in the exhaust of the engine and captured by the exhaust pressure transducer; a measurement that is used as a boundary condition in the 1-D numerical model used to provide the true gas temperature profile.

The time-constant is known to increase with the size of the thermocouple a trend that is captured by the reconstruction method, with the T2 thermocouple having the smallest time-constant and the T10 thermocouple having the highest. Overall the calculated time-constants agree well with the true values irrespective of junction size and pair combination, especially during the period where the exhaust valves are closed (i.e. 0-488 CAD). During the EVO period, however, the accuracy of the reconstructed time-constants is driven by the junction pair combination. More specifically, time-constants calculated using the T5 and T10 thermocouples (i.e. Figure 6.1b and 1c) result in notable deviations from the true values, both in terms of time shift and magnitude. This is attributed to the slower response of both thermocouples and their reduced temporal resolution.

Apart from the obvious effects of this phase delay on the reconstructed temperature, the smaller time-constants predicted with the 5/10 pair will under-predict the dynamic error of the sensor and will thus result in an under-prediction of the true gas temperature. Both of these points will result in a lower estimation of the exhaust enthalpy. On the other hand, reconstruction results using the T2 thermocouple, do not show similar discrepancies, irrespective of the size of the second junction. This can be due to the fact that the T2 thermocouple “carries” enough information to compensate for the negative effects introduced by the T5 and T10 thermocouples in terms of temporal resolution.

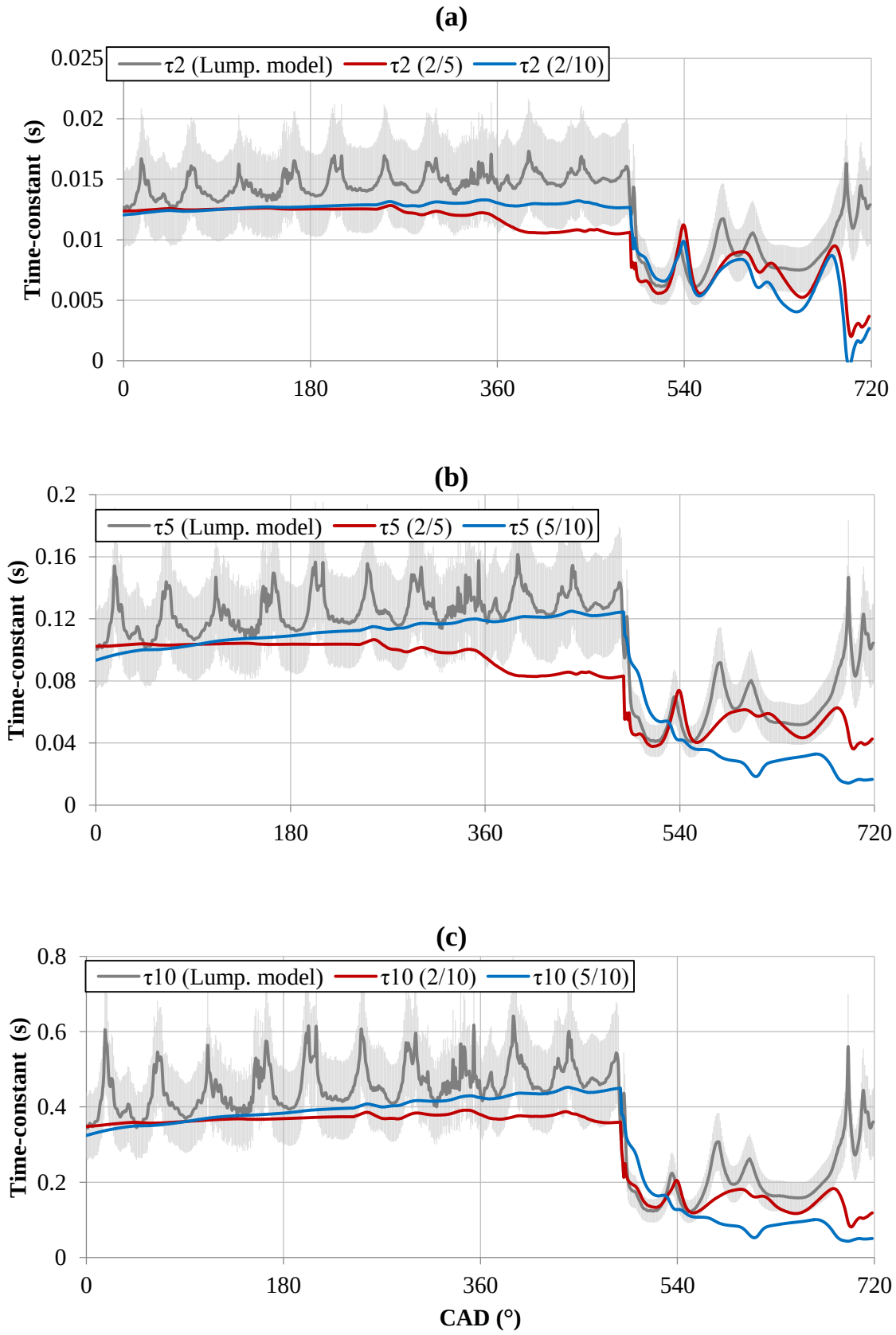

Figure 6.1: Typical time-constant estimation for different size thermocouples using different pair combinations. The dark grey line indicates the "true" time-constant and the light grey band the error ascociated with the Nusselt number correlation used.

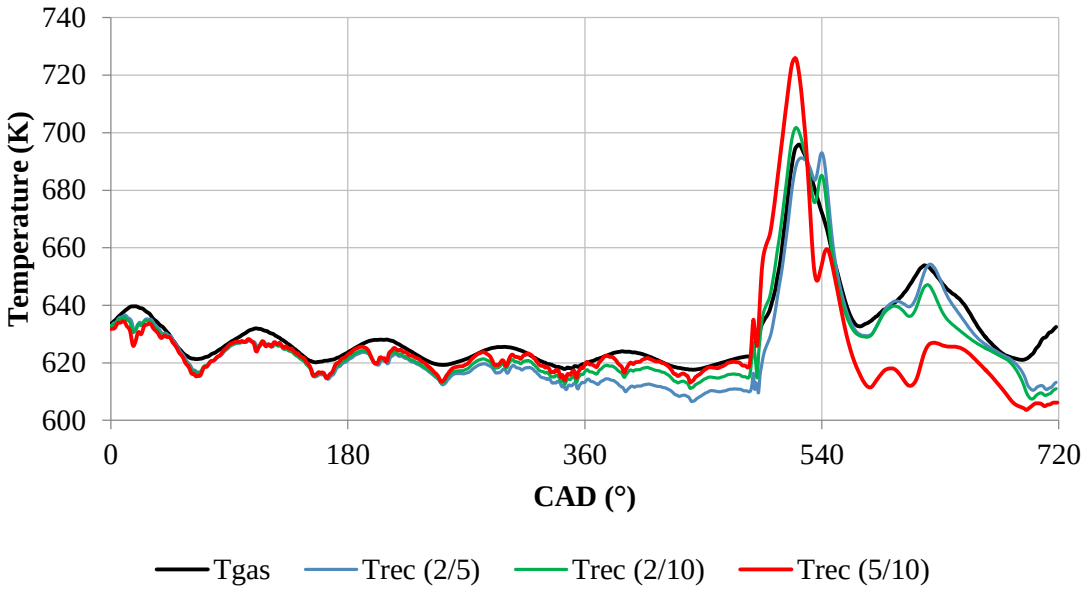

Figure 6.2: Typical temperature reconstruction results using different thermocouple pair combinations. The black line indicates the true gas temperature.

The effect of different thermocouple pair combinations on temperature reconstruction can be seen in Figure 6.2, where the black line indicates the true gas temperature as provided from the 1-D simulations. The results show that when the T2 thermocouple is part of the thermocouple pair, the temperature reconstruction is in closer agreement to the true gas temperature, a result also reflected by the reconstructed time-constants presented in Figure 6.1. Equally, the discrepancies observed in Figure 6.1b and c in terms of time-constant prediction, when the T5 and T10 thermocouples where used, can also be seen in the reconstructed signals (red line in Figure 6.2). More specifically, the over-prediction in the time-constant values seen around 500 CAD in Figure 6.1 1b and c is translated, according to Equation (3.27), to an over-prediction in peak temperature and similarly, the under-prediction in time-constants around 610 CAD, is resulting in a temperature under prediction of ~25 K.

Figure 6.1 and Figure 6.2 thus show that when the 5/10 pair is used the accuracy of the reconstruction is reduced, despite the potential benefits that these thermocouples would offer in terms of service-life due to their bigger size. It is also noted that similar trends were observed at the higher load/speed conditions. Consequently, the reconstruction results presented form this point onwards will be using the 2/5 pair. The following section will present the results of the reconstruction method starting with the results of Equation (3.27) and then followed by the results of Equation (3.30), which is taking into account the effects of conduction and radiation.

6.2 Temperature reconstruction – No conduction and radiation error

The reconstruction method was first validated, by ignoring the effects of conduction and radiation. This was done in order to evaluate the performance of the exponential moving average process during the EVO period, which is essentially what separates this method from the one introduced by Tagawa *et al* [141]. It is recalled that the value of the parameter ζ, i.e. the amount of exponential averaging imposed, was set to $\zeta = 0.08$ as this value was found to provide the best compromise between temporal resolution and non-negative time-constant values for the T2/T5 thermocouple combination. It is acknowledged that this parameter might require readjustment depending on the flow conditions, however, for the two conditions presented here the value of ζ remained constant.

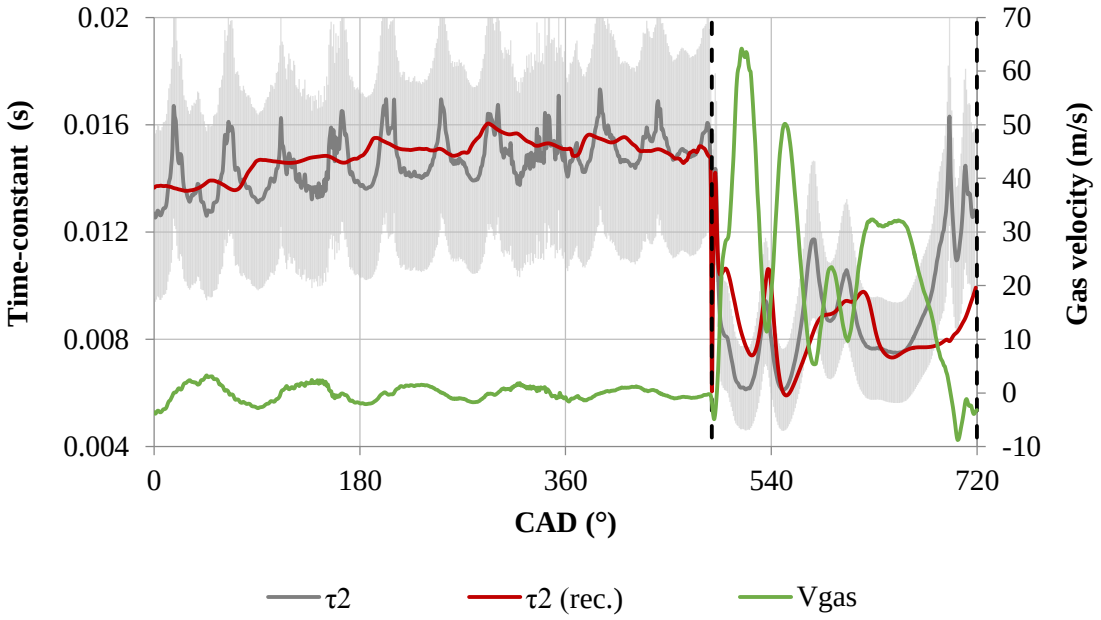

Figure 6.3: Reconstructed time-constant for the T2 thermocouple for the 1500rpm/6.8 bar nIMEP case (Equation (3.28)). The solid grey line indicates the true time-constant values as calculated from the lumped capacitance model. The error bands indicate the error associated with the true time-constant due to the Nusselt number correlation used.

Figure 6.3 shows the calculated time-constant (τ_{rec}) for the T2 thermocouple according to Equation (3.28). The solid line represents the "true" time-constant as calculated from the lumped capacitance model and the green line indicates the 1-D exhaust gas velocity. For the EVC period the reconstructed time-constant follows the true value well, however without capturing the peaks and troughs due to averaging. At the time of the EVO, a sudden drop in the time-constant is observed, which is in agreement with the fast moving gases and the high heat transfer coefficient values during blowdown, reaching a minimum value of ~6 ms. At around 580 CAD the time-constant reaches a local maximum before starting to reduce again, indicating the second part of the EVO event, where the gases are being pushed out of the cylinder due to the piston movement. The erratic behaviour observed at the end of the cycle prior to EVC is due to gas flow-reversal and it is an artefact of the 1-D model, as can be seen from the profile of the exhaust gas velocity. In general, the reconstructed time-constant follows the rapid changes during the EVO

period, with a small discrepancy observed during the point of expected maximum temperature (i.e. 528 CAD). The reconstructed time-constant for the T5 thermocouple is a similarly good match to the "true" value.

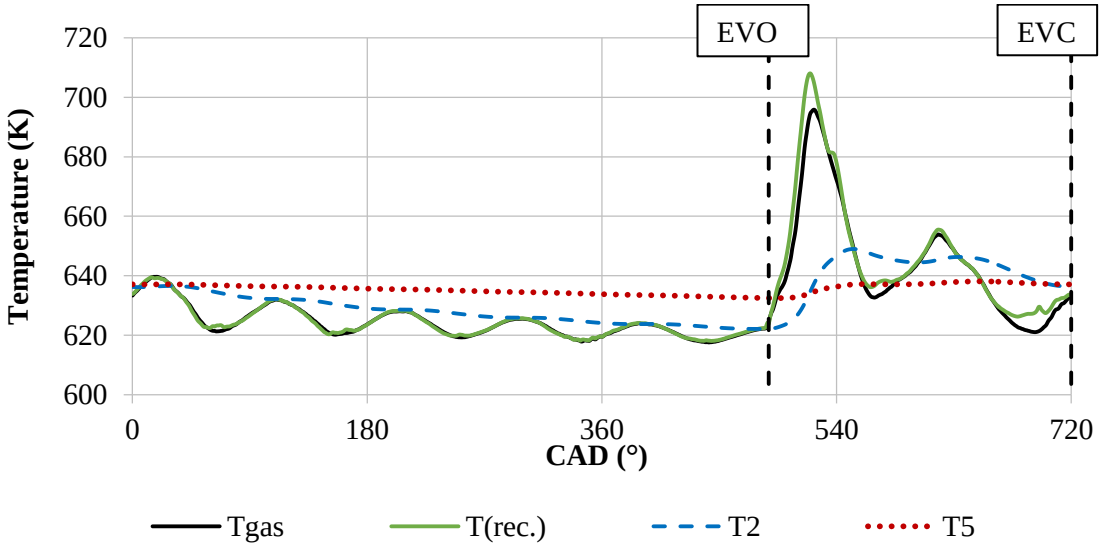

Figure 6.4: Reconstructed gas temperature for the 1500rpm/6.8 bar nIMEP case (Equation (3.27)). The black line indicates the gas temperature from the 1-D model.

Figure 6.4 shows the results of the resultant temperature reconstruction for the 1500 rpm/6.8 bar nIMEP case. The dashed and dotted lines represent the T2 and the T5 thermocouples respectively. During the EVC event the reconstructed temperature is line-on-line with the 1-D model results, which indicates that the choice of a large window size due to the slow gas dynamics for this period is justified. Good agreement is also observed during the EVO period, albeit with a ~1.5% over-prediction in peak temperature. This is attributed to the larger time-constant estimated at this point (Figure 6.1) which consequently leads to a larger dynamic error compensation according to Equation (3.27). Similar results were also observed for the 1750 rpm/13.5 bar nIMEP case however, the discrepancy in peak temperature, under these conditions, was ~2%. These results can be seen in Figure 6.5 below.

The results presented in Figure 6.4 and Figure 6.5 then show that the reconstruction method introduced can predict the true gas temperature sufficiently well, especially during the EVO period, which is of high interest since during this event the residual thermal energy in the cylinder is transferred to the exhaust. Following the findings of the previous chapter, where the importance of conduction error on temperature measurement was highlighted, a complete method that corrects for the errors arising in the measurement of unsteady flows, needs to address the effects of conduction and radiation as well. The following section presents these results, based on Equations (3.30) and (3.34).

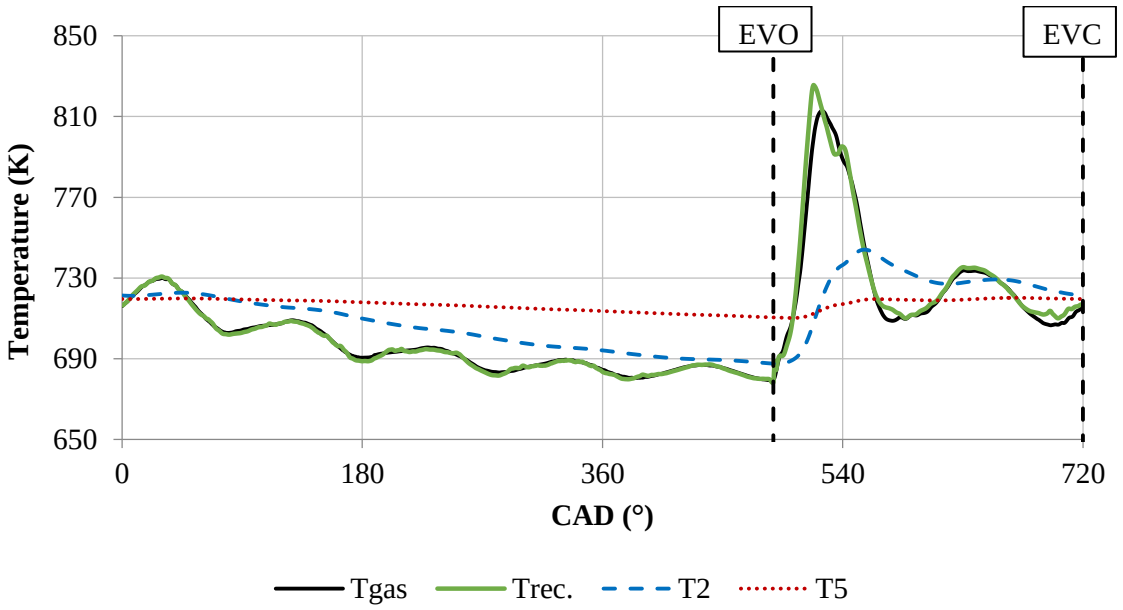

Figure 6.5: Reconstructed gas temperature for the 1750rpm/13.5 bar nIMEP case (Equation (3.27)). The black line indicates the gas temperature from the 1-D model.

6.3 Temperature reconstruction – With conduction and radiation error

The combined effects of conduction and radiation are expected to affect the thermocouple response during the cycle, as the cooling/heating rates of the junction will change due to the additional energy transfer terms considered—when conduction and radiation are not considered in the model the junction is losing energy due to convection to the cooler gas during the EVC period. The reconstruction method thus needs to be capable of capturing this change in response, on top of the effects introduced by the thermocouple's thermal mass—it is recalled that this is accounted for mathematically using the term C as shown in Equation (3.30). It should be noted that for the work presented here the true time-constant is not expected to change by incorporating the effects of conduction and radiation as the properties of the thermocouple have been taken to be independent of temperature and thus a reduction in junction surface temperature will have no effect. Therefore, any change in the true time-constant will be due to changes in exhaust gas velocity.

The reconstructed time-constants, including conduction and radiation errors (i.e. Equation (3.34)), for the T2 thermocouple, under the 1500rpm/6.8bar nIMEP and the 1750rpm/13.5bar nIMEP conditions, can be seen in Figure 6.6 and Figure 6.7 respectively (red line). The reconstructed time-constants ignoring conduction and radiation error (i.e. Equation (3.28)) are also plotted for comparison (blue dotted line). For the lower speed/load case the reconstructed time-constants agree well with the true values throughout the cycle independent of the effects of conduction and radiation. It can also be seen that for the EVC duration, the effect of conduction and radiation is to reduce the value of the time-constant. This is expected as conduction and radiation will increase the rate of change in temperature (in this case a reduction) which according to Equation (3.30), results in a smaller time-constant. During the EVO event, a similarly good

agreement is observed in the reconstructed time-constants, irrespective of conduction and radiation effects, except from a discrepancy observed at ~710 CAD, when conduction and radiation is considered. This is thought to be a result of the rapid change in flow conditions observed at this point (Figure 6.3, an undesirable artefact of the averaging process. A lower value of ζ is expected to improve this discrepancy but with a loss of accuracy at earlier stages of the EVO event, which is not desirable, since this is when peak mass flow rates are occurring and consequently which has the biggest effect on mass-average exhaust enthalpy. Similar results were also observed for the T5 thermocouple and are thus not presented here.

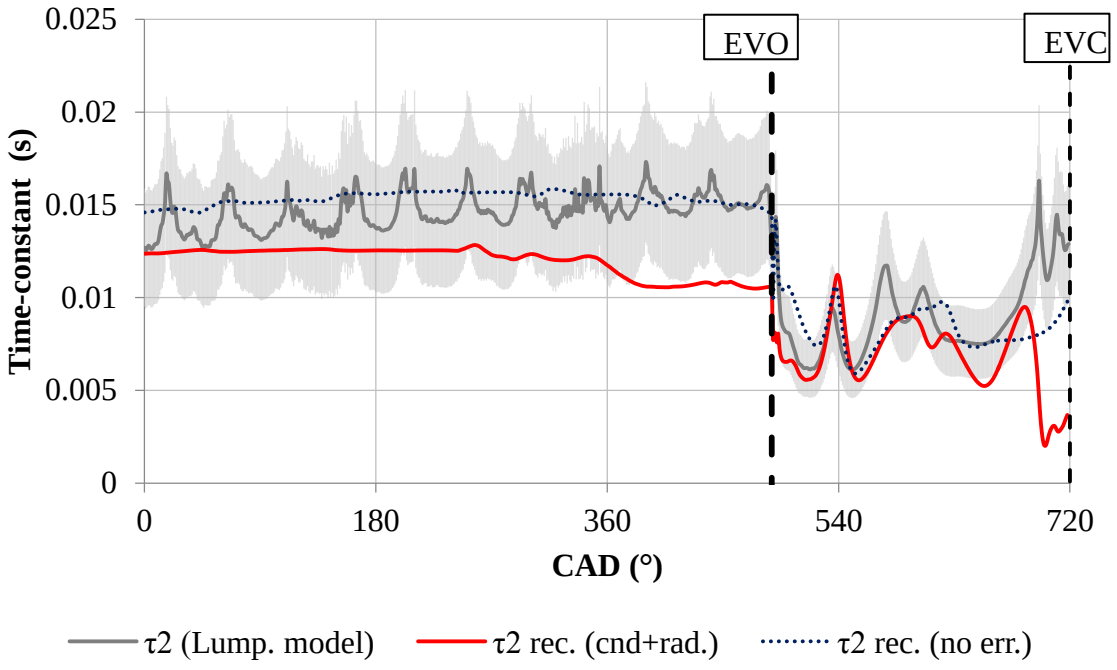

Figure 6.6: Time-constant reconstructed values for the T2 thermocouple under the 1500rpm/6.8bar nIMEP case (Equation (3.34)).The dotted line indicates the reconstructed time-constant ignoring conduction and radiation errors (Equation (3.28)). The solid grey line indicates the true time-constant and the error bands the uncertainty associated with the Nusselt number correlation used.

Under the higher speed/load conditions, the time-constant is reduced, in agreement with the increased heat transfer coefficient, associated with the higher exhaust gas velocities.

The agreement with the true values is equally good to the lower speed/load case, with the effects of averaging being responsible for the deviations observed during the EVO period. Again, the effect of conduction and radiation results in a lower time-constant value during the EVC period as already seen for the lower speed/load conditions. When the valves are open, the time-constants including the effects of conduction and radiation, present generally good agreement during this event. A similar under-prediction to the 1500rpm/6.8bar nIMEP case is also observed around 710 CAD. The effects of averaging are more prevalent under these conditions as the velocity of the gases and the changes in temperature are increased. This is more profound for the case where conduction and radiation effects are not taken into account, where the reconstructed time-constant is taking negative values at the time of EVO. This is obviously not possible and the temperature reconstruction results at this point should not be trusted. Again, this indicates the compromise necessary on the averaging process; less averaging increases the temporal resolution but can result in negative time-constant and vice-versa.

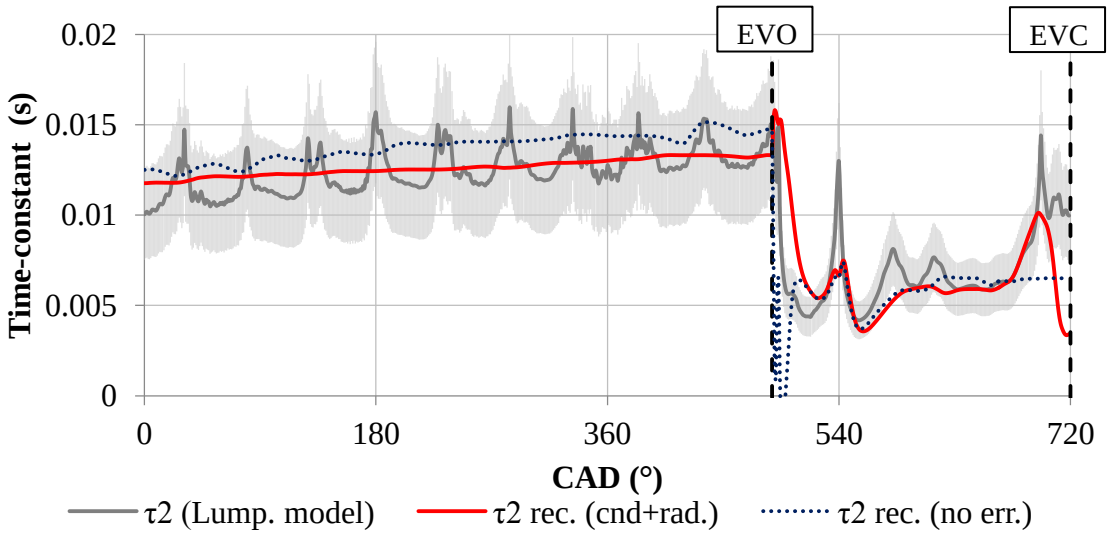

Figure 6.7: Time-constant reconstructed values for the T2 thermocouple under the 1750rpm/13.5bar nIMEP case (Equation (3.34)). The dotted line indicates the reconstructed time-constant ignoring conduction and radiation errors (Equation (3.28)). The solid grey line indicates the true time-constant and the error bands the uncertainty associated with the Nusselt number correlation used.

The temperature reconstruction results, including conduction and radiation effects, for the two speed/load conditions can be seen in Figure 6.8 and Figure 6.9. Following the good agreement observed with the time constants, the reconstructed temperature shows equally good agreement to the true values, independent of load/speed condition. Comparing the two graphs it is immediately clear that the effects of conduction are more pronounced under the 1500rpm/6.8bar nIMEP case. Despite the higher temperature gradient between the gas and the wall at higher speed/load conditions, 390 K compared to 357 K under the lower speed/load, the peak temperature and the EVO frequency are increased which results in a reduction in energy losses during the EVC period and therefore to a higher indicated temperature. This would perhaps indicate that at even higher load/speed conditions the effect of conduction reduces further.

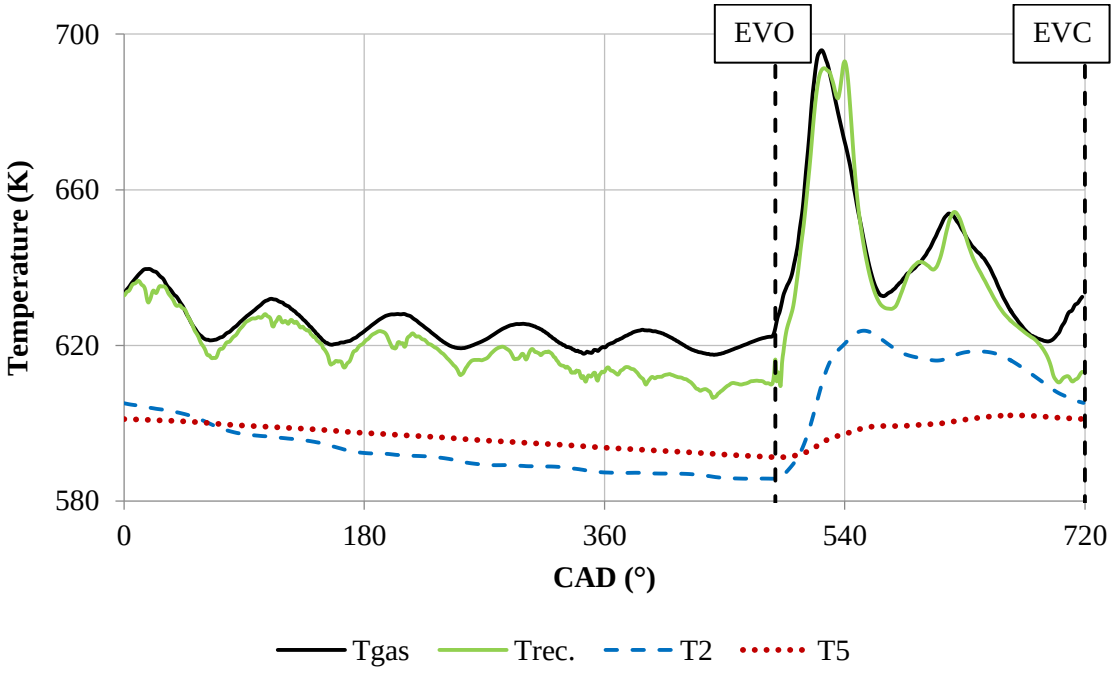

Figure 6.8: Temperature reconstruction results including conduction and radiation error for the 1500rpm/6.8 bar nIMEP case (Equation (3.30)). The black line indicates the true gas temperature and the green line the reconstructed results. The blue and red lines show the thermocouple signals used for the reconstruction. $T_w = 509\ K$.

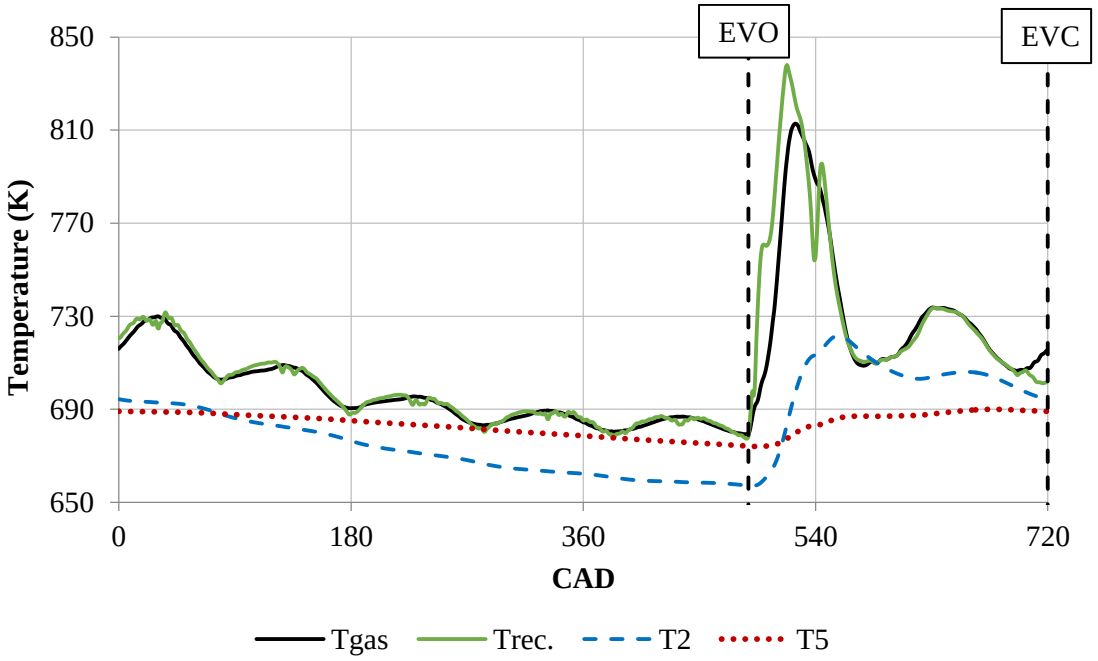

Figure 6.9: Temperature reconstruction results including conduction and radiation error for the 1750rpm/13.5 bar nIMEP case (Equation (3.30)). The black line indicates the true gas temperature and the green line the reconstructed results. The blue and red lines show the thermocouple signals used for the reconstruction.$T_w = 589\ K$.

As already observed, any discrepancies in the reconstructed temperatures are due to deviations in the reconstructed time-constants. More specifically, the under-prediction in the reconsutructed time-constants, presented in Figure 6.6 and Figure 6.7, around 710 CAD is translated in a lower reconstructed temperature at that point. However, in terms of exhaust enthalpy estimation, this is not expected to affect the results significantly as the mass-flow rates at this point are approaching zero (Figure 6.3). The higher dicrepancy during the EVO period is observed for the higher speed/load case and is attributed to the over-prediction of the time-consant at ~525 CAD (Figure 6.7) which indicates a higher dynamic error that the reconstruction method is consequently overcompensating. However, these disrcepancies are translated to a maximum temperature deviation of 0.2%, for the 1500 rpm/6.8 bar nIMEP case, and 3%, for the 1750rpm/13.5 bar nIMEP case. These results are significant considering that the maximum temperature error is

reduced by 12 and 14 percentage points under the higher and lower load conditions respectively. Being able to recover the true gas temperature from thermocouple signals allows, with knowledge of the instantaneous mass flow rate, for the estimation of the mass-average exhaust enthalpy as shown by Equation (1.20). The following section will present and compare first the mass and time-average enthalpies and then their effect on the energy balance calculation.

6.4 Mass-average exhaust enthalpy flow calculation

The previous section has shown how the exhaust temperature measurement can be under predicted when the signal from temperature sensors is not corrected for the inherent dynamic, conduction and radiation errors associated with the measurement process. It is also recalled that an enthalpic, or mass-average basis for the exhaust temperature results in a more accurate estimation of the exhaust thermal energy during the cycle [103].

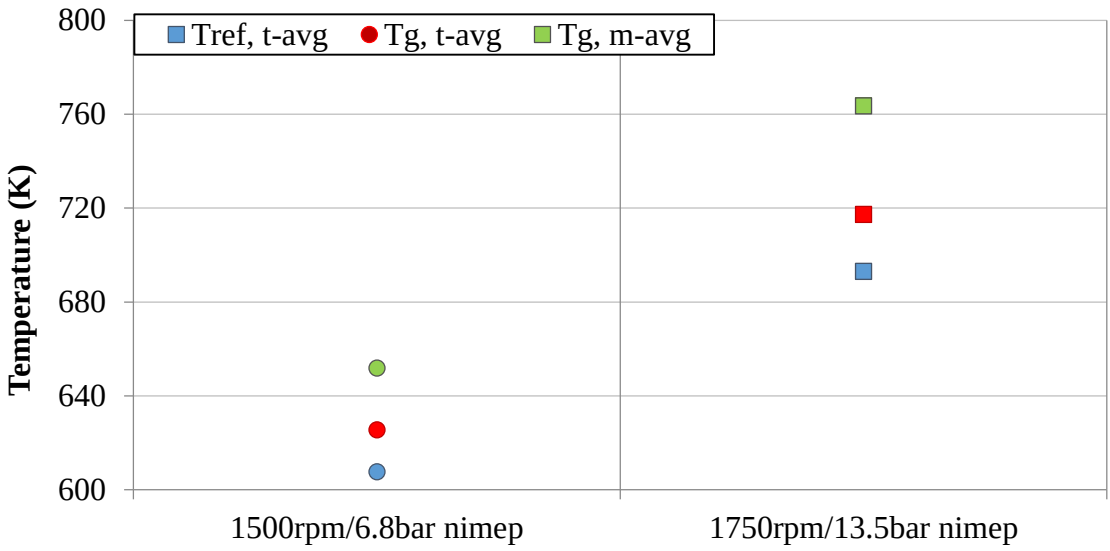

Figure 6.10: Average exhaust temperatures calculated on a different basis. The red colour indicates the time-average temperature (Equation (1.18)) and the green colour the mass-average temperature (Equation (1.21)). The blue colour indicates a typical temperature reading using a 3mm sheathed thermocouple.

Figure 6.10 shows a comparison of average exhaust temperatures, calculated on a different basis for the two speed/load conditions presented above. The red and green markers represent the time-average (Equation (1.18)) and mass-average (Equation (1.21)) temperatures and the blue colour represents a typical temperature reading using a standard 3 mm sheathed thermocouple. Equations 1.18 and 1.21 are presented again below to assist the reader.

$$\overline{T}_{exh} = \int_{0}^{720} T_{exh}\, d\theta \Big/ \int_{0}^{720} d\theta \tag{1.18}$$

$$\widehat{T_{exh}} = \int_{EVO}^{EVC} \dot{m}_{exh}(\theta) T_{exh}\, d\theta \Big/ \int_{EVO}^{EVC} \dot{m}_{exh}(\theta) d\theta \tag{1.21}$$

where it is recalled that the $\dot{m}(\theta)_{exh}$ term is the instantaneous exhaust mass-flow rate.

As expected, the thermocouple reading is the lowest due to the measurement errors discussed previously. What is interesting to note however, is the significant difference between the time and mass-average temperatures which are as high as 40 K at the higher load conditions (~5%). Considering a typical exhaust temperature profile (e.g. Figure 6.9), a time averaging process over the whole cycle will tend to be skewed by the lower temperatures observed during the EVC event, thus resulting in an under-prediction of the time average temperature. Note that this will be true even if the true gas temperature is known (e.g. red markers in Figure 6.10). On the other hand, weighting the measured temperature in terms of the mass flow rate, accounts only for the thermal energy escaping the cylinder during the EVO event, thus providing a more accurate measure of the average temperature during the cycle.

The effect of using a mass-average temperature on the calculated exhaust enthalpy can be seen in Figure 6.11 for the two speed/load conditions presented above. The time-average enthalpy is calculated using Equation (1.17), and the mass-average enthalpy using Equation (1.20), which are again presented below to assist the reader.

$$\overline{\dot{Q}}_{exh} = \overline{\dot{m}}_{exh} c_p \left(\overline{T}_{exh} - T_0\right) \tag{1.17}$$

$$\hat{\dot{Q}}_{exh} = \overline{\dot{m}}_{exh} c_p \left(\hat{T}_{exh} - T_0\right) \tag{1.20}$$

These results show that the exhaust enthalpy is increased by 15% and18%, for the low and high load cases respectively, when calculated on a mass-average basis. When this increase is considered into the first law analysis, an increase of ~5 percentage points in normalised exhaust energy is observed, as can be seen in Figure 6.12 and Figure 6.13. This consequently reduces the extraneous losses by the same amount which reduces the uncertainty associated with the first law analysis model.

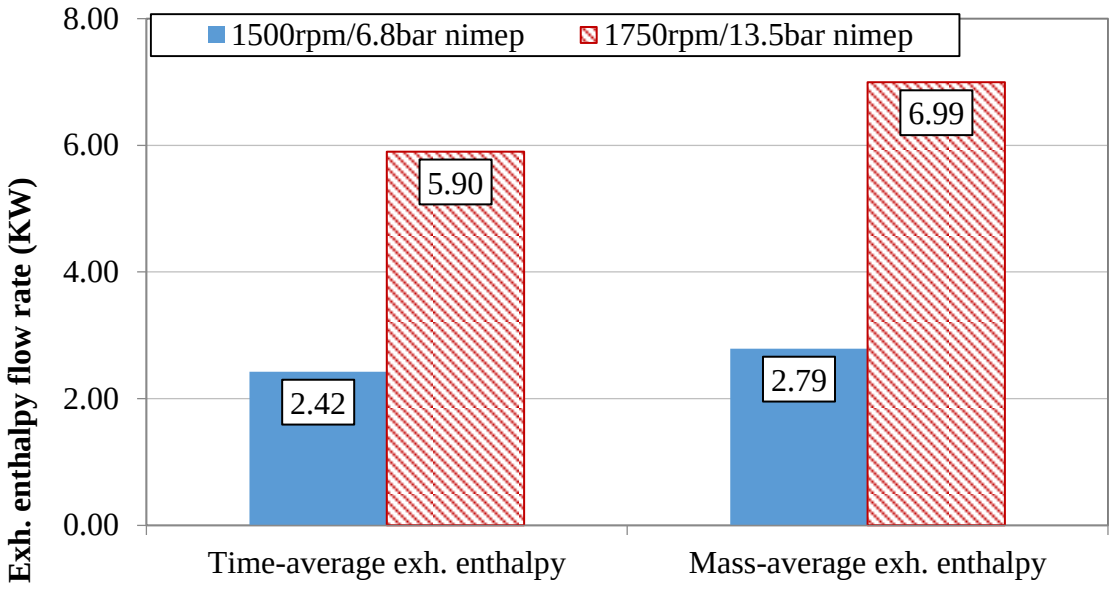

Figure 6.11: Comparison of time (Equation (1.17)) and mass-average (Equation (1.20)) exhaust enthalpy flow rate under two speed/load conditions.

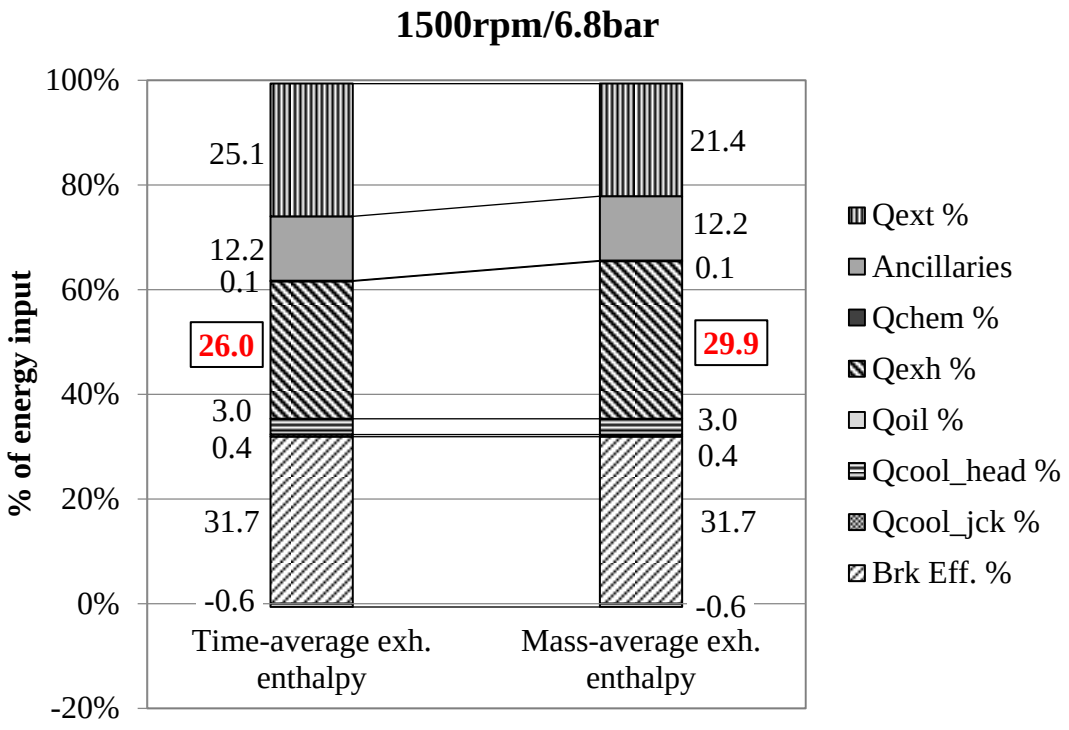

Figure 6.12: Effect of mass-average exhaust enthalpy on energy balance results for the 1500rpm/6.8bar nIMEP case.

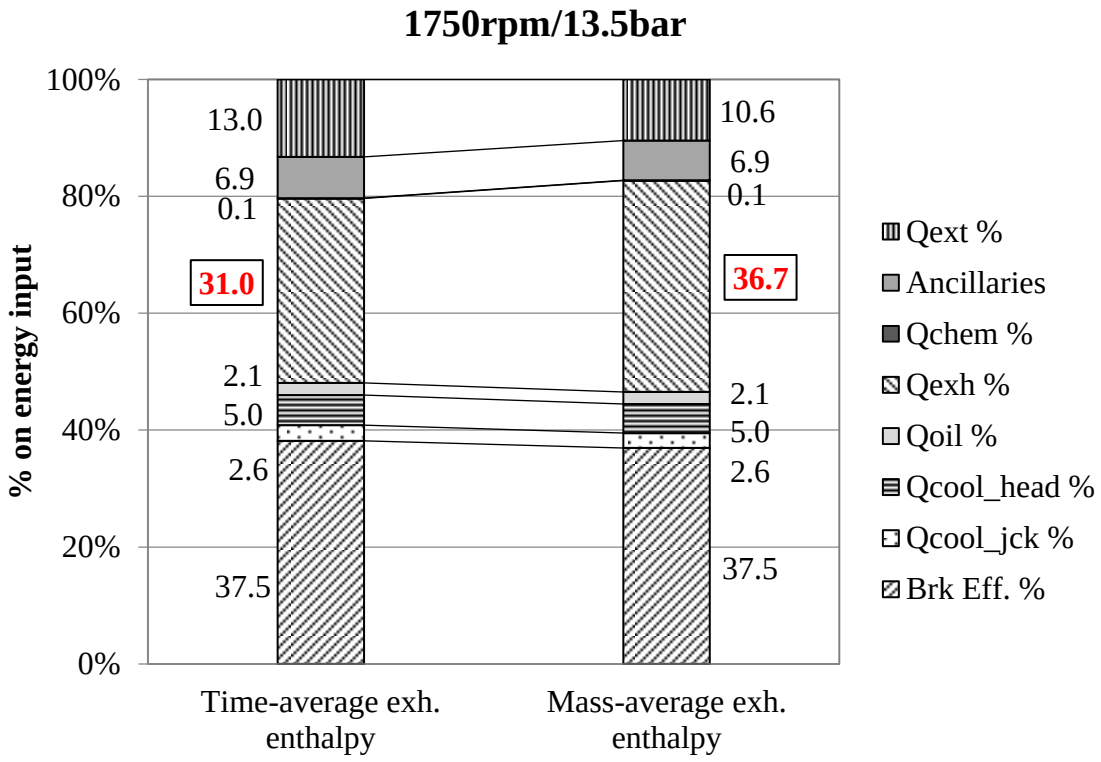

Figure 6.13: Effect of mass-average exhaust enthalpy on energy balance results for the 1750rpm/13.5bar nIMEP case.

These findings are important since they indicate that common measurement practises can lead to misleading observations. An indication of true exhaust temperature, using the reconstruction method presented above, despite providing an accurate indication of the instantaneous temperature during the cycle can still result in an under prediction of exhaust enthalpy flow, if calculated on time-average terms. A mass-average calculation alleviates these issues. However, it is acknowledged that an indication of instantaneous mass-flow rate is usually only available through numerical simulation and as such, on-engine applications might require the use of time-average terms. This work informs on the expected magnitude of error in such applications.

6.5 Summary

This section presented the results of the proposed temperature reconstruction method and the effects that this has on the calculated exhaust enthalpy. The method was validated under two speed/load conditions against 1-D simulation temperature profiles. The effect of conduction and radiation errors were initially ignored to assess the effectiveness of the exponential averaging technique during the EVO period. Upon successful application of this technique conduction and radiation were also considered. Overall, the temperature reconstruction method put forward predicts the true gas temperature very well, throughout the cycle and for both speed/load conditions. Application of this method reduces the maximum temperature error by as much as 14 percentage points. This chapter has also shown that even if we have knowledge of the true gas temperature, estimating the average temperature during the cycle on a time-average basis results in an under prediction of ~40 K compared to a mass-average basis. Finally, when this reconstructed temperature is used to estimate the mass-average enthalpy, an increase in the normalized exhaust energy of 5 percentage points was observed which reduces the extraneous losses and increases the accuracy of the first law analysis applied on the engine.

7 Conclusions and further work

7.1 Conclusions

Diesels still offer an advantage on fuel efficiency over gasoline engines and are expected to play an important role in helping automotive manufacturers meet the upcoming emission legislation limits. Understanding and being able to accurately measure where the chemical energy from the combustion process is transferred is an important step in furthering these efficiency advantages and assisting in the future development of diesels. A common tool used to identify the various energy transfer terms is the first law analysis. This work then focused on the development of a first law analysis tool along with the necessary instrumentation and methods to measure these energy transfer terms more accurately.

Two thermal studies have been carried out; the first looked into the effects of different EGR strategies on smoke emissions and efficiency and the second at the effects of different piston material on engine efficiency. The proposed EGR strategies did lead to a reduction in smoke emissions, but with a subsequent reduction in engine efficiency – due to increased pumping work and heat transfer losses – and an increase in NO_x emissions – due to the increased oxygen presence and faster burn rates observed. The steel piston operation resulted in an increase of ~0.5-1.3% in nisfc, depending on operating conditions. These improvements were attributed to faster burn rates and a reduction in blow-by losses, compared to the aluminium piston. Improvements in bsfc were also observed, most notably at lower load/speed conditions, and where of the order of 2%. Thus a steel piston design has the potential to assist automotive manufactures achieve their future efficiency goals.

Furthermore, the thermal studies carried out have shown that the energy transfer to the coolant and the exhaust enthalpy are responsible for ~30-45% of the total fuel energy. Consequently, a special effort was given in reducing the measurement uncertainty associated with these terms, which has the potential to better highlight improvements in thermal efficiency.

Two sets of differential thermocouples were developed and installed on the cooling lines of the engine to provide a more accurate measurement of the coolant energy transfer. Since the temperature differential between the inlet and the outlet lines is measured directly, rather than being inferred from two independent temperature readings, the measurement uncertainty is reduced. The use of these differential thermocouples reduced the measurement uncertainty to 0.05 K at the 95% confidence interval. However, despite the high accuracy of these sensors, it was found that under low load conditions, where the energy transfer to the coolant is small, 23 test repeats were found to be necessary in order to provide statistically significant comparisons. Consequently, the use of standard methods to estimate the energy transfer to the coolant is expected to increase both the measurement uncertainty as well as the overall testing time, since more repeats will be necessary to achieve similar levels of uncertainty.

Standard 3 mm sheathed thermocouples, commonly used in the measurement of exhaust temperature, are only capable of providing a time-average indication of exhaust temperature due to their thermal mass. This is known to result in a lower indicated temperature, thus resulting in an under-prediction of the exhaust enthalpy. In order to have the potential to recover the true exhaust gas temperature, a thermocouple probe comprising of three fine-wire thermocouples was built. The different size of the thermocouple junctions then allows the use of temperature reconstruction methods that

can correct for the measurement errors associated with unsteady flow temperature measurements.

Experimental results, using both the thermocouple probe and standard 3 mm sheathed thermocouple, have shown that the smaller size thermocouples consistently indicated a lower time-average exhaust temperature compared to the sheathed thermocouple by as much as ~80 K. These results were found to be counterintuitive as the fine-wire thermocouples were installed closer to the exhaust manifold of the engine.

Consequently, a lumped capacitance model was built to model the thermocouples' behaviour under unsteady flow conditions and help understand the findings of the experimental testing. This modelling work has shown that the observed experimental results are attributed to the combined effects of the lower thermal inertia of fine-wire thermocouples combined with the resulting conduction error along the thermocouple length. This is the first time that the importance of conduction error is highlighted for unsteady temperature measurements.

Being able to accurately measure the exhaust temperature and consequently the energy found in the exhaust, thus requires for the correction of the dynamic, conduction and radiation errors introduced by the temperature sensor. The temperature reconstruction method presented in this work does that. This technique uses the signal of two different size thermocouples to reconstruct the true exhaust gas temperature. The effectiveness of this method was tested using simulated signals, created using the lumped capacitance model, mentioned above. The proposed reconstruction method has been shown to predict the true gas temperature very well and reduce the maximum temperature error by 12% for the conditions tested. This method then has the potential to improve the accuracy of a first

law analysis as well as, the development of future turbocharger and exhaust after-treatment systems since a more accurate indication of temperature is available.

Finally, knowledge of the true exhaust temperature allows for the calculation of mass-average exhaust enthalpy. Calculating the exhaust enthalpy on a mass-average basis has been shown to provide a better estimate of the total energy found in the exhaust, compared to the commonly used time-average basis. More specifically, when the exhaust enthalpy was calculated using the mass-average approach an increase in the normalized exhaust energy of 5 percentage points was observed, based on the results of the thermal studies carried out.

Overall, this work has shown that the first law analysis method can be a very useful tool in the development of the future diesel and IC engines in general. However, high fidelity measurements are necessary to be able to identify statistically significant changes especially when the energy terms of interest are of very small magnitude. Failing to do so can result in masking important results due to measurement noise. The developed instrumentation and methods presented here, have provided significant insight into the effects that the measurement field can have on the output signal of the sensor and helped improve the measurement process by removing measurement errors. In turn, this increased the accuracy of the first law analysis model which reduced the extraneous losses thus reducing the overall uncertainty of the model.

7.2 Further work

7.2.1 Experimental equipment and methodology

Following the successful implementation of the differential thermocouples on the coolant lines, these could also be used in the estimation of the energy transfer to the oil. This is

expected to further increase the accuracy of the energy balance model thus giving a better estimate of the energy flows around the engine and reducing the uncertainty associated with the extraneous losses.

7.2.2 Numerical simulations and methodology

Taking into account the effect of temperature on the thermal properties of the thermocouple material would further improve the accuracy of the thermocouple model and also provide a better insight into the effects that temperature has on the sensor's time constant.

Further to this, it is acknowledged that the current approach on modelling conduction on the exhaust thermocouples is not taking into account the effects of the thermal boundary layer. This is expected to reduce the temperature gradient along the length of the thermocouple. Future work should look into the accurate modelling of conduction error.

Finally, drawing from the findings of Chapter 6, the effects of conduction error seem to reduce when the engine speed and load increases. Investigating further the operating conditions under which conduction error is significant will further expand on the understanding of the measurement process. It is also recognised that the frequency of the exhaust event will have an effect on the sensors' indicated temperature since the available time for cooling will change, which in turn will change the effect of conduction error. Simulated signals from a multi-cylinder engine are thus expected to highlight the importance of the findings in Chapter 6 and show if the effects of conduction are as pronounced as on a single-cylinder application.

7.2.3 Thermal studies

The subtle and confounded nature of some of the observed results, for the piston material study, is acknowledged. Future work should include the measurement of piston surfaces

temperatures or heat flux and the use of numerical simulations to help deconvolve the effects of blow-by and faster burn rates on the combustion process and thus provide a better understanding on how a steel piston configuration affects engine performance and efficiency.

7.2.4 Temperature reconstruction

The results of the proposed reconstruction method indicate that this technique offers a clear benefit when trying to estimate the exhaust enthalpy more accurately. Since this method was only validated with simulated thermocouple signals the next step would be to be used on experimental data. However, care should be taken as this technique is very sensitive to signal noise which can affect the reconstruction quality. Therefore, the best compromise between a clean signal and loss of signal information needs to be found with appropriate filtering.

8 References

1. Smith, M.N. *The number of cars is set to double by 2040*. 2016 [cited 2018 August 29]; Available from: https://www.weforum.org/agenda/2016/04/the-number-of-cars-worldwide-is-set-to-double-by-2040.
2. International Energy Agency, “Energy Technology Perspectives 2017”. 2017.
3. International Energy Agency, “World Energy Balances 2017”. 2017.
4. Mock, P., *European vehicle market statistics 2017/2018*. The International Council on Clean Transport. 28 November 2017. https://www.theicct.org/publications/european-vehicle-market-statistics-20172018
5. Tietge, U., *CO2 emissions from new passenger cars in the EU: Car manufacturers' performnace in 2017*. The International Council on Clean Transport. 11 July 2018, https://www.theicct.org/publications/co2-emissions-new-passenger-cars-eu-car-manufacturers-performance-2017
6. European Environmental Agency, *Monitoring of CO2 emissions from passenger cars – Regulation (EC) No 443/2009*. 11 April 2018. https://www.eea.europa.eu/data-and-maps/data/co2-cars-emission-14
7. Mock, P., *European vehicle market statistics 2016/2017*. The International Council on Clean Transport, 13 December 2016. https://www.theicct.org/publications/european-vehicle-market-statistics-20162017
8. Dec, J., "A Conceptual Model of DI Diesel Combustion Based on Laser-Sheet Imaging*," SAE Technical Paper 970873, 1997, https://doi.org/10.4271/970873.
9. Bergin, M., Reitz, R., Oh, S., Miles, P. et al., "Fuel Injection and Mean Swirl Effects on Combustion and Soot Formation in Heavy Duty Diesel Engines," SAE Technical Paper 2007-01-0912, 2007, https://doi.org/10.4271/2007-01-0912.
10. Miles, P., "The Influence of Swirl on HSDI Diesel Combustion at Moderate Speed and Load," SAE Technical Paper 2000-01-1829, 2000, https://doi.org/10.4271/2000-01-1829.
11. Flynn, P., Durrett, R., Hunter, G., zur Loye, A. et al., "Diesel Combustion: An Integrated View Combining Laser Diagnostics, Chemical Kinetics, And Empirical Validation," SAE Technical Paper 1999-01-0509, 1999, https://doi.org/10.4271/1999-01-0509.
12. Ehleskog, R., Ochoterena, R., and Andersson, S., "Effects of Multiple Injections on Engine-Out Emission Levels Including Particulate Mass from an HSDI Diesel Engine," SAE Technical Paper 2007-01-0910, 2007, https://doi.org/10.4271/2007-01-0910.
13. Mingfa, Y., Hu, W., Zunqing, Z., and Yan, Y., "Experimental Study of Multiple Injections and Coupling Effects of Multi-Injection and EGR in a HD Diesel Engine," SAE Technical Paper 2009-01-2807, 2009, https://doi.org/10.4271/2009-01-2807.
14. Ge-qun, S., Hai-qiao, W., and Rui, H., "The Transfer Function of Combustion Noise in DI-Diesel Engine," SAE Technical Paper 2005-01-2486, 2005, https://doi.org/10.4271/2005-01-2486.
15. Tousignant, T., Wellmann, T., Govindswamy, K., Heuer, S. et al., "Application of Combustion Sound Level (CSL) Analysis for Powertrain," SAE Technical Paper 2009-01-2168, 2009, https://doi.org/10.4271/2009-01-2168.

16. Han, Z., Uludogan, A., Hampson, G., and Reitz, R., "Mechanism of Soot and NOx Emission Reduction Using Multiple-injection in a Diesel Engine," SAE Technical Paper 960633, 1996, https://doi.org/10.4271/960633.
17. Ehleskog, R. and Ochoterena, R., "Soot Evolution in Multiple Injection Diesel Flames," SAE Technical Paper 2008-01-2470, 2008, https://doi.org/10.4271/2008-01-2470.
18. Gill, K., Marriner, C., Sison, K., and Zhao, H., "In-cylinder Studies of Multiple Diesel Fuel Injection in a Single Cylinder Optical Engine," SAE Technical Paper 2005-01-0915, 2005, https://doi.org/10.4271/2005-01-0915.
19. Montgomery, D. and Reitz, R., "Effects of Multiple Injections and Flexible Control of Boost and EGR on Emissions and Fuel Consumption of a Heavy-Duty Diesel Engine," SAE Technical Paper 2001-01-0195, 2001, https://doi.org/10.4271/2001-01-0195.
20. Kashdan, J., Anselmi, P., and Walter, B., "Advanced Injection Strategies for Controlling Low-Temperature Diesel Combustion and Emissions," *SAE Int. J. Engines* 2(1):1835-1856, 2009, https://doi.org/10.4271/2009-01-1962.
21. Pierpont, D., Montgomery, D., and Reitz, R., "Reducing Particulate and NOx Using Multiple Injections and EGR in a D.I. Diesel," SAE Technical Paper 950217, 1995, https://doi.org/10.4271/950217.
22. Pierpont, D., Montgomery, D., and Reitz, R., "Reducing Particulate and NOx Using Multiple Injections and EGR in a D.I. Diesel," SAE Technical Paper 950217, 1995, https://doi.org/10.4271/950217.
23. Nehmer, D. and Reitz, R., "Measurement of the Effect of Injection Rate and Split Injections on Diesel Engine Soot and NOx Emissions," SAE Technical Paper 940668, 1994, https://doi.org/10.4271/940668.
24. Romain, N. *Injection Pressure Evolution in Diesel engine*. 28 November 2013, Accessed: 28 August 2015; Available from: http://www.car-engineer.com/injection-pressure-evolution-diesel-engine/.
25. Pickett L. M., Siebers D L., "Soot in diesel fuel jets: effects of ambient temperature, ambient density, and injection pressure," Combustion and Flame, Volume 138, Issues 1–2, 2004, Pages 114-135, https://doi.org/10.1016/j.combustflame.2004.04.006.
26. Heywood, J.B., "Internal Combustion Engine Fundamentals". 1988, MacGraw-Hill
27. Hilliard, J. and Wheeler, R., "Nitrogen Dioxide in Engine Exhaust," SAE Technical Paper 790691, 1979, https://doi.org/10.4271/790691.
28. Merryman E. L., Levy A, "Nitrogen oxide formation in flames: The roles of NO2 and fuel nitrogen," Symposium (International) on Combustion, Volume 15, Issue 1, 1975, Pages 1073-1083, https://doi.org/10.1016/S0082-0784(75)80372-9.
29. Stone, R., "Introduction to Internal Combustion Engines". 4th ed. 2012, UK: Palgrave Macmillan.
30. J. Warnatz, U., U. Mass, and R.W. Dibble, "Combustion". 4th ed. 2006: Springer.
31. Lavoie G. A., Heywood J. B. & Keck J. C. (1970) "Experimental and Theoretical Study of Nitric Oxide Formation in Internal Combustion Engines," Combustion Science and Technology, 1:4, 313-326, DOI: 10.1080/00102206908952211
32. Fenimore C.P., "Formation of nitric oxide in premixed hydrocarbon flames," Symposium (International) on Combustion, Volume 13, Issue 1, 1971, Pages 373-380, https://doi.org/10.1016/S0082-0784(71)80040-1.

33. Blauwens J., Smets B., Peeters J., “Mechanism of “prompt” no formation in hydrocarbon flames,” Symposium (International) on Combustion, Volume 16, Issue 1, 1977, Pages 1055-1064, https://doi.org/10.1016/S0082-0784(77)80395-0.
34. Miller J. A., Bowman C. T., “Mechanism and modeling of nitrogen chemistry in combustion,” Progress in Energy and Combustion Science, Volume 15, Issue 4, 1989, Pages 287-338, https://doi.org/10.1016/0360-1285(89)90017-8.
35. Moskaleva L.V., Lin M.C., “The spin-conserved reaction CH+N2→H+NCN: A major pathway to prompt no studied by quantum/statistical theory calculations and kinetic modeling of rate constant,” Proceedings of the Combustion Institute, Volume 28, Issue 2, 2000, Pages 2393-2401, https://doi.org/10.1016/S0082-0784(00)80652-9.
36. A.A. Konnov, “Implementation of the NCN pathway of prompt-NO formation in the detailed reaction mechanism,” Combustion and Flame, Volume 156, Issue 11,2009, Pages 2093-2105, https://doi.org/10.1016/j.combustflame.2009.03.016.
37. Sun Z.W., Li Z.S., Konnov A.A., Aldén M., Quantitative HCN measurements in CH4/N2O/O2/N2 flames using mid-infrared polarization spectroscopy, Combustion and Flame, Volume 158, Issue 10, 2011, Pages 1898-1904, https://doi.org/10.1016/j.combustflame.2011.03.008.
38. Goos E., Sickfeld C., Mauß F., Seidel L., Ruscic B., Burcat A., Zeuch T., Prompt NO formation in flames: The influence of NCN thermochemistry, Proceedings of the Combustion Institute, Volume 34, Issue 1, 2013, Pages 657-666, https://doi.org/10.1016/j.proci.2012.06.128.
39. Majewski, W. A., Jääskeläinen H. “Exhaust Particulate Matter”. Accessed 28 July 2015; Available from: https://www.dieselnet.com/tech/dpm.php.
40. Ferguson C. R., Kirkpatrick A. T. “Internal Combustion Engines: Applied Thermosciences” 2nd ed. 2001, Wiley.
41. Eastwood, P., “Particulate Emissions from Vehicles” 2008, SAE International and John Wiley
42. Robert Bosch GmbH, “ Automotive Handbook”. 7th ed. 2007: Robert Bosch GmbH.
43. Akihama, K., Takatori, Y., Inagaki, K., Sasaki, S. et al., "Mechanism of the Smokeless Rich Diesel Combustion by Reducing Temperature," SAE Technical Paper 2001-01-0655, 2001, https://doi.org/10.4271/2001-01-0655.
44. Richie H., Roser M., “CO_2 and other Greenhouse Gas Emissions” May 2017, Accessed: October 2018; Available from: https://ourworldindata.org/co2-and-other-greenhouse-gas-emissions#emissions-by-sector.
45. Sims R., R.S., F. Creutzig, X. Cruz-Núñez, M. D’Agosto, D. Dimitriu, M.J. Figueroa Meza, L. Fulton, S. Kobayashi, O. and A.M. Lah, P. Newman, M. Ouyang, J.J. Schauer, D. Sperling, and G. Tiwari, “Climate Change 2014: Mitigation of Climate Change. Report of the Intergovernmental Panel on Climate Change”. 2014: Cambridge University Press.
46. Tietge U., M.P., German J., Bandivadekar A. and L. N., “From laboratory to road: A 2017 update of official and “real-world” fuel consumption and CO2 values for passenger cars in Europe,” The International Council on Clean Transport. November 2017. https://www.theicct.org/publications/laboratory-road-2017-update
47. Scientific Advice Mechanism, “Closing the gap between light-duty vehicle real-world CO2 emissions and laboratory testing”. 11 November 2016, European Comission.

48. Mock P., "*Real-driving emissions test procedure for exhaust gas pollutant emissions of cars and light commercial vehicles in europe"* The International Council on Clean Transport. 12 January 2017. https://www.theicct.org/publications/real-driving-emissions-test-procedure-exhaust-gas-pollutant-emissions-cars-and-light
49. Johnson, T., "Vehicular Emissions in Review," *SAE Int. J. Engines* 7(3):1207-1227, 2014, https://doi.org/10.4271/2014-01-1491.
50. Dimaratos A., T.G., Ntziachristos L., Samaras Z., "Real-world emissions testing on four vehicles" 28 August 2017, EMISIA SA.
51. Ladommatos, N., Abdelhalim, S., & Zhao, H. (2000). "The effects of exhaust gas recirculation on diesel combustion and emissions". *International Journal of Engine Research, 1*(1), 107–126. https://doi.org/10.1243/1468087001545290
52. Ladommatos, N., Balian, R., Horrocks, R., and Cooper, L., "The Effect of Exhaust Gas Recirculation on Soot Formation in a High-Speed Direct-injection Diesel Engine," SAE Technical Paper 960841, 1996, https://doi.org/10.4271/960841.
53. Kreso, A., Johnson, J., Gratz, L., Bagley, S. et al., "A Study of the Effects of Exhaust Gas Recirculation on Heavy-Duty Diesel Engine Emissions," SAE Technical Paper 981422, 1998, https://doi.org/10.4271/981422.
54. Dec J. E., "Advanced compression-ignition engines—understanding the in-cylinder processes," Proceedings of the Combustion Institute, Volume 32, Issue 2, 2009, Pages 2727-2742, https://doi.org/10.1016/j.proci.2008.08.008.
55. Kook, S., Bae, C., Miles, P., Choi, D. et al., "The Effect of Swirl Ratio and Fuel Injection Parameters on CO Emission and Fuel Conversion Efficiency for High-Dilution, Low-Temperature Combustion in an Automotive Diesel Engine," SAE Technical Paper 2006-01-0197, 2006, https://doi.org/10.4271/2006-01-0197.
56. Papaioannou, N., Leach, F. C., Davy, M. H., Weall, A., & Cooper, B. (2018). "Evaluation of exhaust gas recirculation techniques on a high-speed direct injection diesel engine using first law analysis." *Proceedings of the Institution of Mechanical Engineers, Part D: Journal of Automobile Engineering*. https://doi.org/10.1177/0954407017749110
57. Robert Bosch GmbH, Accessed: 28 August 2015, http://de.bosch-automotive.com/en/parts/parts_and_accessories/motor_and_sytems/diesel/common_rail_injection/common_rail_diesel_motorsys_parts.
58. Beard, C., "Diesel engine reference book", Editors: Challen B. and Baranescu. R., 1999, Butterworth Heinemann.
59. Sahoo, D., Miles, P., Trost, J., and Leipertz, A., "The Impact of Fuel Mass, Injection Pressure, Ambient Temperature, and Swirl Ratio on the Mixture Preparation of a Pilot Injection," *SAE Int. J. Engines* 6(3):1716-1730, 2013, https://doi.org/10.4271/2013-24-0061.
60. Naeim A. Henein, "Analysis of pollutant formation and control and fuel economy in diesel engines", Progress in Energy and Combustion Science, Volume 1, Issue 4, 1976, Pages 165-207, https://doi.org/10.1016/0360-1285(76)90013-7.
61. Robert Bosch GmbH, "Diesel-Engine Management". 4th ed. 2006, Wiley-Blackwell.
62. Posada, F., Bandivadekar, A., and German, J., "Estimated Cost of Emission Control Technologies for Light-Duty Vehicles Part 2 - Diesel," SAE Technical Paper 2013-01-0539, 2013, https://doi.org/10.4271/2013-01-0539.
63. Johnson, T., "Diesel Emissions in Review," *SAE Int. J. Engines* 4(1):143-157, 2011, https://doi.org/10.4271/2011-01-0304.

64. Naber, J. and Siebers, D., "Effects of Gas Density and Vaporization on Penetration and Dispersion of Diesel Sprays," SAE Technical Paper 960034, 1996, https://doi.org/10.4271/960034.
65. Andersson, Ö., Somhorst, J., Lindgren, R., Blom, R. et al., "Development of the Euro 5 Combustion System for Volvo Cars' 2.4.I Diesel Engine," SAE Technical Paper 2009-01-1450, 2009, https://doi.org/10.4271/2009-01-1450.
66. Miles, P. C., "Turbulent Flow Structure in Direct-Injection, Swirl-Supported Diesel Engine, in Flow and Combustion in Reciprocating Engines," Editors: C. Arcoumanis and T. Kamimoto, 2009, Springer-Verlag Berlin Heidelberg, Germany.
67. Dec, J. and Tree, D., "Diffusion-Flame / Wall Interactions in a Heavy-Duty DI Diesel Engine," SAE Technical Paper 2001-01-1295, 2001, https://doi.org/10.4271/2001-01-1295.
68. Miles, P. C., & Andersson, Ö. (2016). "A review of design considerations for light-duty diesel combustion systems." *International Journal of Engine Research*, *17*(1), 6–15. https://doi.org/10.1177/1468087415604754
69. Cursente, V., Pacaud, P., and Gatellier, B., "Reduction of the Compression Ratio on a HSDI Diesel Engine: Combustion Design Evolution for Compliance the Future Emission Standards," *SAE Int. J. Fuels Lubr.* 1(1):420-439, 2009, https://doi.org/10.4271/2008-01-0839.
70. Fasolo, B., Doisy, A., Dupont, A., and Lavoisier, F., "Combustion System Optimization of a New 2 Liter Diesel Engine For EURO IV," SAE Technical Paper 2005-01-0652, 2005, https://doi.org/10.4271/2005-01-0652.
71. Dakhore, R., Gandhi, N., Gokhale, N., Aghav, Y. et al., "Effect of Piston Cavity Geometry on Combustion, Emission and Performance of a Medium Duty DI Diesel Engine," SAE Technical Paper 2015-26-0198, 2015, https://doi.org/10.4271/2015-26-0198.
72. Leach, F., Ismail, R., Davy, M., Weall, A. et al., "Comparing the Effect of Fuel/Air Interactions in a Modern High-Speed Light-Duty Diesel Engine," SAE Technical Paper 2017-24-0075, 2017, https://doi.org/10.4271/2017-24-0075.
73. Leach F., Ismail R., Davy M., Weall A., Cooper B., "The effect of a stepped lip piston design on performance and emissions from a high-speed diesel engine," Applied Energy, Volume 215, 2018, Pages 679-689, https://doi.org/10.1016/j.apenergy.2018.02.076.
74. Dahlstrom, J., Andersson, O., Tuner, M., and Persson, H., "Experimental Comparison of Heat Losses in Stepped-Bowl and Re-Entrant Combustion Chambers in a Light Duty Diesel Engine," SAE Technical Paper 2016-01-0732, 2016, https://doi.org/10.4271/2016-01-0732.
75. Sher I., Levinzon-Sher D., Sher E., "Miniaturization limitations of HCCI internal combustion engines," Applied Thermal Engineering, Volume 29, Issues 2–3, 2009, Pages 400-411, https://doi.org/10.1016/j.applthermaleng.2008.03.020.
76. Arato, K. and Takashima, T., "A Study on Reduction of Heat Loss by Optimizing Combustion Chamber Shape," *SAE Int. J. Engines* 8(2):596-608, 2015, https://doi.org/10.4271/2015-01-0786.
77. Binder, C., Abou Nada, F., Richter, M., Cronhjort, A. et al., "Heat Loss Analysis of a Steel Piston and a YSZ Coated Piston in a Heavy-Duty Diesel Engine Using Phosphor Thermometry Measurements," *SAE Int. J. Engines* 10(4):1954-1968, 2017, https://doi.org/10.4271/2017-01-1046.

78. Dickey, D., "The Effect of Insulated Combustion Chamber Surfaces on Direct-Injected Diesel Engine Performance, Emissions and Combustion," SAE Technical Paper 890292, 1989, https://doi.org/10.4271/890292.
79. Kimura, S., Matsui, Y., and Itoh, T., "Effects of Combustion Chamber Insulation on the Heat Rejection and Thermal Efficiency of Diesel Engines," SAE Technical Paper 920543, 1992, https://doi.org/10.4271/920543.
80. Kosaka, H., Wakisaka, Y., Nomura, Y., Hotta, Y. et al., "Concept of "Temperature Swing Heat Insulation" in Combustion Chamber Walls, and Appropriate Thermo-Physical Properties for Heat Insulation Coat," *SAE Int. J. Engines* 6(1):142-149, 2013, https://doi.org/10.4271/2013-01-0274.
81. Fukui, K., Wakisaka, Y., Nishikawa, K., Hattori, Y. et al., "Development of Instantaneous Temperature Measurement Technique for Combustion Chamber Surface and Verification of Temperature Swing Concept," SAE Technical Paper 2016-01-0675, 2016, https://doi.org/10.4271/2016-01-0675.
82. Wakisaka, Y., Inayoshi, M., Fukui, K., Kosaka, H. et al., "Reduction of Heat Loss and Improvement of Thermal Efficiency by Application of "Temperature Swing" Insulation to Direct-Injection Diesel Engines," *SAE Int. J. Engines* 9(3):1449-1459, 2016, https://doi.org/10.4271/2016-01-0661.
83. Kawaguchi, A., Iguma, H., Yamashita, H., Takada, N. et al., "Thermo-Swing Wall Insulation Technology; - A Novel Heat Loss Reduction Approach on Engine Combustion Chamber" SAE Technical Paper 2016-01-2333, 2016, https://doi.org/10.4271/2016-01-2333.
84. Metoki, S. and Negishi, H., "Why are NCI Pistons Not Used in Heavy Duty Diesel Engines?," SAE Technical Paper 2002-01-0164, 2002, https://doi.org/10.4271/2002-01-0164.
85. Kumarasekaran, K. and Safdari, Y., "Thermal Stress Analysis of a Novel Design Air-Gap Insulated Piston," SAE Technical Paper 941069, 1994, https://doi.org/10.4271/941069.
86. Reipert, P., Mielke, S., and Essig, G., "Pistons of DI-Diesel Engines with Reduced Heat Flow," SAE Technical Paper 891899, 1989, https://doi.org/10.4271/891899.
87. Schreer K, Roth I, Schneider S, Ehnis H. "Analysis of Aluminum and Steel Pistons: Comparison of Friction, Piston Temperature, and Combustion." ASME. Internal Combustion Engine Division Fall Technical Conference, *Volume 2: Fuels; Numerical Simulation; Engine Design, Lubrication, and Applications*. https://doi:10.1115/ICEF2013-19114.
88. Gabriel, D. and Hettich, T., "TopWeld® Steel Piston for High Speed Diesel Engines," SAE Technical Paper 2015-01-1723, 2015, https://doi.org/10.4271/2015-01-1723.
89. Cheng, K. Y., Shayler, P. J., & Murphy, M. (2004). "The influence of blow-by on indicated work output from a diesel engine under cold start conditions." *Proceedings of the Institution of Mechanical Engineers, Part D: Journal of Automobile Engineering*, *218*(3), 333–340. https://doi.org/10.1243/095440704322955858.
90. Incropera F., D.D., Bergman T., Lavine A, "Fundamental of Heat and Mass Transfer." 6th ed. 2007, US: John Wiley & Sons.
91. Whitaker, S. (1972), Forced convection heat transfer correlations for flow in pipes, past flat plates, single cylinders, single spheres, and for flow in packed beds and tube bundles. AIChE J., 18: 361-371. doi:10.1002/aic.690180219.

92. Ament, F., Patterson, D., and Mueller, A., "Heat Balance Provides Insight into Modern Engine Fuel Utilization," SAE Technical Paper 770221, 1977, https://doi.org/10.4271/770221.
93. Alkidas, A., "The Use of Availability and Energy Balances in Diesel Engines," SAE Technical Paper 890822, 1989, https://doi.org/10.4271/890822.
94. Alkidas, A. and Cole, R., "The Distribution of Heat Rejection from a Single-Cylinder Divided-Chamber Diesel Engine," SAE Technical Paper 810959, 1981, https://doi.org/10.4271/810959.
95. Anderson, M., Assanis, D., and Filipi, Z., "First and Second Law Analyses of a Naturally-Aspirated, Miller Cycle, SI Engine with Late Intake Valve Closure," SAE Technical Paper 980889, 1998, https://doi.org/10.4271/980889.
96. Payri, F., Martin, J., Garcia, A., and Carreño, R., "Experimental and Theoretical Analysis of the Energy Balance in a DI Diesel Engine," SAE Technical Paper 2015-01-1651, 2015, https://doi.org/10.4271/2015-01-1651.
97. Olmeda, P., Martin, J., Garcia, A., Blanco, D. et al., "Evaluation of EGR Effect on the Global Energy Balance of a High Speed DI Diesel Engine," SAE Technical Paper 2016-01-0646, 2016, https://doi.org/10.4271/2016-01-0646.
98. Romero, C., Torregrosa, A., Olmeda, P., and Martin, J., "Energy Balance During the Warm-Up of a Diesel Engine," SAE Technical Paper 2014-01-0676, 2014, https://doi.org/10.4271/2014-01-0676.
99. Smith, L., Preston, W., Dowd, G., Taylor, O. et al., "Application of a First Law Heat Balance Method to a Turbocharged Automotive Diesel Engine," SAE Technical Paper 2009-01-2744, 2009, https://doi.org/10.4271/2009-01-2744.
100. Donn, C., Zulehner, W., Ghebru, D., Spicher, U. et al., "Experimental Heat Flux Analysis of an Automotive Diesel Engine in Steady-State Operation and During Warm-Up," SAE Technical Paper 2011-24-0067, 2011, https://doi.org/10.4271/2011-24-0067.
101. Mendoza, M. and Woon, P., "E-diesel Effects on Engine Component Temperature and Heat Balance in a Cummins C8.3 Engine," SAE Technical Paper 2002-01-2847, 2002, https://doi.org/10.4271/2002-01-2847.
102. Olmeda, P., Martín, J., Blanco-Cavero, D., Warey, A., & Domenech, V. (2017). Effect of in-cylinder swirl on engine efficiency and heat rejection in a light-duty diesel engine. *International Journal of Engine Research*, *18*(1–2), 81–92. https://doi.org/10.1177/1468087417693078
103. Caton, J., "Comparisons of Thermocouple, Time-Averaged and Mass-Averaged Exhaust Gas Temperatures for a Spark-Ignited Engine," SAE Technical Paper 820050, 1982, https://doi.org/10.4271/820050.
104. Dantec Dynamics, Accessed 29 Septemebr 2018, Available from: https://www.dantecdynamics.com/probe-menu-overview.
105. Papaioannou, N., Leach, F., and Davy, M., "Effect of Thermocouple Size on the Measurement of Exhaust Gas Temperature in Internal Combustion Engines," SAE Technical Paper 2018-01-1765, 2018, https://doi.org/10.4271/2018-01-1765.
106. Chittick, S., Swindell, M., and Raorane, S., "Analytical and Developmental Techniques Utilized in the Structural Optimization of a New Lightweight Diesel Engine," *SAE Int. J. Engines* 8(4):1960-1966, 2015, https://doi.org/10.4271/2015-01-2298.
107. Luff, D., Law, T., Shayler, P., and Pegg, I., "The Effect of Piston Cooling Jets on Diesel Engine Piston Temperatures, Emissions and Fuel Consumption," *SAE Int. J. Engines*5(3):1300-1311, 2012, https://doi.org/10.4271/2012-01-1212.

108. PEAK Sensors. *Compensating cable: What is a Compensating cable?* . Accessed: 13 August 2018, Available from: https://www.peaksensors.co.uk/what-is/compensating-cable/.
109. Hribernik, A., "Statistical Determination of Correlation Between Pressure and Crankshaft Angle During Indication of Combustion Engines," SAE Technical Paper 982541, 1998, https://doi.org/10.4271/982541.
110. AVL GmbH, "AVL CONCERTO Application Notes". 2015.
111. Leach, F., Davy, M., Henry, M., Tombs, M. et al., "A New Method for Measuring Fuel Flow in an Individual Injection in Real Time," *SAE Int. J. Engines* 11(6):2018, https://doi.org/10.4271/2018-01-0285.
112. Doebelin, E.O., *Measuring Systems Application and Design*. 4th ed. 1990: McGraw-Hill
113. Kar, K., Roberts, S., Stone, R., Oldfield, M. et al., "Instantaneous Exhaust Temperature Measurements Using Thermocouple Compensation Techniques," SAE Technical Paper 2004-01-1418, 2004, https://doi.org/10.4271/2004-01-1418.
114. OMEGA Engineering. "Thermocouple Wire". Accessed 13 August 2018, Available from: https://www.omega.co.uk/prodinfo/thermocouple-cable.html.
115. OMEGA Engineeering. "Fine gauge bare wire and insulated thermocouples". Accessed 13 August 2018, Available from: https://www.omega.co.uk/subsection/fine-bare-wire-insulated-thermocouples.html
116. NIST. "NIST ITS-90 Thermocouple Database". Accessed: 13 August 2018. Available from: https://srdata.nist.gov/its90/main/
117. FLUKE Calibration. "Calibration Bath Fluids". Accessed: 13 August 2018, Available from: https://eu.flukecal.com/products/temperature-calibration/calibration-baths/bath-fluids/calibration-bath-fluids?quicktabs_product_details=0.
118. Rusby, R., "Introduction to Temperature measurement", in *Good Practise Guide No. 125*. 2016, National Physical Laboratory.
119. Horiba. "Specifications MEXA-ONE System Line-up". Accessed: 29 July 2015, Available from:http://www.horiba.com/uk/automotive-test-systems/products/emission-measurement-systems/analytical-systems/standard-emissions/details/new-standard-in-emission-testing-mexa-one-16671/.
120. AVL GmbH, "AVL415S Variable sampling smoke meter Operating manual", 2005.
121. Moffat R. J., "Describing the uncertainties in experimental results," Experimental Thermal and Fluid Science, Volume 1, Issue 1, 1988, Pages 3-17, https://doi.org/10.1016/0894-1777(88)90043-X.
122. Abernethy RB, Benedict RP, Dowdell RB. "ASME Measurement Uncertainty". ASME. *J. Fluids Eng.* 1985;107(2):161-164. https://doi:10.1115/1.3242450.
123. Ross, S.M., *Introduction to probability and statistics for engineers and scientists*. 1987, New York: John Wiley and Sons.
124. Abernethy, R. B. and Thompson J. W., "Handbook Uncertainty in Gas Turbine Measurements". 1973, Arnold Engineering Developement Centre.
125. McBride J. B., G.S., Reno A. M., "Coefficients for calculating thermodynamic and transport properties of individual species", in *NASA Technical memorandum 4513*. 1993, NASA.
126. Silvis, W., "An Algorithm for Calculating the Air/Fuel Ratio from Exhaust Emissions," SAE Technical Paper 970514, 1997, https://doi.org/10.4271/970514.

127. Larsson, R., & Andersson, O. (2000). “Lubricant thermal conductivity and heat capacity under high pressure”. *Proceedings of the Institution of Mechanical Engineers, Part J: Journal of Engineering Tribology*, *214*(4), 337–342. https://doi.org/10.1243/1350650001543223
128. Duboc B., “The effect of fuel additives on diesel fuel delivery system and combustion performance”. PhD thesis, 2014, University College London: London.
129. Takeshi Konno, Mitsuru Egashira & Mikihiko Kobayashi (2015) “Welding process and characteristics of fine K-type thermocouple: non-contact discharge welding for fine metal wires”, Welding International, 29:11, 829-837, DOI: 10.1080/09507116.2014.921077
130. Brundage L. A., K.P.S., Burl Donaldson A., Nicolette F. V., Gill W., “A joint computational and experimental study to evaluate Inconel-sheathed thermocouple performance in flames”. 2005, Sandia National Laboratories.
131. Eckert, E.R.G., Drake R.M., “Heat and Mass Transfer”. 1974, New Delhi: TATA McGraw-Hill.
132. Khine, S.M., T. Houra, and M. Tagawa, “Heat-conduction error of temperature sensors in a fluid flow with nonuniform and unsteady temperature distribution”. Review of Scientific Instruments, 2013. **84**(4): p. 044902. https://doi.org/10.1063/1.4801853
133. Shaddix, C. R., “Correcting thermocouple measurements for radiation loss: A critical review.” Sandia National Labs., Livermore, CA (US). Paper NHTC99.282, 1997.
134. Ran Fu T, Bin Tian J, Sheng Wang H. “Apparent Emissivity of Combustion Soot Aggregate Coating at High Temperature.” ASME. *J. Heat Transfer*. 2017;139(4):042701-042701-7. http://doi:10.1115/1.4035102 .
135. Köpple, F., Seboldt, D., Jochmann, P., Hettinger, A. et al., "Experimental Investigation of Fuel Impingement and Spray-Cooling on the Piston of a GDI Engine via Instantaneous Surface Temperature Measurements," *SAE Int. J. Engines*7(3):1178-1194, 2014, https://doi.org/10.4271/2014-01-1447.
136. Dupont, A., et al., “Influence of temperature on the frequency response of fine-wire thermocouples over the range (300K-800K) in airflows.” Journal of Physics E: Scientific Instruments, 1984. **17**(9): p. 808, https://doi.org/10.1088/0022-3735/17/9/019
137. Heitor, M.V., Taylor, A.M.K.P. & Whitelaw, J.H. “Simultaneous velocity and temperature measurements in a premixed flame”, Experiments in Fluids (1985) 3: 323. https://doi.org/10.1007/BF01830191
138. Hopkins, K.C., J.C. Larue, and G.S. Samuelsen, “Effect of Mean and Variable Time Constant on Compensated Thermocouple Measurements, in Instrumentation for Combustion and Flow in Engines”, D.F.G. Durão, J.H. Whitelaw, and P.O. Witze, Editors. 1989, Springer Netherlands: Dordrecht. p. 55-68.
139. Forney, L.J. and G.C. Fralick, “Three- wire thermocouple: Frequency response in constant flow.” Review of Scientific Instruments, 1995. **66**(5): p. 3331-3336. https://doi.org/10.1063/1.1145503
140. Kee, R., Hung, P., Fleck, B., Irwin, G. et al., "Fast Response Exhaust Gas Temperature Measurement in IC Engines," SAE Technical Paper 2006-01-1319, 2006, https://doi.org/10.4271/2006-01-1319.
141. Tagawa, M. and Y. Ohta, *Two-thermocouple probe for fluctuating temperature measurement in combustion—Rational estimation of mean and fluctuating time*

constants. Combustion and Flame, 1997. **109**(4): p. 549-560. https://doi.org/10.1016/S0010-2180(97)00044-8.

142. Cherian A. Idicheria, Lyle M. Pickett, "Effect of EGR on diesel premixed-burn equivalence ratio", Proceedings of the Combustion Institute, Volume 31, Issue 2, 2007, Pages 2931-2938, https://doi.org/10.1016/j.proci.2006.08.022.
143. Kimura, S., Aoki, O., Kitahara, Y., and Aiyoshizawa, E., "Ultra-Clean Combustion Technology Combining a Low-Temperature and Premixed Combustion Concept for Meeting Future Emission Standards," SAE Technical Paper 2001-01-0200, 2001, https://doi.org/10.4271/2001-01-0200.
144. Wagner, R., Green, J., Dam, T., Edwards, K. et al., "Simultaneous Low Engine-Out NOx and Particulate Matter with Highly Diluted Diesel Combustion," SAE Technical Paper 2003-01-0262, 2003, https://doi.org/10.4271/2003-01-0262.
145. Henein, N., Bhattacharyya, A., Schipper, J., Kastury, A. et al., "Effect of Injection Pressure and Swirl Motion on Diesel Engine-out Emissions in Conventional and Advanced Combustion Regimes," SAE Technical Paper 2006-01-0076, 2006, https://doi.org/10.4271/2006-01-0076.
146. Mahle, "Pistons and engine testing." 2 ed. ATZ/MTZ-Fachbuch. 2016: Springer Vieweg.
147. Ladommatos, N., Xiao, Z., & Zhao, H. (2005). "The effect of piston bowl temperature on diesel exhaust emissions". *Proceedings of the Institution of Mechanical Engineers, Part D: Journal of Automobile Engineering*, *219*(3), 371–388. https://doi.org/10.1243/095440705X6550
148. Rao, V., Gardiner, D., and Bardon, M., "Effects of Gas Leakage and Crevices on Cold Starting of Engines," SAE Technical Paper 940078, 1994, https://doi.org/10.4271/940078.
149. Mavropoulos, G. C., "Unsteady Heat Conduction Phenomena in Internal Combustion Engine Chamber and Exhaust Manifold Surfaces". Heat Transfer - Engineering Applications, ed. V. Vikhrenko. 2011, Croatia: Intech.
150. Heuer T, Engels B, Klein A, Heger H. "Numerical and Experimental Analysis of the Thermo-Mechanical Load on Turbine Wheels of Turbochargers". ASME. Turbo Expo: Power for Land, Sea, and Air, *Volume 5: Marine; Microturbines and Small Turbomachinery; Oil and Gas Applications; Structures and Dynamics, Parts A and B* ():325-332. https://doi:10.1115/GT2006-90526.
151. Mollenhauer, K., "Measurement of Instantaneous Gas Temperatures for Determination of the Exhaust Gas Energy of a Supercharged Diesel Engine," SAE Technical Paper 670929, 1967, https://doi.org/10.4271/670929.
152. Tsinoglou, D. N., & Koltsakis, G. C. (2002). "Potential of thermal methods for catalyst on-board diagnosis". *Proceedings of the Institution of Mechanical Engineers, Part D: Journal of Automobile Engineering*, *216*(7), 565-579. https://doi.org/10.1243/095440702760178596
153. W. J. Fleming, "Overview of automotive sensors," in *IEEE Sensors Journal*, vol. 1, no. 4, pp. 296-308, Dec. 2001. https://doi.org/10.1109/7361.983469
154. West W. E. and Westwater J. W., "Radiation-Conduction Correction for Temperature Measurements in Hot Gase**s",***Industrial & Engineering Chemistry* 1953 *45* (10), 2152-2156, https://doi.org/10.1021/ie50526a022.

155. Bradley, D., & J., K. (1968). "Measurement of High Gas Temperatures with Fine Wire Thermocouples". *Journal of Mechanical Engineering Science*, *10*(4), 299–305. https://doi.org/10.1243/JMES_JOUR_1968_010_048_02

156. Kee, R., O'Reilly, P., Fleck, R., and McEntee, P., "Measurement of Exhaust Gas Temperatures in a High Performance Two-Stroke Engine," SAE Technical Paper 983072, 1998, https://doi.org/10.4271/983072.
157. Kar K, Swain AK, Raine R. Identification of Time-Varying Time Constants of Thermocouple Sensors and Its Application to Temperature Measurement. ASME. *J. Dyn. Sys., Meas., Control*. 2008;131(1):011005-011005-10. https://doi:10.1115/1.3023111.
158. Kobus, C.J., "True fluid temperature reconstruction compensating for conduction error in the temperature measurement of steady fluid flows". Review of Scientific Instruments, 2006. **77**(3): p. 034903. https://doi.org/10.1063/1.2186211
159. Leach, F.C.P., et al., "An optical method for measuring exhaust gas pressure from an internal combustion engine at high speed". Review of Scientific Instruments, 2017. **88**(12): p. 125004. https://doi.org/10.1063/1.5005161
160. Warren, R.C., *Design of Thermocouple Probes for Measurement of Rocket Exhaust Plume Temperatures*. 1994, Aeronautical and Maritime Research Laboratory: Melbourne, Australia.
161. Campbell A. B. and Jennings B. H., *Gas Dynamics*. 1958, McGraw-Hill: New York.